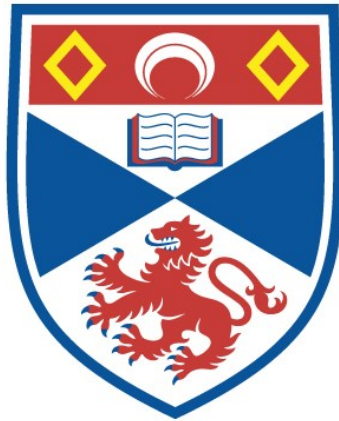


THE BIVARIATE SPACE DENSITY OF GALAXIES

Nicholas James Geraint Cross

**A Thesis Submitted for the Degree of PhD
at the
University of St Andrews**



2002

**Full metadata for this item is available in
St Andrews Research Repository
at:**

<http://research-repository.st-andrews.ac.uk/>

Please use this identifier to cite or link to this item:

<http://hdl.handle.net/10023/12935>

This item is protected by original copyright

The Bivariate Space Density of Galaxies

by

Nicholas James Geraint Cross



A thesis submitted to the
University of St Andrews
for the degree of
Doctor of Philosophy

November, 2001



ProQuest Number: 10166887

All rights reserved

INFORMATION TO ALL USERS

The quality of this reproduction is dependent upon the quality of the copy submitted.

In the unlikely event that the author did not send a complete manuscript and there are missing pages, these will be noted. Also, if material had to be removed, a note will indicate the deletion.



ProQuest 10166887

Published by ProQuest LLC (2017). Copyright of the Dissertation is held by the Author.

All rights reserved.

This work is protected against unauthorized copying under Title 17, United States Code
Microform Edition © ProQuest LLC.

ProQuest LLC.
789 East Eisenhower Parkway
P.O. Box 1346
Ann Arbor, MI 48106 – 1346

π
E164

I, Nicholas James Geraint Cross, hereby certify that this thesis, which is approximately 50000 words in length, has been written by me, that it is the record of work carried out by me and that it has not been submitted in any previous application for a higher degree.

November 2001

I was admitted as a research student in October 1998 and as a candidate for the degree of Ph.D. in October 1998; the higher study for which this is a record was carried out at the University of St. Andrews between 1998 and 2001.

November 2001

In submitting this thesis to the University of St. Andrews I understand that I am giving permission for it to be made available for use in accordance with the regulations of the University Library for the time being in force, subject to any copyright vested in the work not being affected thereby. I also understand that the title and abstract will be published, and that a copy of the work may be made and supplied to any *bona fide* library or research worker.

November 2001

I hereby certify that the candidate has fulfilled the conditions of the Resolution and Regulations appropriate for the degree of Ph.D. in the University of St. Andrews and that the candidate is qualified to submit this thesis in application for that degree.

November 2001

Acknowledgements

I would like to thank my parents for their support and love throughout. They have always encouraged me to choose the career that I enjoy most, and I am glad that I listened to their advice. I would like to thank them and Uncle Nick for their generosity throughout my years at university.

I would like to thank my supervisor, Simon Driver, for his time, patience and advice, not only in astronomy related matters. I would like to thank my colleagues in St Andrews, David Lemon and Jo Liske for their comments, discussions and deserved criticism throughout the last year or two. A big thanks also goes to Rosie Wyse, Ian Bonnell and Phil Armitage for their comments on various chapters. In particular I thank Rosie for the discussions on galaxy formation.

I have been very fortunate to have been part of the Two degree Galaxy Redshift Survey Team. I have learned a lot from the various meetings and discussions and this thesis would not be possible without the huge amount of time that the team have put into collecting, reducing and analysing this huge data set. In particular, I would like to thank Warrick Couch, Shaun Cole, John Peacock and Peder Norberg for their comments and help over the years. I would also like to thank the members of the INT Wide Field Survey Team for helping to collect the data for the Millennium Galaxy Catalogue, which was so essential to this thesis. I would also like to thank Steve Phillipps, who has helped me to understand visibility theory and, along with Simon, Warrick and John, has provided useful job references.

I thank Jayne, Stan and Charles, who have been my closest friends for so many years and have always been there when I need them. Cathy who helped me so much through my first degree and who I can always count on to keep me in touch with friends from Cambridge and to have a party. I would like to say thankyou to Eliza, who has been so kind and cheerful and given me endless cups of tea.

I thank friends from the diving club particularly Warren, Bruce, Maryanne, Frank and Chris who have helped me to enjoy the Fife coastline and the west coast of Scotland. Thanks to Tim Rachel and Yiannis for being good friends over the last few years. Special thanks to Alison and Dave who have put up with sharing an office with me as my sanity has ebbed away.

Thanks must also go to Bill and Czeslawa who put up with me in their house for two years and who were always kind and generous. Many thanks to my flatmates Alan and Jamie for reading through chapters and offering advice.

Lastly, my thanks to Charlotte Bjuren, who has helped me through the final stages. She has been there when I have found it difficult and given me additional incentive to work hard through the last few months. She more than anyone has helped me to remain calm and sane.

Abstract

The luminosity function of galaxies, the measurement of the space density as a function of luminosity, is an important test of cosmology, galaxy formation and evolution. Unfortunately, there is a factor of two variation in recent measurements of the luminosity function. Most of this variation is due to systematic errors, caused by various selection effects. With two large new surveys, the Two degree Field Galaxy Redshift Survey and the Sloan Digital Sky Survey, underway it is important to recognise and eliminate these selection effects if we are going to improve our measurement of the luminosity function and fully utilise these surveys.

By measuring the space density of galaxies as a function of surface brightness as well as luminosity, a bivariate brightness distribution, we can comprehend many of the selection effects such as light loss, incompleteness and the visibility of galaxies. Since galaxies have a variety of shapes and sizes, a distribution in luminosity and surface brightness helps to separate out different types of galaxy. Correlations between the luminosity and surface brightness place extra constraints on models of galaxy formation and evolution.

When we analyse our results, we find that recent surveys that have not taken into account surface brightness selection effects underestimate the luminosity of the bright end by 5-10%. Using the bivariate brightness distribution, we can constrain the luminosity density to a range that varies by $< 20\%$ rather than by a factor of 2. We find that the luminosity function is flat over the range $-19.5 < M < -17$ and then rises sharply as late-type spiral galaxies begin to dominate. The space density does not vary with surface brightness with the result that low surface brightness galaxies are at least as common as normal galaxies. However, low surface brightness galaxies are also intrinsically faint, following the luminosity-surface brightness correlation for spirals, so they do not contribute significantly to the luminosity density.

Contents

Declaration	2
1 Introduction	1
1.1 Introduction	1
1.2 Types of Galaxy	5
1.2.1 Extreme Galaxies	6
1.2.2 Giant Low Surface Brightness Galaxies	8
1.3 Measuring the Space Density of Galaxies	9
1.3.1 Luminosity Functions	9
1.3.2 Modern Measurements of the GLF	12
1.3.3 Why is there so much variation in the LF?	16
1.3.4 Surface Brightness Distributions	17
1.3.5 The Bivariate Brightness Distribution	19
1.3.6 Difficulties with Measuring the Space Density	21
1.3.7 Techniques used to measure the Space Density.	22
1.4 Uses of the Bivariate Brightness Distribution of Galaxies	24
1.4.1 The Luminosity Density and the Star Formation Rate	24
1.4.2 Using the Luminosity Function and Number Counts to Constrain Cosmology and Evolution	24
1.4.3 Constraints on Galaxy Formation Models from the BBD.	25
1.4.4 Mass to Light Ratios and constraints on Ω_M	26
1.5 Summary	26
2 The Methodology Used to Produce the Bivariate Brightness Distribution.	29
2.1 Introduction	29
2.2 Cosmology Equations	30
2.3 Useful Relations Between Photometric Properties of Galaxies	32
2.4 Visibility	35
2.4.1 A Thorough Example: Exponential Profiles.	36
2.5 The Isophotal Correction and Effective Surface Brightness	38
2.6 The Bivariate Brightness Distribution	39
2.6.1 An Empirical Method	40
2.6.2 Stepwise Maximum Likelihood	47
2.6.3 Comparing the Two Methods	52
2.7 An Analytical Function for the Bivariate Brightness Distribution	58
2.7.1 A Bivariate Brightness Function	58
2.7.2 Fitting a Bivariate Brightness Function	59
2.7.3 Comparison with de Jong & Lacey and Blanton	61
2.7.4 Calculating the Luminosity Density	62
2.8 Exploring Surface Brightness Selection Effects	63
2.9 Summary	70
3 A Deep Wide Field Redshift Database: Matching the MGC to the 2dFGRS and the SDSS-EDR.	72
3.1 Introduction	73
3.2 Data	73
3.2.1 The 2dFGRS	73
3.2.2 The MGC.	80
3.2.3 The SDSS-EDR	83
3.3 Matching the 2dFGRS objects to objects in the MGC.	84
3.3.1 The number of matches.	85
3.3.2 Mismatches	86
3.3.3 Multiple 2dFGRS matches	88
3.3.4 Galaxies, Stars and Unclassified objects	88
3.4 Matching the SDSS-EDR to the MGC	88

3.5	Photometric Comparison.	89
3.5.1	Photometric accuracy of 2dFGRS.	89
3.5.2	2dFGRS galaxies	94
3.5.3	Comparison with the SDSS-EDR	97
3.5.4	Variations with Redshift	100
3.6	MGC bright catalogue	105
3.7	Incompleteness of 2dFGRS	108
3.7.1	Types of Galaxy Missing from 2dFGRS	110
3.8	Incompleteness of the SDSS-EDR	111
3.9	Producing the MGC/2dFGRS/SDSS-EDR BBD.	111
3.9.1	The Photometric and Redshift Completeness.	111
3.10	Summary.	117
4	The MGC Bivariate Brightness Distribution.	119
4.1	Introduction	119
4.2	Producing the MGC BBD.	120
4.2.1	The Distribution in the M, μ_e plane	121
4.3	The MGC BBD	127
4.4	The Space Density of Galaxies	134
4.4.1	The Bivariate Brightness Function.	138
4.4.2	The Luminosity Function, Surface Brightness Function and Luminosity Density.	139
4.4.3	Λ -CDM Cosmology.	144
4.5	Summary	145
5	Using the 2dFGRS to measure the the BBD as a Function of Spectral Type.	147
5.1	Introduction	148
5.1.1	Photometric Corrections	149
5.1.2	Incompleteness and Stellar Contamination	152
5.2	Overall BBD	155
5.3	The BBD as a Function of Spectral Type	158
5.3.1	Comparison with Theory	163
5.3.2	Comparison with other Observers	165
5.3.3	Luminosity Functions of η -types.	166
5.4	Missing Galaxies	167
5.5	Summary	167
6	Conclusions	171
6.1	Conclusions	171
6.2	Summary and Future Work.	177
A	Appendix	i
A.1	Magnitudes.	i
A.1.1	Comparison of Magnitude Systems.	viii
A.1.2	Problems of Inclination	xxiv
A.1.3	Summary and Discussion of Magnitude Systems.	xxv
A.2	Detecting Galaxies and Separating them from Stars	xxvi
A.2.1	Demonstrating Visibility	xxix

List of Figures

1.1	The variation amongst recent LFs	3
1.2	The Distribution of Different Types of Galaxy in M_B & μ_e	7
1.3	The Distribution of Different Types of Galaxy from recent surveys	10
2.1	$\phi(z)$ vs z	44
2.2	M vs z and μ vs z	46
2.3	$z_{max}(M, \mu)$ calculated from visibility theory	50
2.4	Visibility applied to SWML.	51
2.5	The apparent BBD for the 2dFGRS	53
2.6	The distribution in M and μ_e for the 2dFGRS	54
2.7	The steps to producing the BBD using the Empirical Method	55
2.8	The Bivariate Brightness Distribution from the 2dFGRS	56
2.9	The Luminosity Function for the 2dFGRS	57
2.10	The error ellipses for the both methods	58
2.11	The Bivariate Brightness Function	60
2.12	$N(M, \mu)$ for a mock catalogue	64
2.13	Visibility plots as a function of μ_{lim}	65
2.14	$N(M)$ for isophotal, corrected and total magnitudes	67
2.15	Variation of the LF as a function of μ_{lim}	68
3.1	2dFGRS NGP & SGP	74
3.2	The APM Survey	75
3.3	Histograms of A_{iso} for the NGP and SGP.	77
3.4	2dF Instrument	78
3.5	Configuration of a 2dFGRS field	79
3.6	Plot showing the arrangement of a MGC field	81
3.7	The SDSS matches to MGC galaxies	83
3.8	$N(z)$ at low redshift, showing stars and galaxies	85
3.9	2dFGRS object 307982	86
3.10	2dFGRS object 304594	87
3.11	Histogram of $\Delta m(MGC - 2dF)$	90
3.12	Objects with large photometric errors	91
3.13	Photometry of multiples	92
3.14	Photometry of Stars	93
3.15	$(MGC - 2dF)$ vs MGC field	95
3.16	$(MGC - 2dF)$ vs UKST plate	95
3.17	$(MGC - 2dF)$ vs B_{MGC}	96
3.18	$(MGC - 2dF)$ vs B_{MGC}	97
3.19	$(MGC - 2dF)$ vs μ_e	98
3.20	$(MGC - 2dF)$ vs μ_e	98
3.21	Histogram of $B_{MGC}(MGC - SDSS)$	99
3.22	$(MGC - SDSS)$ vs MGC field	100
3.23	$(MGC - SDSS)$ vs B_{MGC}	101
3.24	$(MGC - SDSS)$ vs μ_e	101
3.25	2dFGRS cone plot for the MGC region	102
3.26	$(MGC - 2dF)$ vs z	103
3.27	Distribution of μ_e^{app} at $z = 0.02$ and $z = 0.2$	103
3.28	Distribution of $g^* - r^*$ at $z = 0.02$ and $z = 0.2$	104
3.29	$(MGC - SDSS)$ vs z	105
3.30	Comparison of redshifts	106
3.31	Strange merging galaxy.	107
3.32	Incompleteness of 2dFGRS vs B_{MGC}	109
3.33	Incompleteness of 2dFGRS vs μ_e	109
3.34	Apparent BBD showing missing 2dFGRS galaxies	110
3.35	Photometric Incompleteness of SDSS-EDR vs B_{MGC}	112
3.36	Photometric Incompleteness of SDSS-EDR vs μ_e	112

3.37	Photometric completeness of 2dFGRS	114
3.38	Photometric completeness of SDSS-EDR	114
3.39	Apparent BBD of MGC/2dF/SDSS	115
3.40	Overall Photometric Completeness of 2dFGRS & SDSS-EDR	116
3.41	Redshift Completeness of 2dFGRS	116
3.42	Overall Redshift Completeness of 2dFGRS & SDSS-EDR	117
4.1	Apparent Distribution of MGC galaxies	122
4.2	Distribution of MGC galaxies in M, μ_e	123
4.3	A luminous HSBG	125
4.4	$u' - g'$ vs $g' - r'$ for η -type 1 galaxies	126
4.5	Distribution of galaxies in M, μ_e	128
4.6	Bright HSBGs	129
4.7	MGC Galaxies	130
4.8	The arrays used to calculate $\phi(M, \mu)$	131
4.9	The arrays used to calculate $\phi(M, \mu)$	132
4.10	ϕ^* vs z	133
4.11	Incompleteness of galaxies in M, μ_e	135
4.12	$\phi(M, \mu)$ for Subsample 1	136
4.13	$\phi(M, \mu)$ for Subsample 2	137
4.14	Luminosity Functions for the MGC	140
4.15	Luminosity Functions for the MGC	142
4.16	Surface brightness Functions for the MGC	143
4.17	Λ -CDM Luminosity Functions for the MGC	144
5.1	Variation in $\bar{\mu}$ with μ_e	149
5.2	Variation in $\bar{\mu}$ with B_{MGC}	150
5.3	Error in final B_{MGC}	151
5.4	Error in final μ_e	152
5.5	Apparent Distribution of MGC galaxies	153
5.6	Fraction of stars amongst gals without redshifts	154
5.7	Distribution in (M, μ_e) for the 15 plates	155
5.8	$\phi(M, \mu)$	157
5.9	Luminosity Functions for the whole 2dFGRS sample	158
5.10	Distribution of galaxies of each spectral type in M, μ_e	160
5.11	Distribution of galaxies of each spectral type in M, μ_e	161
5.12	$\phi(M, \mu)$ as a function of η -type	162
5.13	$\phi(M, \mu)$ as a function of η -type	164
5.14	LF of eta types	166
5.15	Combined η types	168
5.16	LF for missing galaxies	169
A.1	Galaxy Light Profiles	ii
A.2	Δm vs B/T for Kron and Petrosian	x
A.3	Δm vs z	xi
A.4	Δm vs z , with seeing	xii
A.5	$\Delta \mu$ vs z	xiii
A.6	$\Delta \mu$ vs z , with seeing	xiv
A.7	Δm vs seeing, $z = 0.1$	xv
A.8	Δm vs seeing, $z = 0.25$	xvi
A.9	Δm vs μ_d	xvii
A.10	Δm vs μ_d , with seeing	xviii
A.11	Δm vs μ_{lim}	xix
A.12	Δm vs μ_{lim} , with seeing	xx
A.13	Δm vs M	xxi
A.14	Δm vs M , with seeing	xxii
A.15	Noise limits	xxviii
A.16	Isophotal Visibility plots for different μ_{lim}	xxx
A.17	Isophotal Visibility plots for different d_{iso}	xxxii
A.18	Total Visibility plots for different d_{iso}	xxxiii
A.19	Isophotal Visibility plots for different d_{max}	xxxiv
A.20	Total Visibility plots for different d_{max}	xxxv

List of Tables

1.1	Depth and area of the 8 modern surveys	13
1.2	Schechter parameters and j for recent surveys	15
2.1	Schechter parameters for 2dFGRS LFs	57
2.2	BBF parameters compared with dJL	62
2.3	Schechter parameters and j for simulated surveys	66
3.1	Missing 2dFGRS Objects	87
3.2	Comparison of Stars in SIMBAD, MGC and 2dF	94
4.1	Schechter parameters for MGC LFs	141
5.1	Fitting parameters for each 2dFGRS	150
5.2	Parameters for the 2dFBBDs	156
5.3	Schechter parameters for 2dFGRS LFs	159
A.1	The Properties of the Model Galaxies	i
A.2	Comparison of Gaussian and Exponential Corrections	v
A.3	m_{iso} & r_{iso} of Model Galaxies	ix

Chapter 1

Introduction

1.1 Introduction

Of paramount importance in determining the mechanism(s) and epoch(s) of galaxy formation (as well as the local luminosity density), is the accurate and detailed quantification of the local galaxy population. It represents the benchmark against which both environmental and evolutionary effects can be measured. Traditionally this research area originated with the all-sky photographic surveys coupled with a few handfuls of hard earned redshifts. Over the past decade this has been augmented by both CCD-based imaging surveys and multi-slit/fibre-fed spectroscopic surveys. From these data, a number of perplexing problems have arisen, most notably: the faint blue galaxy problem (Koo & Kron 1992; Ellis 1997), where an excess of blue galaxies has been seen in deep images, the local normalisation problem (Maddox et al. 1990b; Shanks 1990; Driver, Windhorst & Griffiths 1995; Marzke et al. 1998), where the normalisations derived from local redshift surveys result in a severe underestimate of the observed counts at relatively low redshifts, the cosmological significance of low surface brightness galaxies (Disney 1976; McGaugh 1996; Sprayberry et al. 1996; Dalcanton et al. 1997; Impey & Bothun 1997) and dwarf galaxies (Babul & Rees 1992; Phillipps & Driver 1995; Loveday 1997; Babul & Ferguson 1996). These issues largely remain unresolved and arguably await an improved definition of the local galaxy population (Driver 1999).

Recent advancements in technology now allow for wide field-of-view CCD imaging surveys and bulk redshift surveys through purpose built multi-fibre spectrographs such as the common-user two-degree field (2dF) facility at the Anglo Australian Telescope (Taylor, Cannon & Parker 1998). The Sloan Digital Sky Survey elegantly combines these two facets (Margon 1999, York et al. 2000).

The quantity and quality of data that is becoming available allows not only the revision of earlier results but more fundamentally the opportunity to review and enhance the methodology with which the local galaxy population is represented. For instance some criticism that might be levied at the current methodology — the representation of the space density of galaxies using the Schechter Luminosity function (LF, Schechter 1976; Felten 1985; Binggeli, Sandage & Tammann 1988) — is that firstly, it assumes that galaxies are single parameter systems defined by their apparent magnitude alone, and secondly it describes the entire galaxy population by only three parameters; the characteristic luminosity L_* , the normalisation of the characteristic luminosity ϕ_* , and the faint-end slope α , see Eqn 1.1. While it is desirable to represent the population with the minimum number of parameters, important information may be lost.

$$\phi(L) = \phi^* \left(\frac{L}{L^*} \right)^{-\alpha} e^{-(L/L^*)} \quad (1.1)$$

In particular, two recent areas of research suggest a greater diversity in the galaxy population than is allowed by the Schechter function form. Firstly, Marzke et al. (1994), Loveday (1997) and Zucca et al. (1997) report the indication of a change in the faint end slope at faint absolute magnitudes — a possible giant-dwarf transition — and this is also seen in a number of Abell clusters where it is easier to probe into the dwarf regime (e.g., Driver et al. 1994; De Propris et al. 1995; Driver, Couch & Phillipps 1998; Trentham 1998). Secondly a number of studies have shown that the three Schechter parameters, in particular the faint-end slope, have a strong dependence upon: surface brightness limits (Sprayberry, Impey & Irwin 1996; Dalcanton 1998a); colour (Lilly et al. 1996); spectral type (Folkes et al. 1999); optical morphology (Marzke et al. 1998), environment (Phillipps et al. 1998) and wavelength (Loveday 2000). It has been noted (Willmer 1997) that the choice of method for reconstructing the galaxy LF also contains some degree of bias.

More fundamentally, evidence that the current methodology might actually be flawed comes from comparing recent measurements of the galaxy luminosity function as shown in Fig. 1.1. The discrepancy between these surveys is significantly adrift from the quoted formal errors implying an unknown systematic error. The range of discrepancy can be quantified as a factor of 1.5 at the L_* point ($M_B \sim -19.5$) rising to a factor of 10 at $0.01L_*$ ($M_B \sim -14.5$). The impact of this variation is a factor of 2-3, for instance, in assessing the contribution of galaxies to the local baryon budget (e.g. Persic & Salucci 1992; Bristow & Phillipps 1994; and Fukugita, Hogan & Peebles 1998).

This uncertainty is in addition to that introduced from the unanswered question of the space density of low surface brightness galaxies. The most recent attempt to quantify this is by O'Neil & Bothun (2000) — following on from McGaugh (1996), and in turn Disney (1976) — who conclude that the surface brightness function (SBF) of galaxies — the number density of galaxies in intervals of surface brightness — is of similar form to the luminosity function. Thus both the LF and SBF are described by a flat distribution with a cutoff at bright absolute magnitudes or high surface brightnesses. Taking the O'Neil result at face value, this implies a further uncertainty of 2-3 in measures of the local luminosity density - i.e. the contribution to the luminosity- (and hence baryon-) density from galaxies is uncertain to a factor of ~ 10 . However, the significance of low surface brightness galaxies depends upon their luminosity range and similarly the completeness of the LF relies on the surface brightness intervals over which each luminosity bin is valid. Both representations are incomplete unless the information is combined. This leads us to the conclusion that both the total flux and the manner in which this flux is distributed must be dealt with simultaneously.

This thesis attempts to bundle these complex issues onto a more intuitive platform by expanding the current representation of the local galaxy population to allow for: surface brightness detection effects, star-galaxy separation issues, surface brightness photometric corrections and clustering effects. This is achieved by expanding the mono-variate luminosity function into a bivariate brightness distribution (BBD) where the additional dimension is surface brightness.

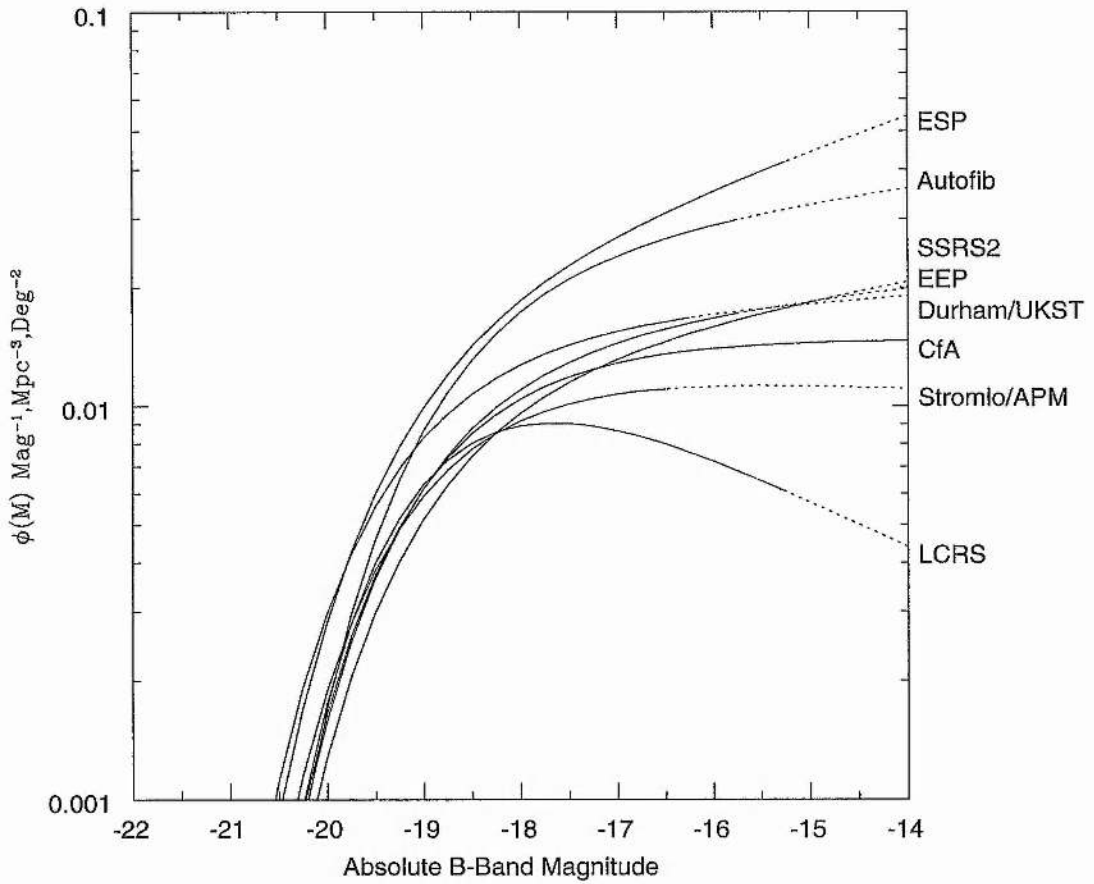


Figure 1.1: The Schechter Function fits to Luminosity Functions from recent redshift surveys. There is a variation in the bright end by a factor of 2, and in the faint end by a factor of 10. This means that estimates on the star formation rate, and the mass density will be uncertain by at least a factor of 2, and that rigorous tests of cosmology and evolution are impossible.

The Two degree Field Galaxy Redshift Survey (2dFGRS) allows us to do this for the first time by having a large enough database to separate galaxies in both magnitude and surface brightness without having too many problems with small number statistics.

Early measurements of the BBD include Chołoniewski 1985; van der Kruit 1987; Sodr  & Lahav 1993). These were for small samples of bright galaxies. Recently several more extensive and independent measurements of the Bivariate Brightness Distribution have been made. Driver (1999) derived the BBD for a volume-limited sample drawn from the Hubble Deep Field, de Jong & Lacey (2000) studied a homogeneous sample of 1000 late-type spirals, Brown et al. (2001) have produced V and R band luminosity-surface brightness relationships of 1250 galaxies from the Century Survey and Blanton et al. (2001) derived the BBD for a sample of 11,275 galaxies from the Sloan Digital Sky Survey. These surveys all confirm the existence of the luminosity-surface brightness correlation, demonstrating that *surface brightness selection biases are luminosity dependent*. Given the luminosity-surface correlation it is hardly surprising if surveys with differing selection criterion recover widely ranging Schechter parameters. Andreon & Cuillandre (2001) have produced a cluster BBD, from the Coma cluster, which also shows a strong luminosity-surface brightness correlation. Bernardi et al. (2001) have produced a BBD for 9000 elliptical galaxies from the SDSS data. The largest published BBD is Cross et al. (2001), containing 45,000 galaxies. We will discuss this in Chapter 2.

A useful next step is to produce an analytical function to fit to these derived BBDs. Chołoniewski (1985) produced a function that incorporates the Schechter luminosity function with a Gaussian distribution in surface brightness and the luminosity-surface brightness correlation. Similar functions have been used by Sodr  & Lahav (1993) and de Jong & Lacey (2000). We use this function ourselves and we discuss our fitting procedure and compare it to the estimation made by de Jong & Lacey (2000).

In this Chapter, we will introduce the reader to the developments associated with measuring the space density of galaxies. We begin by discussing various types of galaxies, and their profiles and distributions, in § 1.2. We pay particular attention to extreme galaxies that are difficult to probe and may be particularly important for theories of galaxy formation and evolution.

In § 1.3, we discuss the measurement of the space density of galaxies. We review the measurement of the luminosity function, paying particular attention to recent large redshift surveys. We then consider the surface brightness distribution, paying attention to selection effects and low surface brightness galaxies before discussing the bivariate brightness distribution. We discuss some of the recent results and the correlations seen between absolute magnitude and surface brightness.

We describe the difficulties with measuring the space density in § 1.3.6 and the techniques used to measure it in § 1.3.7. In particular we review the problems of light loss, incompleteness and inhomogeneities.

Finally we examine the reasons for measuring the space density. We discuss the use of the luminosity density to trace the star formation history, the use of the luminosity function and number counts to constrain the cosmological model and evolutionary effects, the constraints on galaxy formation models from the bivariate brightness distribution. Lastly we examine constraints on the number density from the combination of the BBD and mass-to-light ratios.

1.2 Types of Galaxy

Galaxies have been classified in many ways (van den Bergh 1998 and references therein), but the best known and used set of morphological classifications is the Hubble tuning fork, Hubble (1926). This describes galaxies as ellipticals, spirals or irregulars.

Ellipticals are galaxies, with an old stellar population, with little or no current star formation, and have little or no gas or dust. Their 3-dimensional shape is a tri-axial ellipsoid. They are mainly supported by the motions of stars although they have some net rotation. The dynamics of ellipticals is reviewed by de Zeeuw & Franx (1991). Ellipticals are classified as E0, E1 to E7, where the number describes the eccentricity of the galaxies: E0s are circular, E7s are extremely elongated. They are usually well described by de Vaucouleurs profiles (de Vaucouleurs 1948, see Eqn 2.11). They are most commonly found in the centres of clusters (Dressler 1980).

Spirals have a thin disk, which contains young, blue, star forming regions, and a bulge, which contains an old stellar population. The disk is supported by rotation, and contains large amounts of gas and dust, and spiral arms. The spiral arms can be highly symmetric and regular, with arms extending right around the galaxy for one to one and a half turns in the case of rare “grand-design” spirals, but usually they are short and fragmented. Spiral arms are thought to occur as a result of density waves which travel slowly (as compared to the stars) around the galaxy, triggering star formation (Lin & Shu 1964). They are characterised by young, bright blue stars which have short life times and so do not get far from the spiral arms before they run out of fuel and explode as supernovae. The bulge is supported by the random velocities of stars, as in elliptical galaxies. Spirals are split into two types, normal spirals (S) and barred spirals (SB). Barred spirals have a central bar, with spiral arms protracting from each end. Spirals (barred and unbarred) are described by an extra parameter, a to d , which describes the bulge-to-total ratio and tightness of the spiral arms. Sa (SBa) galaxies have large bulge-to-total ratios and tightly wound spiral arms, whereas Sd (SBd) galaxies have small bulge-to-total ratios and loosely wound spiral arms. Irregulars are disk galaxies which have no bulge, lots of gas, dust and star forming regions, but no obvious spiral arms. Spirals are found predominantly in the outer parts of galaxy clusters and small groups (Dressler 1980).

Ellipticals and bulges have a surface brightness profile that is well described by a de Vaucouleurs profile (de Vaucouleurs 1948). Spiral disks and irregulars are well described by an exponential. These profiles are described in § 2.3.

In later publications, Hubble added an extra class, lenticular galaxies or S0 galaxies, which were placed between spirals and ellipticals (Hubble 1936c). As van den Bergh (1998) points out, there is no clear definition of the S0 class - they do not appear to contain much dust or gas, like ellipticals, but have disks with spiral arms and sometimes bars, like spiral galaxies. The bulge-to-total ratio is high, $B/T \sim 0.65$ (Kent 1985).

cD galaxies (Matthews, Morgan & Schmidt 1964, Morgan & Lesh 1965) are particularly luminous galaxies, generally found at the centres of rich clusters. They have an elliptical-like $r^{-1/4}$ core, with an extensive power-law envelope.

Dwarf galaxies are faint galaxies $M_B > -16$. The profiles of these galaxies are well fit by exponential profiles, even dwarf ellipticals (Ferguson & Binggeli 1994). There are many

types of dwarfs, dwarf irregulars (dI), dwarf ellipticals (dE) and dwarf spheroidals (dSph), with absolute magnitudes as low as $M_B \sim -8$ seen in some local group dwarfs (Mateo 1998).

The most recently discovered type of galaxies are Low Surface Brightness Galaxies (LSBG). However, these are not consistently defined. Some authors choose a value of $\sim 1\sigma$ from the Freeman Law (see § 1.3.4) as the limit for LSBGs: $\mu_{0,B} \gtrsim 22 \text{ mag arcsec}^{-2}$. Impey & Bothun (1997) define them as galaxies with $\mu_{0,B} > 23 \text{ mag arcsec}^{-2}$, although this usually means the central surface brightness of the disk, not the whole galaxy. They tend to be faint, gas and dark matter rich, giving them high mass-to-light ratios (de Blok, McGaugh & van der Hulst 1996). In § 1.3.4 we will discuss recent searches for LSBGs and the measurement of the space density of LSBGs. The Impey & Bothun (1997) review is a good introduction to their properties.

The different types of galaxies as well as the extreme galaxies in the next section are displayed in the absolute magnitude-surface brightness plane in Fig 1.2.

Galaxies have also been classified by spectral characteristics, such as specific features, e.g. line equivalent widths of Hydrogen α (Bland-Hawthorn et al. 2001), which give information about star formation rates, or a more continuous parameterisation such as that employed by the 2dFGRS (Folkes et al. 1999, Madgwick et al. 2001). Madgwick et al. (2001) relate their parameter η , which varies from ~ -5 for strong absorption systems to ~ 10 for strong emission systems, to the Hubble type, using galaxies taken from the Kennicutt (1992) atlas. The η parameter splits the galaxies into four classes: η -type 1 galaxies are correlated with early type galaxies (ellipticals and lenticulars), η -type 2 galaxies are correlated with Sa/Sb galaxies, η -type 3 galaxies are correlated with Sb/Scd galaxies, and η -type 4 galaxies are correlated with Scd galaxies and later types.

1.2.1 Extreme Galaxies

Many surveys have shown a luminosity-surface brightness correlation amongst galaxies, see § 1.3.5. Galaxies which lie a long way from this relationship may be counted as extreme, and as Fig 1.2 demonstrates, these are the most difficult galaxies to detect in a survey. The high surface brightness dwarf galaxies are difficult to detect since they will have small angular sizes and will therefore become unresolved at a relatively small distance and be rejected as stars. Giant low surface brightness galaxies like Malin 1 are often missed because of the difficulty of detecting low surface brightness objects with a noisy background. If the sky subtraction is poor then these objects may be missed when smaller low surface brightness galaxies are detected.

High surface brightness dwarf Galaxies

The archetypal high surface brightness dwarf galaxy / compact elliptical (cE) is M32 (Mateo 1998), a local group member and satellite of M31. As Fig 1.2 demonstrates, this is a very high surface brightness galaxy, particularly for its absolute magnitude. Disney (1976) pointed out that compact objects could be mistaken for stars. Surveys such as the APM (Maddox et al. 1990a) have strict limits on the star-galaxy separation, excluding all objects with $r_{iso} \gtrsim 3.6$ arcsec due to a combination of poor seeing and poor resolution (Pimblet 2001). Even modern CCD catalogues cannot separate stars from galaxies beyond $B \sim 20$ (Liske et al. 2002). To

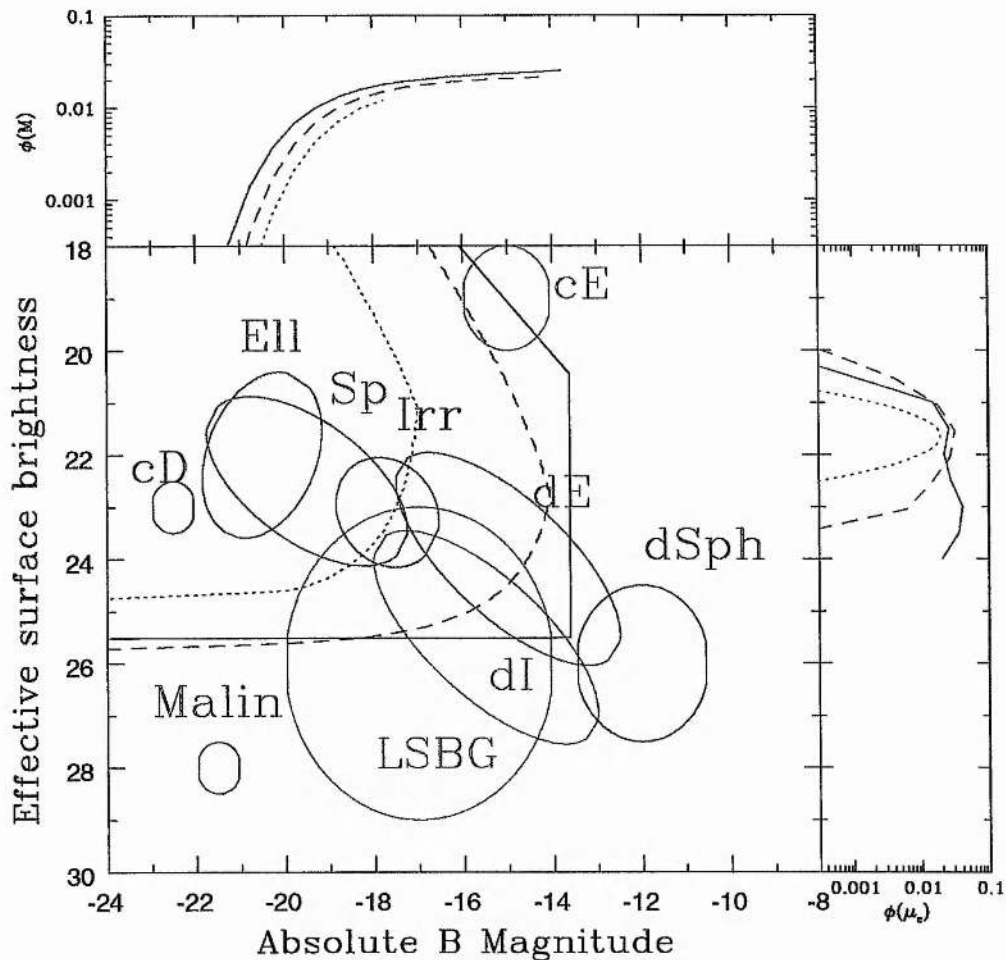


Figure 1.2: This plot shows the approximate distribution in M_B and μ_e of different galaxy types, described in the text. The black dotted lines show various selection functions for different surveys. The inner most selection function is approximately the Freeman Law with an isophotal limit $\mu_{lim} = 24 \text{ mag arcsec}^{-2}$, a diameter limit of $D_{24} \sim 20''$ and an apparent magnitude limit $m = 16.0$. The other two dotted lines approximate modern surveys. One has an isophotal limit $\mu_{lim} = 24.7 \text{ mag arcsec}^{-2}$, an isophotal diameter limit of $D_{24} = 7.2''$ and an apparent isophotal magnitude limit $m = 19.0$. The other has $\mu_{lim} = 24.4 \text{ mag arcsec}^{-2}$, a half-light diameter limit of $D_{24} = 1.6''$ and an apparent total magnitude limit $m = 19.0$. The estimated luminosity functions calculated from each data set is shown above the distribution of galaxies, as dotted, dashed and solid lines respectively. The estimated surface brightness functions are shown on the right hand side. The extreme galaxies such as Malins and cEs are not accessible by these surveys. Neither are dwarf spheroidals nor the majority of the low surface brightness population.

measure the BBD of very small dwarf galaxies, either space based telescopes are required (e.g. Driver 1999), or it is necessary to measure the redshift of every object within a field. Since stars outnumber galaxies 3 to 1 at bright apparent magnitudes, low redshift surveys such as the 2dFGRS and SDSS would require four times as much telescope time as they currently require.

Drinkwater et al. (1999) have done a complete redshift survey of 14,000 objects in the direction of the Fornax cluster and found 13 unresolved galaxies with $18.5 < B_J < 20.1$ and $0.05 < z < 0.21$. These all have absolute magnitudes $-21.5 < M_B < -18.0$, making them significantly brighter than M32. However, since they are unresolved it is not possible to measure their surface brightnesses. These galaxies would add $3.2 \pm 1.2\%$ more galaxies to the 2dFGRS. Phillipps et al. (2001) found that 5 more of these galaxies were at the distance of the Fornax cluster and had Half Width Half Maximum (HWHM) sizes $< 1.1''$, corresponding to $R < 100\text{pc}$. These galaxies have $-13 < M_B < -10$ and minimum surface brightness $\mu_0 \sim 20 \text{ mag arcsec}^{-2}$ which puts them several mag arcsec^{-2} brighter than the luminosity-surface brightness correlation, see Fig 1 of Phillipps et al. (2001). Phillipps et al. (2001) suggest several possibilities for these galaxies: They could be 1) a new type of galaxy, i.e. primordial high central density galaxies; 2) super massive globular clusters; 3) nuclei of extremely low surface brightness dE galaxies; 4) the tidally distorted remnants of normal dwarfs.

Bekki et al. (2001) have run N-body simulations that suggest that cE type galaxies were originally spiral galaxies that were tidally stripped by a larger companion, M31 in the case of M32. Their simulations suggest that cE galaxies are very rare since there is a narrow parameter space for the tidal interactions and the cE galaxies will shortly ($\lesssim 10^9\text{yr}$) be swallowed by their neighbours.

1.2.2 Giant Low Surface Brightness Galaxies

The largest galaxy ever discovered, with a disk scale length, $h = 55\text{kpc}$, is Malin 1 (Bothun et al. 1987). It has a disk with $\mu_{0,B} = 26.6 \text{ mag arcsec}^{-2}$ and a total absolute magnitude $M_B = -21.2$. Even though it has a significant bulge, 72% of its total light is emitted from the disk. Since its disk is below many current survey limits, including our own survey, the Millennium Galaxy Catalogue (MGC), this galaxy will appear as a dwarf elliptical in many surveys (Cross et al. 2001). Since dwarf ellipticals are very common in clusters, being the most common type of galaxy in clusters with $M_B > -17$, (Binggeli, Sandage & Tammann 1988, Ferguson & Binggeli 1994) it is important to ask how many of these could be crouching giants. In the field these galaxies are less common, but the number density increases rapidly as the luminosity decreases for $M_B > -16$.

Several surveys of very low surface brightness galaxies have been made over the last decade. These include Turner et al. (1993), Schwartzberg et al. (1995), Dalcanton et al. (1997), O'Neil, Bothun & Impey (2000) and Bomans & Habertzettl (2001). While many LSBGs have been found, the difficulty of obtaining redshifts has meant that it is difficult to distinguish between a close by dwarf LSBG and a further away giant LSBG or a high redshift normal galaxy that has been cosmologically dimmed, see Fig 1.3. Schwartzberg et al. (1995) compared the expected isophotal areas and magnitudes of cosmologically dimmed normal galaxies with those

of their population and concluded that these are real LSBGs.

Sprayberry et al. (1997) characterised a sample of 8 LSBGs, with scale lengths greater than ordinary spirals. While none of these galaxies is as extreme as Malin 1 they found that like Malin 1 they all had high HI column densities.

O'Neil (2000) has discovered a red ($(B - V) > 1$) LSBG which appears to have a redshift, $z = 0.1035$. If this velocity is correct, then this galaxy is even larger than Malin 1.

1.3 Measuring the Space Density of Galaxies

The space density of galaxies is usually defined as the mean number of galaxies in a 1Mpc volume, over some range of parameters as a function of some variable. The space density is most commonly described as a function of absolute magnitude (M); the galaxy luminosity function (GLF). The surface brightness distribution, the space density as a function of intrinsic surface brightness (μ), has also been measured, as has the bivariate brightness distribution, the space density as a function of both M and μ . As the absolute magnitude, intrinsic surface brightness and the size of the galaxy (R) are simply related by Eqn 1.2, the bivariate brightness distribution is often described in terms of M and R or μ and R ,

$$M = \mu_e - 5 \log_{10} R_e - 38.57, \quad (1.2)$$

where M is the total absolute magnitude, μ_e is the intrinsic effective surface brightness in mag arcsec^{-2} and R_e is the half light radius in kpc. If the surface brightness and size are defined in different ways, then a similar expression with a different constant can be used. This is derived using $m = \mu_e^{app} - 2.5 \log_{10} 2\pi r_e^2$, the definition of effective surface brightness and Eqns 2.8 and 2.9 which relate the apparent magnitude and apparent surface brightness to absolute magnitude and absolute surface brightness.

1.3.1 Luminosity Functions

The Galaxy Luminosity Function (GLF) is an important tool in cosmology. It describes the space density of galaxies ϕ as a function of absolute magnitude. It is used to test cosmological and evolutionary models by comparing the $z = 0$ LF to number counts (e.g. Metcalfe et al. 1991, Metcalfe et al. 1995, Yasuda et al. 2001). Luminosity functions are also essential in producing mock catalogues (e.g. Cole et al. 1998, Cross & Driver 2001), which are then used to test which features are important in the power spectrum (Percival et al. 2001) or selection biases (Cross & Driver 2001).

In this thesis we concentrate on the overall space density, and not the space density in special environments such as clusters or groups or the field. The space density in clusters is a separate thesis in itself, with numerous papers over the years. We will mention a few of these where relevant, but instead direct the reader to the following articles, which discuss the cluster luminosity function and the relationship between the cluster and field luminosity functions: Bingeli, Sandage & Tammann (1988), Trentham (1998) and Paolillo et al. (2001). We concentrate on the optical space density and in particular the B-band space density.

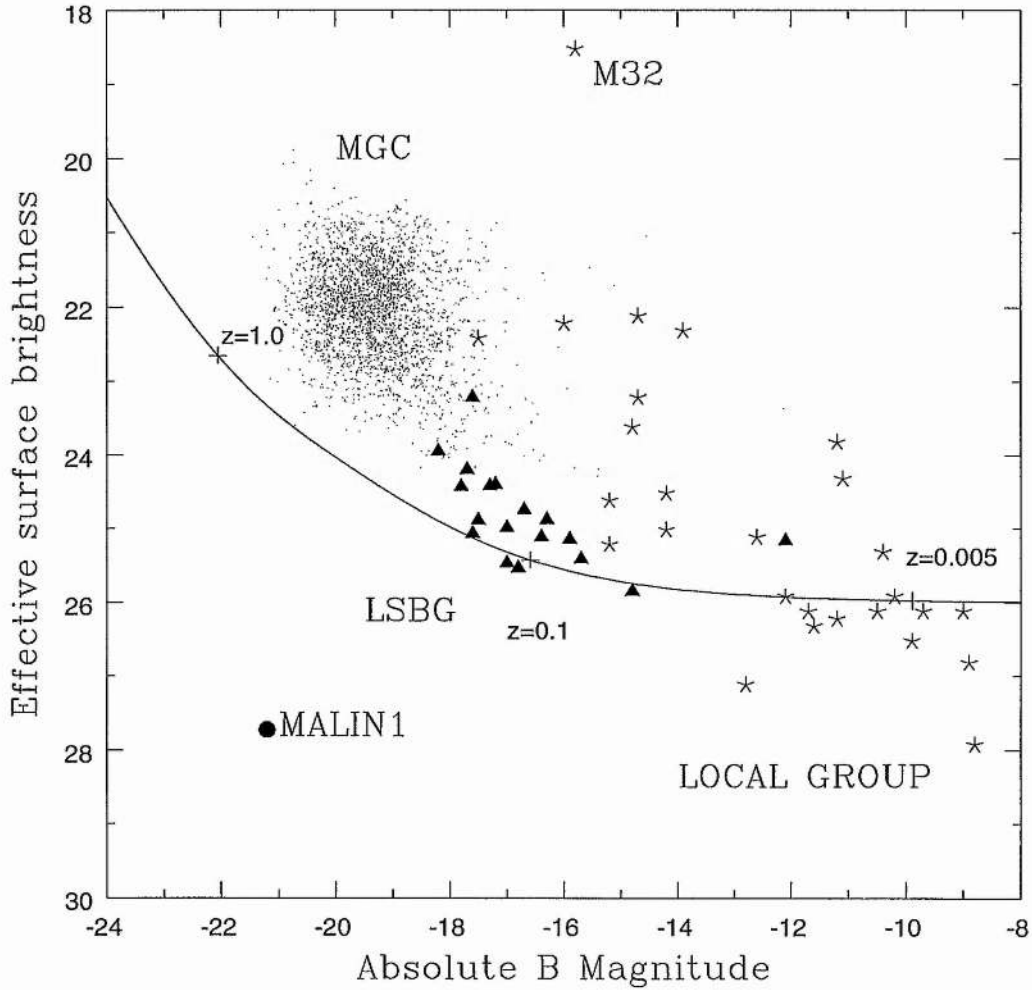


Figure 1.3: This plot shows the distribution of galaxies from several different surveys, including the Millennium Galaxy Catalogue (MGC), represented by dots, the Local Group (Mateo 1998), represented by stars, LSBGs (McGaugh 1996), represented by triangles, and Malin 1 (Bothun et al. 1987), represented by the solid circle. The line describes the locus of a low surface brightness galaxy ($B = 21, \mu_e^{app} = 26$), with increasing redshift. The crosses along the line represent the redshifts $z = 0.005$, $z = 0.1$ and $z = 1.0$. Thus an apparently faint LSBG, may be a low redshift intrinsically faint LSBG, a medium redshift bright LSBG or a high redshift normal galaxy.

Early Measurements of the GLF

The earliest measurement of the GLF was by Hubble (Hubble 1936a,b, henceforth H36a, H36b). In H36a, the distances were measured using the brightest stars in resolved galaxies as standard candles. In H36b, the distances were measured using Hubble's well known velocity-distance relation:

$$v = H_0 d. \quad (1.3)$$

In H36a, Hubble measured a Gaussian-like luminosity function for nearby field galaxies, with mean $\bar{M} = -14.2$ and width $\sigma_M = 0.85$. A similar result was found for H36b. Sandage (1958) showed that most of these "brightest" stars were in fact HII regions and a value $H_0 = 526 \text{ kms}^{-1}\text{Mpc}^{-1}$ was used in H36b. The modern value is $H_0 = 72 \pm 8 \text{ kms}^{-1}\text{Mpc}^{-1}$ (Freedman et al. 2001).

Zwicky (1957) measured the luminosity function in clusters and found that the brightest members were well described by a cubic and fainter members by an exponential. Kiang (1961) discusses the differences between Hubble's GLF (H36a) and Zwicky's result. Kiang recalculated Hubble's value \bar{M} using the correct magnitude of the brightest HII regions rather than the brightest stars. The shape of Hubble's GLF remained the same. Kiang concluded that Zwicky's function fits both the field and cluster environment and that Hubble had neglected selection effects. In H36b, the frequency distribution was directly equated to the luminosity function, without taking into account the varying volume over which a galaxy can be seen, which depends primarily on the apparent magnitude. This bias is usually referred to as Malmquist bias or Scott bias (Scott 1957). While it is not so obvious that H36a suffers from Malmquist bias, since it was the apparent magnitudes of the brightest "stars" that selected the sample, Hubble did see a correlation between the absolute magnitude of the brightest stars and the absolute magnitude of the galaxies. As we will demonstrate further on, selection effects are a problem in many measurements of the space density of galaxies. Since clusters are all at one distance, and cover the same volume, Malmquist bias does not affect the shape of the cluster luminosity function.

Zwicky's fit, a combination of a cubic and an exponential, has been superseded by the Schechter (1976) analytic fit, shown in Eqn 1.4. The Schechter Function is a function with three parameters, the turn-over point L^* , the faint end slope α and the normalisation ϕ^* . This is the expected distribution following non-linear collapse as calculated by Press & Schechter (1974), but also allowing α , the faint end slope to vary.

$$\phi(L)dL = \phi^*(L/L^*)^\alpha \exp(-(L/L^*))d(L/L^*) \quad (1.4)$$

or in terms of magnitudes:

$$\phi(M)dM = 0.4\phi^*(\ln 10)10^{(0.4(M^*-M))(\alpha+1)} \exp(-10^{(0.4(M^*-M))})dM \quad (1.5)$$

The luminosity function can be integrated with the luminosity of the galaxy to give the total luminosity density of galaxies (Eqn 1.6). If a Schechter Function is used then the luminosity density is easily calculated from the parameters (Eqn 1.7).

$$j = \int_0^{\infty} L \phi(L/L^*) d(L/L^*) \quad (1.6)$$

$$j = \phi^* L^* \Gamma(\alpha + 2) \quad (1.7)$$

While many surveys find a good fit to the Schechter function, e.g. Efstathiou, Ellis & Peterson (1988), Blanton et al. (2001), Norberg et al. (2002), others such as Driver et al. 1994, Zucca et al. (1997), Andreon, Cuillandre & Pelló (2000) and Madgwick et al. (2001) do not. We will discuss how well the Schechter function fits the LF in Chapters 4 and 5.

1.3.2 Modern Measurements of the GLF

To test the reliability of the luminosity function, a comparison of the GLF derived in 8 major surveys has been undertaken. The surveys compared are the Second Southern Sky Redshift Survey (SSRS2, Marzke et al. 1998), the Durham/UKST Galaxy Redshift Survey (Dur/UKST, Ratcliffe et al. 1998), the ESO Slice Project Galaxy Redshift Survey (ESP, Zucca et al. 1997), the Las Campanas Redshift Survey (LCRS, Lin et al., 1996), a comparison of small surveys by Efstathiou, Ellis & Peterson (EEP, Efstathiou, Ellis & Peterson 1988), the Stromlo-APM Redshift Survey (APM, Loveday et al. 1992), the Autofib Redshift Survey (Autofib, Ellis et al. 1996), and the Centre for Astrophysics Redshift Survey (CfA, Marzke et al. 1994). More recent surveys such as the 2dFGRS (Cross et al. 2001, Norberg et al. 2002) and the Sloan Digital Sky Survey (SDSS, Blanton et al. 2001) will be discussed later on in this thesis, in Chapters 3,4 and 5.

These surveys measured the luminosity function for the whole galaxy population, rather than the luminosity function of clusters. The surveys varied in the selection criteria for spectroscopic targets, the number of objects observed, the completeness of the survey, the filter used, and the method for evaluating the luminosity function. Table 1.1 shows the depth and survey area of the eight surveys.

Most of the surveys were wide field, low redshift surveys. These include SSRS2 with a magnitude limit $B(0) = 15.5$ and a solid angle of 1.69sr, CfA with a magnitude limit of $m_z = 15.5$ and a solid angle of 2.1sr, Dur/UKST, with a magnitude limit of $b_j = 17.0$ and a solid angle of 1500 deg^2 (0.457sr), LCRS with a solid angle of 720 deg^2 (0.219sr) and a magnitude limit $R = 17.7$, and the Stromlo-APM with a magnitude limit of $b_j = 17.15$ and a solid angle of 4300 deg^2 (1.31sr).

The Autofib has a limiting magnitude of $b_j = 24.0$, and a maximum redshift $z = 1.1$. The Autofib Redshift Survey uses 6 different sets of data, to probe as large an apparent magnitude range as possible. It uses data from the Anglo- Australian Redshift Survey (AARS) ($11.5 < b_j < 17.0, s.a. = 70.84 \text{ deg}^2$), Autofib (AF)-bright ($17.0 < b_j < 20.0, s.a. = 5.52 \text{ deg}^2$), AF-faint ($19.5 < b_j < 22.0, s.a. = 4.67 \text{ deg}^2$), the Durham/Anglo-Australian Telescope faint

Table 1.1: A comparison of the limiting magnitude and solid angle of 8 recent redshift surveys.

Survey	Filter	m_{lim} / mag	Survey area / sr
SSRS2	B(0)	15.5	1.69
CfA	m_Z	15.5	2.1
Durham/UKST	b_j	17.0	0.457
LCRS	R	17.7	0.219
Stromlo-APM	b_j	17.15	1.31
Autofib	b_j	24.0 ^{*1}	$2.9 \times 10^{-5*1}$
ESP	b_j	19.4	7.1×10^{-3}
EEP	B_T	14.5 ^{*1}	0.84 ^{*1}

^{*1} These papers use data from a variety of surveys with different depths and areas. The full range of depths and areas are discussed in the text.

galaxy redshift survey ($20.0 < b_j < 21.5$, $s.a. = 0.499 \text{ deg}^2$), the Low Dispersion Survey Spectrograph (LDSS)-1 ($21.0 < b_j < 22.5$, $s.a. = 0.124 \text{ deg}^2$) and LDSS-2 ($22.5 < b_j < 24.0$, $s.a. = 0.096 \text{ deg}^2$).

The ESP attempts to fill the gap between the wide field and the evolution surveys, by looking down to a magnitude limit of $b_j = 19.4$ and looking over a solid angle of 23.2 deg^2 ($7.07\text{E-}3\text{sr}$). EEP consists of AARS data, ($\mu_{b_j} = 23.6 \text{ mag arcsec}^{-2}$, $s.a. = 70.31 \text{ deg}^2$), Kirshner, Oemler & Schechter (1979, KOS) data ($J_{KOS} = 15$, $s.a. = 121.8 \text{ deg}^2$), Kirshner et al. (1983, KOSS) data ($F_{KOS} = 16$, $s.a. = 12 \text{ deg}^2$), the Revised Shapley Ames (RSA) catalogue ($B_T \leq 12.5$, $b \geq 30^\circ$) and Centre for Astrophysics (CfA) catalogue, ($B_T \leq 14.5$, $b > 40^\circ$ or $B < -30^\circ$). EEP developed the Stepwise Maximum Likelihood Estimator (SWML, see § 2.6.2) to analyse the data from each of these surveys. EEP converted all the magnitudes to the B_T system.

Filters

It is necessary to convert all magnitudes to the same system, in this case the standard Johnson B filter. The following equations are used to convert from the other filters.

$$B = b_j + 0.28(B - V) \quad (1.8)$$

Eqn 1.8 is the filter conversion from photographic b_j to Johnson-B, given in Blair & Gilmore (1982). A mean $(B - V)$ (Eqn 1.9) for the low redshift galaxy population is given in Coleman, Wu & Weedman (1980).

$$\overline{(B - V)} = 0.8 \quad (1.9)$$

This gives an offset between B and b_j of $B = b_j + 0.224$. Gaztañaga & Dalton (2000), find a scale error in the Zwicky magnitudes used in the CfA survey, see Eqn 1.10. They also show evidence of an observer bias effect; fainter galaxies are more likely to be picked up close to bright galaxies than in empty regions. The overall effects give the colour term in Eqn 1.11 and a reduction in the normalisation by 60%.

$$\Delta(m_Z) = (0.62 \pm 0.05)\Delta B \quad (1.10)$$

$$B = m_Z - 0.35 \pm 0.15 \quad (1.11)$$

EEP use B_T magnitudes from the ESO-LV system (Lauberts & Valentijn 1989). They use the conversion in Eqn 1.12 to convert between photographic b_j and B_T . From Eqn 1.8 we get the final offset $B = B_T + 0.514$.

$$b_j = B_T + 0.29 \quad (1.12)$$

The SSRS2 uses the B(0)-Zwicky (Huchra 1976). The conversion in Felten (1985) is shown in Eqn 1.13. The final offset is $B = B(0) + 0.254$.

$$B_T = B(0) - 0.26 \quad (1.13)$$

The LCRS is measured in the R-band. Lin et al. (1996) use a mean colour term from (Tucker 1994) given in Eqn 1.14. The final offset is $B = R + 1.324$.

$$\overline{(b_j - R)} = 1.1 \quad (1.14)$$

The SDSS is measured in the Sloan u^* , g^* , r^* , i^* and z^* filters. Using the equations in Fukugita et al. (1996) we calculate the filter conversion to be:

$$B = g^* + 0.419(g^* - r^*) + 0.216 \quad (1.15)$$

These conversions are applied to the M^* values given in the papers.

Surface Brightness Limits

The input catalogues had various surface brightness limits, and total number of galaxies. The SSRS2 was selected from the non-stellar list of the HST Guide Star Catalogue (Lasker et al. 1990) and the photometry was calibrated by Alonso et al. (1993, 1994). There are 5404 galaxies with photometry equivalent to isophotal magnitudes at $\mu_B = 25.3 \text{ mag arcsec}^{-2}$.

The Durham/UKST and ESP surveys were based on UKST plates scanned on COSMOS as part of the Edinburgh-Durham Southern Sky Catalogue. The Stromlo/APM survey is based on APM scans of UKST plates. These plates have a limiting isophote $24.7 < \mu_{B,lim} \leq 25.2$, but have Gaussian isophotal corrections (Maddox et al. 1990; Heydon-Dumbleton, Collins & MacGillivray 1989). These corrections are discussed in § A.1. The Stromlo/APM survey contains 1769 galaxies, the Durham/UKST contains ~ 2500 and the ESP contains 3342

Table 1.2: A comparison of the local luminosity density from recent magnitude-limited redshift surveys.

Survey	$M_B^* - 5 \log h$	$\phi^*/10^{-2}h^3$	α	$j_B/10^8 h L_\odot \text{Mpc}^{-3}$
SSRS2	-19.18 ± 0.06	(1.28 ± 0.02)	-1.12 ± 0.05	(1.02 ± 0.08)
Durham/UKST	-19.46 ± 0.10	(1.7 ± 0.3)	-1.04 ± 0.08	(1.65 ± 0.35)
ESP	-19.39 ± 0.08	(2.0 ± 0.4)	-1.22 ± 0.06	(2.11 ± 0.47)
LCRS	-18.97 ± 0.02	(1.9 ± 0.1)	-0.70 ± 0.05	(1.02 ± 0.08)
EEP	-19.17 ± 0.10	(1.56 ± 0.34)	-1.07 ± 0.05	(1.18 ± 0.29)
Stromlo/APM	-19.28 ± 0.13	(1.40 ± 0.17)	-0.97 ± 0.15	(1.10 ± 0.25)
Autofib	-18.98 ± 0.30	(2.6 ± 0.8)	-1.09 ± 0.10	(1.68 ± 0.71)
CfA*	-19.15 ± 0.3	(1.6 ± 0.4)	-1.00 ± 0.2	(1.14 ± 0.48)
2dFGRS	-19.20 ± 0.07	(2.15 ± 0.09)	-1.18 ± 0.02	(1.83 ± 0.17)
SDSS	-19.42 ± 0.04	(2.69 ± 0.34)	-1.22 ± 0.05	(1.83 ± 0.17)

* We have corrected the CfA luminosity function as suggested by Gaztañaga & Dalton (2000).

galaxies. The Autofib Redshift survey also uses UKST plates. The deep plates have limits of $\mu_{lim,B} = 26.7$, but some of the intermediate data had $\mu_{lim,B} = 25.2$.

The CfA contained 9063 galaxies, but the surface brightness limits are hard to determine, because the objects are selected by eyeball classification (Zwicky et al. 1961-1968) as shown in Gaztañaga & Dalton (2000). The EEP contains ~ 3000 galaxies, with various limits. The AARS data has $\mu_{lim,B} = 23.8$, the KOS data has $23.1 \leq \mu_{lim,B} \leq 24.4$, the KOSS data has $\mu = \mu_{SKY} + 1.9 \rightarrow \mu_{lim,B} \sim 24$.

The LCRS is a R-band survey rather than a B-band survey and has an equivalent $\mu_B = 24.3$, and contains 18678. The LCRS have also specified the spectroscopic limits, due to how much light can pass down the fibre (Schectman et al. 1996). This puts an additional surface brightness limit of $\mu_B = 23.1$, although this varies with apparent magnitude.

Other surveys suffer from these surface brightness problems, but only the LCRS is explicit about them. Their object selection is done by isophotal magnitudes, although they get $12''$ aperture magnitudes to correct to total magnitudes. A fixed aperture reduces the light loss if the objects are small, but can increase it if they are big. This correction suffers from many of the same problems as isophotal magnitudes - strong redshift and profile dependence, although it reduces the variation with seeing and sky background. Unfortunately, while they discuss the limits and correct for the magnitudes they do not correct for the volume over which they can see the galaxies.

Luminosity Function Parameters

Table 1.2 shows the Schechter parameters and the luminosity density, j , for the surveys above. All M^* values have been converted to the standard Johnson B filter, and all values of M^* and ϕ^* have been converted to $H_0 = 100 \text{kms}^{-1} \text{Mpc}^{-1}$. The luminosity density is calculated using Eqn 1.6.

The Luminosity Functions for these surveys are shown in Fig 1.1. There is a variation of a factor ~ 1.5 at the bright end and a factor ~ 10 at the faint end. The luminosity densities show a variation of a factor of ~ 2 as well. Even though some of the quoted errors are large, they cannot fully explain the large variation in luminosity functions. If the luminosity

function is going to be a reliable tool to test cosmological and evolution models and produce mock catalogues then the random errors must be significantly reduced and the systematic errors must be eliminated as far as possible. This work will concentrate on eliminating the systematic errors, but will include data from much larger catalogues and data with much better photometry, so the random errors will be reduced too.

1.3.3 Why is there so much variation in the LF?

There are many possible reasons for the huge variation in the published values of the Luminosity Function. We will briefly consider the main contenders.

One source of variation is the filter. The LCRS, which shows the most shallow faint end slope, was measured in the R-band. Intrinsically faint galaxies tend to be bluer (Blanton et al. 2001; Brown et al. 2001) as are LSBGs (Brown et al. 2001), so it suggests that the R-band LF should be shallower. However all of the other surveys are measured through a b_j filter, or similar filters, and the variation should be confined to M^* , with a small change in α . ϕ^* should be relatively unaffected by small variations in the filters, assuming that most of the variation comes from differences in the measured magnitude rather than the number of galaxies detected. However a large range in ϕ^* is seen amongst the surveys. This cannot be explained by variations in the filter.

Another possible error comes from inhomogeneities in the density of galaxies. Some regions of space are heavily clustered, others have large voids. Galaxies which are seen over volumes of the same scale as the cluster scale may be biased towards a high number density in a heavily clustered region or a low number density in a void. To avoid this problem surveys such as the APM are sparsely sampled; taking 1 galaxy in 20 at random and thereby covering a greater area of sky. This reduces the chance that the area of sky sampled is significantly under dense or over dense. EEP developed the Step Wise Maximum Likelihood method which uses maximum likelihood techniques to use information on as many scale lengths as possible to reduce the problems of clustering. Clustering will tend to affect dwarf galaxies more because they are seen over smaller volumes due to Malmquist bias. Therefore it is likely that the greatest effects will be seen in the faint end slope, with little variation at the bright end.

Number or luminosity evolution will change the luminosity function parameters, but all of the LFs apart from the ESP, LCRS and Autofib have $z \leq 0.05$. At such a low redshift evolution should not be a factor, but there is still a variation of 50% at the bright end and a large variation in the faint end slope. ESP and LCRS both have $\bar{z} \sim 0.1$, but have radically different LFs. While Autofib is an evolutionary survey, and does show substantial variation for different redshift cuts, the parameters in Table 1.2 are for $z < 0.1$ galaxies.

Photometric errors such as those seen in the CfA by Gaztañaga & Dalton (2000) may be the source of some of the problems. These photometric errors may be caused by non-linearities in the photometric plates, or by light loss due to the surface brightness profiles of galaxies, see § A.1.

Most of the surveys use some deep CCD data to test the calibration, and light loss after some corrections, such as a Gaussian correction (Maddox et al. 1990), a mean exponential correction (EEP) or a fixed aperture correction (Shectman et al. 1994). However, as we will

show in § A.1 there are no perfect methods to correct light loss; for LSBGs and late type galaxies these methods can miss a significant fraction of the light.

The extended surface brightness profiles of galaxies and the bright sky background not only lead to light loss, which causes photometric errors by underestimating the flux, but also leads to incompleteness as galaxies with underestimated fluxes drop below the survey limits, or in some cases are simply lost in the noise. At the other extreme small angular-scale galaxies can be missed if they cannot be distinguished from stars. Thus the completeness, and hence the reliability of the luminosity function, depends on the surface brightness limit and the seeing. The surveys have various surface brightness limits, the Autofib has the deepest limits; the LCRS and EEP have the brightest. Autofib has one of the highest luminosity densities, the LCRS, SSRS2, EEP and CfA have rather low luminosity densities. The SSRS2, has photometry equivalent to isophotal magnitudes at $\mu_B = 25 - 26$, but is selected from the Guide Star Catalogue (Lasker et al. 1990) which is only complete for stars to $b_j \sim 20$, so the surface brightness limit for completeness is much shallower. However, the ESP with the highest luminosity density, and the APM with one of the lowest have very similar surface brightness limits and isophotal corrections.

In this work the variations in the luminosity functions will be explored. In particular surface brightness selection issues will be thoroughly explored and removed from the Luminosity Function. While much of the photometric data will come from the same photographic Schmidt plates used in some of the previous surveys, CCD data from the Millennium Galaxy Catalogue and Sloan Digital Sky Survey will be used to test the photometry and remove any nonlinearities and losses due to surface brightness.

In addition, variations in the luminosity function with the Madgwick et al. (2001) spectral types, taking into account surface brightness selection effects.

1.3.4 Surface Brightness Distributions

In the previous section we found a large variation in recent measurements of the luminosity function. It was speculated that surface brightness selection effects were a principal cause of this variation. In this section we will discuss the distribution of space density with surface brightness.

'Normal' Galaxies

Fish (1964), found a narrow distribution amongst elliptical galaxies with mean $\mu_0 = 14.80$ mag arcsec⁻² and standard deviation $\sigma = 0.9$ mag arcsec⁻². This was calculated using a sample of nearby ellipticals, which had large angular size. Fish first confirmed that the light profiles corresponded to a de Vaucouleurs profile and then measured the surface brightness by fitting the best fit de Vaucouleurs to the distribution. Freeman (1970) measured the central surface brightness distribution of spiral galaxies to be a Gaussian with mean $\mu_0 = 21.65$ mag arcsec⁻² and standard deviation $\sigma = 0.3$ mag arcsec⁻², across a range in absolute magnitude of 5 magnitudes.

Disney (1976) challenged these results, and suggested that both could be explained by surface brightness selection effects. Due to the small dynamic range of photographic plates,

galaxies were being selected principally by diameter rather than magnitude. When a surface brightness limit $\mu_{lim} = 24.0 \text{ mag arcsec}^{-2}$ was applied, the peak of the apparent radius distribution was at $\mu_0 = 21.83 \text{ mag arcsec}^{-2}$ for spirals and $\mu_0 = 15.31 \text{ mag arcsec}^{-2}$ for ellipticals, close to the Freeman and Fish values. This suggests that the Fish and Freeman distributions are dominated by surface brightness selection effects.

Allen & Shu (1979) agree that selection effects dominate the low surface brightness edge of both the Fish and Freeman distributions, but the high surface brightness ends are real. They argue that Disney's use of intrinsic scale size rather than apparent scale size leads to a miscalculation of when the star-galaxy separation will become a problem. van der Kruit (1987) applied diameter selection as suggested by Disney to the Uppsala General Catalogue (UGC) and found a distribution with peak $\mu_0 = 21.8 \pm 0.6 \text{ mag arcsec}^{-2}$. When van der Kruit measured the distribution for Sc galaxies only, the result was, $\mu_0 = 21.5 \pm 0.4 \text{ mag arcsec}^{-2}$, close to the Freeman result.

LSB Galaxies

Bothun et al. (1987) discovered a giant LSBG (Malin 1) with a disk central surface brightness $\mu_B = 26.6 \text{ mag arcsec}^{-2}$ and total absolute magnitude $M_B = -21.2$. The surface brightness of this disk is $\sim 15\sigma$ from the mean of the Freeman distribution and $\sim 8\sigma$ from the mean of the van der Kruit distribution. The fraction of objects expected to lie 10σ away from the mean of a normal distribution is $\sim 10^{-20}$, so in an observable universe of $10^{10} - 10^{11}$ galaxies we would not expect to see any Malin 1s if the Freeman Law is correct.

Binggeli, Sandage & Tammann (1988) noted that the luminosity-surface brightness relationship could explain much of the observations: low surface brightness galaxies are generally faint and therefore van der Kruit would miss these galaxies even when he used a carefully selected sample. This still suggests that galaxies like Malin 1 are rare. They did suggest caution though until the relationship between Malin 1 and other galaxies is understood.

Davies et al. (1994) argued that the van der Kruit sample had hidden magnitude limits that lead to an overestimate of the sample volume for LSBGs and therefore an underestimate of the number density of these galaxies. In a diameter limited catalogue there will be a magnitude when the surface brightness of a galaxy is too low for a detection. Davies et al. (1994) find an effective magnitude limit $m_L^e = 14.1 \text{ mag}$ in van der Kruit's sample. They select a sample from the ESO-LV catalogue (Lauberts & Valentijn 1989) with $D_{26} > 1 \text{ arcmin}$ and $m_L^e = 15.4 \text{ mag}$. They use the redshifts from the sample to define the median volume of each surface brightness bin. They find that the volumes agree well with those calculated using visibility theory (Davies 1990). They find that the distribution of galaxies is well matched to the volume distribution implying a flat distribution in surface brightness.

McGaugh, Bothun & Schombert (1995) and O'Neil & Bothun (2000) also find a flat distribution in surface brightness. McGaugh et al. (1995) criticise Disney & Phillipps (1983) and Davies (1990) for not applying the volume correction in absolute magnitude as well as surface brightness, instead just scaling the results at one magnitude to all. They argue that although their visibility functions are equivalent mathematically, size and surface brightness are more fundamental than absolute magnitude and surface brightness, suggesting that two

galaxies with the same scale size but different surface brightnesses and therefore different absolute magnitudes are more physically related than two galaxies with the same magnitude but different surface brightnesses and therefore different scale sizes. This would be a fair point if galaxies always remained the same size and just varied in surface brightness as the stellar population aged and star formation varied, but in reality this is just a statement of preference for scale size and surface brightness than a good scientific case for using these parameters. O’Neil & Bothun find a distribution that is flat from the Freeman value $\mu_0 = 21.65$ to $\mu_0 = 25.0$ mag arcsec⁻².

vLSB Galaxies

Dalcanton et al. (1997) looks specifically at the low surface brightness galaxies ($23 < \mu_0 < 25$ mag arcsec⁻²). These are found to have the same or greater number density as “normal” ($\mu_0 < 22$ mag arcsec⁻²) galaxies. Recent surveys of low surface brightness galaxies include Bomans & Habertzettl (2001) in a small region of the Hubble Deep Field South and the Kambas et al. (2000) survey of NGC 1291, near the Fornax cluster. Bomans & Habertzettl (2001) find a significant number density of very LSBGs (vLSBGs, $\mu_0 > 25$ mag arcsec⁻²) with one galaxy in particular having $\mu_{0,B} = 27.1$ mag arcsec⁻². Kambas et al. (2000) see a decrease in the numbers of galaxies away from the Fornax cluster, which then increase as they get close to NGC1291. Assuming that these galaxies are companions of NGC1291, they find a significant number of vLSBGs around NGC1291 and conclude that if most high surface brightness galaxies are surrounded by a population of vLSBGs, with high mass-to-light ratios, then vLSBGs may contribute more to the mass density of galaxies than bright high surface brightness galaxies. However, since it has not been possible to get redshifts for either of these samples, there is still a lot of uncertainty about the density of vLSBGs.

Beginning with the Fish and Freeman results, the surface brightness distribution has been shown to be dominated by selection effects. Most modern measurements of the surface brightness distribution appear flat to $\mu_0 = 25$ mag arcsec⁻², with large numbers at even lower surface brightnesses. However, Binggeli, Sandage & Tammann (1988) have pointed out that there is a strong luminosity-surface brightness correlation, and so most of the low surface brightness galaxies are in fact dwarfs. Since Malin 1 was discovered only a couple of other giant LSBGs have been found suggesting that it is indeed rare and LSBGs only contribute significantly to the faint end of the luminosity function and contribute very little to the overall luminosity or matter density. To decide whether this is true, we must look at the bivariate brightness distribution.

1.3.5 The Bivariate Brightness Distribution

In the section on luminosity functions (§ 1.3.1) we showed that there is a great deal of variation among recent determinations of the luminosity function and speculated whether these could be due to surface brightness incompleteness caused by selection effects. In the section on surface brightness distributions we mentioned the problems with surface brightness selection effects and how they have dominated the early measurements. However correlations between luminosity and surface brightness that vary with type make it difficult to use the luminosity

or surface brightness distributions by themselves.

To understand the selection effects and calculate the space density it is necessary to look at the distribution of galaxies in absolute magnitude and intrinsic surface brightness at the same time, $\phi(M, \mu)$ and calculate the number density as a function of both parameters, i.e. a bivariate brightness distribution (BBD), see Fig 1.2.

Some earlier attempts have been made to measure the BBD (e.g. Choloniewski 1985; van der Kruit 1987; Sodr  & Lahav 1993). The Choloniewski sample contained 248 E/S0 galaxies with $-22 < M_B < -18$; the van der Kruit sample contained 51 galaxies with isophotal diameters $> 2'$ at 26.5 mag arcsec $^{-2}$ (in the photographic IIIa-J band) and the Sodr  & Lahav sample contained 529 galaxies with isophotal diameters $> 1'$ at 25.6-26.0 mag arcsec $^{-2}$ in the B-band. These are very strict limits, and only intrinsically very bright and large galaxies were well sampled. The Choloniewski sample has isophotal magnitude $m_{est} \leq 14$ and diameter limits $D(ESO) = 1$ arcmin. The isophotal magnitude m_{est} is roughly estimated by Sadler (1984) who reports that the diameter limit becomes important at $m_{est} = 14.5$. van der Kruit's sample was discussed in § 1.3.4 and was found to have missed the apparent magnitude limits. Sodr  & Lahav (1993) took data from the ESO-LV catalogue (Lauberts & Valentijn 1989) and used the selection limits $B_{25} < 14.5$, $\theta_{25}^B \geq 1.9$ arcmin and $V_{corr} \geq 500$ km s $^{-1}$. While van der Kruit did take account of the changes in the diameter of a galaxy with surface brightness (Disney & Phillipps 1983), Choloniewski and Sodr  & Lahav did not; nor did they take into account the fraction of light lost from galaxies. Choloniewski and Sodr  & Lahav both saw correlations between the diameters and absolute magnitudes of elliptical galaxies. Since the selection limits have not properly been taken into account we should be careful when interpreting this. van der Kruit (1987) produced a BBD for spirals in diameter and surface brightness. There was no significant correlation between diameter and surface brightness. However, given the Davies et al. (1994) argument that van der Kruit has missed selection effects, discussed in § 1.3.4, we must be wary of this result.

In recent, more extensive measurements of the Bivariate Brightness Distribution the existence of the luminosity-surface brightness correlation has been confirmed. The luminosity-surface brightness correlation for the overall galaxy population is measured to be $M_{b_j} = (2.4 \pm 1.5) \mu_e - (72.3 \pm 11.0)$ from Cross et al. (2001). This equates to $\mu_e \sim (0.42 \pm 0.10) M_{b_j} + (30.2 \pm 2.1)$. From Hubble Deep Field data, Driver (1999) found a steeper gradient ($M_{F450W} \propto 1.5 \mu_e$) as did Ferguson & Binggeli (1994) in the Virgo cluster ($M_B \propto 1.4 \mu_o$). The number density of galaxies is a maximum along this line, falling away at both higher and lower surface brightnesses. Given the $M - \mu$ correlation it is hardly surprising if surveys with differing selection criterion recover widely ranging Schechter parameters.

The de Jong & Lacey (2000) BBD uses a population of ~ 1000 Sb-Sdm galaxies taken from the ESO-Uppsala Catalog of Galaxies (Lauberts 1982). The subsample was originally selected by Mathewson, Ford & Buchhorn (1992) to study peculiar motions of galaxies. They use galaxies where the ESO-Uppsala diameter $1.65' \leq D_{maj} \leq 5.05'$, morphological type $3 \leq T \leq 8$ and axis ratio $0.1736 \leq D_{min}/D_{maj} \leq 0.776$. This sample is 81.2% complete for redshifts and surface photometry. Since they use large galaxies, it is possible to extrapolate the last few measured points of the surface brightness profile of each galaxy to infinity to

recover total magnitudes. The average redshift was small $\bar{z} = 0.01$ so cosmological effects are negligible. They fit the Choloniewski (1985) function, see Eqn 2.56, to their data and found that it fitted the data well. They find that the the local luminosity function is not significantly biased against low surface brightness galaxies, even when LSBGs are selected from photographic plates, but warn that this may not be true for high redshift observations such as those from the Hubble Deep Fields.

The Blanton et al. (2001) BBD is based on 11,275 galaxies from the Sloan Digital Sky Survey (SDSS). This will eventually measure the redshifts of $\sim 10^6$ galaxies over $10,000\text{deg}^2$ in 5 colours. The magnitude limit is $r^* = 18.1$, and this subsample has a surface brightness limit $\mu_e = 23.5 \text{ mag arcsec}^{-2}$. The survey uses Petrosian magnitudes which have no dependence on the isophote, see § A.1 and recover 99% of the light for exponential profiles, although only 82% for ellipticals. They display a BBD (Fig. 9, Blanton et al. 2001), but do not fit a function. However, they find a strong luminosity-surface brightness correlation, a broader surface brightness distribution at lower luminosities and a steeper luminosity function at lower surface brightnesses. Our results match the SDSS results in the main. While our overall distribution does not show a strong luminosity- surface brightness correlation, we find that galaxies with moderate to strong emission lines (i.e. spirals and irregulars) do have a strong luminosity- surface brightness correlation.

1.3.6 Difficulties with Measuring the Space Density

Selection Effects

As we have discussed above, many early measurements of the space density have been dominated by selection effects. Even recent surveys have produced a wide range of measurements of the luminosity function. These effects have been mentioned in relation to the surface brightness and bivariate brightness distributions. In Chapter 2 we discuss whether the variation in surface brightness limits could be responsible for the variation in the recent values of the LF.

The basic measure of selection effects in the luminosity function is visibility, the volume over which a galaxy with certain parameters (e.g. M , μ_e) can be observed. We have used the visibility theory developed by Disney (1976), Disney & Phillipps (DP, 1983), Phillipps & Disney (1986), Davies (1990) and Phillipps, Davies & Disney (1990). In particular we have used the equations given in Phillipps, Disney & Davies (PDD 1990), in our calculations. Disney (1976) first suggested that the brightness of the background would affect the completeness of the observed galaxy distribution. In DP a quantitative approach to the visibility was developed, which took account of how the fraction of the total flux and the apparent scale length varied with surface brightness. In Phillipps & Disney (1986) this was applied to spiral clusters in the Virgo cluster selected from the RC2 catalogue. Phillipps and Disney found galaxies right up to the low surface brightness limits. In PDD, cosmological effects such as surface brightness dimming due to expansion ($\frac{1}{(1+z)^4}$) and to the K-correction were incorporated. We discuss visibility theory in § 2.4 and demonstrate it in § A.2.1.

McGaugh et al. (1995) discuss selection limits in surveys and come to the conclusion that *to adequately characterise the local galaxy population, it is necessary to perform a survey which*

- *is complete to rigorously defined and applied limits,*
- *explicitly quantifies a uniform isophotal level at which fluxes or diameters are measured,*

and

- *actually characterises galaxy images with at least two parameters such as surface brightness and scale length.*

In Chapter 3 we quantify the completeness of our data and set limits in terms of magnitude, half-light radii, surface brightness and redshift. We characterise our galaxies in terms of absolute magnitude and effective surface brightness. Although our galaxies are extracted at a constant isophotal level $\mu_{lim} = 26 \text{ mag arcsec}^{-2}$, we use Kron magnitudes (see § A.1) rather than isophotal magnitudes, and we use the half-light radius rather than the radius at $26 \text{ mag arcsec}^{-2}$.

Dalcanton (1998a) discusses light loss when isophotal and other magnitude systems are applied and found that the standard $\langle V/V_{max} \rangle$ tests do not diagnose incompleteness and unusual systematics. Dalcanton showed that the magnitudes can be well behaved to a certain redshift and then rapidly become in error by several magnitudes. The redshift at which this happens depends on the surface brightness of the galaxy and the seeing. It was shown that these effects can severely affect the luminosity function, even at the bright end. Fitting exponential or de Vaucouleur profiles can reduce the light loss, but can lead to biases when the profile is very different. A second paper (Dalcanton 1998b) which included bulges and disks convolved with a Moffat PSF shows that the seeing can lead to an overestimate of fluxes if the underlying profile is close to the fitted profile.

In Dalcanton (1998a), Kron magnitudes were shown to give $\Delta M > 0.3$ when $\mu_{lim} - \mu_0 < 3$, but this was not seen in Dalcanton (1998b). It was suggested that the conflict is due to slightly different definitions of the Kron radius. These papers submit that Petrosian magnitudes (see § A.1) are the best magnitudes to use as they have no surface brightness dependence. In § A.1 we do a thorough examination of the light loss as a function of redshift, disk surface brightness, isophotal limit, bulge to total ratio, seeing and absolute magnitude for isophotal, Gaussian corrected, exponentially corrected, Kron and Petrosian magnitudes. We conclude that both Kron and Petrosian magnitudes have very little isophotal, surface brightness, seeing, redshift or absolute magnitude dependence, but Petrosian magnitudes have a greater dependence on the bulge-to-total ratio and can sometimes give large deviations due to the small annulus that defines them. We have decided to use Kron magnitudes for the MGC.

1.3.7 Techniques used to measure the Space Density.

The measurement of the space density not only requires high quality data, and an understanding of the selection effects, it also needs an unbiased estimator to convert the number of galaxies seen at an absolute magnitude (M) and/or an effective surface brightness (μ). Many different approaches have been used over the years. Here we will describe some of the ones used in recent surveys.

The first of the modern estimators to be developed was the $\frac{1}{V_{max}}$ method (Schmidt 1968), which was first applied to quasi-stellar objects (QSOs) in the Revised 3C Catalogue of Radio Sources (Bennett 1962). In this method, each galaxy is given a weight, $w = \frac{1}{V_{max}}$, where V_{max} is the maximum volume over which the object in question can be seen given the selection criteria. The luminosity function is then calculated by summing up the number weighted distribution, i.e. $\phi(M) = \sum_{M_i > M - \Delta M}^{M_i < M + \Delta M} w_i$. Schmidt also demonstrated the $\frac{V}{V_{max}}$ test for uniform density.

Lynden-Bell (1971) developed the C^- method, the first estimator to use maximum likelihood methods. This calculates a function $C^-(M_i)$ which is the weighted sum of all the points brighter¹ than M_i , taking account of other selection criteria, where M_i is the absolute magnitude of the i^{th} galaxy. The function C^- is used to calculate $\Psi(M) = \prod_i (\frac{C^-(M_i)}{C^-(M_i) + w_i})$, where w_i is the weight of the i^{th} galaxy. The weighting is based on Schmidt's $1/V_{max}$, but with evolutionary effects included. $\phi(M) = -\frac{d\Psi(M)}{dM}$.

The Lynden-Bell (1971) method is particularly useful for small samples, where it takes into account errors when C^- is small. The weight attached to a galaxy with $L = L_i$ will be important if there are only a few galaxies. This method has led to others based on it, such as the Turner (1979) and Chołoniewski's (1987) methods.

Another maximum likelihood method is the Sandage, Tammann & Yahil (STY 1979). This method fits the data to an analytic expression (generally the Schechter 1976 function). The stepwise maximum likelihood method (SWML, Efstathiou, Ellis & Peterson 1988) is based on the STY method, but uses a non-parametric form i.e. it calculates the relative number density in each bin, avoiding any assumptions of the form that the luminosity function should have. Like the STY method the result is not normalised. The SWML approach has been improved by Koranyi & Strauss (1997) who interpolated between bins. Springel & White (1998) have included evolution and developed a piecewise approach, where the selection function is parameterised as a series of stepwise power laws. This has an advantage over the SWML method since it does not require iterations.

The surface brightness distributions and bivariate brightness distributions have often used a $\frac{1}{V_{max}}$ method based on visibility theory (e.g. McGaugh, Bothun & Stromberg 1995, O'Neil & Bothun 2000). However Chołoniewski (1987) used a bivariate estimator based on the Chołoniewski (1985) approach, Sodr  & Lahav (1993) developed a bivariate approach to the SWML method. Unfortunately neither of these methods used a rigorous approach to the selection function, see § 2.4. Davies et al. (1994) used the data to define V_{median} , which he found gave a good match to the result from a traditional V_{max} defined from visibility theory. This approach has the advantage that any selection effects that have been overlooked will automatically be taken care of. However it does require large data sets.

In the last few years there have been several papers that have looked at bias in these estimators. Willmer (1997) concluded that the STY and C^- methods gave the best results, although they agreed with the EEP result that STY is slightly biased towards flat faint end slopes. Willmer also found that $\frac{1}{V_{max}}$ gave estimates of the luminosity function biased toward steeper faint end slopes even in homogeneous samples but found that the observed discrepancy

¹In Lynden-Bell's example, $C^-(L_i)$ is calculated as the weighted sum of the QSOs with a brighter optical to radio flux than L_i .

between local and distant galaxies cannot be attributed to different estimators. Takeuchi, Yoshikawa & Ishii (2000) found that $\frac{1}{V_{max}}$ was a good estimator if the distribution was spatially uniform but the shape of the LF is severely affected if there is a large cluster or void. They found that when the sample size is small that there were large fluctuations in the Choloniewski method, but the Choloniewski method was fastest and therefore best for large samples. They show that the Choloniewski, SWML and a refined version of the C^- method, the Lynden-Bell-Choloniewski-Caditz-Petrosian method (LCCP) are all robust when large clusters and voids are added.

When we have produced BBDs and LFs, we have avoided making assumptions about the shape of the luminosity function, so we have not used the STY method. Since the $\frac{1}{V_{max}}$ method is biased when there is strong clustering, and depends on a good knowledge of the selection effects, we have avoided this method. We have used two methods, so that we can spot any bias due to the estimator. The first method uses the data as much as possible, so that subtle selection effects are automatically picked up. We also use a second, more theoretical estimator, which has been shown to be robust to clustering.

In Cross et al. (2001) we developed a modification of the Davies et al. (1994) method for the bivariate brightness distribution. As in Davies et al. (1994) we use the data to define the volume, although we use the 90th percentile galaxy rather than the median in each bin. We also are careful to define the minimum redshift of each bin and correct for clustering and redshift incompleteness as a function of absolute magnitude and intrinsic effective surface brightness. Since we make these corrections, the criticisms above of a $\frac{1}{V_{max}}$ do not apply. This method is described in § 2.6.1.

In § 2.6.2 we introduce a refinement to the Sodr e & Lahav (1993) bivariate SWML by incorporating visibility theory. This gives an independent estimator to the Cross et al. (2001) method, which makes the same type of corrections but in a completely different way. These methods should give the same result if they are unbiased and the correct selection effects have been applied. In Chapter 4, we will demonstrate that they do give the same results. We use the SWML method because it is the most popular and it is simple to incorporate visibility theory.

1.4 Uses of the Bivariate Brightness Distribution of Galaxies

1.4.1 The Luminosity Density and the Star Formation Rate

Measurements of the star formation history can be made by comparing the luminosity density in the UV (where massive stars dominate) at different redshifts. At higher redshifts, the UV output will be detected at longer wavelengths, in the optical and eventually the near infrared. Observations from the Canada-France Redshift Survey (Lilly et al. 1996) for the range $0.5 < z < 1.0$ and the Hubble Deep Field (Madau, Pozzetti & Dickinson 1998) for the range $2 < z < 6$ combined with the $z = 0$ result from line emitting galaxies (Gallego et al. 1995) suggests that the star formation rate increases rapidly until from $z = 0$ to $z \sim 1.5$ and then falls slowly. This is in line with the Pei & Fall (1995) model, although significantly lower at high redshifts.

1.4.2 Using the Luminosity Function and Number Counts to Constrain Cosmology and Evolution

Since measuring the spectrum of a galaxy to calculate its redshift requires many more photons than detecting a galaxy on a photographic plate or CCD, and each object targeted by a spectrometer requires its own slit or fibre, it is possible to measure number counts for much fainter galaxies than it is possible for luminosity functions or bivariate brightness distributions. One can use the luminosity function to predict number counts (e.g. Tyson 1988; Metcalfe et al. 1991, 1995; Hogg et al. 2000; McCracken et al. 2001; Liske et al. 2002).

Unfortunately the counts do not fit the models well and this has led to problems such as the *faint blue galaxy* problem (Koo & Kron 1992; Ellis 1997) and the normalisation problem (Maddox et al. 1990; Shanks 1990; Driver, Windhorst & Griffiths 1995; Marzke et al. 1998; Cross & Driver 2001; Liske et al. 2002).

The faint end of the number counts depends on the cosmology, the evolution of galaxies and of course the accurate measurement of the luminosity function. To measure any one, a degree of certainty in the other two is needed, although Driver (2002) demonstrates that in the range covered by the MGC, it is errors in the faint end slope α that dominates the variation in the faint number counts

Nagashima et al. (2001) use semi analytical models to predict the number counts in the HDF, incorporating surface brightness selection effects. They find that when they do this that a low density universe ($\Omega_M = 0.3$) with or without a cosmological constant is preferred over the standard Einstein de-Sitter universe ($\Omega_M = 1, \Omega_\Lambda = 0$).

1.4.3 Constraints on Galaxy Formation Models from the BBD.

Various papers have related galaxy formation models to the bivariate galaxy distribution. Dalcanton Spergel & Summers (1997) used the Fall & Efstathiou (1980) disk formation model to predict the BBD. They linked mass and angular momentum with luminosity and surface brightness. Low angular momentum proto-galaxies form high surface brightness galaxies, since the same mass of gas is able to collapse further when the angular momentum is low. Their model predicts that $\mu_0 < 21$ mag arcsec⁻² disk galaxies will be unstable, forming bars, bulges or elliptical galaxies. This prediction is in line with the Freeman (1970) result and the interpretation by Allen & Shu (1979). Dalcanton et al. (1997) predict galaxies with $\mu_0 > 27$ mag arcsec⁻², and find that their galaxies obey the Tully-Fisher law. They predict that current surveys are missing a significant fraction of the total number of galaxies and that the faint end of the luminosity function is severely underestimated.

de Jong & Lacey (2000) also use the Fall & Efstathiou (1980) model to explain the BBD. They concentrate on the luminosity-scale size relation (this can be converted to the luminosity-surface brightness relation using Eqn 1.2) which is predicted from their models. They find a reasonable match to the gradient from using a sample of 1000 late type spirals, but find a significantly narrower width than the model.

Wyse & Jones (1984) found correlations between the surface brightness and the rotational parameter of elliptical galaxies. They also saw a looser correlation between absolute magnitude and the rotational parameter of elliptical galaxies. They suggest that the properties of elliptical

galaxies depend on the amount of dissipation that has occurred. High surface brightness ellipticals have had more dissipation, and therefore have a larger ratio of rotational velocity to velocity dispersion. Low surface brightness ellipticals have had less dissipation, so have a smaller ratio of rotational velocity to velocity dispersion. High surface brightness ellipticals tend to be intrinsically fainter (Kormendy 1977; Thomsen & Franzen 1983). This may be due to the time constraints necessary for dissipation. de Zeeuw & Franx (1991) showed that since the dynamical time-scale in the outer parts of giant elliptical galaxies is similar to the Hubble time, only the centres will be in equilibrium. Smaller galaxies will be closer to equilibrium and therefore have undergone more dissipation.

Zhang & Wyse (2000) use dynamical models to explain the Hubble sequence. They found that disk galaxies can be formed by either monolithic collapse of a dark halo or by quiescent merging of sub haloes onto a primary dark halo. This initial stage follows the Fall & Efstathiou (1980) model mentioned above. They discuss the formation of bulges from bar instabilities. This works well for smaller bulges, which follow an exponential profile, but larger bulges and elliptical galaxies are thought to be the result of mergers.

1.4.4 Mass to Light Ratios and constraints on Ω_M

Given the luminosity density as a function of M and μ it is possible to multiply by the mass-to-light ratio and calculate the mass-density.

$$\rho_M = \sum_M \sum_\mu j(M, \mu) \frac{M}{L}(M, \mu) \Delta M \Delta \mu \quad (1.16)$$

In Cross et al. (2001) we applied a constant maximum mass-to-light ratio, based on the mass-to-light ratios of clusters (since clusters have the largest measured mass-to-light ratios) to put upper limits on the mass density Ω_m . We found that the implied upper limit was $\Omega_m = 0.24 \pm 0.05$, consistent with the Λ -CDM universe, or a low density $\Omega = 0.3$ universe, but not the standard Einstein-de Sitter model.

To calculate the actual mass density is more difficult as the variation in the mass-to-light ratio is not well known. Zwaan et al. (1995) and de Blok et al. (1996) have used HI observations of HI galaxies to calculate the mass-to-light ratios. They find that the observed masses are close to the expected masses from the Tully-Fisher relationship, and therefore $\frac{M}{L} \propto \Sigma_0^{-1/2}$ for spiral galaxies. Thus a disk with $\mu_0 = 26$ mag arcsec⁻² will have a mass-to-light ratio 55 times that of a Freeman Law disk. Mateo (1998) noted that the mass-to-light ratio of dwarf galaxies also increased rapidly as they became fainter. He found that they fitted a model based on a disk with a stellar population with constant mass-to-light ratio ($\frac{M}{L_V} = 2.5$) contained in a dark matter halo of constant mass ($M = 10^7 M_\odot$). However the data for both LSBGs and dwarf galaxies is based on small samples with many outliers. New HI surveys, such as the HI Parkes All Sky Survey (HIPASS, Kilborn, Webster & Stavely-Smith 1999) should place better constraints on the mass-to-light ratio.

1.5 Summary

In this chapter, we have reviewed the literature surrounding the measurement of the space density of galaxies. We have mentioned many of the various types of galaxy, and discussed some of their properties.

We then studied many recent surveys of galaxies and found that there is still significant variation in the measurement of the space density of intrinsically bright galaxies, and even more uncertainty in the space density of faint or low surface brightness galaxies.

We have examined the potential bias in the data and methods of measuring the space density and discussed the improvements that have been made over recent years. Finally, we have discussed the uses of the space density in constraining cosmology, as well as the testing models of the formation and evolution of galaxies.

In Chapter 2, we set out the tools that we will use to calculate the BBD. We introduce visibility theory which describes the volume over which a galaxy can be seen when many different selection effects are present, taking into account the surface brightness profile of the galaxy. We introduce two different estimators to reduce the chance that our results are biased by the estimator and we discuss the use of an analytical fit to the BBD, and demonstrate that surface brightness selection effects have lead to biased measurements of the luminosity function.

It is important throughout to understand the selection effects introduced by the survey and to have accurate photometric data and a complete sample to the specified limits. The Century Survey (Brown et al. 2001) estimates that they are $> 98\%$ redshift complete to their limits, which are relatively bright $V_0 < 16.7$ and $R_0 < 16.2$. The 2dFGRS has $\sim 91\%$ redshift completeness. However, these numbers assume that the input catalogue is complete. In Chapter 3 we discuss the data sets we use and quantify the photometric accuracy and completeness of our data. We use 3 datasets, the 2dFGRS, the Sloan Digital Sky Survey Early Data Release (SDSS-EDR) and the MGC.

In Chapter 4 we use an almost complete dataset consisting of MGC photometry with redshifts from the 2dFGRS and the SDSS-EDR to measure the space density of galaxies, free from selection effects. We find that the 2dFGRS and SDSS-EDR have underestimated the bright end by ~ 0.1 mag. However, the MGC is too small to accurately probe the faint end of the distribution $M_B > -16$. We find a flat surface brightness distribution, confirming recent results.

In Chapter 5, we use the MGC photometric data to correct the 2dFGRS data on plates that overlap with the MGC, so that we can use a much larger sample of galaxies. We are able to measure the faint end to $M = -14.5$, and find that the faint end slope rapidly steepens when $M > -17$. We are also able to measure the bivariate brightness distributions as a function of the 2dFGRS spectral type (Madgwick et al. 2001). We find that type 1 galaxies (Ellipticals and S0s) do not have a strong correlation between luminosity and surface brightness, but types 2-4 (Spirals/ Irregulars) do have a strong correlation. Type 1 galaxies have two populations, a bright population, tightly bound well within the selection boundaries, and a faint population that is rapidly increasing in space density at the selection boundaries. Types 2 to 4 all have similar luminosity-surface brightness correlations, in which both the gradient and width vary

little between types. The typical luminosity gets fainter with increasing type and the faint end slope becomes steeper with increasing type.

At the bright end, the completeness is high, as the space density drops considerably before the selection limits are reached. However, at the faint end the space density is still high at the low surface brightness boundary, demonstrating that the luminosity functions are underestimating the space density of faint galaxies.

Chapter 2

The Methodology Used to Produce the Bivariate Brightness Distribution.

This chapter lays out all the tools used throughout this thesis. We begin by writing down the cosmological equations and relationships between photometric parameters. Then we describe Visibility Theory, the two methodologies we use for calculating the Bivariate Brightness Distribution (BBD) and the analysis of a function fitted to the BBD.

The first method used to calculate the BBD is an empirical method which uses the data as much as possible. We utilize the distribution of galaxies to define the redshift limits of each bin. We correct for clustering and incompleteness in both magnitude and surface brightness. The second method is a bivariate Stepwise Maximum Likelihood method, incorporating Visibility Theory.

Finally an analytic function is fitted to the BBD and this is used to derive random catalogues to demonstrate the effects of different surface brightness limits on the luminosity function. We find that all the variation at the bright end can be explained by the variation in surface brightness limits.

2.1 Introduction

In this chapter we introduce the methodology that we will use throughout this thesis. First, we set down the cosmological equations in § 2.2 and the relationships between photometric variables that we will employ (§ 2.2).

In § 2.4 we introduce visibility theory, derived by Phillipps, Davies & Disney (1990). This is used to calculate the maximum and minimum redshift that a galaxy can have and still be within the selection limits of the survey. When the measurements are isophotal parameters these redshift limits can become strong functions of the surface brightness.

In § 2.5, we describe the corrections that we used initially to determine the total magnitude and effective surface brightness. Then we discuss the methodologies that we use to calculate

the space density of galaxies, one which we refer to as the empirical method, in § 2.6.1, and the other is a version of the Bivariate Stepwise Maximum Likelihood (SWML) method (Sodré & Lahav 1993), incorporating visibility theory in § 2.6.2.

The two methods, the Empirical and the SWML, are compared in § 2.6.3. They are found to agree well at the bright end, but the SWML gives a steeper faint end slope. However, the data used here, are preliminary data from the Two degree Field Galaxy Redshift Survey (2dFGRS, see § 3.2.1), which has since been recalibrated, so the plots presented in this chapter are not the final BBD plots.

We have used the preliminary 2dFGRS data to fit the Choloniewski (1985) analytic function (Eqn 2.56), which gives a good fit at the bright end, but a poor fit at the faint end. When selection limits with isophotal limits varying over the range ($23 < \mu_{lim} < 26$) are applied to random catalogues calculated from this function the variation in the luminosity functions produced matches the variation seen in Chapter 1, suggesting that surface brightness selection effects are the primary cause of the variation in the luminosity function.

2.2 Cosmology Equations

As one moves to higher redshifts the effects of cosmology and evolution become important. Below are the cosmological equations used throughout this thesis. These are derived from the Friedmann equations and taken from Peacock (1999). The general formula for the co-moving (proper) distance and the redshift is given in Eqn 2.1.

$$\begin{aligned} d_p(z) &= \frac{c}{H_0} \int_0^z \frac{dz'}{\sqrt{(1-\Omega)(1+z')^2 + \Omega_v + \Omega_m(1+z')^3 + \Omega_r(1+z')^4}} \\ &= \frac{c}{H_0} \int_0^z \frac{dz'}{X[(1+z'), \Omega, \Omega_v, \Omega_m, \Omega_r]} \end{aligned} \quad (2.1)$$

where $\Omega = \Omega_v + \Omega_m + \Omega_r$, c is the speed of light and H_0 is Hubble's constant. Throughout this thesis we use $H_0 = h 100 \text{kms}^{-1} \text{Mpc}^{-1}$. Ω is the total energy density of the Universe, Ω_m is the matter density of the Universe, Ω_r is the radiation density of the Universe and Ω_v is the vacuum energy density of the Universe. The luminosity and angular diameter distances are related to the proper distance by Eqns 2.2 & 2.3

$$d_L(z) = (1+z)d_p(z) \quad (2.2)$$

$$d_A(z) = \frac{d_p(z)}{1+z} \quad (2.3)$$

To calculate the density of galaxies, it is essential to be able to compute the volume as a function of the redshift. The volume between two redshift limits is calculated using Eqn 2.4.

$$V = \frac{c\sigma}{H_0} \int_{z_{min}}^{z_{max}} \frac{d_L^2 dz}{(1+z)^2 X[(1+z), \Omega, \Omega_v, \Omega_m, \Omega_r]} \quad (2.4)$$

where σ is the area on the sky in steradians. X is defined in Eqn 2.1.

Cosmological dimming occurs because of the universal expansion. In a non-expanding Universe, the surface brightness of an object would remain constant, irrespective of distance. As the distance doubles, the luminosity is reduced by a factor of 4, but at the same time, the area is reduced by a factor of 4, keeping the surface brightness constant. In contrast, in an expanding Universe, the luminosity is reduced by a factor of $[d_p(1+z)]^2$, see Eqn 2.2, due to the reduction of energy of each photon by $(1+z)$ and the time dilation effect increasing the time between the emission of each photon by $(1+z)$. The surface brightness on the other hand is reduced by $[d_p/(1+z)]^2$; see Eqn 2.3.

$$\Sigma = \frac{l}{\pi \theta^2} = \frac{L}{[d_p(1+z)]^2} \frac{[d_p/(1+z)]^2}{\pi r^2} = \frac{L}{\pi r^2(1+z)^4} \quad (2.5)$$

where Σ is the apparent surface brightness in lum arcsec^{-2} . l is the apparent luminosity, θ is the apparent radius, L is the absolute luminosity and r is the intrinsic radius.

Most of the analysis was done using an Einstein-de Sitter cosmology $\Omega_m = 1.0$, $\Omega = 1.0$ for reasons of efficiency. The Einstein-de Sitter equations can be solved analytically whereas more complicated cosmologies have to be solved numerically. However some analysis has been done using a Λ -CDM cosmology, $\Omega_m = 0.3$, $\Omega_v = 0.7$, $\Omega = 1.0$, the favoured cosmology today (Efstathiou et al. 1999; Tegmark, 1999).

As the redshift of a galaxy increases, two other effects, the K-correction and evolution become important. The K-correction comes from the change in wavelength of the emission with redshift. [For simplicity consider a perfect filter, which passes all photons with $\lambda_1 < \lambda < \lambda_2$ and none outside this range. Radiation emitted at λ_1 by a galaxy at redshift z_1 will be detected at $\lambda = \lambda_1(1+z_1)$. This will no longer be at the short wavelength edge of the filter. Instead shorter wavelength emission from the galaxy ($\lambda = \lambda_1/(1+z_1)$) will be detected at λ_1 .] The difference in magnitude can be calculated using Eqn 2.6, Oke & Sandage (1968).

$$10^{0.4K(z)} = \frac{\int T(\lambda) f_{\log}(\lambda) d \ln \lambda}{\int T(\lambda) f_{\log}(\lambda/[1+z]) d \ln \lambda} \quad (2.6)$$

where $f_{\log}(\lambda)$ is the logarithmic flux density of the galaxy and $T(\lambda)$ is the filter transmission function, i.e. the efficiency of the filter at each wavelength. Both are complicated functions. However, $K(z)$ can be approximated by simple parametric equations such as:

$$K(z) = k_1 z + k_2 z^2 + O(z^3) \quad (2.7)$$

The K-correction can either dim or brighten a galaxy. In the B-band for instance it tends to dim galaxies because stars emit more light as 400nm photons than as 300nm photons. However, in the near infra-red, the situation is reversed because more photons are emitted at 800nm than 900nm. K-corrections can vary widely between galaxy types.

The magnitude of a galaxy will evolve with time due to varying star formation rates, the aging of the stellar population or growth of the galaxy. When mergers trigger a starburst the

change in magnitude can be extremely large and very rapid. Other galaxies such as elliptical galaxies evolve slowly as their stellar populations age.

We will use the (K+e) corrections determined by Norberg et al. (2002) based on the Bruzual & Charlot (1993) stellar population synthesis code. These correct the magnitudes to a $z = 0$ magnitude, assuming purely luminosity evolution, and are not dependent on the cosmology. These have been calculated for each of the spectral types defined by Madgwick et al. (2001).

Madgwick et al. (2001) use a Principal Components Analysis (PCA) to identify the components of the spectral data that are the most discriminatory between each galaxy. They find that two thirds of the variance comes from the first two components. A combination of these two components, $\eta = a pc_1 - pc_2$ (with $a = 0.5 \pm 0.1$) describes the average absorption/emission from each galaxy. A small value of η indicates a strongly absorbing spectrum and a high value of η denotes strong emission. Madgwick et al. (2001) split the distribution of η into four broad bins - the four spectral types used in Chapters 3, 4 and 5. The divisions are determined by the shape of the histogram of η values, shown in Fig. 4 of Madgwick et al. 2001. η -type 1 galaxies include all galaxies within the strong peak in this histogram. η -type 2 galaxies are all those along the flat part of the histogram, η -type 3 galaxies are all those in the rapidly decreasing part of the histogram and η -type 4 galaxies are all those along the tail of the histogram. η -type 1 galaxies are predominately ellipticals and lenticulars, η -type 2 galaxies are mainly Sa and Sb galaxies, with η -type 3 and η -type 4 galaxies being mainly late type spirals and irregulars.

The (K+e) corrections for each type are: Type 1, $(K + e)(z) = (2z + 2.8z^2)/(1 + 3.8z^3)$; Type 2, $(K + e)(z) = (0.6z + 2.8z^2)/(1 + 19.6z^3)$; Type 3, $(K + e)(z) = (z + 3.6z^2)/(1 + 16.6z^3)$; Type 4, $(K + e)(z) = (1.6z + 3.2z^2)/(1 + 14.6z^3)$. For galaxies without a spectral classification the general correction is $(K + e)(z) = (z + 6z^2)/(1 + 20z^3)$.

Using the equations above we can calculate the absolute magnitude M and intrinsic surface brightness μ at a given redshift z .

$$M = m - 5 \log_{10} d_L - 25. - (K + e)(z) \quad (2.8)$$

$$\mu = \mu^{app} - 10 \log_{10}(1 + z) - (K + e)(z) \quad (2.9)$$

where m and μ_{app} are the apparent magnitude and surface brightness respectively.

2.3 Useful Relations Between Photometric Properties of Galaxies

The surface brightness profiles of galaxies are usually well described by an exponential profile for the disk combined with a de Vaucouleurs' profile for the bulge. Irregular galaxies are usually well fitted by an exponential profile only, whereas Ellipticals are well fitted by a de Vaucouleurs' only. These profiles are described in the equations below. The exponential is described in Eqn 2.10

$$\begin{aligned}\Sigma(r) &= \Sigma_0 \exp\left(-\frac{r}{\alpha}\right) \\ \mu(r) &= \mu_0 + 1.0857\frac{r}{\alpha}\end{aligned}\quad (2.10)$$

where Σ_0 and μ_0 are the central surface brightness in $\text{Wm}^{-2}\text{Hz}^{-1}\text{arcsec}^{-2}$ and in magnitudes arcsec^{-2} respectively. α is the exponential scale length. The de Vaucouleurs' (1959) profile is described in Eqn 2.11.

$$\begin{aligned}\Sigma(r) &= \Sigma_{r_e} \exp\left\{-7.669 \left[\left(\frac{r}{r_e}\right)^{1/4} - 1\right]\right\} \\ \mu(r) &= \mu_{r_e} + 8.327 \left[\left(\frac{r}{r_e}\right)^{1/4} - 1\right]\end{aligned}\quad (2.11)$$

where r_e is the half-light radius, the radius which encloses half the flux of the galaxy. Σ_{r_e} and μ_{r_e} are the surface brightness at r_e . The constants above, are calculated such that when the profile is integrated to r_e , the fraction of light is $\frac{1}{2}$. The equations needed to calculate this will be laid down shortly. Eqns 2.10 and 2.11 are the usual representations of the exponential and de Vaucouleurs' profiles, although the exponential profile can be described in terms of the half-light properties and the de Vaucouleurs' profile can be described in terms of the central surface brightness and scale length as described below.

Spiral galaxies contain a disk which is well described by an exponential profile and a bulge which is well described by a Sersic profile (Sersic 1968), given in Eqn 2.12.

$$\begin{aligned}\Sigma(r) &= \Sigma_e \exp\left\{-k \left[\left(\frac{r}{r_e}\right)^{1/\beta} - 1\right]\right\} \\ \mu(r) &= \mu_{r_e} + 1.0857k \left[\left(\frac{r}{r_e}\right)^{1/\beta} - 1\right]\end{aligned}\quad (2.12)$$

where $k = 1.9992\beta - 0.3271$ (Capaccioli et al. 1989). $\beta \sim 1$ for Dwarf spirals and increases to ~ 4 for Giant spirals (de Jong 1996, Courteau et al. 1996 and Andredakis 1998). The exponential and de Vaucouleurs' profiles above are just special cases of Eqn 2.12. For an exponential profile $k = 1.678$, $\beta = 1$ and for a de Vaucouleurs' profile $k = 7.669$, $\beta = 4$. To switch between half-light parameters (r_e , μ_{r_e}) and the central surface brightness (μ_0) and scale length (α), use Eqns 2.13 and 2.14. Some typical galaxy profiles are shown in Fig A.1.

$$\mu_{r_e} = \mu_0 + 1.0857k \quad (2.13)$$

$$r_e = k^\beta \alpha \quad (2.14)$$

The fraction of light within a radius r for a Sersic profile is determined by integrating the profile in a circle of radius, r .

$$f = \frac{\int_0^r 2\pi\Sigma(r')r' dr'}{\int_0^\infty 2\pi\Sigma(r')r' dr'} \quad (2.15)$$

The result of this calculation is given in Eqn 2.16 for a Sersic profile.

$$f = 1 - \sum_{n=1}^{2\beta-1} \frac{g^n}{n!} e^{-g} \quad (2.16)$$

where g is a function of the number of scale lengths at the isophotal limit, as shown in Eqn 2.17.

$$g = k \left(\frac{r}{r_e} \right)^{1/\beta} \quad (2.17)$$

g is also simply related to the difference between the isophote μ_{lim} at which r is measured and the central surface brightness.

$$g = 0.4 \ln(10)(\mu_{lim} - \mu_0) \quad (2.18)$$

When cosmology is taken into account μ_{lim} must be modified according to Eqn 2.9. These relationships are important in visibility theory, as will be demonstrated in § 2.4

The isophotal magnitude is the total amount of light measured within the connected pixels brighter than the isophote. Parts of the galaxy where the surface brightness profile falls below the isophote will be missed. The relationship between the isophotal magnitude and the total magnitude is given in the following equation.

$$m_{tot} = m_{iso} + 2.5 \log_{10} f \quad (2.19)$$

The simplest measurement of surface brightness is the mean surface brightness above the isophote.

$$\bar{\mu} = m_{iso} + 2.5 \log_{10}(A_{iso}) \quad (2.20)$$

where A_{iso} is the isophotal area. However, the mean surface brightness will change with the depth of the survey and redshift. A more robust measurement of surface brightness is the effective surface brightness. This is the mean surface brightness above the half-light radius. One advantage of the effective surface brightness, is that its definition does not assume a particular profile shape and it can be calculated simply from images without having to fit a function to the light profile.

$$\mu_e = m_{tot} + 2.5 \log_{10}(2\pi r_e^2) \quad (2.21)$$

Using Eqns 2.8 and 2.9 we can convert this to absolute parameters.

$$\mu_e = M_{tot} + 2.5 \log_{10}(2\pi R_e^2) + 36.57 \quad (2.22)$$

where R_e is the half-light radius in kpc, μ_e is the intrinsic effective surface brightness and M_{tot} is the total absolute magnitude.

Sometimes the surface brightness at the half-light radius μ_{r_e} is referred to as the effective surface brightness or labeled μ_e . We have been careful to distinguish them. The subsequent work uses the effective surface brightness as described in Eqn 2.21. To convert from μ_{r_e} to μ_e , use the following equation.

$$\mu_e = \mu_{r_e} + 5\beta \log_{10} k - 1.0857k - 2.5 \log_{10} \frac{(2\beta)!}{2} \quad (2.23)$$

For an exponential disk this equates to $\mu_e = \mu_{r_e} - 0.698$ and to $\mu_e = \mu_{r_e} - 1.393$ for a de Vaucouleurs' profile. The conversion from central surface brightness to effective surface brightness is given in Eqn 2.24

$$\mu_e = \mu_0 + 5\beta \log_{10} k - 2.5 \log_{10} \frac{(2\beta)!}{2} \quad (2.24)$$

For an exponential disk the conversion is $\mu_e = \mu_0 + 1.124$ and for a de Vaucouleurs' profile it is $\mu_e = \mu_0 + 6.933$.

2.4 Visibility

In the Appendix we will discuss magnitude types, § A.1, and the detection of galaxies, § A.2, and give a demonstration of visibility theory, § A.2.1. These sections give a broader view of the topic and useful demonstrations of the problems. In this section we will lay down the basic equations of visibility theory, used to calculate the volume over which a galaxy can be seen. This framework makes it possible to incorporate many different limits at once.

To start with let us imagine what happens to our measurements when a galaxy of constant intrinsic luminosity and size is viewed at different redshifts. As the galaxy is moved further away it appears fainter, eventually approaching the faint magnitude limit. It also appears to be smaller, approaching the minimum diameter limit. In a static, Euclidean Universe, with no background light, it is very easy to calculate the maximum distance to which the galaxy can be seen to with these two limits.

$$\begin{aligned} d_1 &= 10^{0.2(m_{faint} - M - 25)} \text{Mpc} \\ d_2 &= 206.3 \frac{D}{\theta_{min}} \text{Mpc} \\ d_{max} &= \min(d_1, d_2) \end{aligned} \quad (2.25)$$

where M and D are the absolute magnitude and intrinsic size of the galaxy (in kpc) and m_{faint} and θ_{min} are faint magnitude limit and minimum angular diameter limit (in arcsec). The factor

of 206.3 comes from converting the angular size to radians (2.063×10^5) and converting kpc to Mpc.

However, there are extra complications such as the optical background, which has a similar surface brightness as the centres of disk galaxies. This causes the light loss problems discussed at length in § A.1, which are shown to be profile dependent. Also since the Universe is expanding there are important cosmological effects, such as surface brightness dimming (see Eqn. 2.5) and the effect of the K-correction (see Eqn. 2.6) and evolution. Thus the same galaxy will differ in the amount of light loss and ratio of apparent diameter to scale size if it is viewed at a different redshift.

This means that both d_1 and d_2 are surface brightness dependent. They are functions of the surface brightness profile of the galaxy, which depends on morphological type and redshift, and also the detection isophote.

2.4.1 A Thorough Example: Exponential Profiles.

Below is the full visibility treatment of face-on disk galaxies with isophotal magnitudes. The equations below are reproduced from Disney & Phillipps (1983) and Phillipps, Davies and Disney (1990). These are used to calculate the volume over which a galaxy of absolute magnitude M , and central surface brightness μ_0 can be seen. The theory determines the maximum distance to which a galaxy can be seen, using two constraints: the apparent magnitude that the galaxy would have, and the apparent size that the galaxy would have. The first constraint sets a limit on the luminosity distance to the galaxy, which is the distance that a galaxy is at when it becomes too faint to be seen.

$$d_1 = [f(\mu_{lim} - \mu_0)]^{\frac{1}{2}} 10^{[0.2(m_{lim} - M - 25 - (K+e)(z))]} \text{ Mpc} \quad (2.26)$$

where $f(\mu_{lim} - \mu_0)$ is the fraction of light above the isophotal detection threshold and is profile dependent, see Eqn 2.16. Using $\beta = 1$ and $k = 1.678$, the fraction of light seen is:

$$f(\mu_{lim} - \mu_0) = 1 - [1 + 0.4 \ln(10)(\mu_{lim} - \mu_0)] 10^{[-0.4(\mu_{lim} - \mu_0)]} \quad (2.27)$$

where μ_{lim} is modified according to Eqn 2.9 to take into account cosmological dimming and the (K+e) correction.

Thus the maximum distance has a surface brightness dependence. The luminosity distance is a function of redshift and cosmological parameters, calculated from the proper distance, see § 2.2.

The maximum distance can be found numerically by, for instance, a Newton- Raphson iteration using the fact that

$$d_1(z) - d_L(z) = 0 \quad (2.28)$$

at the maximum distance.

The second constraint, the size limit is found by a similar method. The size limit is:

$$d_2 = C g(\mu_{lim} - \mu_0) 10^{[0.2(\mu_0 - M)]} / \theta_{lim} \text{ Mpc} \quad (2.29)$$

where C is a profile dependent constant. $g(\mu_{lim} - \mu_0)$ is related to the isophotal limit by Eqn 2.18 and is equivalent to the isophotal radius in scale lengths, see Eqn 2.17 for an exponential disk. θ_{lim} is the minimum apparent diameter. For a spiral disk with an exponential profile:

$$C = \sqrt{\frac{2}{\pi}} 10^{-5} \quad (2.30)$$

In this case d_2 is an angular-diameter distance, not a luminosity distance. In the same way as for the magnitude limit, the maximum redshift can be found numerically by solving Eqn 2.31.

$$d_2(z_2) - d_A(z_2) = 0 \quad (2.31)$$

Once the redshifts z_1 and z_2 , which are the solutions of Eqn 2.28 and Eqn 2.31, have been found, the maximum redshift is the minimum of z_1 and z_2 .

$$z_{max} = \min(z_1, z_2) \quad (2.32)$$

The equations can also be used to find the minimum redshift.

$$z_{min} = \max(z_3, z_4) \quad (2.33)$$

where z_3 is calculated in the same way as z_1 , using the bright magnitude limit rather than the faint magnitude limit and z_4 is calculated in the same way as z_2 , using the maximum apparent diameter limit rather than the minimum apparent diameter limit.

Additional cuts for minimum or maximum redshift can be imposed at this stage. Many surveys have a minimum redshift cut to avoid problems with peculiar velocities dwarfing the Hubble flow velocity. Cuts are made at high redshift to avoid the worst photometric problems or evolutionary problems. Also cuts are made to produce luminosity functions or BBDs within a redshift range to test evolution.

The visibility $V(M, \mu_0)$ is calculated using Eqn 2.4 and these limits. It represents the volume over which a spiral disk galaxy of absolute magnitude M and central surface brightness μ_0 can be observed. The central surface brightness can be converted to effective surface brightness using Eqn 2.24.

As well as isophotal magnitude and diameter limits, there are similar limits used for total magnitudes, half-light diameters and apparent surface brightness limits. These are particularly useful if the magnitudes have been corrected to total magnitudes. In these cases, the isophotal limit only affects the completeness of the survey.

The total magnitude limits are simple to calculate. For total magnitudes $f(\mu_0 - \mu_{lim})$ in Eqn 2.26 is equal to 1. Thus:

$$d_1 = 10^{[0.2(m_{i,lim} - M - 25 - (K+e)(z))]} \text{ Mpc} \quad (2.34)$$

Similarly, the half-light diameter does not depend on the isophote, only on the central surface brightness. Thus Eqn 2.29 becomes:

$$d_2 = 1.678 C 10^{[0.2(\mu_0 - M)]} / \theta_{lim} \text{ Mpc} \quad (2.35)$$

where $g(\mu_0 - \mu_{lim})$, the number of scale lengths at the isophote is replaced by 1.678, the number of scale lengths at the half-light radius, see Eqn 2.14. d_1 and d_2 can be related to the luminosity and angular-diameter distances as before and solved to get z (see Eqns 2.2 - 2.31).

In Chapters 4 and 5 we have also used apparent surface brightness limits μ_e^{app} , to avoid regions of low completeness. These are different from the isophotal limit. An isophotal limit is the surface brightness level that isophotal magnitudes and areas are measured at, whereas an apparent surface brightness limit is a simple cut removing some detected objects. The redshift can be found by solving Eqn 2.36 for z .

$$10 \log_{10}(1+z) + (K+e)(z) + \mu_e - \mu_e^{app} = 0 \quad (2.36)$$

2.5 The Isophotal Correction and Effective Surface Brightness

In Cross et al. (2001) we corrected the APM magnitudes for light loss below the isophotal threshold by fitting an exponential profile to the isophotal magnitude and radius. We use this dataset in this Chapter to demonstrate the techniques, but as we will discuss later, it is only a preliminary dataset.

The APM magnitudes have already been corrected for light loss assuming a Gaussian profile (see Maddox et al. 1990b for full details). This was aimed primarily at recovering the light lost due to the seeing and is crucial for compact objects. It is known to significantly underestimate the isophotal correction required for low surface brightness disks. Such systems typically exhibit exponential profiles with disks which can extend a substantial distance beyond the isophote, the most famous example being Malin 1 (Bothun et al. 1987). Once thought of as a Virgo dwarf this system is actually a luminous field galaxy ($M_B = -21.2$) with an incredibly large ($\alpha = 55\text{kpc}$), low surface brightness ($\mu_{0,B} = 26.6\text{mag arcsec}^{-2}$) disk.

To complement the Gaussian correction (required for compact objects but ineffectual for extended sources) we introduce an additional correction (ineffectual for compact sources but suitable for extended disks). This correction assumes all objects can be represented by a pure exponential surface brightness profile extending from the core outwards as in Eqn 2.10.

Under this assumption, a galaxy's observed isophotal luminosity is the integrated radial profile out to r_{iso} , and calculated using Eqn 2.16. For an exponential profile this becomes:

$$m_{iso} = \mu_0^{app} - 2.5 \log_{10} \{ 2\pi [\alpha^2 - \alpha(\alpha + r_{iso}) \exp(-r_{iso}/\alpha)] \} \quad (2.37)$$

(here μ_0^{app} denotes the apparent surface brightness uncorrected for redshift.) μ_{lim} , the detection/photometry isophote, can be expressed as:

$$\mu_{lim} = \mu_0^{app} + 1.086(r_{iso}/\alpha) \quad (2.38)$$

As m_{iso} , r_{iso} and μ_{lim} are directly measurable quantities, equations (2.37 and 2.38) can be solved numerically to obtain μ_0^{app} and α . The total magnitude is then calculated using Eqn 2.39.

$$m^{tot} = \mu_0^{app} - 2.5 \log_{10}(2\pi\alpha^2) \quad (2.39)$$

From this description an extrapolated central surface brightness can be deduced numerically from the specified isophotal area and isophotal magnitude (after the seeing correction). Note that this prescription ignores the possible presence of a bulge, opacity, and inclination leading to an underestimate of the isophotal correction. This is unavoidable with the 2dFGRS as the data quality is insufficient to establish bulge-to-disk ratios. To verify the impact of this we explore the accuracy of the isophotal correction for a variety of galaxy types in § A.1. The tests show that the isophotal correction is a significant improvement over the isophotal magnitudes for all types - apart for ellipticals where the introduced error is negligible compared to the photometric error - and a dramatic improvement for low surface brightness systems. The final magnitudes, after isophotal correction, now lie well within the quoted uncertainty of ± 0.2 mag for the 2dFGRS for both high- and low-surface brightness galaxies.

Most results cited in the literature use the central surface brightness, μ_0 or the effective surface brightness, μ_e . The central surface brightness, as described above, is the extrapolated surface brightness at the core under the assumption of a perfect exponential disk. The effective surface brightness is the mean surface brightness within the half-light radius. The conversion between these measurements of surface brightness is described in § 2.3, in Eqn 2.24, for a Sersic light profile.

Hence from the isophotal magnitudes and isophotal areas we can derive the total magnitude and effective surface brightness for each galaxy, quantities which are intrinsic to the galaxy, and are not dependent on the survey that measured the galaxy. We use the effective surface brightness as it can be compared directly to the effective surface brightness that we will calculate from the measured half-light radius in the Millennium Galaxy Catalogue (MGC); see § 3.2.2.

2.6 The Bivariate Brightness Distribution

In response to the Freeman (1970) result showing that spiral galaxies have a narrow range $\sigma_\mu = 0.3$ in surface brightness centred on $\mu_0 = 21.65$, Disney (1976) showed that surface

brightness selection effects alone could account for the distribution; i.e. Freeman was not seeing the intrinsic surface brightness distribution of galaxies. Disney & Phillipps (1983), Phillipps & Disney (1986), Phillipps, Davies & Disney (1990) and Davies (1990) have developed Visibility Theory (see § 2.4), to model these selection effects, which they claim also affect the measurement of the luminosity function. Many of the surveys discussed in § 1.3.2 have bright surface brightness limits, so low surface brightness galaxies within the magnitude limits will either be missed (if $\mu_0 > \mu_{lim}$) or have their fluxes significantly underestimated. In addition one needs to worry about surface brightness dimming due to cosmological expansion and the K+e-correction (see § 2.2).

To take surface brightness selection effects into account, we will calculate the number density as a function of both absolute magnitude M and intrinsic effective surface brightness μ_e , producing a *Bivariate Brightness Distribution*. We can take into account the effects of light loss using the apparent surface brightness of the galaxy and then take into account redshift incompleteness, the volume over which the galaxies are seen and clustering in terms of both M and μ_e , thereby removing the surface brightness issue. In § 2.6.1 we describe an empirical method that uses the data to define the selection limits. In § 2.6.2 we present the SWML method of EEP, updated for the BBD (Sodré & Lahav 1993) and to include visibility, and apply it to the same data.

Since the data used in this chapter were published in Cross et al. (2001), the 2dFGRS photometry has been recalibrated using a mixture of data from the 'Two Micron All Sky Survey' (2MASS, Jarrett et al. 2000) and optical CCD surveys, see Colless et al. (2001). The spectroscopic dataset has also been expanded. In Chapter 3 we compare the updated dataset to a deep wide field CCD survey, the MGC. With a view to the changes and the results of Chapter 3, the BBDs in § 2.6.1 and § 2.6.2 must be viewed as preliminary. However, while the 2dFGRS photometry has non-linearities and had calibration errors, the data is similar quality (in some cases significantly better quality) to the surveys presented in § 1.3.2.

2.6.1 An Empirical Method

Here we develop a method for calculating the luminosity density, j , which incorporates a number of corrections for surface brightness selection biases. In particular, a surface brightness dependent Malmquist correction, a surface brightness redshift completeness correction and an isophotal magnitude correction, see § 2.5. We also correct for clustering. What is not included here, and will be pursued in Chapter 3, is the photometric accuracy, star-galaxy separation accuracy and the photometric completeness of the 2dFGRS.

Implementing these corrections requires re-formulating the path to j . Firstly, we replace the luminosity function representation of the local galaxy population by a BBD. The bivariate brightness distribution is the galaxy number density, ϕ , as a function of absolute, total, b_j -band magnitude, M_{b_j} , and absolute, effective surface brightness, μ_e , i.e., $\phi(M, \mu)$. To construct a BBD we need to convert the observed distribution to a number density distribution taking into account the Malmquist bias and the redshift incompleteness correction, i.e.,

$$\phi(M, \mu) = \frac{1}{\Delta M \Delta \mu} \frac{O(M, \mu) + I(M, \mu)}{V(M, \mu)} W(M, \mu) \quad (2.40)$$

where:

- $O(M, \mu)$ is an array of bins containing the number of galaxies as a function of absolute magnitude, M , and absolute effective surface brightness, μ , for galaxies with redshifts. Each bin has the range $M \pm \frac{\Delta M}{2}$ in absolute magnitude and $\mu \pm \frac{\Delta \mu}{2}$ in surface brightness.
- $I(M, \mu)$ is the array of the number of galaxies as a function of absolute magnitude, M , and absolute effective surface brightness, μ , for those galaxies for which redshifts were not obtained.
- $V(M, \mu)$ is the volume over which a galaxy with absolute magnitude, M , and absolute effective surface brightness, μ , can be seen (see also Phillipps, Davies & Disney 1990).
- $W(M, \mu)$ is the array that weights each bin to compensate for clustering.

Deriving these matrices is discussed in detail later. The luminosity density, j , is then defined as:

$$j = \sum_M \sum_\mu L(M) \phi(M, \mu) \Delta M \Delta \mu \quad (2.41)$$

or in practice,

$$j = \sum_M \sum_\mu 10^{-0.4(M-M_\odot)} \phi(M, \mu) \Delta M \Delta \mu \quad (2.42)$$

in units of $h L_\odot \text{Mpc}^{-3}$ where M_\odot is the absolute magnitude of the Sun. h is defined as the Hubble constant divided by $100 \text{kms}^{-1} \text{Mpc}^{-1}$, see § 2.2. The Sun has $(B - V) = 0.65$ and $M_{\odot B} = 5.48$. Converting to the APM and MGC filters this becomes $M_{\odot b_j} = 5.30$ and $M_{\odot B_{MGC}} = 5.39$, using the filter conversions in § 1.3.2.

Our formalism has two key advantages over the traditional luminosity function: Firstly, it adds the additional dimension of surface brightness allowing for surface brightness specific corrections. Secondly, it represents the galaxy population by an empirical rather than an analytic distribution, thus requiring no fitting procedures or assumption of any underlying parametric form and it does not miss any subtle selection effects.

This method, however, does not use the data as efficiently as some other methods such as the stepwise maximum likelihood or Sandage, Tammann & Yahil (1979) methods, see § 1.3.7. This method, in common with many of the non-parametric methods, uses a binning scheme. This has the disadvantage that all galaxies within a bin are treated in the same way, even though some are brighter than others, and the choice of bins, is rather ad hoc.

Constructing the BBD

We now develop the methodology outlined above. This requires constructing the four matrices, $O(M, \mu)$, $I(M, \mu)$, $V(M, \mu)$ and $W(M, \mu)$.

Deriving $O(M, \mu)$ For those galaxies with redshifts, we obtain their absolute magnitude and absolute effective surface brightness as calculated in Eqns 2.8 and 2.9, after isophotal corrections have been implemented. $O(M, \mu)$ is the number of galaxies which have absolute magnitude, X , such that $M - \frac{\Delta M}{2} \leq X < M + \frac{\Delta M}{2}$ and absolute effective surface brightness, Y , such that $\mu - \frac{\Delta \mu}{2} < Y \leq \mu + \frac{\Delta \mu}{2}$.

Deriving $I(M, \mu)$ Not all galaxies targeted by the 2dFGRS will have a measured redshift. This may be due to lack of spectral features, selection biases or misplaced/defunct fibres. One method to correct for these “missing” galaxies is to assume that they have the same observed BBD as those galaxies for which redshifts have been obtained. One can then simply scale up all bins by this known incompleteness, $I(M, \mu) = \frac{N_I}{N_O} O(M, \mu)$.

However, the incompleteness is likely to be a function of both the apparent magnitude and the apparent surface brightness. There is no completely reliable way of converting these values to absolute values without redshifts and to obtain an incompleteness correction, $I(M, \mu)$, some assumption must be made. Here we assume that a galaxy of unknown redshift with apparent magnitude, m , and apparent effective surface brightness, μ_e , has a range of possible BBD bins that can be *statistically* represented by the BBD distribution of galaxies with $m \pm \frac{\Delta m}{2}$ and $\mu_e \pm \frac{\Delta \mu_e}{2}$. The underlying assumption is that galaxies with and without redshifts with similar observed m and μ have similar redshift distributions. In other words, the detectability of a galaxy is primarily dependent on its apparent magnitude and apparent surface brightness. [While these factors are obviously crucial, one could also argue that additional factors, not incorporated here, such as the predominance of spectral features are also important. The true probability distribution for the missing galaxies could be somewhat skewed from that derived here.]

In the preliminary dataset, used in this chapter, we have taken into account neither the missing galaxies in the input catalogue, nor the contamination from stars. In Chapter 3, we discuss the input catalogue, or photometric incompleteness of the 2dFGRS and Sloan Digital Sky Survey Early Data Release (SDSS-EDR), and the stellar contamination of the 2dFGRS. In Chapter 4, we use the MGC as the input catalogue. Since we have shown (in Chapter 3) that we are not missing any galaxies from the 2dFGRS, which could not be accounted for because of nearby bright stars, CCD defects or other similar reasons. We have also made a careful eyeball classification of all objects originally classified as “non-stellar” in the MGC, and found that this gives a good match to spectroscopic results. Thus no extra incompleteness correction is necessary for Chapter 4.

However, in Chapter 5, we use the 2dFGRS as the input catalogue, over a much larger area of sky. We make additional corrections for the photometric incompleteness and stellar contamination, using the same basic method as above. We also correct for varying incompleteness among different spectral types, when we split the data into subsamples of each type.

Deriving $V(M, \mu)$ To convert the number of observed galaxies to a number density per Mpc^3 it is necessary to divide by the volume over which a galaxy with absolute magnitude, M and effective surface brightness, μ_e can be observed, *i.e.*, $V(M, \mu)$. One option is to use Visibility

Theory as prescribed by Phillipps, Davies & Disney (1990), and discussed in § 2.4. While Visibility is clearly a step in the right direction, and preferable to applying a magnitude-only dependent correction, its limitation is that it assumes idealised galaxy profiles (*i.e.* it neglects the bulge component, seeing, star-galaxy separation and other complications). Ideally one would like to extract the volume information from the data themselves and this is possible by using a $1/V_{\text{Max}}$ type prescription, *i.e.*, within each $O(M, \mu)$ bin, the maximum redshift, at which a galaxy can be seen, is determined and the volume derived from this redshift. The advantage of using the dataset rather than theory is that this approach naturally incorporates all redshift-dependent selection biases. However the maximum redshift is susceptible to scattering from higher-visibility bins. An improved version is therefore to use the 90th percentile redshift, z_{90} and to reduce $O(M, \mu)$ and $I(M, \mu)$ accordingly.

Although this requires rejecting 10% of the data, it has two distinct advantages. Firstly it ensures that the redshift distribution in each bin has a sharp cutoff (as opposed to distributions which “peter out”). Secondly it uses the entire dataset as opposed to the maximum redshift only. Using these redshifts the volume can be calculated independently for each bin using Eqn 2.4 and $z_{\text{max}} = z_{90}(M, \mu)$, $z_{\text{min}} = z_{\text{min}}(M, \mu)$. $z_{\text{min}}(M, \mu)$ is calculated from Visibility Theory since there are too few galaxies at the typical minimum redshift to derive a reliable value from the data.

Clustering $W(M, \mu)$ The effects of clustering on the measurement of the space density of galaxies can be summed up in Fig 2.1. The average space density, see Eqn 2.43, varies from $\bar{\phi} = 0.0044$ for $0.015 < z < 0.02$ ($M < -15$), through $\bar{\phi} = 0.0031$ for $0.015 < z < 0.054$ ($M < -17$) to $\bar{\phi} = 0.0055$ for $0.015 < z < 0.12$ ($M < -19$). These variations in space density are primarily caused by inhomogenities along the line of sight. Thus a survey looking through a local void, will measure an underdensity of dwarf galaxies, whereas a survey looking through a local cluster will measure an overdensity of dwarf galaxies. The density of bright galaxies is likely to vary less, since they will be distributed over a much larger volume and so they will be seen in both voids and clusters. Therefore the shape of the luminosity function or bivariate brightness distribution can be skewed by local inhomogenities that either underestimate or overestimate the contribution of the dwarf population. The term $W(M, \mu)$ weights each bin to correct for local inhomogenities.

$$\begin{aligned} \bar{\phi}(z_1, z_2) &= \int_{z_1}^{z_2} \int_{M_1}^{M_2} \int_{\mu_1}^{\mu_2} \phi(M, \mu, z) dM d\mu dz \\ &= \int_{z_1}^{z_2} \phi(z) dz \end{aligned} \quad (2.43)$$

where M_1 , M_2 , μ_1 and μ_2 define the range of absolute magnitudes and surface brightnesses in the volume limited sample, see Fig. 2.1.

To calculate the weighting in each bin, we simply average $\phi(z)$ in Fig 2.1 over the whole redshift range and divide by the average $\phi(z)$ in the redshift range of the bin in question, as shown in Eqn 2.44. If the average density in the redshift range of the bin is lower than the

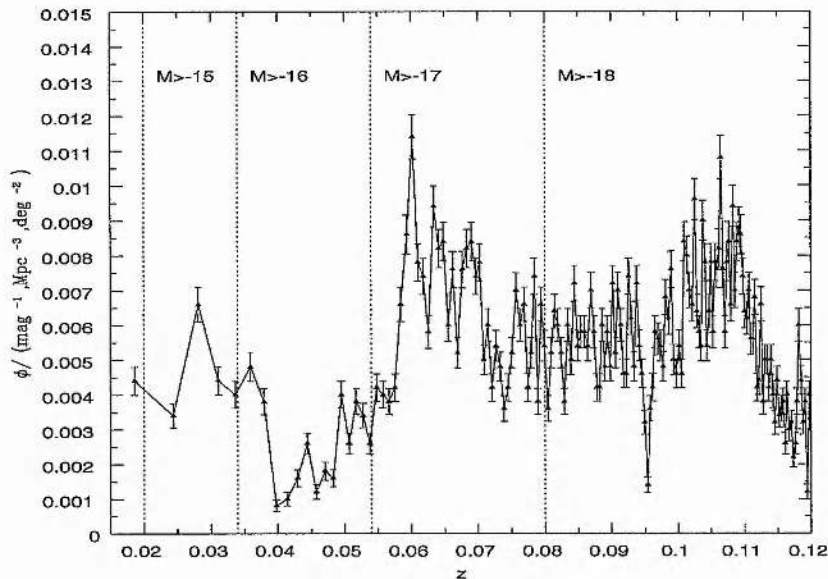


Figure 2.1: This figure shows the preliminary 2dFGRS data plotted as $\phi(z)$ vs z . The variation in density is calculated from a volume limited sample, described later in the text. The plot shows that there is a large variation in the space density of galaxies with redshift. Since faint galaxies can only be seen over a limited redshift range, the calculation of the number density can be biased due to the particular inhomogenities along the line of sight of the survey.

overall average density, indicating a void, then the final space density will be increased, whereas if the average density in the redshift range of the bin is greater than the overall average density, indicating a cluster, then the final space density will be decreased.

$$W(M, \mu) = \frac{\bar{\phi}(ZMIN, ZMAX)}{\phi(zmin(M, \mu), zmax(M, \mu))} \quad (2.44)$$

where $ZMIN$, $ZMAX$ are the redshift limits of the whole sample and $zmin(M, \mu)$, $zmax(M, \mu)$ are the redshift limits of the bin centred on (M, μ) .

Care must be taken to ensure that any galaxy viewed at a particular redshift, could be viewed at all redshifts, so that in a homogeneous universe the space density would not vary within the volume, except for statistical fluctuations. Therefore we must use a volume limited sample, i.e. a sample of galaxies seen over the same volume, rather than a magnitude limited sample, i.e. a sample of galaxies seen to a particular magnitude limit. Fig 2.1, is produced from a volume limited sample. As can be seen from Fig 2.2 (in the region marked by the lines with short dashes) this sample will only include bright galaxies with a small range in absolute magnitude and surface brightness. Since the surface brightness limits are dependent on the absolute magnitude (see § 2.4), the surface brightness limits displayed are for the point halfway between the absolute magnitude limits.

To increase the range in absolute magnitude and effective surface brightness covered, and thereby reduce the statistical fluctuations, we decrease the redshift range of the sample. This is demonstrated by the second volume limited sample, marked out by large dashes in Fig 2.2. In

particular, by increasing the minimum redshift limit we have increased the range of M covered by the volume limited sample. The redshift range can be chosen to maximise the number of galaxies within the volume limited sample, thereby improving the statistics in the clustering correction. This must be weighed up against decreasing the number of galaxies in the whole sample and reducing the range in absolute magnitude over which galaxies can be measured. In Fig 2.2, the sample with the larger range in redshift (short dashes) includes 20663 galaxies with $M > -14$, whereas the other sample only includes 14643 galaxies with $M > -15$.

The volume-limited sample is constructed from only the galaxies within bins that extend across the redshift range. At the high redshift end, galaxies are seen over a large volume, so there will be plenty of galaxies beyond the chosen value of z_{max} . Therefore the data can be used to determine whether galaxies with absolute magnitude M and effective surface brightness μ_e are found at z_{max} . At the low redshift end, the volume over which galaxies are seen can be very small, so statistical effects become important. There is a high probability that no galaxies with absolute magnitude M and effective surface brightness μ_e will have $z < z_{min}$; therefore we use visibility theory to determine whether the low redshift limit of the bin is less than or equal to the chosen value of z_{min} .

Throughout the volume limited sample, each type of galaxy can be seen at all redshifts, so that any changes in density are due to clustering, evolution or statistical effects, rather than the average value of M or μ_e . Evolutionary effects will be noticeable as a gradual change in density with redshift. Statistical effects can be reduced by increasing the size of the subsample and will be different if an independent subsample is selected. Clustering is recognisable as large variations over small redshift ranges (e.g. $\Delta z \sim 0.003 - 0.01$, equivalent to a typical clustering scale of $\sim 10 - 30 h\text{Mpc}$, Colberg et al. 2000). These variations are much larger than the random errors expected from Poisson statistics. Since this dataset is from the 2dFGRS SGP region which covers hundreds of clusters and voids, individual clusters are difficult to discern. However, Fig 4.10 shows the variation of space density with redshift for galaxies in the Millennium Galaxy Catalogue (see § 3.2.2). This shows strong peaks in the space density at the redshifts of some previously known clusters.

Once this volume limited sample has been produced, the weighting array $W(M, \mu)$ is calculated. We assume that all galaxies are clustered in the same way, i.e. if there is an overdensity by a factor of 2 at $z = 0.05$ for $M = -19$ galaxies, then we assume that there will be an overdensity by a factor of 2 at $z = 0.05$ for $M = -14$ galaxies. While it is known that some galaxies, such as dwarf ellipticals are predominantly found in clusters, and others such as LSBGs are predominantly found in the field, the first order effect will be an increase in all types of galaxy in a cluster. The weight $W(M, \mu)$ of the bin at M, μ is the ratio of the mean density of galaxies along the whole redshift range to the density of galaxies within the redshift range for this bin, as shown in Eqn 2.44.

The BBD

Finally we combine the four matrices, $O(M, \mu)$, $I(M, \mu)$, $V(M, \mu)$ and $W(M, \mu)$ (see Eqn 2.40), to generate the bivariate brightness distribution. By summing the BBD along the surface brightness axis we recover the luminosity distribution. By summing along the magnitude axis

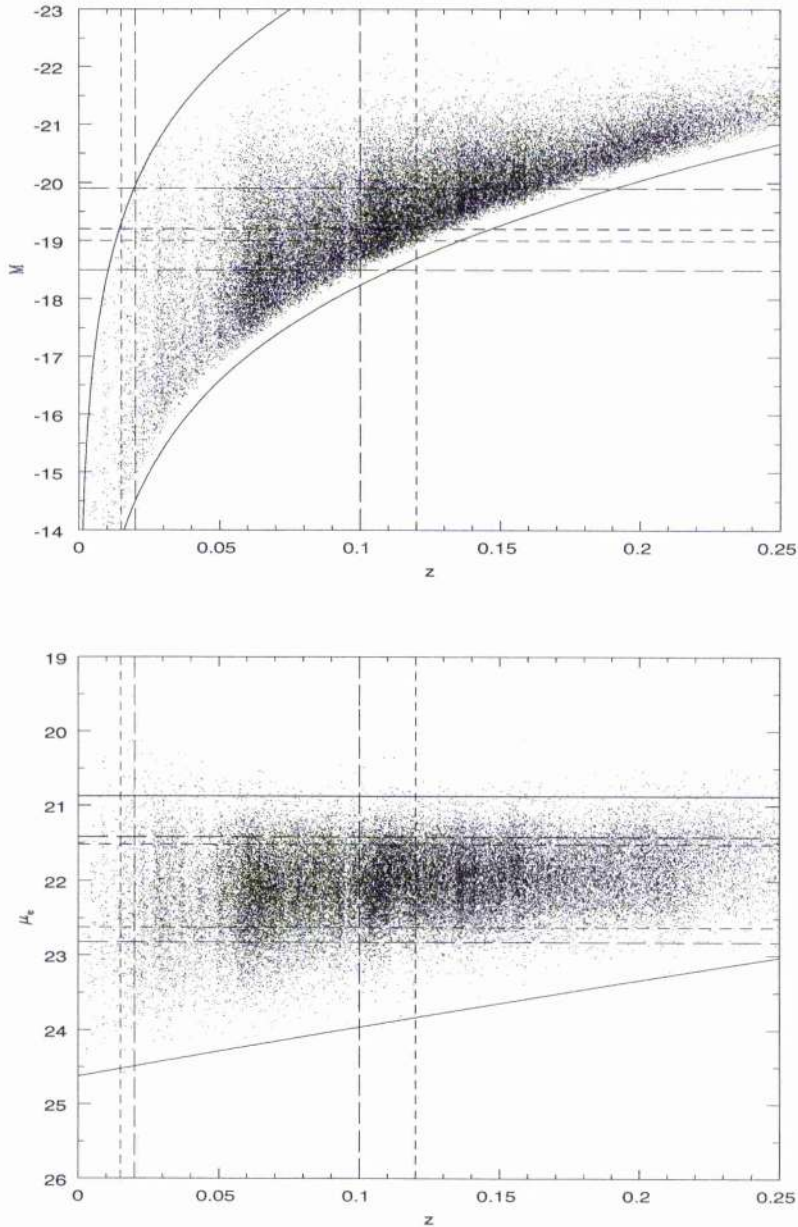


Figure 2.2: This figure shows the preliminary 2dFGRS data plotted as M vs z and μ_e vs z . The solid lines show some of the selection boundaries. On the first plot the two solid lines represent the $b_j = 19.45$ and $b_j = 14.00$ limits. The small gap between the $b_j = 19.45$ and the data is due to the isophotal correction. The horizontal solid line on the second plot is the line 3σ brighter than the Freeman Law - demonstrating the Allen & Shu (1979) result that the Freeman limit represents the upper limit to surface brightness distribution. The lower limit is a surface brightness limit set at $\mu_{lim} = 23.5$ mag arcsec $^{-2}$. Although the isophotal limit of the input catalogue is deeper $\mu_{lim} = 24.67$ mag arcsec $^{-2}$, the redshift incompleteness suggests that there are additional spectroscopic limits. The vertical short dashed lines represent the redshift limits at $z = 0.015$ and $z = 0.12$, used in Cross et al. (2001). The horizontal short dashed lines in the upper plot represent the absolute magnitude limits for this volume limited sample. The horizontal short dashed lines in the lower plot represent the effective surface brightness limits at the point midway between the absolute magnitude limits for this volume limited sample. The long dashed lines are the equivalent of the short dashed lines for a sample with redshift limits at $z = 0.02$ and $z = 0.1$. This volume limited sample, although covering a smaller range in z , covers a larger range in M and μ .

we obtain the surface brightness distribution. The uncertainties were initially determined via Monte-Carlo simulations, assuming a Gaussian error distribution of ± 0.2 mag, in the APM magnitudes. This confirmed that the uncertainties were proportional to $\sqrt{(1/N_{tot})}$, where $N_{tot} = N_O + N_I$ is the total number of galaxies in the bin. Since $\sqrt{(1/N_{tot})}$ is much faster to calculate, we used this throughout the calculations. These uncertainties were then combined in quadrature with the additional error in the volume estimate, assuming Poisson statistics in the number of galaxies with redshifts N_O . The total error is given by:

$$\sigma_\phi = \phi \sqrt{\left(\frac{1}{N_{tot}(M, \mu)}\right) + \left(\frac{1}{N_O(M, \mu)}\right)} \quad (2.45)$$

2.6.2 Stepwise Maximum Likelihood

The Stepwise Maximum Likelihood (SWML) method (Efstathiou, Ellis & Peterson 1988, hereafter EEP) parameterises the Luminosity Function as a sequence of number densities, $\phi(L_i)$, rather than as a Schechter Function, and then maximises the probability that these number densities fit the data. SL93 update this method to include diameter limits. Here we interchange diameter for surface brightness to get an analogous estimate for our Bivariate Brightness Distribution. To start with we outline the basic SWML method for the simple case of the Luminosity Function. Discussion and comparisons of the standard SWML and other estimators can be found in e.g. EEP, Willmer (1997), Koranyi & Strauss (1997) and Takeuchi, Yoshikawa & Ishii (2000).

Basic Concepts

The Luminosity Function $\phi(M)$ can be cast into N_P magnitude bins $M_k \pm \frac{\Delta M_k}{2}$.

$$\phi_k \equiv \frac{1}{\Delta M_k} \int_{M_k - \Delta M_k/2}^{M_k + \Delta M_k/2} \phi(M) dM \quad (2.46)$$

The probability that the i^{th} galaxy, with magnitude M_i and redshift z_i is seen in a magnitude limited catalogue is p_i .

$$p_i \propto \frac{\phi(M_i)}{\int_{-\infty}^{M_{max}(z_i)} \phi(M) dM} = \frac{\sum_k W_{ik} \phi_k}{\sum_{j=1}^{N_P} H_{ij} \phi_j \Delta M} \quad (2.47)$$

where $W_{ik} = W(M_i - M_k)$, with

$$W(x) = \begin{cases} 1 & \text{if } -\Delta M/2 \leq x \leq \Delta M/2 \\ 0 & \text{otherwise} \end{cases}$$

and $H_{ij} = H[M_j - M_{max}(z_i)]$, with

$$H(x) = \begin{cases} 0 & \text{if } x \geq \Delta M/2 \\ (x/\Delta M + 1/2) & \text{if } -\Delta M/2 \leq x \leq \Delta M/2 \\ 1 & \text{if } x \leq -\Delta M/2 \end{cases}$$

$M_{max(z_i)}$ is calculated from the redshift of the i^{th} galaxy and the magnitude limit of the survey, as shown in Eqn 2.48.

$$M_{max(z_i)} = m_{lim} - 5 \log_{10}(d_{L,i}) - 25 - K(z_i) \quad (2.48)$$

where $d_{L,i}$ is the luminosity distance to the i^{th} galaxy in the preferred cosmology.

The likelihood is the product of p_i for every galaxy, Eqn 2.49. The set of N_P parameters that best fits the data gives the maximum value of the likelihood. This can be found by finding when the derivative is equal to zero.

$$\begin{aligned} \mathcal{L} &= \prod_i p_i \\ \ln \mathcal{L} &= \sum_{i=1}^N \ln \left(\sum_k \phi_k W_{ik} \right) - \sum_{i=1}^N \ln \left(\sum_{j=1}^{N_P} \phi_j \Delta M H_{ij} \right) + const \end{aligned} \quad (2.49)$$

When the derivative of Eqn 2.49 with respect to ϕ_k is found and set to zero, the solution, Eqn 2.50, is determined.

$$\phi_k = \frac{\sum_i W_{ik}}{\sum_{i=1}^N \{H_{ik} / \sum_{j=1}^{N_P} \phi_j H_{ij}\}} \quad (2.50)$$

where ϕ_k is the k^{th} estimator.

While the values of ϕ_k calculated above can be used give good estimates of the M^* point and α , they are not normalised, so they cannot be used to give ϕ^* . \mathcal{L} can be increased indefinitely by increasing ϕ^* , so maximising \mathcal{L} does not put constraints on ϕ^* . The normalisation can be found using a variety of methods, e.g. EEP. We have chosen to use the luminosity function to produce number counts and to find the ϕ^* that best fits CCD number count data measured in Liske et al. (2002). We calculate errors in the same way as § 2.6.1. We will use these methods in the modified SWML method outlined below.

The Bivariate version of SWML

In this section we have adapted the SL93 formalism to take into account visibility theory. We have also exchanged diameter bins for surface brightness bins. We have also added bright magnitude limits and maximum diameter limits. SL93 have included a redshift completeness function in their derivation, which will be particularly useful since in § 3.9.1 we will test the photometric and redshift completeness of the 2dFGRS and SDSS.

Visibility Theory is described in detail in Phillipps, Davies & Disney (1990) and in § 2.4. A visibility surface (see Fig 2.3) is a surface in M, μ, z space describing the locus of the limits of the observable galaxy population for a particular survey. In Phillipps, Davies & Disney (1990), and § 2.4, $z(M, \mu)$ is evaluated. However, in this case, we need to evaluate the limits at a particular redshift, i.e. either the effective surface brightness as a function of the absolute

magnitude and the redshift, $\mu(M, z)$, or the absolute magnitude as a function of the effective surface brightness and the redshift $M(\mu, z)$. Either function is simpler to evaluate than $z(M, \mu)$. However, there are two solutions for most values of $\mu(M, z)$ when diameter limits are applied. Moreover, $M(\mu, z)$ is the easiest to calculate, requiring no numerical iteration. Therefore we calculate the absolute magnitude limits in Eqn 2.51 for the bright and faint apparent magnitude limits and the absolute magnitude limits in Eqn 2.52 for the maximum and minimum diameter limits.

$$M = m_{lim} - 5 \log_{10} d_L - 25 - K(z) + 2.5 \log_{10} f \quad (2.51)$$

where f is the fraction of light above the isophote (see Eqn 2.16).

$$M = \mu_0 - 5 \log_{10} \frac{d_A \theta_{lim}}{C g} \quad (2.52)$$

where g is the number of scale lengths (α) at the isophote (see Eqn 2.17) and C is a constant converts the final result to Mpc and corrects for the shape of the galaxy. C is given for a disk galaxy in Eqn 2.30.

The bright and faint limits are calculated for each surface brightness and redshift - $M_{bright}(\mu, z)$ and $M_{faint}(\mu, z)$ from the apparent magnitude and diameter limits:

$$\begin{aligned} M_{bright} &= \max[M(\mu, z, m_b), M(\mu, z, d_{max})] \\ M_{faint} &= \min[M(\mu, z, m_f), M(\mu, z, d_{min})] \\ M_j^+ &= M_j + \frac{\Delta M}{2} \\ M_j^- &= M_j - \frac{\Delta M}{2} \\ \mu_k^+ &= M_k + \frac{\Delta \mu}{2} \\ \mu_k^- &= M_k - \frac{\Delta \mu}{2} \\ M_{i,j}^A(\mu, z) &= \min(M_j^+, M_{faint,i}) \\ M_{i,j}^B(\mu, z) &= \max(M_j^-, M_{bright,i}) \end{aligned} \quad (2.53)$$

W_{ik} and H_{ik} have been converted to W_{ijk} and H_{ijk} to include the variation in surface brightness. We have modified the derivation of H_{ijk} in SL93 to account for the above changes. H_{ijk} is determined using Eqn 2.54.

$$H_{ijk} = \frac{1}{\Delta M \Delta \mu} \int_{\mu_k^-}^{\mu_k^+} d\mu \int_{M_{i,j}^B(\mu, z)}^{M_{i,j}^A(\mu, z)} dM C_z(M, \mu) \quad (2.54)$$

These limits take into account the variation in μ , so there is no need for additional constraints in surface brightness. $C_z(M, \mu)$ is the completeness as a function of M and μ and is equivalent to C_V in Sodr e & Lahav (1993). Since we have already calculated the incompleteness as a function of M and μ_e for the Empirical method, we take the matrices $I(M, \mu_e)$ and $O(M, \mu_e)$ and calculate $C_z = [O/(O + I)]$.

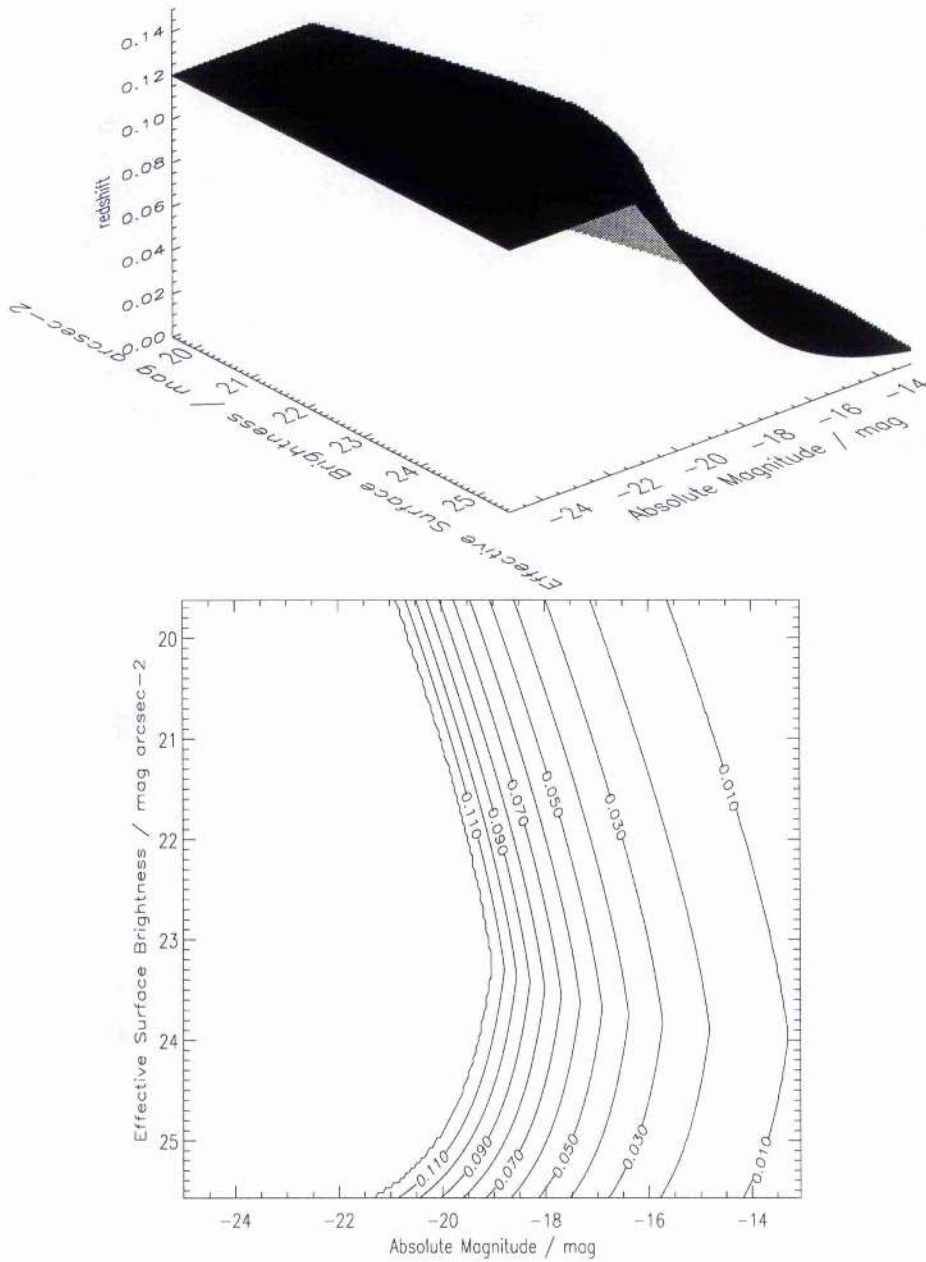


Figure 2.3: This shows the visibility surface described in the text for the limits presented in Cross et al. (2001). The contours are at 0.01, 0.02, 0.03, 0.04, 0.05, 0.06, 0.07, 0.08, 0.09, 0.10, 0.11, 0.12. $z = 0.12$ was the limit placed on the data for reliability of the isophotal correction. While M is the most important factor, there is a dependence on μ too. If the space density is only calculated as a function of M then this dependency is missed and the estimate of ϕ is biased.

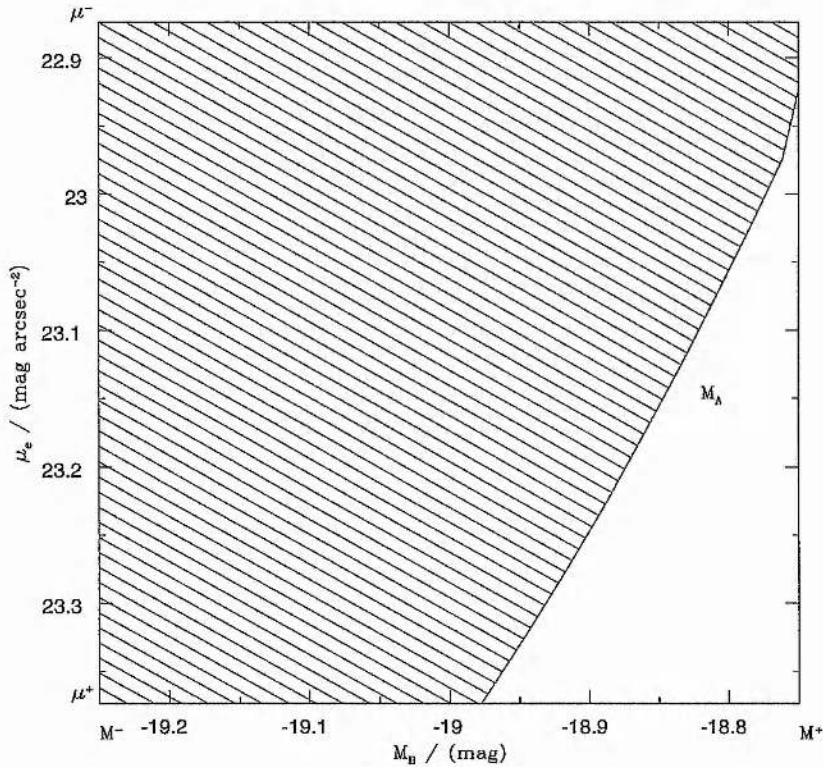


Figure 2.4: This represents the limits used to calculate the H_{ijk} using visibility. The curved line is $M^A(\mu, z)$ and the left hand edge of the bin is $M^B(\mu, z)$. The shaded region represents the area of the bin in which a galaxy with $z_i = 0.10$ could be detected. If the completeness is 100% then this area is equal to $H_{ijk} \Delta M \Delta \mu$, where $\Delta M = M^+ - M^-$ and $\Delta \mu = \mu^+ - \mu^-$. When the completeness is taken into account $H_{ijk} \Delta M \Delta \mu$ is the integral of the completeness over this area.

Fig. 2.4 represents the calculation of H_{ijk} in a particular bin ($M = -19.0$, $\mu_e = 23.12$).

We calculate the parameters in exactly the same way as SL93, with the final estimators calculated in Eqn 2.55.

$$\phi_{jk} = \frac{\sum_i W_{ijk}}{\sum_{i=1}^N \{H_{ijk} / \sum_{l=1}^{N_L} \sum_{m=1}^{N_M} \phi_{lm} H_{ilm}\}} \quad (2.55)$$

2.6.3 Comparing the Two Methods

Fig. 2.5 shows the final 2dFGRS sample (*i.e.* after isophotal correction) for those galaxies with (upper panel) and without (lower panel) redshifts. The galaxies are plotted according to their apparent total magnitude and apparent effective surface brightness. The curved boundary at the faint end of both plots is due to the isophotal corrections which are strongly dependent on μ_e for a constant m . As $\mu_e - 1.124$ tends towards μ_{lim} , the isophotal limit, the correction tends towards infinity, making it impossible to see galaxies close to μ_{lim} . The average isophotal correction is 0.33 mag (for $\mu_{lim} = 24.67$ mag arcsec⁻²). The isophotal limits of the 2dFGRS are $14.0 < m_{iso} \leq 19.45$ and $7.2'' \leq d_{iso} < 200''$. The dataset also used a K-correction $K(z) = 2.5z$.

The observed mean magnitude and observed mean effective surface brightness for those galaxies with and without redshifts are: 18.06 ± 0.01 mag and 22.66 ± 0.01 mag arcsec⁻² and 18.54 ± 0.01 mag and 23.17 ± 0.01 mag arcsec⁻², respectively. These figures imply that galaxies closer to the detection limits are preferentially under-sampled. When the upper panel is converted to absolute parameters using Eqns 2.8 and 2.9, the distribution in Fig 2.6 is seen. Since these data are preliminary we will discuss the distribution galaxies in absolute magnitude and effective surface brightness in chapter 4.

Fig 2.7 shows the intermediate steps used to produce the BBD by the Empirical method. Of particular note is the fact that the array $I(M, \mu)$ contains a greater proportion of galaxies at the low surface brightness end than $O(M, \mu)$, as expected from the apparent distribution above. In Chapter 3 we show that the redshift incompleteness increases with increasing surface brightness, with little variation in absolute magnitude. The contours of $V(M, \mu)$ closely match the shape of the visibility curve, demonstrating the surface brightness selection effects.

The resultant BBDs produced using both methodologies are shown in Fig 2.8. The two BBDs are very similar, with the main difference being the gradient of the faint end slope. The SWML calculates a BBD with a steeper faint end slope, *i.e.* a greater space density of faint galaxies. While the SWML uses more of the data, especially for the clustering correction, it is dependent on a good understanding of the selection limits, whereas the empirical method will automatically take into account unknown selection limits in M , μ and z .

The BBD plots in Fig 2.8 can be summed in surface brightness to produce luminosity functions, Fig 2.9. The best fit Schechter parameters (Table 2.1) are $M^* - 5 \log h = -19.90 \pm 0.04$, $\phi^* = (1.67 \pm 0.09) \times 10^{-2} h^3$ galaxies Mpc⁻³ and $\alpha = -1.31 \pm 0.02$ for the SWML and $M^* - 5 \log h = -19.84 \pm 0.04$, $\phi^* = (1.83 \pm 0.09) \times 10^{-2} h^3$ galaxies Mpc⁻³ and $\alpha = -1.21 \pm 0.02$, for the Empirical method. The SWML method gives a good fit with $\chi^2 = 13.6$ for $\nu = 11$, however the Empirical method gives a poor fit with $\chi^2 = 61.5$ for $\nu = 11$. The errors in the

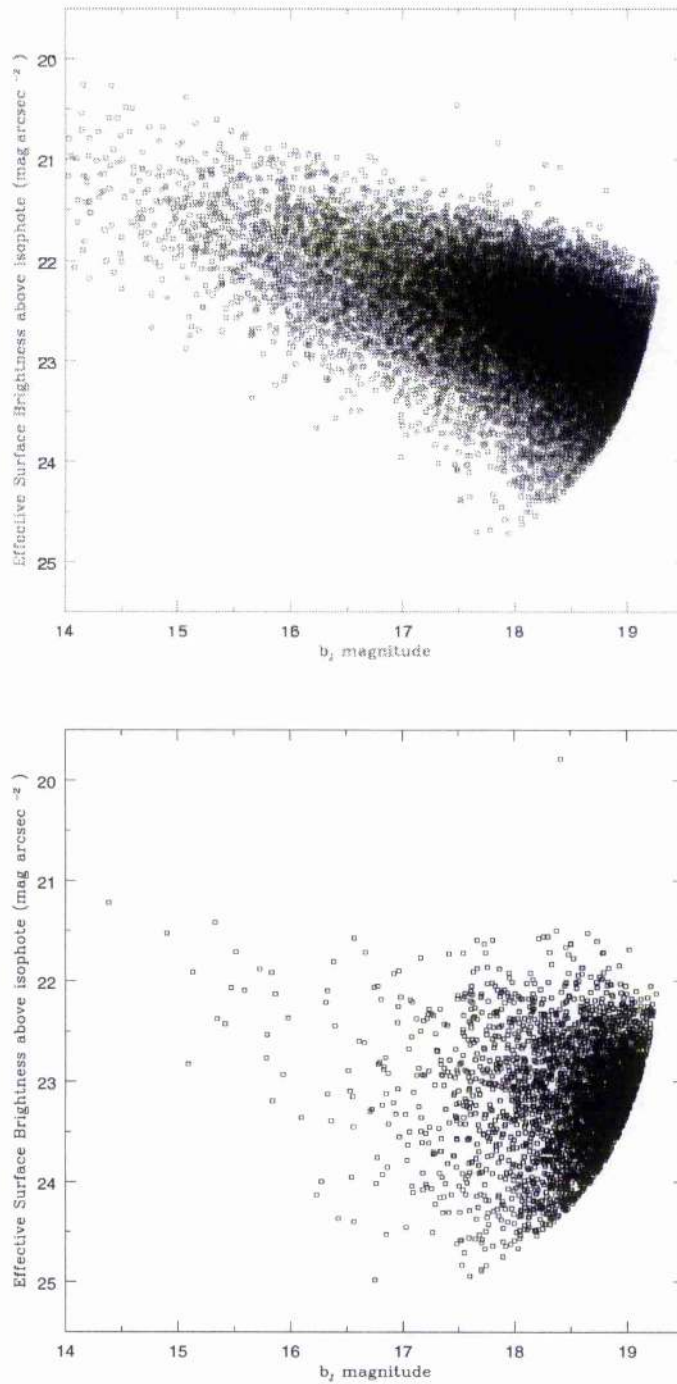


Figure 2.5: Galaxies with (upper) and without (lower) redshifts for the current 2dFGRS sample plotted according to their apparent extinction corrected total magnitude and apparent effective surface brightness.

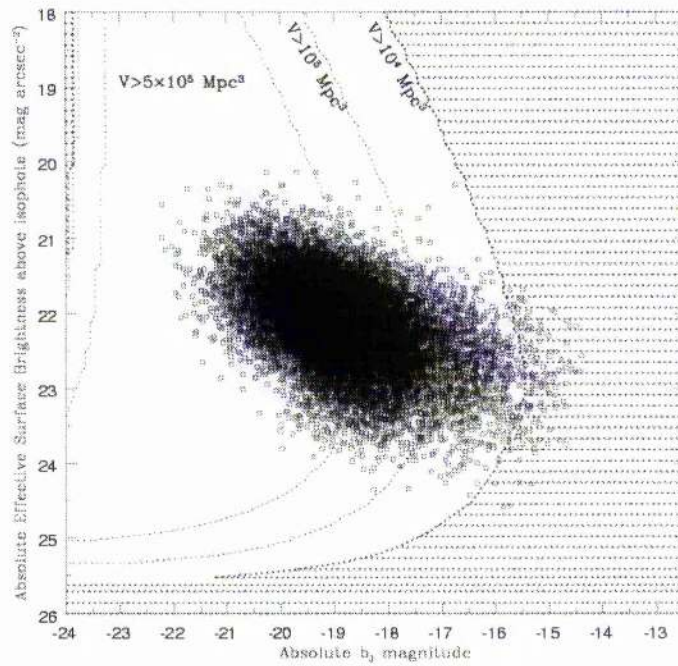


Figure 2.6: This shows the intrinsic properties of galaxies in the 2dFGRS sample. The shaded region shows where the volume drops below $V = 10,000 \text{ Mpc}^3$. The dotted lines show the constant volume lines $V = 100,000 \text{ Mpc}^3$ and $V = 500,000 \text{ Mpc}^3$. All the volumes are calculated from visibility theory, see § 2.4. There is a clear gap between the data and the constant volume limits at the bright, low surface brightness limit, suggesting that luminous low surface brightness galaxies are very rare.

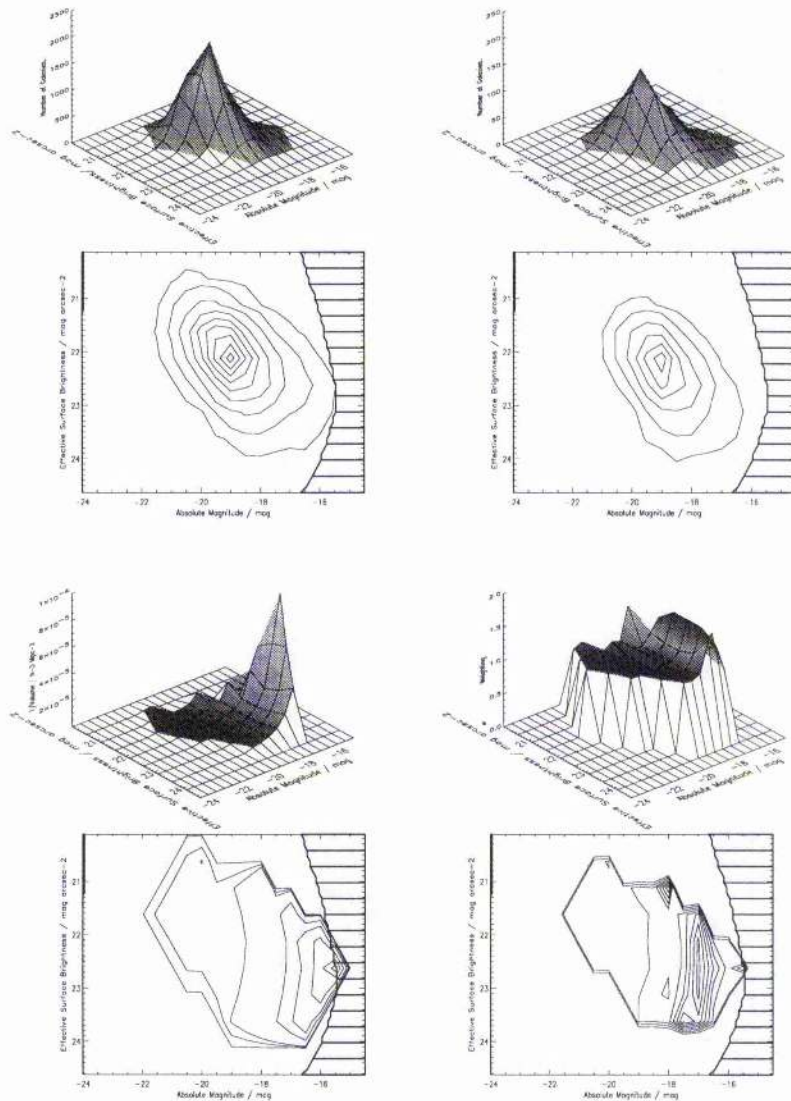


Figure 2.7: This set of figures demonstrates the steps used to produce the BBD using the Empirical method outlined in § 2.6.1. In the top left hand corner is the array $O(M, \mu)$, the number of galaxies with redshifts. In the top right hand corner is the array $I(M, \mu)$, the number of galaxies without redshifts. In the bottom left hand corner is the array $V(M, \mu)$, the volume over which 90% of the galaxies are seen. Finally in the bottom right is the array $W(M, \mu)$, the weight that each bin is given because of the clustering correction. The shaded region in each contour plot shows where the $V < 10,000 \text{ Mpc}^3$.

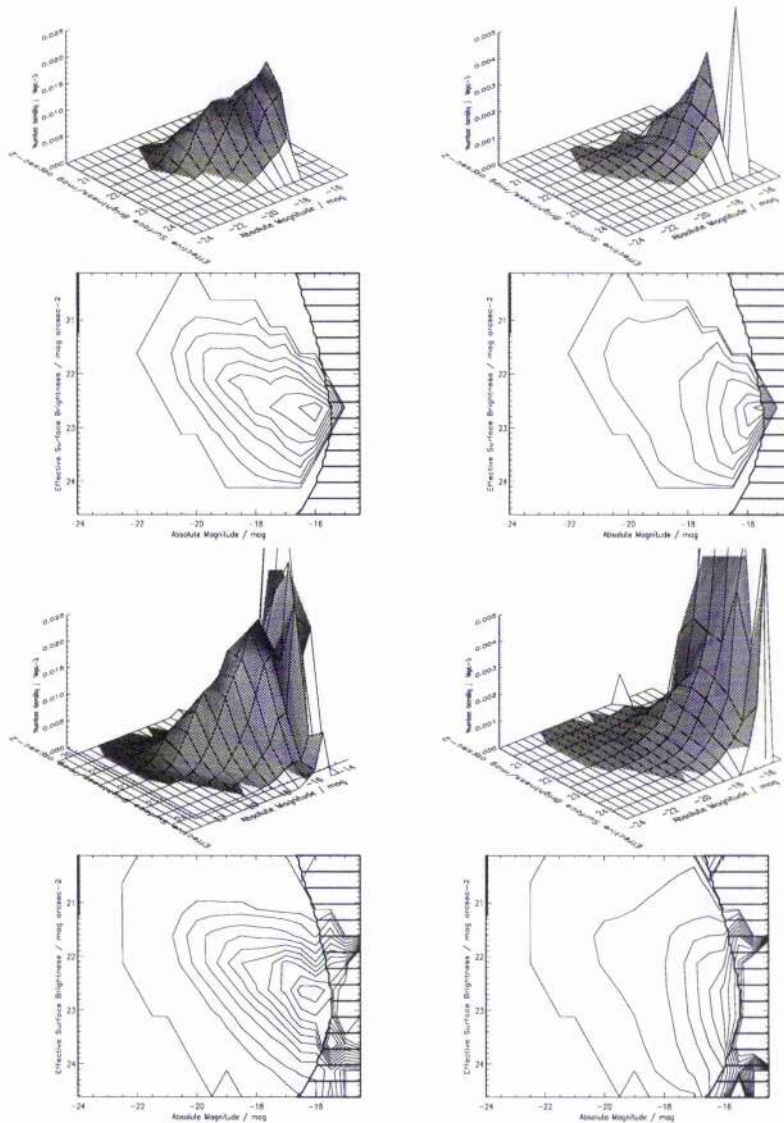


Figure 2.8: This shows the BBD calculated using both the Empirical method (top left) and the SWML method of SL93, as modified in the text (bottom left). The error bars are shown in the top right and bottom right respectively. The contour lines for the BBDs are set at 1.0×10^{-7} , 1.0×10^{-3} , 2.5×10^{-3} , 5.0×10^{-3} , 7.5×10^{-3} , 1.0×10^{-2} , 1.25×10^{-2} , 1.5×10^{-2} , 1.75×10^{-2} , 2.0×10^{-2} , and 2.25×10^{-2} galaxies Mpc^{-3} . The contour lines for the errors are set at 1.0×10^{-7} , 1.0×10^{-4} , 5×10^{-4} , 1.0×10^{-3} , 1.5×10^{-3} , 2.0×10^{-3} , 2.5×10^{-3} , 3.0×10^{-3} , and 3.5×10^{-2} galaxies Mpc^{-3} . The shading represents the regions where $V \leq 10,000 \text{ Mpc}^3$.

Table 2.1: A comparison of the fits found using both methods.

Method/Sample	$M_{b_j}^* - 5 \log h$	$\phi^*/10^{-2}h^3$	α	χ^2	ν	$j/10^8 h L_\odot \text{Mpc}^{-3}$
EMP	-19.84 ± 0.04	(1.83 ± 0.09)	-1.21 ± 0.02	61.5	11	(1.64 ± 0.17)
SWML	-19.90 ± 0.04	(1.67 ± 0.09)	-1.31 ± 0.02	13.6	11	(1.61 ± 0.16)

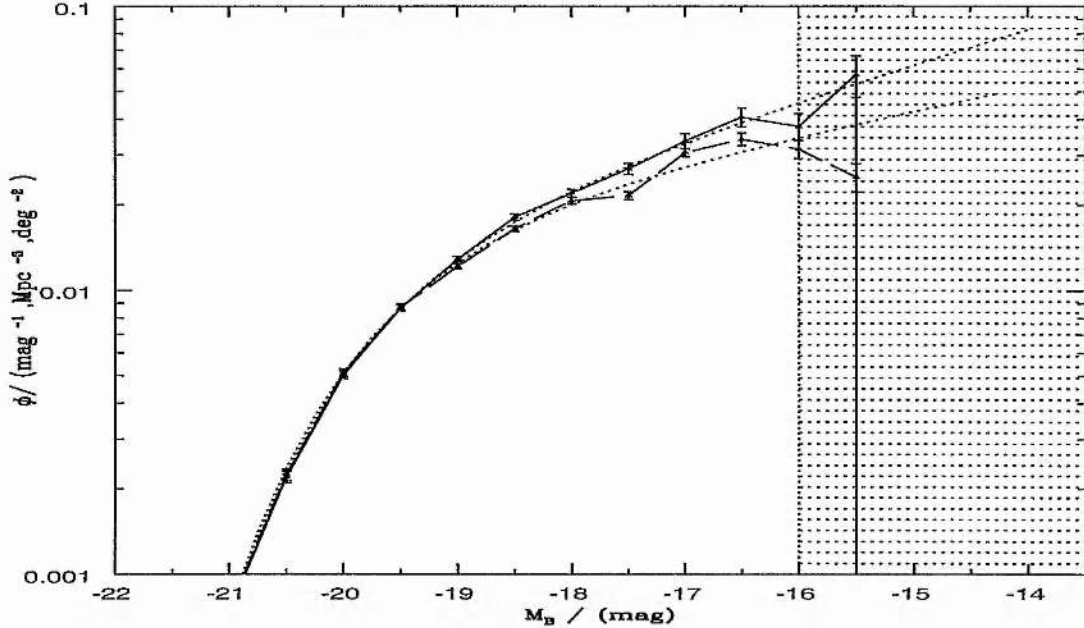


Figure 2.9: This shows the luminosity function calculated using the SWML as a solid line, and calculated using the empirical method as a dashed line. The shaded region shows the region where the volume over which galaxies can be seen is too small for a statistically significant result. The dotted lines show the best fit Schechter functions.

M^* , ϕ^* and α are calculated from the $\Delta\chi^2 = 1$ ellipsoid (the projection of this onto the M^* , α plane is shown in Fig 2.10). The SWML gives a very smooth curve, apart from at $M = -16$. This could be either real structure, or an underdensity too great in size for the SWML to deal with. However, since there are only a few galaxies at this magnitude, it is impossible to say for certain. The deviation from the best fit solution is only 2σ .

The two LFs are nearly identical at the bright end, but the SWML has a steeper faint end slope, predicting more faint galaxies. However Fig 2.9 makes it clear that there is a significant variation in the faint end slope that cannot be explained by the fit or lack of fit. This is where the difference in the assumptions used by the two methods becomes important. While both methods correct for light loss in the same way, they correct for surface brightness selection effects and clustering in different ways. While it is possible to separate these effects out in method 1, it is impossible to do this for method 2, so the reasons behind the difference are difficult to understand. When it comes to the surface brightness selection effects, the Empirical method uses the data to calculate the 90th percentile volume for each bin directly and finds that it fits visibility theory well (see Fig. 2.7) whereas the SWML uses visibility theory explicitly and fits the estimator to the data on a bin by bin basis. While these are very different approaches,

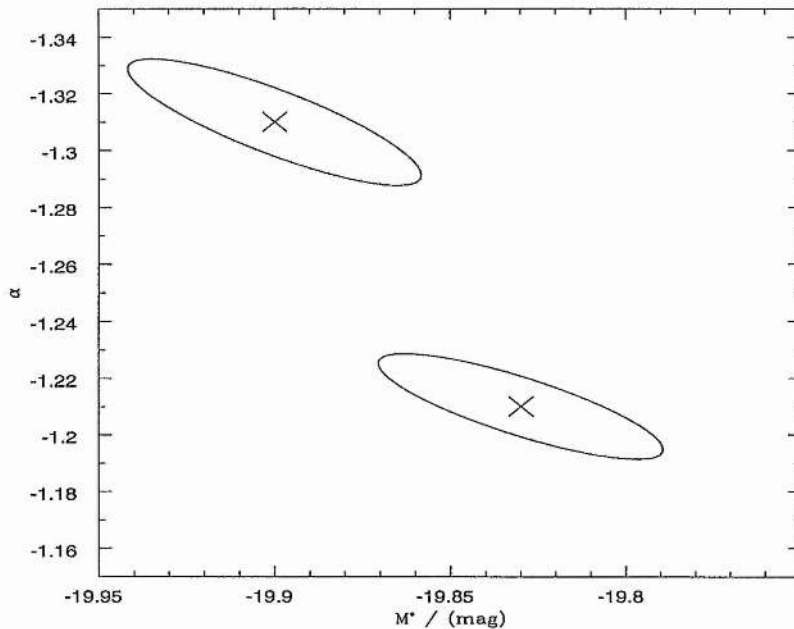


Figure 2.10: This shows a comparison of the error ellipses in M^* , α for the two methods. While the ellipses show that the random errors in the parameters are ~ 0.04 in M^* and ~ 0.02 in α , the systematic error is ~ 0.1 in α .

they are based on similar assumptions, so it seems unlikely that the result will be very different. On the other hand the Empirical method assumes explicitly that bright galaxies are clustered in the same way as faint galaxies, and that the clustering is a function of redshift only. The SWML includes information across the range of magnitudes and surface brightnesses within the selection limits for each redshift for the clustering correction. This seems to be the most likely cause of the difference in the two methods.

The two results can be used to produce a mean value for each of the Schechter parameters. The mean values are $M_{b_j}^* - 5 \log h = -19.87 \pm 0.03$, $\phi^* = (1.75 \pm 0.08) \times 10^{-2} h^3$ galaxies Mpc^{-3} and $\alpha = -1.26 \pm 0.05$. This gives a value of $j_{b_j} = 2.54 \pm 0.18 \times 10^8 h L_\odot \text{Mpc}^{-3}$. This is equivalent to $j_B = 2.36 \pm 0.17 \times 10^8 h L_\odot \text{Mpc}^{-3}$, using Eqn 1.8 and $(\overline{B - V}) = 1.0$. $M_B^* = -19.59$.

2.7 An Analytical Function for the Bivariate Brightness Distribution

2.7.1 A Bivariate Brightness Function

The luminosity function is traditionally described by the Schechter Function (Schechter 1976), is shown in Eqn. 1.4.

This equation contains three parameters M^* , ϕ^* and α , which describe the “characteristic magnitude”, the “normalisation constant” and the “faint end slope”, respectively. Containing no surface brightness information, this function provides a good fit to the space density of field galaxies albeit over a fairly restricted range of luminosities ($-22 < M_{b_j} < -16$) in the field. However, the Schechter Function provides a poorer fit to the luminosity distri-

bution in clusters (e.g. Driver et al. 1994, Andreon, Cuillandre & Pelló 2000) and when the population is subdivided according to spectral type (Madgwick et al. 2001). Current estimates constrain the three Schechter parameters, for field galaxies, to lie in the range: $-19.75 < M^* < -19.15$; $0.013 < \phi^* < 0.027$; $-1.22 < \alpha < -0.7$, resulting in a luminosity density range of: $1.1 < j_{b_j} < 3.2 \times 10^8 h L_\odot \text{Mpc}^{-3}$.

Empirically we find that the distribution of the galaxy population in surface brightness appears symmetrical about a ridge and can be approximated by a Gaussian distribution. The ridge is described by $\mu = \beta_\mu M + C$, the luminosity-surface brightness correlation. Clearly a bivariate brightness function (BBF) needs to relate closely to the Schechter function in luminosity. Hence by multiplying the classical Schechter function with a Gaussian in surface brightness we can construct the following BBF:

$$\phi(M, \mu_e) = \frac{0.4 \ln(10)}{\sqrt{2\pi} \sigma_\mu} \phi_* 10^{0.4(M^* - M)(\alpha + 1)} e^{-10^{0.4(M^* - M)}} \exp \left[-\frac{1}{2} \left(\frac{\mu_e - \mu_e^* - \beta_\mu (M - M_*)}{\sigma_\mu} \right)^2 \right] \quad (2.56)$$

where β_μ is the gradient of the luminosity-surface brightness correlation and σ_μ is the dispersion in the surface brightness. This function is identical to that presented by Chołoniewski (1985), and derived by Dalcanton, Spergel & Summers (1997) and de Jong & Lacey (1999a,b 2000) using the Fall & Efstathiou (1980) disk-galaxy formation model. Note that the new term contains a normalisation coefficient $\frac{1}{\sqrt{2\pi}\sigma_\mu}$ ensuring that ϕ^* , M^* and α are identical to the traditional Schechter parameters.

2.7.2 Fitting a Bivariate Brightness Function

We choose to fit the BBF to the BBDs described in § 2.6.3; this is the largest available dataset. This BBD was derived from a subset of 45,000 galaxies from the 2dFGRS, and is shown on Fig. 2.11 (thin contours). Also shown in Fig. 2.11 is the selection boundary derived from Visibility Theory (shaded region, see § 2.4). In the shaded region insufficient volume is surveyed to make any meaningful statement of the space-densities.

The BBF can be fitted to the BBD by minimising the χ^2 of the model compared to the data. The BBF is a non-linear six parameter equation and to find the minimum, we use the Levenberg-Marquardt Method (see Press et al. 1986). We use the data in those bins with 25 or more galaxies.

The best fit parameters we derive are: $\phi^* = (0.0206 \pm 0.0009)h^3 \text{Mpc}^{-3}$, $M^* - 5 \log h = (-19.72 \pm 0.04) \text{mag}$, $\alpha = -1.05 \pm 0.02$, $\beta_\mu = 0.281 \pm 0.007$, $\mu_e^* = (21.90 \pm 0.01) \text{mag arcsec}^{-2}$ and $\sigma_\mu = 0.517 \pm 0.006$. All errors are 1σ errors. Fig. 2.11 shows the BBF for these parameters (thick lines) overlaid on the data (thin contour lines). The errors in the parameters were found using a Monte-Carlo simulation, that is the observed distribution was randomised within the quoted 1σ errors and the BBF fit re-derived. The final BBF fit yields a χ^2 value of 164, for $\nu = 49$, where ν is the number of data points minus the number of parameters. This gives a

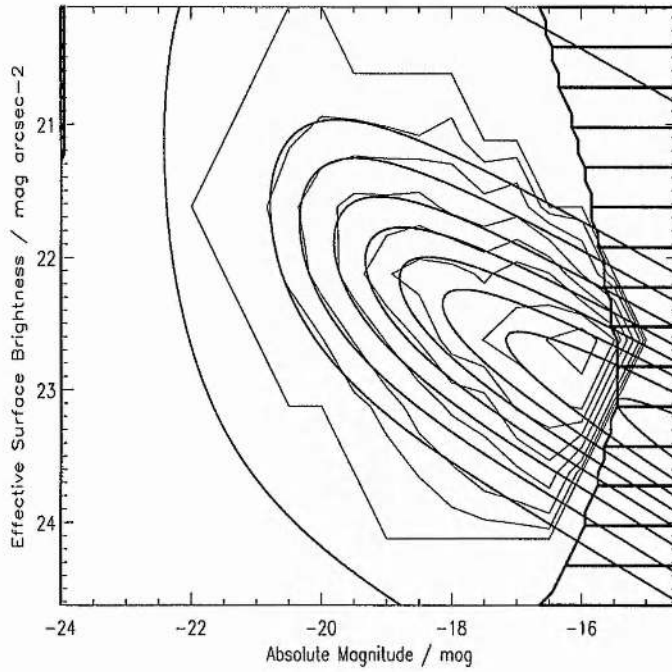


Figure 2.11: The thick lines show the BBF computed for the best fit parameters. The thin lines depict the 2dFGRS BBD (Fig. 2.8). The contours are at 1.0×10^{-7} , 1.0×10^{-3} , 2.5×10^{-3} , 5.0×10^{-3} , 7.5×10^{-3} , 1.0×10^{-2} , 1.25×10^{-2} , 1.5×10^{-3} , 1.75×10^{-2} , 2.0×10^{-3} galaxies $\text{Mpc}^{-3} \text{mag}^{-1} (\text{mag arcsec}^{-2})^{-1}$. The shaded area shows the selection boundary - see § 2.6.3 for details.

probability of 2.6×10^{-14} that the differences between the data and the model are caused by statistical fluctuations alone.

Hence, although the BBF appears to describe the BBD, the fit is poor. It is important to understand where the differences are occurring. From Fig. 2.11 we see that the model fits the data well brightwards of $M = -18$, and less well in fainter bins. The errors become comparable to the space density faintwards of $M = -16$, so the main error in the fit occurs in the range: $-16 > M > -18$. The data (Fig. 2.11) show an upturn towards the faint end in this range whereas the Schechter function gradually flattens towards the faint end. Thus it is the Schechter function part that does not describe the data well. Note that the BBF provides Schechter parameters comparable to the range from previous surveys.

The model fits the data well in the surface brightness direction, implying that a Gaussian distribution is a good description of the space density as a function of surface brightness, for a constant absolute magnitude.

2.7.3 Comparison with de Jong & Lacey and Blanton

Table 2.7.3 compares our BBF with the de Jong & Lacey (2000) BBF which was determined for Sb-Sdm galaxies only. As de Jong & Lacey use 95% confidence intervals for their errors, we have quoted 2σ errors rather than 1σ errors for our values. We converted their half-light radius parameters to our effective surface brightness parameters. De Jong & Lacey fit disks and exponential bulges to their data, taking into account inclination and internal extinction. In Appendix A, we estimate the uncertainty in our results due to not taking this into account and find that the error is ~ 0.1 mag in M^* and ~ 0.55 mag arcsec $^{-2}$ in μ_e^* . We note that the de Jong & Lacey (2000) parameters are their total galaxy parameters, not their disk-only galaxy parameters. In each case, these have been converted to b_j -band magnitudes using $B - I = 1.7$ mag from de Jong & Lacey (2000), and $b_j = B - 0.28(B - V)$ (Maddox, Efstathiou & Sutherland 1990), using a value of $(B - V) = 0.5$ for a late type spiral (Coleman, Wu & Weedman, 1980, Driver et al. 1994). Finally we convert from $H_0 = 65$ km s $^{-1}$ Mpc $^{-1}$ to $H_0 = 100$ km s $^{-1}$ Mpc $^{-1}$. In addition, the de Jong & Lacey sample has tighter selection criteria and more accurate CCD photometry (± 0.05 mag compared to ± 0.2 mag), but it only includes late-type galaxies and has a redshift completeness of 80% compared to $> 90\%$ for the 2dFGRS. In spite of this, we find a similar spread in μ ($\sigma_\mu = 0.52$ q.v. 0.61) and we find that the α values of the two surveys are equal within the errors. The 2dFGRS has a brighter M^* by 0.05 mag, and a brighter μ_e^* by 0.85 mag arcsec $^{-2}$. Taking into account the effects of bulges and inclination as mentioned above, the 2dFGRS distribution has become 0.15 mag brighter than the de Jong & Lacey distribution and has a brighter μ_e^* by 0.4 mag arcsec $^{-2}$. Considering that late-type galaxies tend to be fainter and lower surface brightness, these results appear fully consistent.

Our value of β_μ can be converted to a luminosity-scale size gradient $\beta_{r_e} = -0.360 \pm 0.004$. Although this differs from the de Jong & Lacey (2000) value, it agrees more closely with their theoretical prediction of $\beta_{r_e} = -\frac{1}{3}$ (see de Jong & Lacey 2000). One possible reason for the variation in β_μ may be a correlation between colour and absolute magnitude. Blanton et al. (2001) find a strong correlation between $(g^* - r^*)$ colour and M_{r^*} : brighter galaxies are redder,

Table 2.2: Bivariate Brightness Function Parameters

Parameter	2dFGRS	dJ & L (2000)
$M_{b_j}^* - 5 \log h / \text{mag}$	-19.72 ± 0.08	-19.67 ± 0.17
α	-1.05 ± 0.04	-0.93 ± 0.10
β_μ	0.281 ± 0.014	0.494 ± 0.04
$\mu_{e,b_j}^* / \text{mag arcsec}^{-2}$	21.90 ± 0.02 (22.45 ± 0.02)	22.82 ± 0.19
σ_μ	0.517 ± 0.012	0.61 ± 0.04

fainter galaxies are bluer. Making estimates of the colour-magnitude correlation from Fig. 13 of Blanton et al. (2001), we find that $M_{r^*} = -8.75 \pm_{-2}^4 (g^* - r^*) - 14.88 \pm_{-2}^1$. Using a mean $b_j - r^* = 1.1$ (calculated from Fukugita, Shimasaku & Ichikawa 1995 and Maddox, Efstathiou & Sutherland 1990), and assuming that the additional colour term $\Delta(b_j - r^*) = \Delta(g^* - r^*)$ we calculate that the expected $\beta_{\mu,r^*} = 0.36 \pm 0.23$. The value estimated from Fig. 10 of Blanton et al. (2001) is $\beta_{\mu,r^*} = 0.50 \pm_{0.1}^{0.2}$. Thus the r^* band luminosity-surface brightness correlation appears steeper than the b_j band luminosity-surface brightness correlation. A similar colour-magnitude correlation in $(b_j - I)$ could explain the discrepancy between our result and de Jong & Lacey (2000) result.

The generally good overall agreement between these substantially different surveys is an important vindication of both results. Our results extended the de Jong & Lacey conclusions to the full range of galaxy types with $M < -16$. However, the different values obtained for the luminosity surface brightness correlation may reflect a colour or morphologically dependent luminosity-surface brightness correlation. Blanton et al. (2001) seem to have found similar results, but have not fitted a function or tabulated their results.

2.7.4 Calculating the Luminosity Density

As for the Schechter function it is trivial to calculate the luminosity density, j , by integrating the product of the BBF and the luminosity over the complete range of surface brightness and absolute magnitude.

$$\begin{aligned}
 j &= \int_{-\infty}^{\infty} \int_{-\infty}^{\infty} L(M) \phi(M, \mu) dM d\mu \\
 &= \phi^* L^* \Gamma(\alpha + 2) = \phi^* 10^{-0.4(M^* - M_\odot)} \Gamma(\alpha + 2)
 \end{aligned}
 \tag{2.57}$$

The solution is the same as the solution to the integral obtained from the Schechter function. When calculated using the best fit parameters, the value of the luminosity density, $j_{b_j} = (2.16 \pm 0.14) \times 10^8 h L_\odot \text{Mpc}^{-3}$.

In Blanton et al. (2001), the Sloan team get a 40% higher value for the luminosity density in the b_j filter than the 2dFGRS team. Does this mean that 2dFGRS is missing some galaxies, or at least underestimating their fluxes? For a start the values of M^* are consistent, suggesting that both surveys are correcting magnitudes properly. However the measurement of ϕ^* is over 30% higher in Blanton et al. (2001). A more recent paper (Yasuda et al. 2001) revises the SDSS luminosity density of Blanton et al., to $j_{b_j} = (2.43 \pm 0.21) \times 10^{-2} h L_\odot \text{Mpc}^{-3}$. This

revision is based on a fit to the galaxy number counts, suggesting that the Blanton et al. region was overdense by 30%. The revised ϕ^* value ($\phi^* = 2.05 \pm 0.12_{-0.28}^{+0.66} \times 10^{-2} h^3 \text{ Mpc}^{-3}$) is now consistent with our measurement of $\phi^* = (2.06 \pm 0.09) \times 10^{-2} h^3 \text{ Mpc}^{-3}$, in the b_j band.

Given this revised value of ϕ^* , the Blanton result is still 10% higher, but Blanton used a colour term $b_j = B - 0.35(B - V)$, whereas the correct colour term for the APM, tested using EIS data, is $b_j = B - 0.28(B - V)$, Norberg et al. (2002). When these two factors are taken into account, the luminosity densities are entirely consistent.

As demonstrated in Cross et al. (2001) the peak of the luminosity density lies well inside the selection boundaries. When the function is integrated over the range $-24 < M < -15.5$, $20.1 < \mu_e < 24.1$, the value obtained is $j_{b_j} = 2.14 \times 10^8 h L_\odot \text{ Mpc}^{-3}$ as compared to the summed BBD which gives: $j_{b_j} = (2.11 \pm 0.20) \times 10^8 h L_\odot \text{ Mpc}^{-3}$. These are the approximate selection boundaries, so the correspondence is excellent. Unless the distribution shows an upturn outside the selection boundary, the 2dFGRS data have uncovered over 98% of the local B-band luminosity density.

2.8 Exploring Surface Brightness Selection Effects

In Chapter 1, Fig 1.1 showed the variation in the LF as measured from a number of recent redshift surveys. It was postulated that the large variation was due to surface brightness selection effects. In this section the variation of the luminosity function with the limiting detection isophote is explored and compared to the range of published luminosity functions. Throughout, an exponential surface brightness profile and an Einstein-de Sitter cosmology ($\Omega_m = 1, \Omega = 1$) are assumed.

To calculate a derived luminosity function, we start with our fit to the BBF. We take into account the overestimate in μ_e^* by $0.55 \text{ mag arcsec}^{-2}$, calculated in Appendix A of Cross & Driver 2002, and use a value of $\mu_e^* = 22.45 \text{ mag arcsec}^{-2}$ [Note that in Cross et al. (2001) we used a less sophisticated method to estimate the offset caused by the bulge and arrived at a figure of $0.55 \text{ mag arcsec}^{-2}$].

We multiply our updated BBF by a visibility volume § 2.4 to construct an apparent observed number in M and μ (see Fig. 2.12). The parameters adopted to derive the visibility surface are: $m_{faint} = 20.0 \text{ mag}$, $m_{bright} = 14.0 \text{ mag}$, $d_{min} = 2.0''$, $d_{max} = 250.0''$, $z_{max} = 0.5$, $z_{min} = 0$. The solid angle used was $300 \square^\circ$. These parameters are typical of the observed ranges for the most recent surveys. The only parameter allowed to vary is the detection isophote which took the values 26, 25, 24, 23.5 and 23 mag arcsec^{-2} . Fig. 2.13 shows the complicated Malmquist bias for $\mu_{lim} = \infty, 26, 24, 23 \text{ mag arcsec}^{-2}$ (top to bottom). The shaded region shows the approximate location of the galaxy population. The lines are contours of constant volume for that μ_{lim} . As the limiting isophote becomes brighter, the surface brightness dependency of the Malmquist bias increases.

Given the observed distribution, each galaxy within each bin is then randomly assigned a volume out to the maximum derived from Visibility Theory. This volume is converted to a redshift assuming an Einstein-de Sitter cosmology and a standard K-correction. We assume that the number density does not vary within the bin as a function of redshift, i.e. there is no evolution and no clustering. The exact absolute magnitude and surface brightness value is

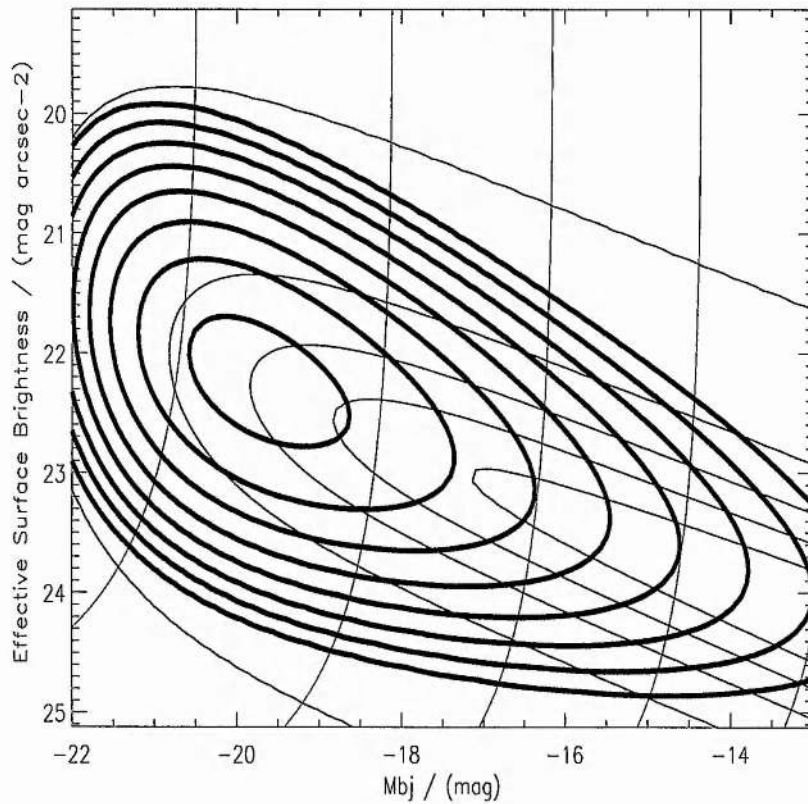


Figure 2.12: This figure shows 3 contour plots. The thin lines show the contours of the visibility surface, in Mpc^3 . Each line is a decade apart. The five lines shown range from 10^7 to 10^3 , from the bright end to the faint end respectively. This visibility surface has a detection threshold of $26.0 \text{ mag arcsec}^{-2}$ and the limits are in isophotal magnitudes. The medium thickness lines show the BBF from Fig. 2.11, offset in surface brightness by $0.55 \text{ mag arcsec}^{-2}$. The thick lines show the number of galaxies detected in each bin. The contours levels are at 1.0, 3.2, 10, 32, 100, 320, 1000, 3200 and 10000 galaxies bin^{-1} , where each bin has $\Delta M = 0.5 \text{ mag}$ and $\Delta \mu = 0.5 \text{ mag arcsec}^{-2}$.

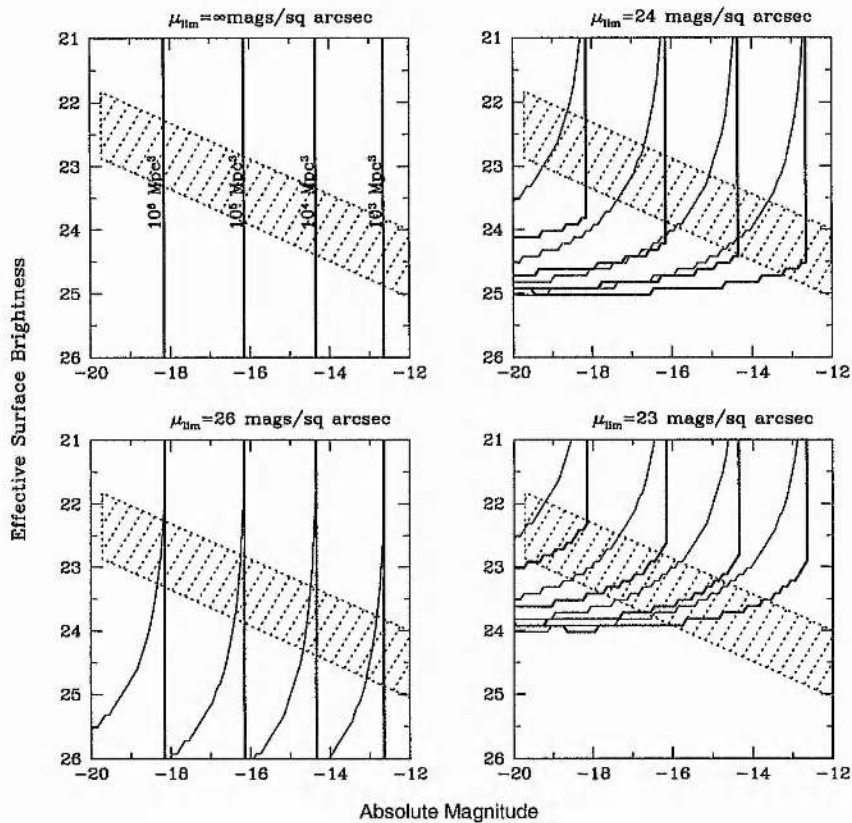


Figure 2.13: This plot shows contours of equal volume for different selection functions. The top, left plot shows the selection function for $\mu_{lim} = \infty$. The selection lines have no surface brightness dependence. The other plots show isophotal (thin lines) and total (thick lines) selection functions, for the detection thresholds 26, 24, and 23 mag arcsec⁻². As one goes to brighter thresholds, the volume becomes a stronger function of surface brightness. Thus the mean volume at any M decreases, and a volume correction or estimator which is only magnitude dependent becomes more biased. The shaded parallelograms represent the number density distribution, in terms of the luminosity-surface brightness correlation, and the width of the surface brightness distribution. Where the contour lines are vertical, an estimator with magnitude dependence only is unbiased, elsewhere it is biased. Where the contour line crosses the distribution, the luminosity function can be recovered using an estimator which takes into account surface brightness. Where the distribution is missed, there is input catalogue incompleteness, and so there is not enough information to recover the luminosity function. When total magnitudes are used: at 26 mag arcsec⁻², there is no surface brightness dependency within the shaded region for $M < -12$, so a magnitude-only will give an unbiased luminosity function; at 24 mag arcsec⁻², it will be unbiased for $M < -14.3$, but an estimator with surface brightness built in, such as the methods described in § 2.6.1 and 2.6.2, will be unbiased $M < -12$; at 23 mag arcsec⁻², the magnitude only estimator will be biased at all magnitudes, but a surface brightness estimator will recover the luminosity function for $M < -16$. Using isophotal magnitudes, all luminosity function estimators will be biased if they are only magnitude dependent.

Table 2.3: Table of Schechter parameters for Fig 2.15

μ_{lim}	Magnitude	$M_{b_j}^* - 5 \log h$	$\phi^*/h^3 \text{ Mpc}^{-3}$	α	$j_{b_j}/10^8 h L_\odot \text{ Mpc}^{-3}$
26.0	Isophotal	-19.54 ± 0.02	$(1.99 \pm 0.04) \times 10^{-2}$	-1.052 ± 0.01	1.77 ± 0.05
25.0	Isophotal	-19.38 ± 0.02	$(1.88 \pm 0.04) \times 10^{-2}$	-1.052 ± 0.01	1.45 ± 0.05
24.0	Isophotal	-19.08 ± 0.02	$(1.66 \pm 0.04) \times 10^{-2}$	-1.057 ± 0.01	0.972 ± 0.05
23.5	Isophotal	-18.96 ± 0.02	$(1.33 \pm 0.04) \times 10^{-2}$	-1.106 ± 0.01	0.723 ± 0.05
23.0	Isophotal	-18.68 ± 0.02	$(1.13 \pm 0.04) \times 10^{-2}$	-1.098 ± 0.01	0.471 ± 0.05
26.0	Corrected	-19.68 ± 0.02	$(1.89 \pm 0.04) \times 10^{-2}$	-1.064 ± 0.01	1.93 ± 0.05
25.0	Corrected	-19.60 ± 0.02	$(1.85 \pm 0.04) \times 10^{-2}$	-1.071 ± 0.01	1.77 ± 0.05
24.0	Corrected	-19.42 ± 0.02	$(1.74 \pm 0.04) \times 10^{-2}$	-1.074 ± 0.01	1.41 ± 0.05
23.5	Corrected	-19.28 ± 0.02	$(1.61 \pm 0.04) \times 10^{-2}$	-1.068 ± 0.01	1.14 ± 0.05
23.0	Corrected	-19.10 ± 0.02	$(1.38 \pm 0.04) \times 10^{-2}$	-1.049 ± 0.01	0.819 ± 0.05
26.0	Total	-19.74 ± 0.02	$(2.00 \pm 0.04) \times 10^{-2}$	-1.066 ± 0.01	2.16 ± 0.05
25.0	Total	-19.74 ± 0.02	$(2.00 \pm 0.04) \times 10^{-2}$	-1.066 ± 0.01	2.16 ± 0.05
24.0	Total	-19.74 ± 0.02	$(1.97 \pm 0.04) \times 10^{-2}$	-1.071 ± 0.01	2.14 ± 0.05
23.5	Total	-19.68 ± 0.02	$(1.85 \pm 0.04) \times 10^{-2}$	-1.045 ± 0.01	1.87 ± 0.05
23.0	Total	-19.64 ± 0.02	$(1.16 \pm 0.04) \times 10^{-2}$	-0.995 ± 0.01	1.09 ± 0.05

then randomly assigned within each bin, (this assumes that the number density does not vary within the bin as a function of M or μ_e). Around the M^* point particularly, this assumption fails, but a Monte Carlo simulation done at higher resolution finds no significant differences. The numbers in Table 2.3, and the plots in in Fig 2.12- 2.15 were produced from this Monte Carlo simulation.

The net result is a magnitude-limited sample with objects randomly distributed within their allowed volume. We now calculate each galaxy's isophotal magnitude, a Gaussian¹ corrected magnitude and their total magnitude and sum the final number distribution according to absolute magnitude. This is plotted in Fig 2.14 for total, corrected and isophotal absolute magnitudes.

We then reconstruct the luminosity function using a $1/V_{Max}$ prescription (as our simulations contain no clustering this should be an optimal estimator). Fig. 2.15 shows the recovered luminosity functions. The LFs of Fig. 2.15 demonstrate the impact of surface brightness selection as they are all drawn from the same BBF; the only difference is the limiting isophote and the choice of magnitude measurement. The range of published values is shown as the shaded area (excluding the LCRS Lin et al. 1996). Also shown is the limit solution, for our model BBF. The left panel assumes isophotal magnitudes are measured, the central panel assumes Gaussian corrected magnitudes were used and the right panel assumes some procedure has been implemented to recover the total magnitudes. The results are also tabulated in Table 2.3.

¹One simple and popular method to correct for light lost is the Gaussian correction employed by Maddox, Efstathiou & Sutherland (1990) on the APM, and used as a correction in the Source Extractor code (Bertin & Arnouts 1996). It works by fitting a Gaussian with central surface brightness, μ_0 , and standard deviation, σ , to the light profile of the galaxy, such that the isophotal radius of the Gaussian matches the isophotal radius of the galaxy and the isophotal magnitude of the Gaussian is equivalent to the isophotal magnitude of the galaxy. The Gaussian corrected magnitude is then the total flux under the Gaussian. This works well for compact objects such as stars and high surface brightness galaxies where the seeing dominates the profile.

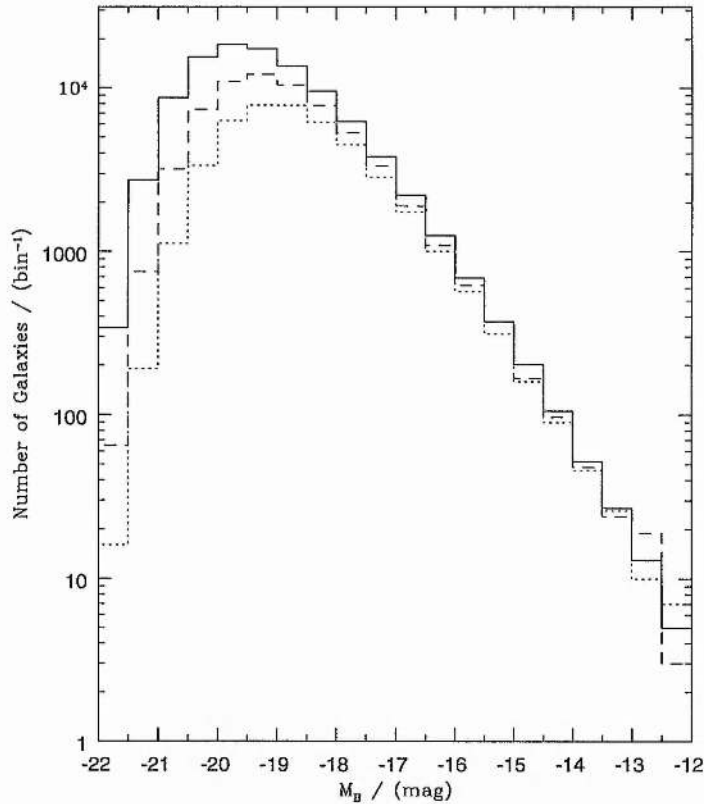


Figure 2.14: This is a plot of the number of galaxies detected as a function of absolute magnitude, for a limiting isophote of $24.0 \text{ mag arcsec}^{-2}$. The solid line shows the plot for total magnitude, the dashed line shows the corresponding corrected magnitudes and the dotted line shows the corresponding isophotal magnitude. The difference between each line is a combination of an offset in magnitude and fewer galaxies being detected going from total to isophotal magnitudes. The peak of the total magnitudes is $\sim 0.3 \text{ mag}$ brighter than the peak in the corrected magnitudes which is $\sim 0.35 \text{ mag}$ brighter than the peak in the isophotal magnitudes.

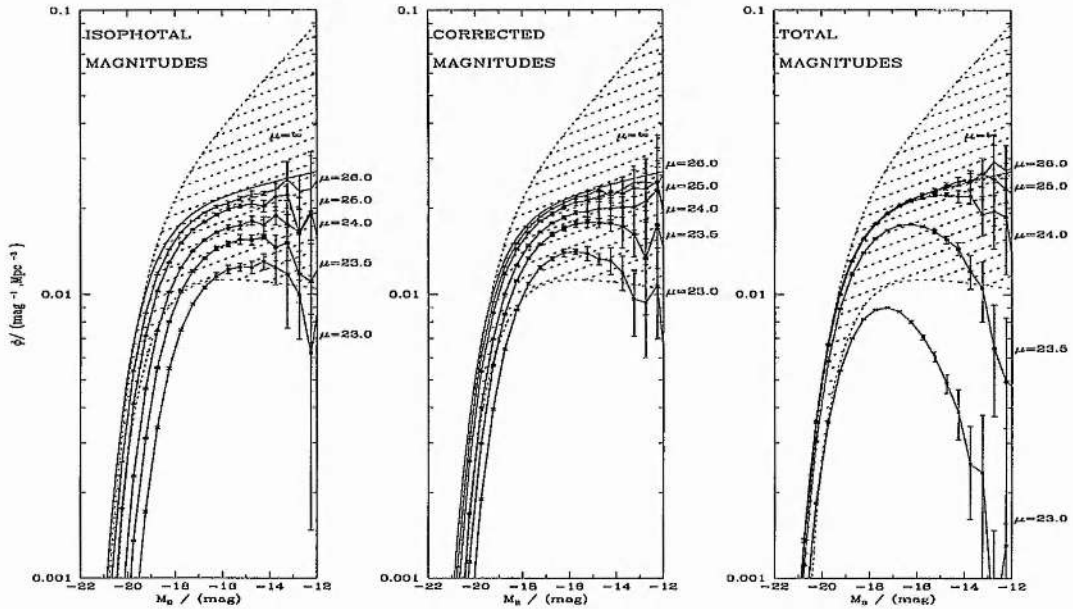


Figure 2.15: The variation of LFs with μ_{lim} for isophotal (left), corrected (middle) and total (right) magnitudes. μ_{lim} varies from 26 mag arcsec⁻² to 23 mag arcsec⁻². The shaded region shows the variation of recent surveys from Sloan (with the new ϕ^*) to APM. The LCRS is not shown as it has an additional surface brightness constraint that significantly reduces the faint end.

Isophotal magnitudes

If isophotal magnitudes are adopted and the surface brightness limit is bright, the luminosities of galaxies are severely underestimated. Thus both the number density and the M^* value are severely underestimated (see Table 2.3 and Fig 2.15). The variation in ϕ^* is up to 30% and in M^* up to 0.8 mag. This tallies well with the range of Schechter parameter values recovered over the range tested ($23 < \mu_{lim} < 26$). To some extent it is surprising that ϕ^* is not more drastically affected; this is because the observed distribution of galaxies is skewed towards the faint end, see Fig. 2.14. As a simple $1/V_{max}$ correction or maximum likelihood estimator based on the isophotal magnitudes does not take into account surface brightness issues, especially light loss, it *underestimates* the volume over which the galaxy can be seen, leading to an overestimate of the number density, see Fig 2.13. This is tempered by a lower number density at brighter absolute magnitudes.

Perhaps most surprising is the robustness of the faint end slope, whose value is recovered correctly regardless of the isophote.

Corrected magnitudes

Most surveys attempt to correct their isophotal magnitudes to total magnitudes. We used a Gaussian correction as described above. Fig. 2.15 and Table 2.3 demonstrate that corrected magnitudes recover 65% of the luminosity density at 24 mag arcsec⁻² compared to the 45% that

isophotal magnitudes recover and the 99% that total magnitudes recover. As with isophotal magnitudes, corrected magnitudes give a luminosity function biased at all values of M , although the bias has been significantly reduced.

Total magnitudes

If some method is employed to correct the galaxies to total magnitudes (e.g. Kron magnitudes or Petrosian magnitudes) we find that the parameters are very robust for $\mu_{lim} \geq 24$ mag arcsec $^{-2}$. However, at $\mu_{lim} = 23$ mag arcsec $^{-2}$ the number density is underestimated throughout the distribution. Fig 2.13 illustrates why this occurs.

The volume has almost no surface brightness dependency for the thresholds $24 < \mu_{lim} < 26$ provided $M < -14$, but it has significant surface brightness dependency for $-22 < M < -14$ at $\mu_{lim} = 23$. The bright absolute magnitudes are affected because of cosmological dimming and the K-correction. Galaxies at the maximum redshift of $z = 0.5$ have an apparent surface brightness that is 3 mag arcsec $^{-2}$ fainter than their intrinsic surface brightness (1.7 mag arcsec $^{-2}$ due to cosmological dimming and 1.3 mag arcsec $^{-2}$ due to the K-correction, where $K(z) = 2.5z$). Even galaxies at $z = 0.25$ will be fainter by 1.6 mag arcsec $^{-2}$. Thus a galaxy with central surface brightness of 21.5 mag arcsec $^{-2}$ ($\mu_e = 22.6$ mag arcsec $^{-2}$) and $z = 0.25$ will not be detected with a threshold of 23 mag arcsec $^{-2}$.

Recovering total magnitudes beforehand will give good estimators for the luminosity function, provided that significant numbers of galaxies are not missing. This is a particular problem if your maximum redshift is very high. However, if galaxies are missing because of cosmological effects, rather than being too intrinsically dim even at $z \sim 0$, the number density can be recovered using the methodologies discussed in § 2.6.1 and § 2.6.2.

Overall Effects

Overall the variations recovered in M^* , ϕ^* and α between simulated surveys with limits of $24 < \mu < 26$ (i.e., comparable to existing surveys) are $-19.74 < M^* < -19.08$, $0.020 < \phi^* < 0.017$ and $-1.07 < \alpha < -1.05$. Fig. 2.15 shows that the observed variation in Schechter function parameters has been recovered at the bright end for $24 < \mu_{lim} < 26$ when either isophotal or Gaussian corrected magnitudes are used. However, Fig. 2.15 demonstrates that the observed variation in the faint end slope has not been accounted for and is testament to the fact that surface brightness selection effects *do not* reproduce all the variation seen in the faint-end slope. This supports the suggestion in Cross et al. (2001) that the faint-end slope depends more critically on the clustering correction than surface brightness issues.

Blanton et al. (2001) find a 0.08 change in the faint end slope going from $\mu_{e,r^*} = 23.5$ to $\mu_{e,r^*} = 24.5$, with no change at the bright end. Using a $(b_j - r^*) = 1.1$, this leads to a b_j -band isophote of $\mu_{lim} = 23.5$ for $\mu_{e,r^*} = 23.5$. The change in the faint end can be compared to the changes seen in Table 2.3, for total magnitudes. For the faint end slope $\alpha \sim -1.045$ for $\mu_{lim} = 23.5$ and ~ -1.07 for $\mu_{lim} = 24.5$; this gives a 0.025 change over a similar interval. This is lower than the Sloan result. However, Sloan has a red selected sample, which gives a steeper luminosity-surface brightness correlation. This could account for a greater change in α .

In § 2.6.3 we took an isophotally selected sample and apply corrections in surface brightness as well as absolute magnitude. These corrections imply that we will not underestimate M^* or ϕ^* . SDSS calculated Petrosian magnitudes before selecting their sample. Petrosian magnitudes are aperture magnitudes and therefore do not show such a pronounced variation with redshift as isophotal magnitudes. Thus the sample is selected from pseudo-total limits.

For deep isophotes, the volume correction has virtually no surface brightness dependence, as shown in Fig 2.15, so the number density can be calculated at the bright end trivially and is only underestimated at the faint end where some galaxies have too low a surface brightness to gain admission to the sample. Using either of the techniques outlined in the previous paragraph (§ 2.6.3, Blanton et al. 2001) should give accurate values of $M_{b_j}^* - 5 \log h$ and ϕ^* , -19.75 ± 0.05 mag, $(2.02 \pm 0.02) \times 10^{-2} h^3 \text{ Mpc}^{-3}$ for 2dFGRS and -19.70 ± 0.04 mag, $(2.05 \pm 0.12) \times 10^{-2} h^3 \text{ Mpc}^{-3}$ for SDSS (Blanton et al. 2001, Yasuda et al. 2001). The caveat is that no correction to total magnitudes is perfect, and the corrected magnitudes will tend to have some surface brightness dependency as is demonstrated by the Gaussian corrected luminosity function. Even when isophotal magnitudes have been corrected to pseudo-total magnitudes it is better to use a $1/V_{max}$ or maximum likelihood estimator which is a function of both M and μ .

While a good understanding of Visibility Theory will account for galaxies within the surface brightness limits, galaxies with very low central surface brightness, but bright total magnitudes can be missed. These are one source of mismatches between the estimates of α in different surveys. Another reason for different estimates is inhomogeneities in the space density of galaxies. Surveys looking at different parts of the sky will encounter variations in the Large Scale Structure. Dwarf galaxies are seen over a smaller volume, so they can have large clustering corrections. Differences in clustering corrections between different surveys will tend to bias α rather than ϕ^* .

2.9 Summary

In this chapter we have laid out the tools that we will use in subsequent chapters to produce, understand and use the Bivariate Brightness Distribution. We started by listing the relevant cosmological equations and (K+e) corrections. We then discussed galaxy profiles and listed important relationships between photometric variables, such as surface brightness, the half-light radius, and the Sersic parameter before discussing Visibility Theory and our methodology to correct isophotal magnitudes and calculate effective surface brightnesses.

We adopt two methods to generate the BBD, one that uses the data directly to find the redshift limits as a function of (M, μ) . It corrects for clustering by assuming that the inhomogeneities are independent of luminosity and surface brightness, and are just a function of redshift. Throughout, the analysis is transparent and it is very easy to see the relative contribution of each correction to the final result.

The second method is a modified version of the bivariate Stepwise Maximum Likelihood (SL93). This method does corrections for all the same problems as the Empirical method, and gets a similar result for the BBD at the bright end, but a steeper faint end slope. While there are corrections for the same type of problem, the method for each correction is totally different. SWML corrects for inhomogeneities, completeness and clustering at the same time,

and it is impossible to separate these effects.

We find good agreement at the bright end for the two methods, but differences at the high surface brightness end and the faint end slope. While the SWML uses the all the information available, it is dependent on a good understanding of the selection limits. The Empirical method takes into account all the selection limits automatically. As many issues such as stellar contamination, photometric accuracy and completeness have yet to be addressed, we will wait until later chapters for a thorough analysis of the results.

To analyse and use the BBD, we fit a simple analytic function first used by Chołoniewski (1985). It combines the Schechter function in luminosity with a Gaussian in surface brightness, and incorporates the luminosity-surface brightness correlation observed in the BBD. It gives a good fit at the bright end, but a poor fit at the faint end. The analytic fit can be used in the same way as the Schechter Luminosity Function. We have used it to derive mock catalogues to test how the Luminosity Function varies with the surface brightness limit for isophotal magnitudes, corrected magnitudes and total magnitudes. We show that variations at the bright end can be explained by the variation in surface brightness limits of recent surveys. However, we cannot account for all the variation at the faint end with surface brightness selection effects only.

The methodology developed in this chapter is useful in determining the effects of surface brightness limits, redshift incompleteness and clustering. However, it has ignored photometric errors and photometric completeness. These issues will be discussed in Chapter 3.

Chapter 3

A Deep Wide Field Redshift Database: Matching the MGC to the 2dFGRS and the SDSS-EDR.

The Millennium Galaxy Catalogue (MGC) provides a high quality database to study cosmology and galaxy evolution. It is a deep ($\sim 26\text{mag arcsec}^{-2}$), wide field CCD imaging database, covering $\sim 35\text{ deg}^2$, that overlaps with data from both the Two degree Field galaxy redshift survey (2dFGRS) and the Sloan Digital Sky Survey-early data release (SDSS-EDR).

In this chapter, we describe the construction of a catalogue containing data from these surveys and test the accuracy of the data. In particular we test the photometry and completeness of the 2dFGRS and the SDSS-EDR. We find that the 2dFGRS is fainter by 0.078mag than the MGC, with a scatter of 0.157mag . However, the 2dFGRS suffers from a non-linearity which is apparent in the photometric variation with surface brightness. We also find that the 2dFGRS is $8.2 \pm 0.5\%$ incomplete at $B_{MGC} < 19.0$. The SDSS matches the MGC photometry with a mean difference $\Delta m = -0.009 \pm 0.100$. There are no major scale errors in magnitude or surface brightness. The incompleteness is much lower than the 2dFGRS at $< 2\%$ for $B_{MGC} < 19.0$.

The combined MGC-2dF-SDSS database provides deep CCD photometry, redshifts, colours and spectral types for ~ 5500 galaxies. The photometry and colours are available for another ~ 6000 galaxies. In the near future morphological types and structural parameters will be available for all $\sim 12,000$ bright galaxies in the MGC. We test the overall photometric and redshift completeness of this survey in the B_{MGC}, μ_e plane to pull out a subsample with high completeness and well defined boundaries to produce

Bivariate Brightness Distributions and Luminosity Functions. These will be produced in Chapters 4 & 5.

3.1 Introduction

Over the past decade multi-fibre spectrographs have improved to the point where 100s of spectra can be taken in an hour and thousands of spectra in one night's observing. This has resulted in redshift surveys increasing in size from a few thousand (e.g. APM, Loveday et al. 1992, Durham/UKST, Ratcliffe et al. 1998) to tens of thousand (e.g. LCRS, Lin et al. 1996) to hundreds of thousands (e.g. 2dFGRS, Colless et al. 1999, and SDSS, York et al. 2000).

However, the input catalogues that these surveys are drawn from are mainly photographic surveys. Until very recently all wide field cameras were photographic and wide format CCDs are a new technology. While it is possible to cover much larger areas with photographic plates, such as the 5.8 deg \times 5.8 deg UK Schmidt Telescope plates, they have a smaller dynamic range than CCDs and suffer from a non-linear photometric response. Thus calibration is difficult and large scale errors are possible.

Many redshift surveys are designed to measure the Large Scale Structure (LSS) of the Universe (e.g. Peacock et al. 2001, Percival et al. 2001) where the structural properties of individual galaxies are not important. However, the robust measurement of the surface brightness (see Chapter 2), required to remove systematic errors in the Luminosity Function (see Chapter 2), and to add new dimensions to the parameter space of galaxies, needs a well defined photometric catalogue under good seeing conditions.

The Millennium Galaxy Catalogue (MGC, Liske et al. 2002) has been designed to provide high quality input catalogue for a portion of the 2dFGRS. It goes much deeper ($\sim 1.3\text{mag arcsec}^{-2}$) and was taken under good seeing conditions $\sim 1.3''$, so it should provide a good check on the photometry and completeness of the 2dFGRS.

The Sloan Digital Sky Survey (SDSS) is the latest large redshift survey. It combines wide field CCD imaging and multi-fibre spectroscopy. This will not only measure redshifts for $\sim 10^6$ galaxies but will also provide 5 colour photometry for galaxies over 10,000 deg². The SDSS Early Data Release includes the MGC strip. While it does not go as deep as the MGC, it provides colours and redshifts, although not as many redshifts as the 2dFGRS.

Combining the 3 data sets provides a wealth of information. The MGC provides the basic photometric data and classification for the galaxies in question. The 2dFGRS provides the bulk of the redshifts and spectroscopic classification (Madgwick et al. 2001) and the SDSS provides colours and additional redshifts.

3.2 Data

3.2.1 The 2dFGRS

Overview of the 2dFGRS

The "Two-degree Field Galaxy Redshift Survey" (2dFGRS, <http://www.mso.anu.au/2dFGRS>) is the largest redshift survey to date (Colless et al. 2001), covering 2000 deg² to a limiting magnitude of $b_j = 19.45$. The survey region is shown in Fig. 3.1. The 2dFGRS will contain

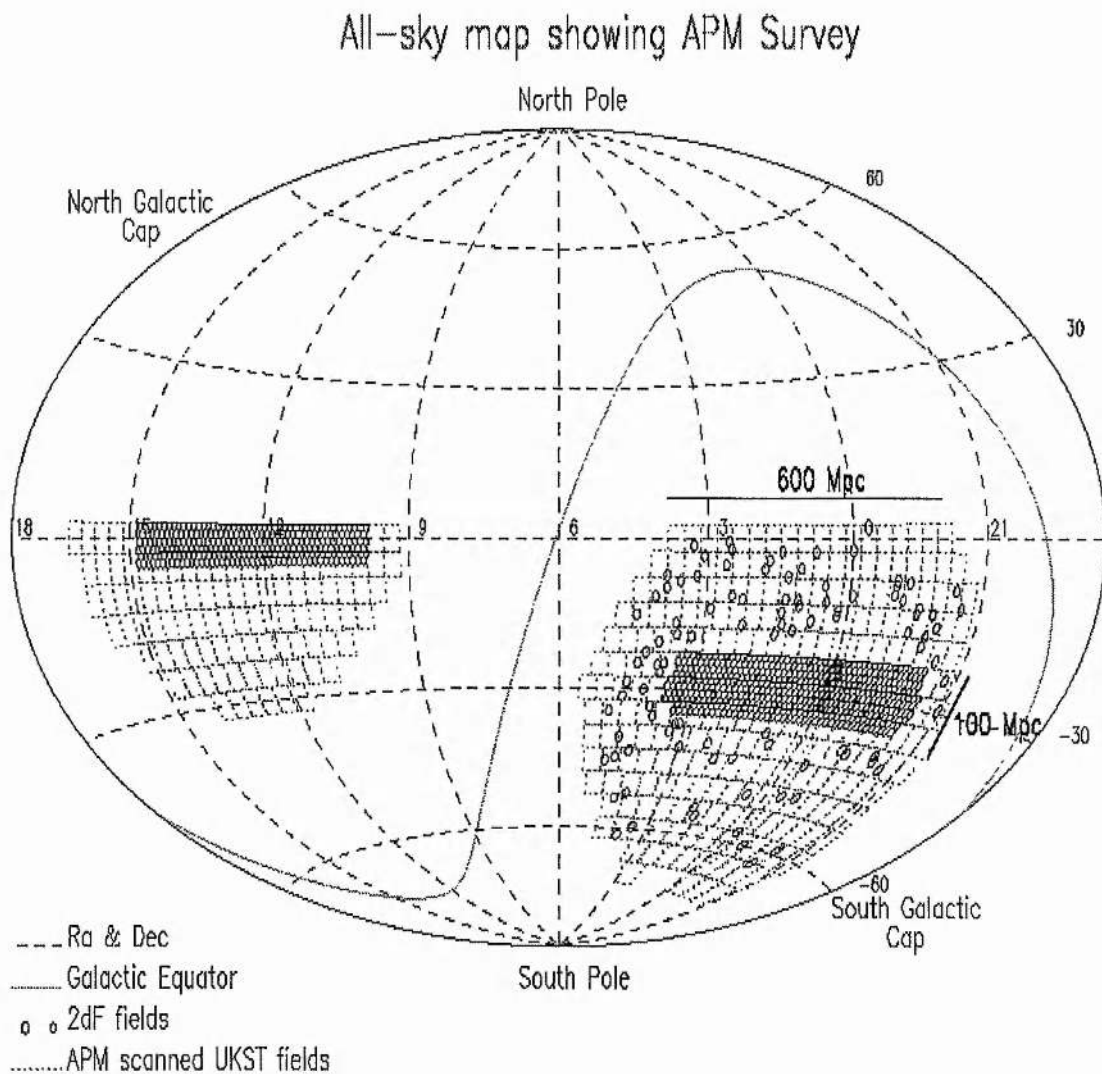


Figure 3.1: This figure shows the 2dFGRS survey regions in equatorial coordinates. The MGC and SDSS-EDR cover the equatorial region of the North Galactic Cap strip. Figure courtesy of the 2dFGRS Team.

both photometric and spectroscopic data for 250,000 galaxies selected from the Automated Plate Measuring-machine galaxy catalogue (APM; Maddox et al. 1990a,b), see Fig. 3.2.

The 2dFGRS has a wide range of goals. These include measurements of the power spectrum of galaxy clustering (Percival et al. 2001), the measurement of the redshift space distortion pattern (Peacock et al. 2001), determination of variations in the spatial and velocity distribution of galaxies (Norberg et al. 2001), a study of groups and clusters (de Propris et al. 2001) the measurement of the Luminosity Function (Cross et al. 2001) and the Luminosity Function as a function of spectral type (Folkes et al. 1999, Madgwick et al. 2001). There have also been comparison between the 2dFGRS and catalogues at other wavelengths such as radio sources (Sadler et al. 2001, Magliocchetti et al. 2001) and 2MASS in the infrared (Cole et al. 2001).

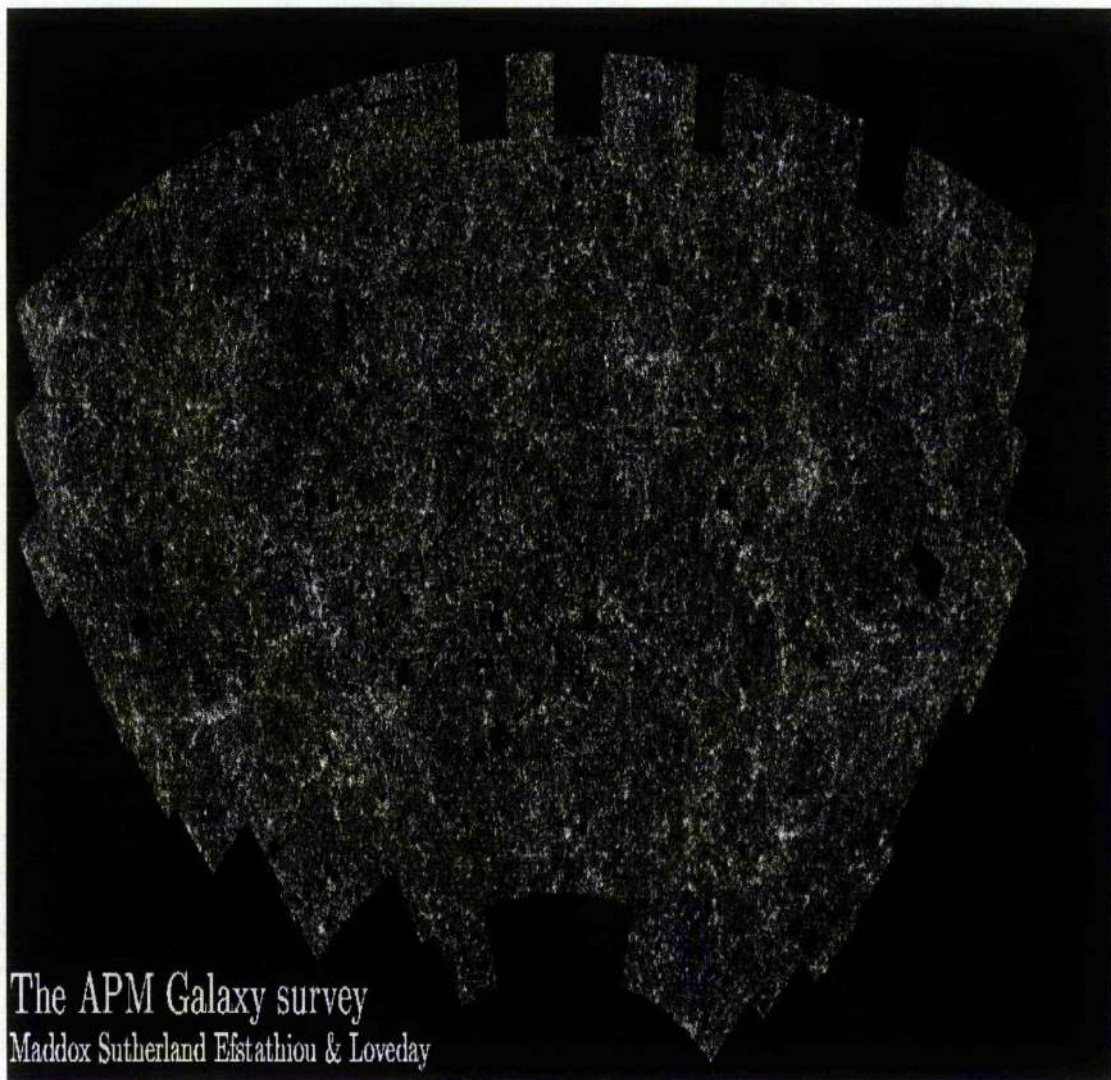


Figure 3.2: This figure shows the APM galaxy catalogue, the input catalogue for the 2dFGRS. The dark rectangles and grooves mark the positions of bright stars and satellite trails, which make the photometry unreliable in a small region. Figure courtesy of Steve Maddox and the 2dFGRS Team.

The input catalogue

The APM catalogue contains ~ 5 million objects with $b_j < 22$ mag over ~ 10000 deg². A bright catalogue was selected as the input catalogue for the 2dFGRS, with a dust-corrected limiting magnitude $b_{j,lim} = 19.45$. The magnitudes were originally measured to have a random error $\Delta b_j = \pm 0.2$ mag (Maddox 1990a, Colless 1999). The 2dFGRS covers two continuous regions, one around the Northern Galactic Pole (NGP) and one around the Southern Galactic Pole (SGP) plus random fields. The APM images come from photographic plates collected on the UK Schmidt Telescope over 10 years ago and digitised by the APM team. These images do not have the photometric accuracy of modern CCD cameras (the error in photographic magnitudes is typically 0.2mag compared to < 0.05 mag for CCDs) and are also difficult to calibrate. Calibration errors have been found in the data, and in the last year it has been recalibrated (Colless et al. 2001) using a mixture of 2MASS and optical CCD data. The recalibration included the use of MGC data in the final stage, so to make a fair comparison we have used the penultimate magnitudes in any comparison, i.e the product of recalibration with 2MASS and other CCD magnitudes, but not the MGC.

To avoid stellar contamination, the APM galaxy catalogue has a strict star-galaxy separation (Maddox et al. 1990a). Fig 3.3 shows a histogram of isophotal area. There is a sharp drop at $A_{iso} \sim 40 \square''$, indicating that the minimum isophotal radius $r_{iso} \sim 3.6''$. Merged objects are removed if they are star-star mergers or bright star-faint galaxy mergers, but galaxy-galaxy and bright galaxy-faint star mergers are kept.

The surface brightness limit is $\mu_{b_j} \sim 24.67$ mag arcsec⁻² (Cross et al. 2001). However, as we will show, this varies from plate-to-plate. The magnitudes have been corrected using a Gaussian profile (see Maddox, Efstathiou & Sutherland 1990 and § A.1 for details). To further reduce the amount of light loss the corrected magnitudes are compared to corrected deep CCD images. The mean difference in the magnitudes between the 2dFGRS and CCD magnitudes is added on to the 2dFGRS. This is done in discrete magnitude intervals to correct for scale errors in magnitude.

The Spectroscopic Data

The spectroscopic data have been collected in dark time on the Anglo-Australian Telescope (AAT) from October 1997 and will continue to be collected until January 2002. As of August 2001, $\sim 200,000$ redshifts had been measured. The redshifts are measured by the "Two-degree Field" spectrograph, Fig. 3.4. The 2dF incorporates 2 fibre fed spectrographs. Each set of fibres runs from a plate to the spectrograph. As can be seen in Fig. 3.4, the two plates are either side of a tumbler, so that one plate can be configured while the other plate is observing. An Atmospheric Dispersion Corrector (ADC) prevents the spectrum spreading out too much away from the main axis. The 2dF facility is described in detail in Lewis et al. (2001).

The 2dF instrument sits at prime focus on the AAT, where it can have the maximum field of view. Each field is 2° across, and 400 objects can be measured at once, although there are restrictions on the minimum separation of fibres, see Fig 3.5. Four fibres are used to target stars for accurate tracking and 20 are targeted at blank pieces of sky for sky subtraction.

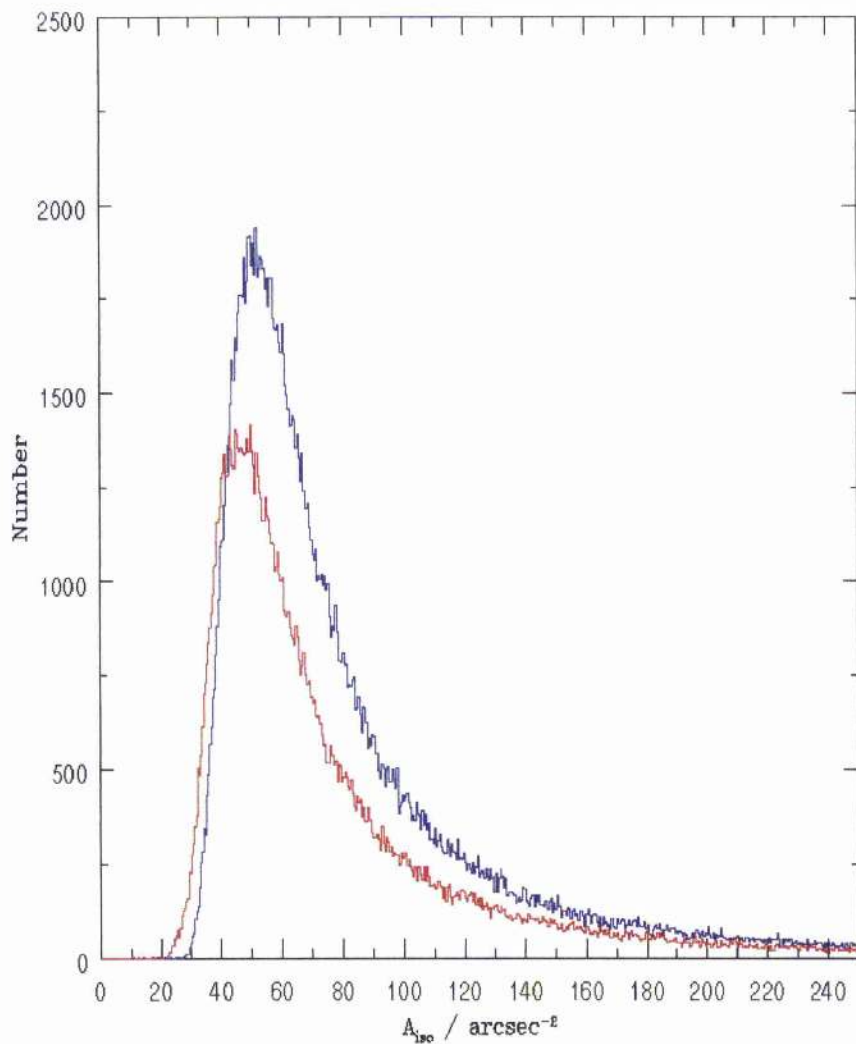


Figure 3.3: This figure shows the distribution of isophotal areas for the NGP (red) and SGP (blue). The NGC has a smaller isophotal area on average. The minimum area limit occurs in the range $30 < A_{iso} < 50 \text{ arcsec}^{-2}$.

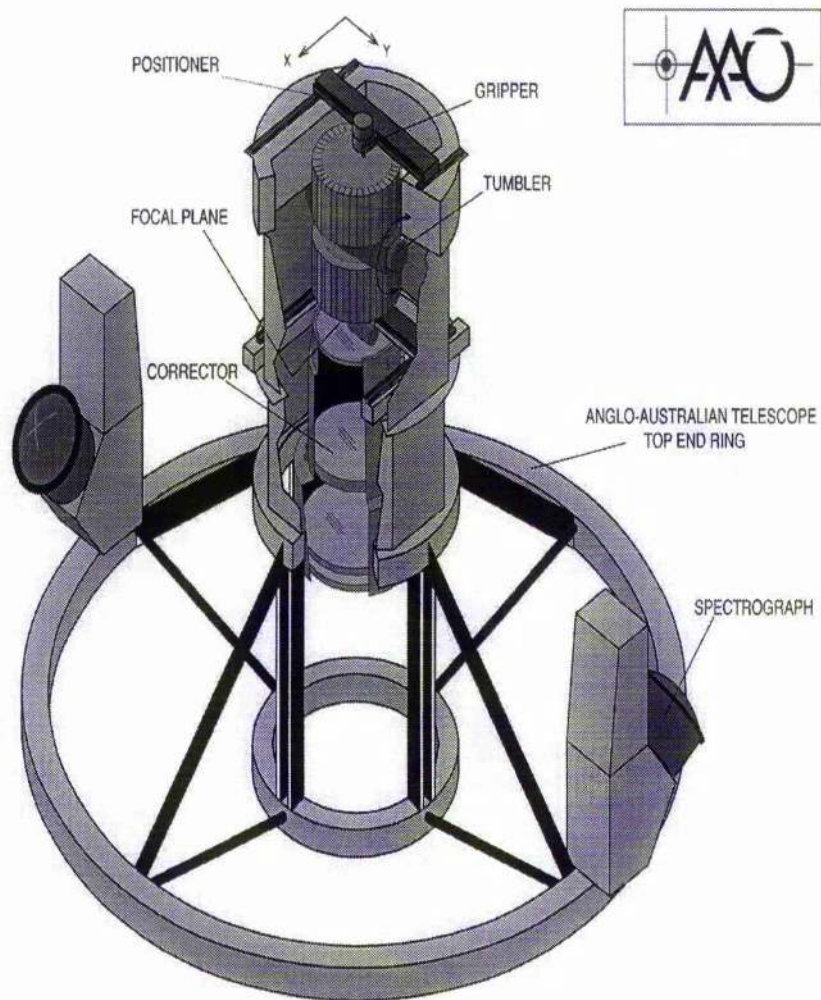


Figure 3.4: This figure shows the top end of the 2dF spectrograph. The instrument has two separate spectrographs fed by two sets of fibres, attached to two plates. This means that one plate can be observed while the other is configured. The gripper is used to move the fibres to the correct configuration. The tumbler changes the plates over between observations. Figure courtesy of the 2dFGRS Team.

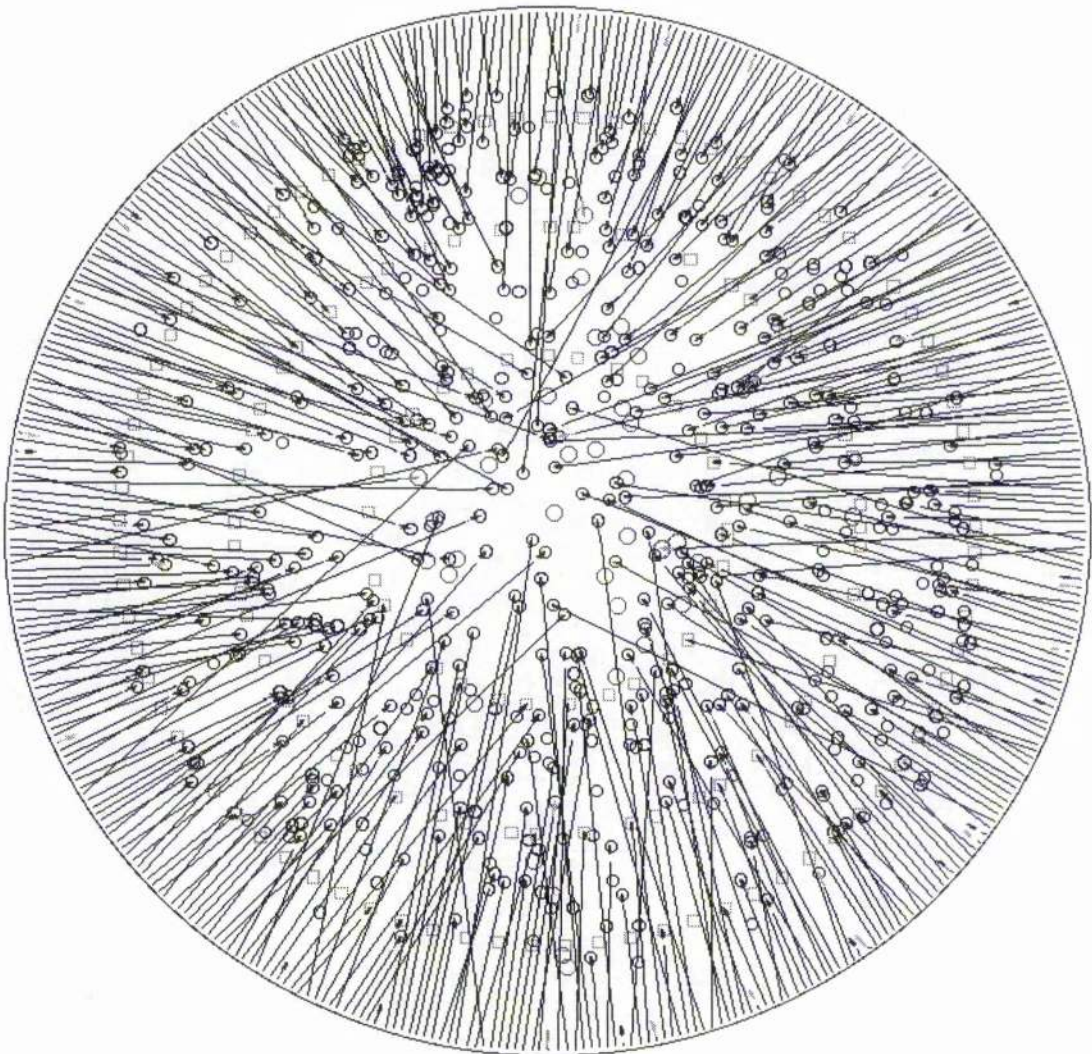


Figure 3.5: This figure shows a configured 2dFGRS field. There are 400 fibres. 20 are used for sky subtraction and 4 are used for guiding. The field is 2° across, and the fibres must not get closer than $\sim 30''$. Configuring the survey is a tricky minimisation problem. Figure courtesy of the 2dFGRS Team.

Each field is configured by a robotic gripper which takes 60 – 65 minutes to configure one field. The exposure time is ~ 60 minutes, separated into 3 exposures of ~ 20 minutes, to minimise the effects of cosmic rays and other transient events.

The effects of clustering mean that some parts have more than 400 galaxies within the field and others have fewer than 400. Therefore many fields overlap each other. Deciding which galaxies to target in dense regions is very tricky because the magnetic buttons cannot be placed closer than $12''$ to each other. This is an absolute minimum, as the fibres also constrain the minimum separation. A good rule of thumb is not to place them closer than $30''$ to each other. The trick is to minimise the total number of observations. Broken fibres, poor seeing and thin cloud can all reduce the completeness of one particular field, which has an impact on future observations. The observing strategy is discussed in more detail in Colless et al. (2001).

Each fibre is $\sim 2''$ across, so that only a fraction of the light of the galaxy enters. The

completeness of low surface brightness galaxies is thus poorer than normal galaxies (see Chapter 4). The spectrum of a typical galaxy varies with distance from the centre of the galaxy, going from a bulge dominated spectrum to a disk dominated spectrum. There can also be problems with contamination of merged objects such as stars or other galaxies. Sky lines can also reduce the chance of picking up galaxies at certain redshifts. These problems are discussed in more detail in Colless et al. (2001), who also compare the redshift results with other surveys. Only 1.6% of objects are “blunders”, i.e. with $|\Delta(cz)| > 600\text{kms}^{-1}$. The rms redshift error is found to be 76kms^{-1} (Colless et al. 2001).

Each redshift is quality controlled by observers with a quality flag $1 \leq Q \leq 5$. A spectrum with many easily distinguished, high S/N lines will have $Q = 5$, a spectrum with no distinguishable lines will have $Q = 1$. $Q = 1, 2$ have unreliable redshifts, $Q = 3 - 5$ have reliable redshifts. The overall redshift completeness is $\sim 91\%$.

Spectral Types and K-corrections

Madgwick et al. (2001) have used principle components analysis (PCA) to define the parameters that produce the greatest variation in the spectra. Using the two components that produce the most variation, they define a continuous parameter η , which is a linear combination of the first principle component (pc1) and the second principle component (pc2). Madgwick et al. (2001) have defined four spectral classes based on η : Type 1 $\eta < -1.4$; Type 2 $-1.4 \leq \eta < 1.1$; Type 3 $1.1 \leq \eta < 3.5$; Type 4 $\eta \geq 3.5$. Each of these types have different K-correction: Type 1 $K(z) = 2.6z + 4.3z^2$; Type 2 $K(z) = 1.9z + 2.2z^2$; Type 3 $K(z) = 1.3z + 2.0z^2$; Type 4 $K(z) = 0.9z + 2.3z^2$. The overall K-correction is found to be $K(z) = 1.9z + 2.7z^2$.

A subsample with deep Wide Field CCD data

The large quantity of low resolution spectral data provided by the 2dFGRS will make a nice complement to wide-field CCD data. We have selected data from an equatorial (J2000) strip in the NGP coinciding with the CCD data set below. There are 7686 2dFGRS galaxies in this strip ranging from $9^{\text{h}}58^{\text{m}}$ to $14^{\text{h}}48^{\text{m}}$ (J2000) and spanning the declinations $-0^{\circ}18'$ to $+0^{\circ}18'$ (J2000).

3.2.2 The MGC.

Overview of the MGC

The Millennium Galaxy Catalogue (Liske et al. 2002) is a $\sim 36\text{deg}^2$ deep CCD imaging survey of an equatorial strip between $9^{\text{h}}58^{\text{m}}28^{\text{s}}$ and $14^{\text{h}}46^{\text{m}}45^{\text{s}}$ with a declination range from $-0^{\circ}17'15''$ to $+0^{\circ}17'15''$. The imaging was carried out using the Wide Field Camera on the Isaac Newton Telescope between March 1999 and April 2000. We took 144 images, each 0.5deg apart in R.A. starting from Field 1 where CCD 4 is centred at $10^{\text{h}}00^{\text{m}}0^{\circ}0'$. Each field contains 4 CCDs, (see Liske et al. 2002 for details), although CCD 3 is heavily vignetted. Most of this vignetting is removed by flat fielding and only affects the completeness and photometry of very faint objects.

The CCDs are arranged in a square with a corner missing (see Fig 3.6). Between each pair

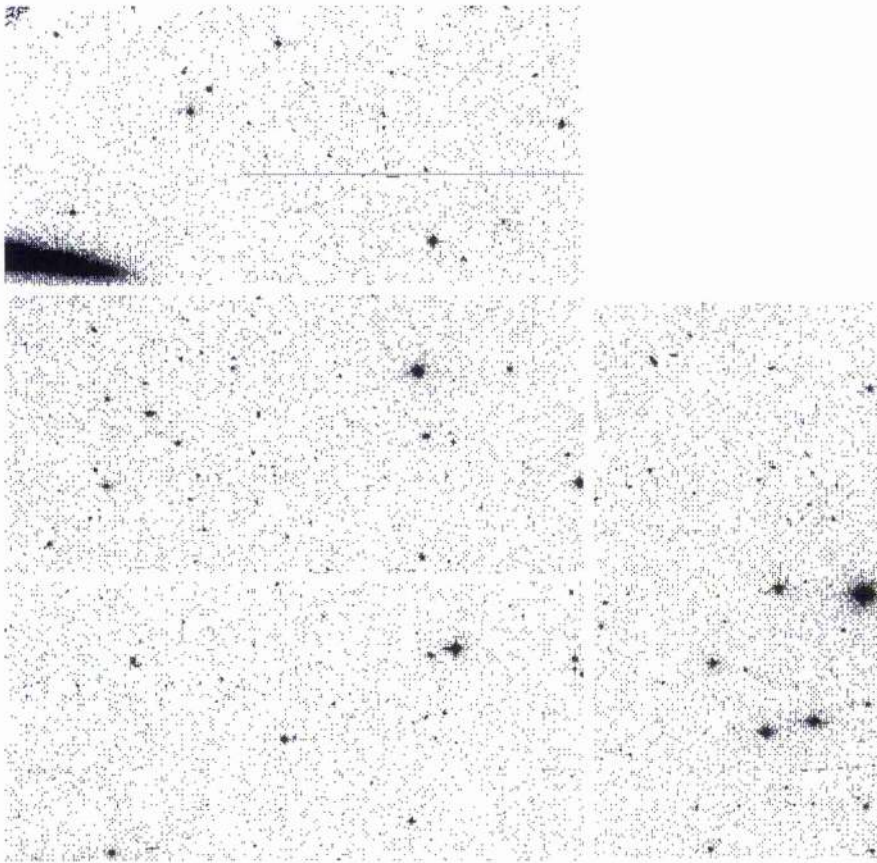


Figure 3.6: Plot of field, MGC077, showing the arrangement of the 4 CCDs, and the gaps between them. CCD 4, the central CCD is centred on $12\text{h}32\text{m}00\text{s} +00^{\circ}00'00''$ (J2000). Features such as a large galaxy on CCD 3 and satellite trails can be seen.

of CCDs there are gaps ($\sim 20 - 30''$) for the input and output. Galaxies lying within these gaps will be missed.

The MGC catalogue contains four measurements of magnitude, each before and after dust correction. The four measurements are isophotal ($B_{26,MGC}$), a Gaussian corrected magnitude ($B_{gau,MGC}$), a Kron magnitude ($B_{KRON,MGC}$) and a “best” magnitude which is the Kron magnitude unless a nearby neighbour has interfered, and the magnitude is likely to be in error by $\geq 10\%$ in which case the Gaussian corrected magnitude is used.

Kron magnitudes have very little dependence on surface brightness, redshift or profile (see § A.1) and so may be regarded as total magnitudes. The Gaussian corrected magnitudes show more variation, but only show extreme variation when the central surface brightness is close to the isophotal limit. Bertin & Arnouts (1996) show that SExtractor best magnitudes have an offset of ~ 0.06 at $26 \text{ mag arcsec}^{-2}$. Therefore “best” magnitudes should behave more like total magnitudes than isophotal magnitudes when Visibility Theory is used. We have used the dust corrected “best” magnitude B_{MGC} throughout.

The half light radii are measured along the major axis of the ellipse that contains half of the flux of the galaxy. The effective surface brightness is calculated assuming a circular aperture. If the galaxy is an inclined optically thin disk galaxy, this will correct the effective surface brightness to the face on values. Not correcting spiral galaxies can produce a mean

offset of $\Delta\mu_e = 0.48 \text{ mag arcsec}^{-2}$, with a large scatter, see § A.1.2 for an optically thin galaxy. However, ellipticals will have the effective surface brightness underestimated slightly. Morphological classification will separate the ellipticals and spirals so that inclination and photometric corrections can be applied separately. However the most consistent way to treat galaxies with various bulge-total ratios and inclinations is to do a full bulge-disk decomposition.

Internal dust can affect both the magnitude and surface brightness through absorption and scattering (see de Jong & Lacey 2000, Matthews & Wood 2001). This problem will be discussed in future work.

Observations

The MGC images were taken through the KPNO-B filter on the Isaac Newton Telescope (INT) as part of the INT Wide Field Survey (INTWFS). The observations were taken over a period of 4 weeks, 1 in March 1999, 1 in June 1999, and 2 consecutive weeks in March/April 2000. However, due to the nature of the INTWFS only 2 weeks of these data were MGC data, the rest going to a variety of projects. The data were gathered in dark or grey time. The aim was to have good ($< 1.5''$) seeing on each field, so some fields with poor seeing were re-observed. Each observation was 750s in duration, apart from a few longer exposures (see Liske et al. 2002 for details). Only one image was taken of each field (apart from fields 1-8) because of the slow readout time of each CCD at the beginning of the survey. This has substantially speeded up, from $\sim 180s$ to $\sim 30s$. Each field is 0.26 deg^2 with $0.333''$ per pixel.

The field-to-field photometry was calibrated using the overlap regions and the Landolt standards, as described in Liske et al. (2002). The final mean offset between objects in the overlap regions between adjacent fields is $-6.4 \times 10^{-5} \pm 0.023 \text{ mag}$.

Bright and Faint Catalogues

The MGC has been split into a bright catalogue ($B_{MGC} \leq 20.0$) and a faint catalogue ($B_{MGC} > 20.0$). The objects in the bright catalogue are easily classified by eye (see Liske et al. 2002) whereas the objects in the faint catalogue are generally too small for reliable classification. The bright catalogue has been classified and contains almost 70,000 objects, of which $\sim 12,000$ are galaxies. In addition, the bright catalogue contains a quality flag (MQ) and half-light radius for every galaxy, with $MQ \leq 2$. $MQ = 1$ are "good" galaxies, $MQ = 2$ are "compromised" galaxies and $MQ = 3$ are "poor" galaxies. In practice, this means that the photometry of "compromised" galaxies is only useful for completeness statistics and the photometry of "poor" galaxies cannot be trusted at all. The half light radii are important for determining the effective surface brightness of the galaxies.

Galaxy Classification

We are currently classifying all the bright galaxies using software developed by Odewahn, Cohen & Windhorst (2000) and are also running GIM2D (Simard et al. 2001) to get structural parameters.

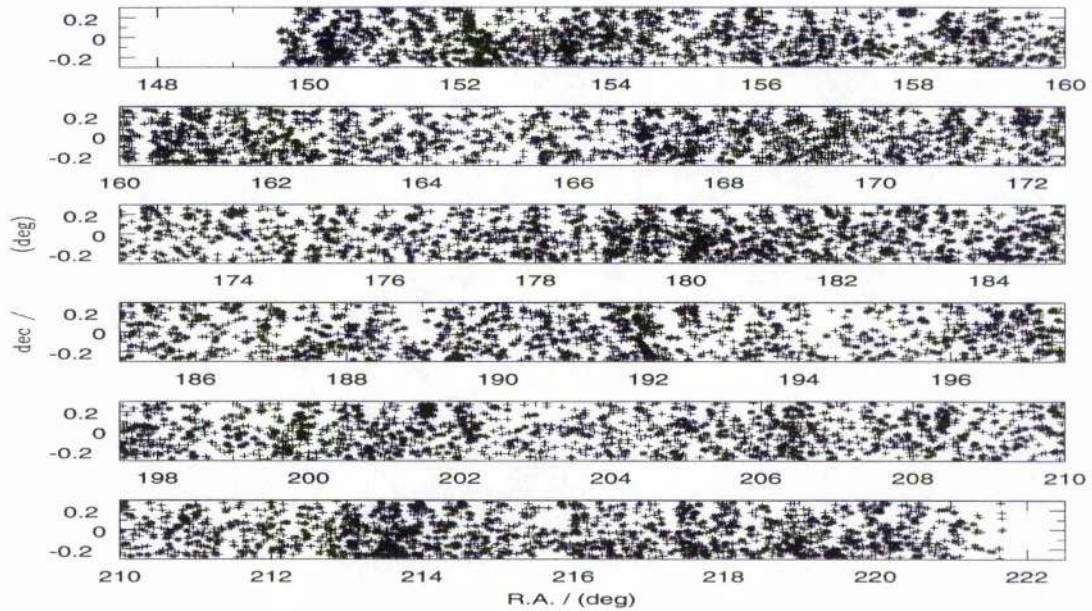


Figure 3.7: This plot shows the positions of all SDSS-EDR galaxies (vertical crosses) along the MGC strip. Those with redshifts are marked by diagonal crosses. Most of the strip has been targeted photometrically, apart from a few holes (e.g. $\alpha = 215.5, \delta = 0.1$), but large parts still have to be targeted spectroscopically (e.g. $168.5 < \alpha < 171$).

3.2.3 The SDSS-EDR

Overview of the SDSS-EDR

The Sloan Digital Sky Survey (SDSS, York et al. 2001, <http://www.sdss.org>) is the most ambitious redshift survey to date. When completed, it will cover $\sim 10,000 \text{ deg}^2$, mainly around the North Galactic Cap, but with 3 strips close to the South Galactic Cap. It uses a dedicated 3.5m telescope at Apache Point Observatory to collect the photometric and spectroscopic data.

It will get 5 colour photometry (u^* , g^* , r^* , i^* and z^*) for $> 10^8$ objects with $r^* < 24.1$ and $\sim 10^6$ spectra; 9×10^5 $r^* < 18.2$ galaxies, 10^5 $g^* < 19.2$ QSOs and 10^5 $z < 0.4$ luminous red galaxies. SDSS uses Petrosian magnitudes for galaxies (see Fukugita et al. 1996 and § A.1 for details), which have no surface brightness dependence for a given profile shape.

The Early Data Release covers 462 deg^2 , including the 36 deg^2 of the MGC. The positions of bright $B_{MGC} \leq 20$ galaxies within the MGC strip are shown in Fig 3.7. The diagonal crosses represent galaxies with SDSS redshifts.

Photometry

Each image covers 7.5 deg^2 , with the images recorded on 30 CCDs, with $0.4''$ pixels. The SDSS uses a drift scanning to improve flat fielding. When a survey uses drift-scanning, the CCD columns are aligned in the east-west direction and the telescope tracking is stopped, so that the light of each object tracks across the CCDs at the sidereal rate. The CCDs are read out continuously, taking an image of a strip of sky over time (see Kent, Ramella & Nonino 1993). The magnitude system (Fukugita et al. 1996) is calibrated to AB magnitudes. The isophotal limits are $\mu_{g,lim} = 24.3$ and $\mu_{r,lim} = 24.1$.

Spectroscopy

SDSS is a multifibre spectrometer similar to 2dF. Unlike 2dF, it does not have a system to reconfigure each plate. Instead thousands of individual plates have been pre-drilled and the fibres have to be inserted the day before. Each plate holds 640 fibres with a minimum separation of $55''$.

3.3 Matching the 2dFGRS objects to objects in the MGC.

The catalogue of 2dFGRS objects described in § 3.2.1 was compared to all the MGC objects $B_{MGC} < 21.0$. Although all the 2dFGRS objects have $b_j < 19.52$, ($B_{MGC} < 19.66$, using a colour term of $B_{MGC} = b_j + 0.1353(B - V)$ and $\overline{B - V} = 1.0$) a few will fall outside the bright catalogue, especially faint 2dFGRS objects which are separated into two with the improved resolution of the MGC.

2dFGRS objects which were not matched were checked to see if they lay outside the boundary of the MGC. Failing this, the appropriate MGC image was checked to determine why the 2dFGRS object was missed, and the object was given a flag to describe the problem. The results are in § 3.3.2.

Each 2dFGRS object was checked for multiple matches within an ellipse defined by its area, eccentricity and orientation. If an MGC object contributes to the flux of the 2dFGRS object, its centre should lie within the area of the 2dFGRS object. The edge, s of the 2dFGRS object is defined below.

$$s = \left[\left(\frac{\cos(\theta)}{a} \right)^2 + \left(\frac{\sin(\theta)}{b} \right)^2 \right]^{-\frac{1}{2}} \quad (3.1)$$

where a is the length of the semi-major axis, b is the length of the semi-minor axis and θ is the difference between the bearing from the 2dFGRS object to the MGC object and the orientation of the 2dFGRS object on the sky; e.g. if the 2dFGRS object is orientated with the major axis 30° from North, and the bearing from the 2dFGRS object to the MGC object is 110° from North, then the angle $\theta = 80^\circ$. a and b are defined from the area (A) and the eccentricity (e) below.

$$\begin{aligned} a &= \sqrt{\left(\frac{A}{\pi}\right)(1 - e^2)^{-0.25}} \\ b &= \sqrt{\left(\frac{A}{\pi}\right)(1 - e^2)^{0.25}} \end{aligned} \quad (3.2)$$

If the MGC object lies at $r \leq s$ then it is a component of the 2dFGRS object. The main component is deemed to be the brightest component, unless the redshift is incompatible. Fig 3.8 shows that the stellar population has $z \leq 1.0 \times 10^{-3}$, at which redshift there are very few galaxies. If an object has 2 components, with the brightest being a star and the faintest a galaxy, and it has $z = 0.23$, then the main component is the galaxy. If the components are transitory or spurious objects such as satellite trails or CCD defects then they are removed. If the components have $B_{MGC} > 20$ or are galaxies/stars with poor photometry they are deemed

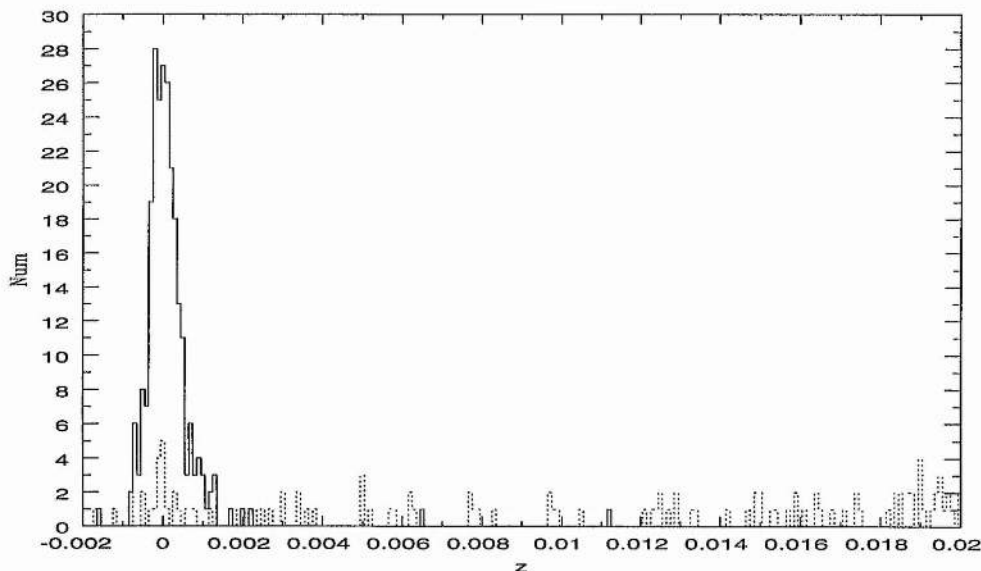


Figure 3.8: Histograms of the redshift distributions of stars (solid line) and galaxies (dotted line) of 2dFGRS objects at low redshift. Stars have a narrow distribution with width $\sim 1.0 \times 10^{-3}$ centred on $z = 0$.

unclassified. A component flag of 1 is given for a galaxy, 10 for a star and 100 for unclassified. The total component flag is the sum of all the components. The combined magnitude is the total flux from the properly classified stars and galaxies only.

3.3.1 The number of matches.

Out of the 7686 objects in the 2dFGRS subsample, 6281 had MGC counterparts. However this leaves 1405 galaxies with no counterpart. The galaxies selected from the 2dFGRS catalogue are in a rectangular area that is slightly larger than the region covered by the MGC. Each field in the MGC is a square 34.5' in length, with a corner missing, and gaps between the 4 CCDs, see Fig 3.6. The rectangle is 36' in width, and the corner represents one ninth of the field. Thus one would expect to lose ~ 320 galaxies around the edges and ~ 820 in the missing corners. ~ 230 will lie within gaps between the CCDs. This should account for ~ 1370 of the missing objects. However when the overlap between fields is taken into account, it is clear that some objects are counted twice in these estimates. Thus the total number of objects missing outside the MGC region reduces to ~ 1150 missing objects. This leaves ~ 250 objects unaccounted for. The actual numbers found are shown below. The missing objects are classified by error.

The number of multiple objects found was 526, with 1078 components. The different types of multiple objects will be dealt with below. Thus there are 6833 MGC objects matched to 6281 2dFGRS objects. A cross check has established that no MGC object is the component of two or more 2dFGRS objects.

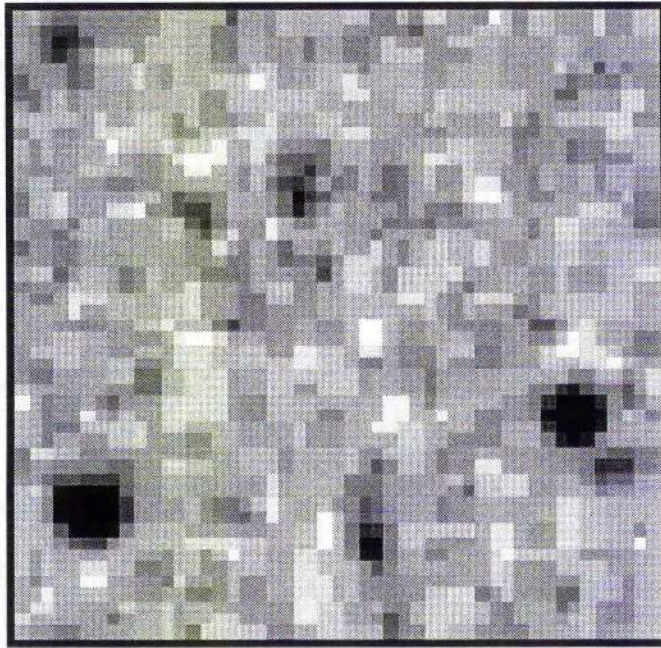


Figure 3.9: This plot shows the DSS image of 2dFGRS object 307982, which was missed by the MGC. It appears to be a blank piece of sky.

3.3.2 Mismatches

The 1405 galaxies without counterparts were checked to discover the reason why they had failed. $79.5 \pm 3.2\%$ lay outside the areas covered by the CCDs.

The other 20.5% of missing galaxies were carefully checked to see why they had failed. The majority of these, $52.4 \pm 5.3\%$ lay too close to bright stars, and thus had poor positions and photometry. $12.8 \pm 2.2\%$ were on CCD defects, $4.5 \pm 1.3\%$ were satellite trails and $4.5 \pm 1.3\%$ were parts of large galaxies which the APM had broken up into more than one object. One 2dFGRS object had $B_{MGC} > 20$ mag and was classified as a faint object. 23.8% of objects close to bright stars were classified as 2dFGRS eyeball rejects, and in many cases are stars. $69 \pm 30\%$ of the large galaxies that the APM had broken up were classified as 2dFGRS eyeball rejects.

Of the remainder, $4.2 \pm 1.2\%$ were classified as diffraction spikes. These objects were all half on, half off the CCD. 3, $1.0 \pm 0.6\%$, were classified as “other”, 2 of these were on the edge of a CCD and one was in the strongly vignetted part of CCD 3.

There were 59 objects that were missing. Of these 42 were 2dFGRS eyeball rejects and 17 were blank pieces of sky. The 17 blank pieces of sky were compared with the Digitised Sky Survey (DSS). 9 appeared blank on DSS (e.g. see 3.9) and 8 appeared to be odd objects such as asteroids (e.g. see 3.10). These were the same plates as used in the APM survey, so it appears as if there was a simple misclassification.

The numbers and percentages of missing 2dFGRS objects are shown in Table 3.1

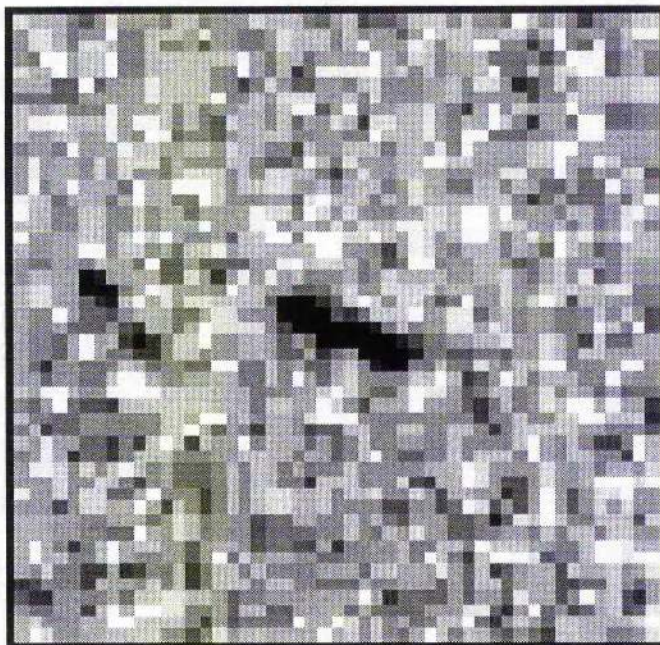


Figure 3.10: This plot shows the DSS image of 2dFGRS object 304594, which was missed by the MGC. It appears to be an asteroid.

Table 3.1: These table tallies up the reasons why 2dFGRS objects were missing from the MGC. The first column gives the reason, the second gives the total number of objects that failed for that reason. The third column converts this to a percentage of overall objects, and the fourth column gives the percentage of missing objects in terms of objects within the MGC CCDs. Objects in brackets give the breakdown for the nearest object above not in brackets.

Reason	Number	Percentage	% of objects within MGC CCDs
Out of bounds	1117	79.5	0.
(Of which 2dFGRS reject)	(30)	(2.1)	(0.)
Near to bright star	151	10.7	52.4
(Of which 2dFGRS reject)	(36)	(2.6)	(12.5)
On CCD defect	36	2.6	12.5
Crossed by Satellite	13	0.9	4.5
Broken Up Large Galaxies	13	0.9	4.5
(Of which 2dFGRS reject)	(9)	(0.6)	(3.1)
Faint Objects	1	0.1	0.3
Diffraction Spikes	12	0.9	4.2
Other	3	0.2	1.0
No MGC image	59	4.2	20.5
(Of which 2dFGRS reject)	(42)	(3.0)	(14.6)
(Of which missing in DSS)	(9)	(0.6)	(3.1)
(Of which odd in DSS)	(8)	(0.6)	(2.8)
Total	1405	100.0	100.0

3.3.3 Multiple 2dFGRS matches

There are 526 2dFGRS objects with 2 or more MGC matches. These can be categorised as galaxy-galaxy doubles, star-galaxy doubles, star-star doubles etc. $96.0 \pm 6.0\%$ are doubles, $3.0 \pm 0.8\%$ are triples, and $1.0 \pm 0.4\%$ are quadruple systems. The doubles contain $22.6 \pm 2.3\%$ galaxy-galaxy doubles, $20.0 \pm 2.2\%$ galaxy-star doubles, $7.5 \pm 1.3\%$ star-star doubles, $33.9 \pm 3.0\%$ galaxy-unclassified, $10.9 \pm 1.5\%$ star-unclassified and $5.1 \pm 1.0\%$ unclassified-unclassified systems. The triples contain $18.8 \pm 11.8\%$ galaxy-galaxy-galaxy, $18.8 \pm 11.8\%$ galaxy-galaxy-star, $12.5 \pm 9.4\%$ galaxy-star-star, $18.8 \pm 11.8\%$ galaxy-galaxy-unclassified, $18.8 \pm 11.8\%$ galaxy-star-unclassified, $6.3 \pm 6.4\%$ star-unclassified-unclassified and $6.3 \pm 6.4\%$ unclassified-unclassified-unclassified systems. The quadruples contain 1 galaxy-galaxy-galaxy-star, 1 galaxy-galaxy-galaxy-unclassified, 1 galaxy-galaxy-star-unclassified and 2 galaxy-galaxy-unclassified-unclassified systems.

These systems seem to have been picked up as doubles because of the relatively poor seeing of the 2dFGRS. A cross check has been performed to make sure that no MGC component is part of two 2dFGRS galaxies.

3.3.4 Galaxies, Stars and Unclassified objects

Of all the matches, 5470 are classified as single galaxies, 252 as single stars and 33 as single unclassified objects. These 33 objects have $B_{MGC} > 20.0$. 233 of the galaxies are classified as having poor photometry, and one has $B_{MGC} > 20.0$ and does not have a quality flag leaving 5236 2dF-MGC galaxies with good photometry.

205 out of 526 multiple systems contain at least one star and 40 contain two. The fraction of single systems that are stars is at least 4.4%, and up to 5.0% if all the unclassified objects are stars. The total fraction of 2dFGRS objects containing stars is between 7.3% and 11.1%. The fraction of MGC components that are stars is between 7.3% and 12.1%. The fraction of main objects that are stars (single stars and multiples in which the star is the main component) is 6.0%. This agrees with the measurement of stellar contamination in the spectroscopic data (Colless et al. 2001).

The fraction of single objects that are galaxies is between 95.0% and 95.6%. The fraction of 2dFGRS objects containing galaxies is between 93.5% and 95.4% and the fraction of MGC components that are galaxies is between 87.9% and 92.7%. Altogether 4.8% of MGC components are unclassified, but only 0.6% of single objects are unclassified. 1.0% of all objects have no classified component.

3.4 Matching the SDSS-EDR to the MGC

The MGC was also matched to the Sloan Digital Sky Survey Early Data Release (SDSS-EDR) which covers the same area of sky. This provides photometric data in 5 colours, Gunn u^* , g^* , r^* , i^* and z^{*1} and also has redshifts for a number of objects. We selected objects classified as galaxies in the SDSS-EDR for matching purposes. These were then matched to objects in the MGC with $B_{MGC} \leq 20.0$. The objects that constitute the MGC bright catalogue are described in § 3.6.

¹The final SDSS photometry will be labelled u' , g' , r' , i' and z' . The Early Data Release data has been designated u^* , g^* , r^* , i^* and z^* to distinguish it from the final catalogue.

The matching was done as above for the 2dF-MGC matching, but because the data quality is similar for the MGC and SDSS-EDR it is not safe to assume that most doubles are caused by poor seeing in one catalogue. To avoid this problem, a nearest object routine was employed as well. Thus if a galaxy A in the MGC is the nearest object to galaxy B in the SDSS-EDR and galaxy B is the nearest object to galaxy A then they are a match. If galaxy C in the SDSS-EDR has A as the nearest object too, then it is a secondary component. Each matched MGC object will have a number of components from either method. Only components found using both methods are counted.

There are 13682 SDSS-EDR objects matched to MGC objects. Of these, 11495 are matched to galaxies, meaning that 97.6% of MGC galaxies are matched. When two large holes in the SDSS-EDR are taken into account this figure increases to 97.9%.

3.5 Photometric Comparison.

3.5.1 Photometric accuracy of 2dFGRS.

The photometry of the 2dFGRS can be compared to the MGC. As each catalogue is measured in a different filter, it is first necessary to calculate the filter conversion. The MGC was measured through a KPNO B band filter and the INT optics, which can be corrected to the Landolt system using:

$$B = B_{MGC} + 0.1447(B - V) \quad (3.3)$$

This conversion comes from Liske et al. (2002). The APM uses a photographic b_j filter. The conversion to the Johnson-Cousins system is

$$B = b_j + 0.28(B - V) \quad (3.4)$$

This was measured in Maddox et al. (1990a) and has since been confirmed using ESO Imaging Survey (EIS) data (Peacock, private communication). However, without colours for each of the objects, a mean colour for galaxies ($B - V = 1.00$, Peacock, private communication) is used. This leads to a filter conversion:

$$B_{MGC} - b_j = 0.1353(B - V) = 0.1353 \quad (3.5)$$

Henceforth $\Delta m(MGC - 2dF) = B_{MGC} - b_j - 0.1353$

Selecting a good photometric sample.

To test the 2dFGRS photometry, it is pointless to use MGC photometry that is known to be poor. We have carefully checked all the galaxies for contamination with cosmic rays, CCD defects and satellite trails amongst other problems (see Liske et al. 2002). 2dFGRS was targeted at galaxies, so any stars picked up are likely to have odd morphological or photometric properties in 2dF.

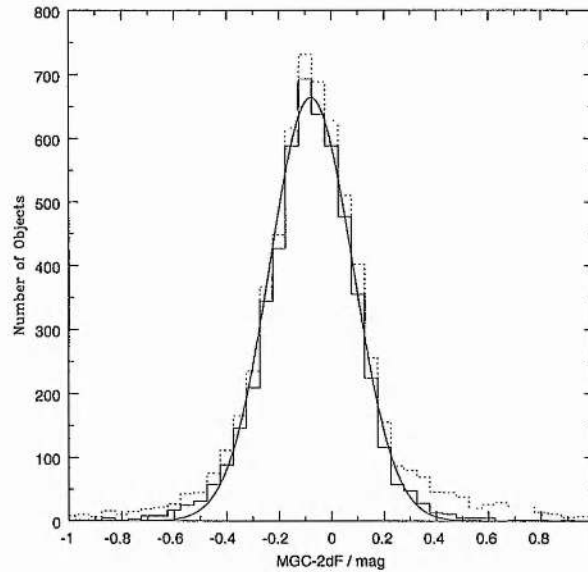


Figure 3.11: Histograms of the difference between the MGC and 2dFGRS magnitudes, $\Delta m = B_{MGC} - b_{j,APM} - 0.1353$. The dotted histogram shows all the matched objects, while the solid histogram shows the population of good single galaxies. The Gaussian distribution shown by the solid line represents the $3 - \sigma$ clipped mean and standard deviation.

As we have shown above, many 2dFGRS objects have been resolved into multiple MGC components. In these cases the magnitude is likely to be closer to the combined magnitude of both objects. For the photometric comparison, we have selected only galaxies that have 1 MGC component which is classified as a galaxy and has good photometry. There are 5236 objects in this category.

Fig 3.11 shows the whole distribution of 2dFGRS matches as a dotted line compared to the photometrically selected objects shown as a solid line. The photometrically good objects are well fitted by a Gaussian, with mean -0.078 and standard deviation 0.157 . The whole population contains many outliers.

Outliers

Fig. 3.12 shows that the outliers are dominated by multiple objects at the faint end and by stars at the bright end. The poorer seeing for the APM has meant that a few 2dFGRS objects have been resolved into multiples. Fig. 3.13 shows the combined fluxes of these objects. The combined fluxes show a Gaussian of mean -0.078 and width 0.157 , with a few outliers at the bright end.

The bright outliers from combining multiples may be systems where the APM had resolved both components and ignored one because it was too faint, or they could be saturated objects. To test this hypothesis, the combined fluxes of all components with stars are plotted. Fig. 3.13 shows that they are responsible for the bright outliers. As stars are known to produce bright outliers amongst single objects, the evidence suggests that the majority of multiple systems picked up are seen as one galaxy in the APM implying that the APM suffers from poor

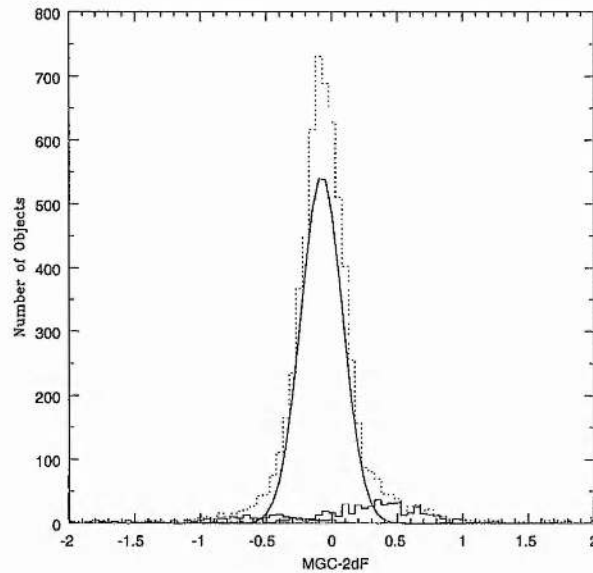


Figure 3.12: Histograms of the difference between the MGC and 2dFGRS magnitudes, $\Delta m = B_{MGC} - b_{j,APM} - 0.1353$. The solid histograms show the population of stars, on the left and multiple 2dFGRS objects on the right. The dotted histogram represents the complete distribution and the Gaussian (solid line) represents the photometric sample as described above. The outliers on the right are dominated by multiples. The 2dFGRS magnitude is the composite of several MGC objects. The outliers at the bright end are dominated by stars and show a very broad distribution. Here, the 2dFGRS magnitude is an underestimate because of non-linearities in the photometric plates.

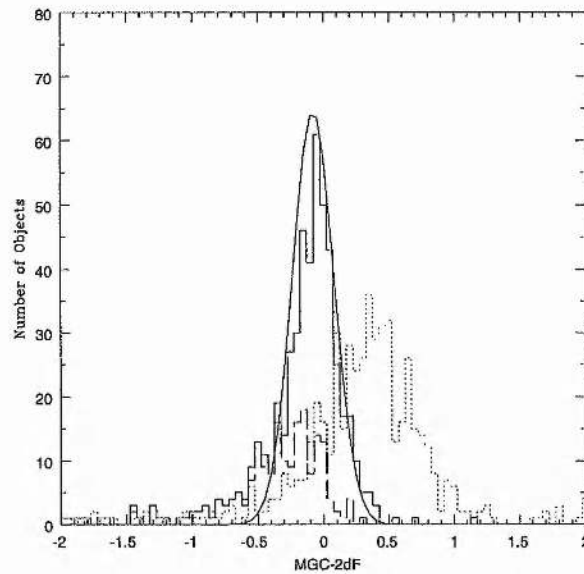


Figure 3.13: Histograms of the difference between the MGC and 2dFGRS magnitudes, $\Delta m = B_{MGC} - b_{j,APM} - 0.1353$. The dotted histogram shows the population of multiples. The solid histogram represents these galaxies when the flux of all the MGC components is combined; the distribution has the same mean and width as the photometric sample of single galaxies, given by the Gaussian. The long dashed histogram represents multiples where one or more component is a star. It is clear that the majority of multiples are true examples of unresolved objects in the 2dF, rather than nearby neighbours ignored by the 2dFGRS.

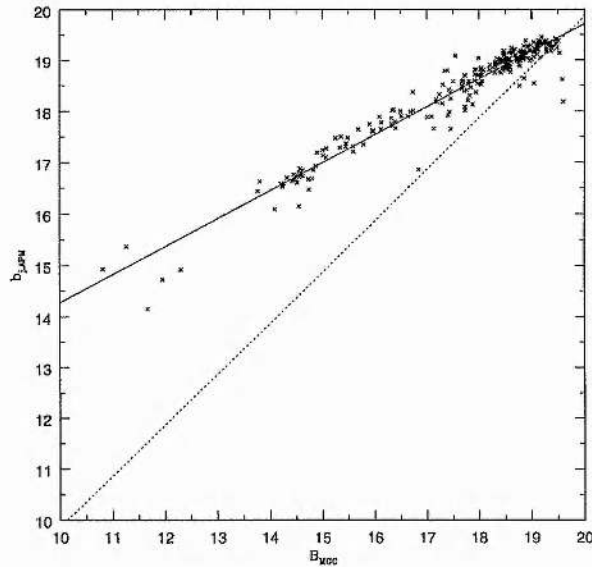


Figure 3.14: This plot shows the $b_{j,APM}$ magnitude as a function of the B_{MGC} magnitude for stars. The dashed line shows the expected variation, i.e. $b_{j,APM} = B_{MGC} - 0.1353$. The solid line shows the actual relationship, $b_{j,APM} = 0.544B_{MGC} + 8.836$. The lines cross at $b_j = 19.54$. The difference is likely to be due to non-linearities.

resolution.

The bright outliers are mainly stars. There is a broad distribution, with many objects several magnitudes brighter than the 2dFGRS object. Fig. 3.14 shows the $b_{j,APM}$ magnitude against the B_{MGC} magnitude for stars.

The photographic plates scanned by the APM have a dynamic range of ~ 100 (i.e. they can reliably measure objects with central surface brightnesses differing by up to 5 mag arcsec $^{-2}$ at the same time) and have a non-linear response (i.e. the density of silver grains produced is not directly proportional to the number of photons) whereas the CCDs used by the MGC have a dynamic range of $\sim 10^4$ (i.e. they can reliably measure objects with central surface brightnesses differing by up to 10 mag arcsec $^{-2}$ at the same time) and a linear response (the number of electrons trapped in the potential well is proportional to the number of photons) so even though the MGC goes deeper, saturation is less of an issue. Even so the brightest stars shown here do saturate badly. Stars in the MGC saturate at $B_{MGC} \sim 15$. To test whether the MGC magnitudes are reliable we tested the brighter ones against magnitudes in SIMBAD (while the brightest stars are not the best test since the MGC will have saturated, SIMBAD does not contain any fainter stars in this part of the sky).

Five stars with $B_{MGC} < 13$ appeared in SIMBAD. Table 3.2 lists their I.D.s, and B magnitudes for each survey. The MGC and APM magnitudes are converted to the Johnson-Cousins system.

Table 3.2 shows that $0.39 < B(MGC) - B < 2.26$ whereas $3.53 < B(2dF) - B < 4.99$. Both sets of magnitudes are therefore unreliable, at this magnitude, but the 2dFGRS magnitudes are much worse. The stellaricity (a star-galaxy classification in SExtractor, based on an artificial

Table 3.2: Comparison of Stars in SIMBAD, MGC and 2dF

I.D.	MGC	2dFGRS name	B	V	B(MGC)	B(2dF)
HD102058	24399	TGN377Z172	10.6	9.45	10.99	15.25
BD+002619	2987	TGN355Z135	10.9	10.3	11.36	15.54
BD+003023	41818	TGN328Z062	10.95	9.76	11.84	14.48
HD107090	31712	TGN319Z225	10.13	9.53	12.04	14.89
HD91513	8623	TGN360Z192	10.16	9.34	12.42	15.15

neural network, see Bertin & Arnouts 1996) plot (Fig. 10) in Liske et al. (2002) shows that stars saturate at $B_{MGC} = 15$. At that magnitude $b_{j,APM} = 17$ for stars.

3.5.2 2dFGRS galaxies

After considering the problems above, we decided to use only single component galaxies with a quality (MQ) 1 flag to compare the 2dFGRS and MGC photometry. This gave a total of 5236 objects. The mean and standard deviation were found using a sigma clipping method to remove any outliers beyond 3 standard deviations. All the results include the filter correction. Using the MGC best magnitude, it was found that $MGC - 2dF = -0.078 \pm 0.157$, where the error is the error in an individual galaxy. The quoted error will be for an individual galaxy throughout this thesis, unless stated.

Variation with Plate no.

It is important to see how the photometry varies across MGC fields and UKST plates, to check for inconsistencies. The variation in Δm , the mean $MGC - 2dF$, over the 144 MGC fields is shown in Fig. 3.15.

Fig. 3.15 shows that the largest field to field changes occur at UKST plate boundaries, e.g. 46-47, 87-88 and 127-128. The variation between fields within a UKST plate is small (typically 0.03 mag, which includes the 0.15 mag spread averaged over ~ 30 galaxies), consistent with a field to field error of ~ 0.01 , for the first 80 fields. The MGC photometry is not as well constrained after field 80, where a systematic error of up to 0.05 mag is possible. Larger variations between MGC fields are seen for fields greater than 80, but the largest errors are still seen at UKST plate boundaries. The final 2dFGRS photometry has been recalibrated using these plate to plate offsets.

The variation over the 15 UKST plates is shown in Fig. 3.16. The UKST plate-to-plate variation is 0.0643mag. While the variation is greater than expected for a distribution with Gaussian errors of 0.16mag, as can be seen from the error bars (~ 0.01 mag), it does not appear to suffer from systematic errors greater than ~ 0.1 mag.

Scale Errors

To check for scale errors in the photometry, we looked at how Δm varies as a function of B_{MGC} for the UKST plates. Fig. 3.17 shows the plot of Δm vs B_{MGC} for each UKST plate.

There is very little scale error across each plate, apart from 864 and possibly 858. These do not show particularly large mean Δm . The mean scale error over all the plates (see Fig 3.18) is

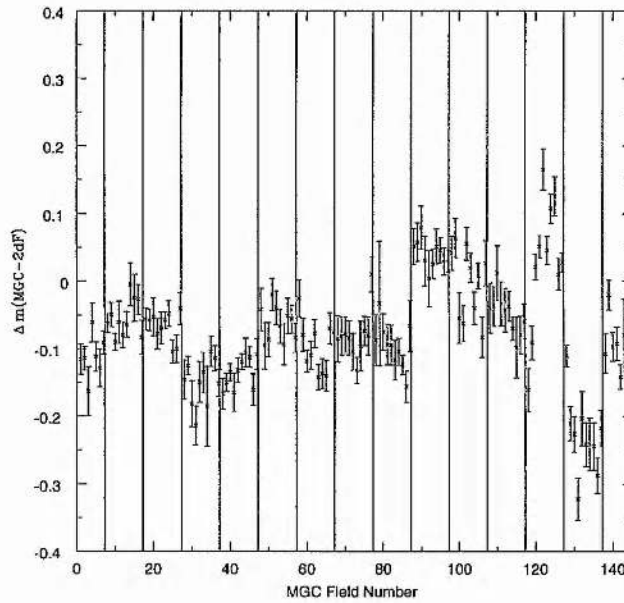


Figure 3.15: The variation of the difference between the MGC and 2dFGRS magnitudes, $\Delta m = B_{MGC} - b_{j,APM} - 0.1353$ with MGC field no. The solid lines show the UKST plate boundaries. The greatest changes appear to occur at UKST plate boundaries, suggesting that there are discrepancies between the plates. In Liske et al. (2002), it is shown that the MGC photometry is consistent to 0.05 mag, with the first 80 fields consistent to < 0.01 mag. The worst variations within an UKST plate occur between fields 80 and 144, where there are changes of ~ 0.2 mag at several plate boundaries.

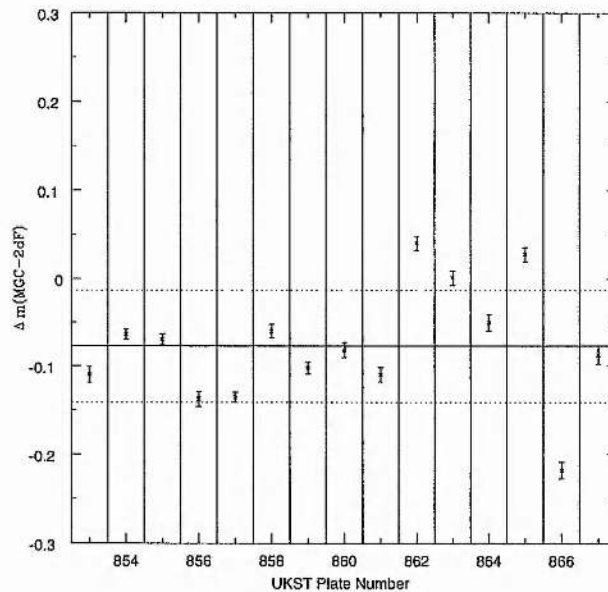


Figure 3.16: The variation of the difference between the MGC and 2dFGRS magnitudes, $\Delta m = B_{MGC} - b_{j,APM} - 0.1353$ with UKST plate no. The solid vertical lines show the UKST plate boundaries. The solid horizontal line shows the mean and the dotted lines the 1σ standard deviation of the mean Δm for each plate. The mean of the means is -0.0772 ± 0.0643 .

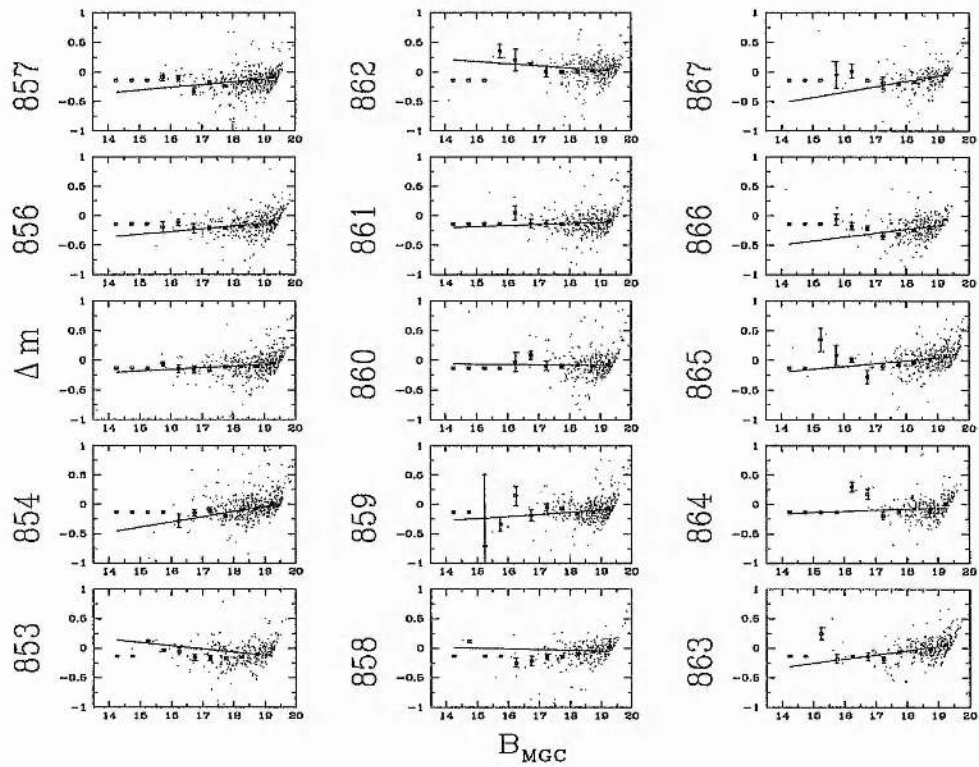


Figure 3.17: The variation of $\Delta m = B_{MGC} - b_{j,APM} - 0.1353$ as a function of B_{MGC} for each UKST plate no. The dots show each object, the points with error bars show the mean Δm at each B_{MGC} and the line shows the best χ^2 fit to the points.

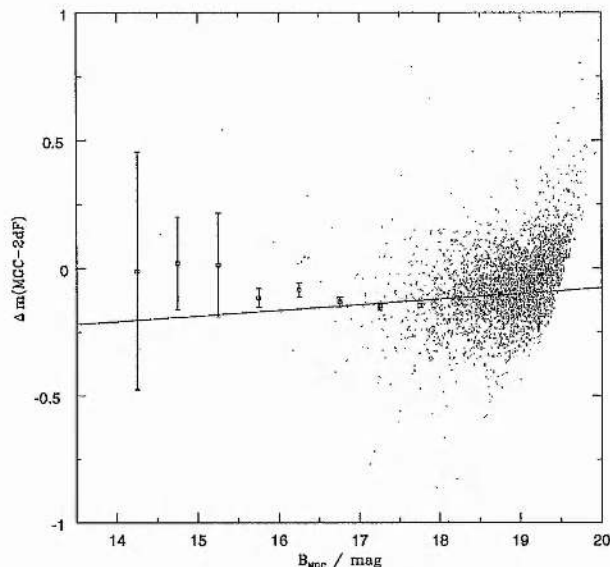


Figure 3.18: The variation of $\Delta m = B_{MGC} - b_{j,APM} - 0.1353$ as a function of B_{MGC} . The dots show each object, the points with error bars show the mean Δm at each B_{MGC} and the line shows the best χ^2 fit to the points. As the last bin is obviously affected by the 2dFGRS magnitude limit, this bin is not included in the calculation of χ^2 .

fit by the equation $\Delta m = a + b(B_{MGC} - 19.45)$, where $a = 0.0467$ and $b = 0.0221$. The gradient, b , is rather shallow, giving a variation $\Delta(\Delta m) = 0.120$ over the range $14 < B_{MGC} < 19.45$.

The effective surface brightness, $\mu_e = B_{MGC} + 2.5 \log_{10}(2\pi r_e^2)$, Fig 3.19 shows a significant scale error. The mean scale error over all the plates is shown in Fig 3.20. Δm is constant for $22 < \mu_e < 25$ but decreases non-linearly with μ_e for $\mu_e < 22$ mag arcsec $^{-2}$. The most likely explanation is non-linearities or saturation of high surface brightness galaxies in the APM, as seen in § 3.5.1 for stars.

3.5.3 Comparison with the SDSS-EDR

We used the conversions from the Johnson-Cousins (UBVRI) system to the SDSS-EDR system given in Fukugita et al. (1996), Eqn 3.6 & 3.7, and the conversions from B_{MGC} to the Johnson-Cousins system, Eqn 3.3, to calculate the filter correction from SDSS-EDR to MGC, Eqn 3.8.

$$\begin{aligned} g' &= V + 0.56(B - V) - 0.12 \\ &= B - 0.44(B - V) - 0.12 \end{aligned} \quad (3.6)$$

$$g' - r' = 1.05(B - V) - 0.23 \quad (3.7)$$

$$B_{MGC} = g' + 0.281(g' - r') + 0.185 \quad (3.8)$$

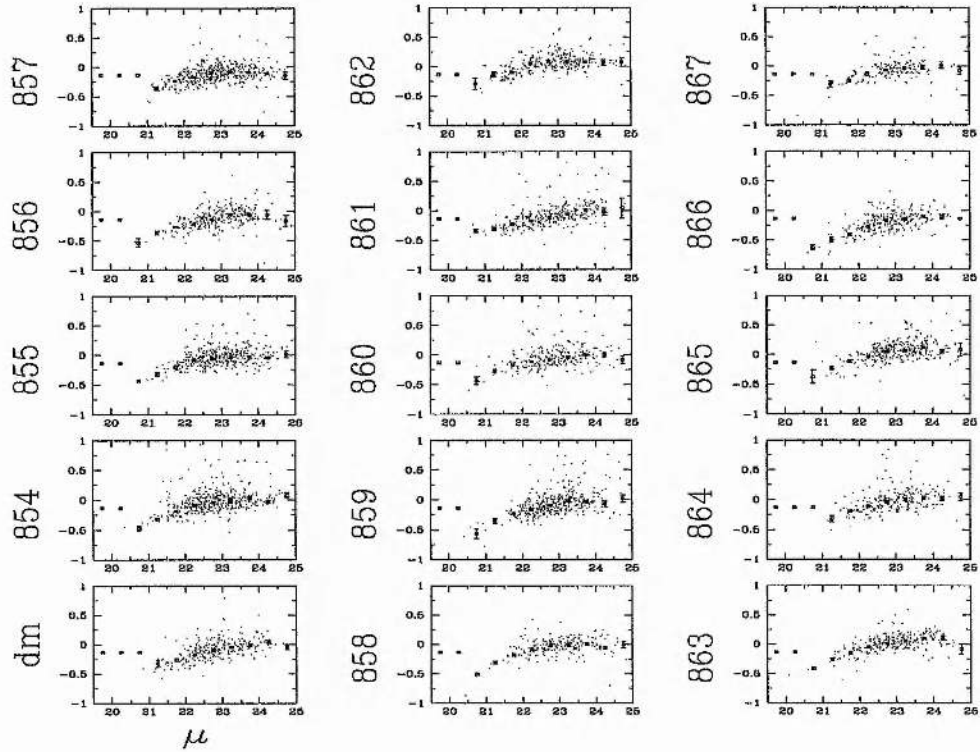


Figure 3.19: The variation of $\Delta m = B_{MGC} - b_{j,APM} - 0.1353$ as a function of μ_e for each UKST plate no. The points with error bars show the mean Δm at each μ_e .

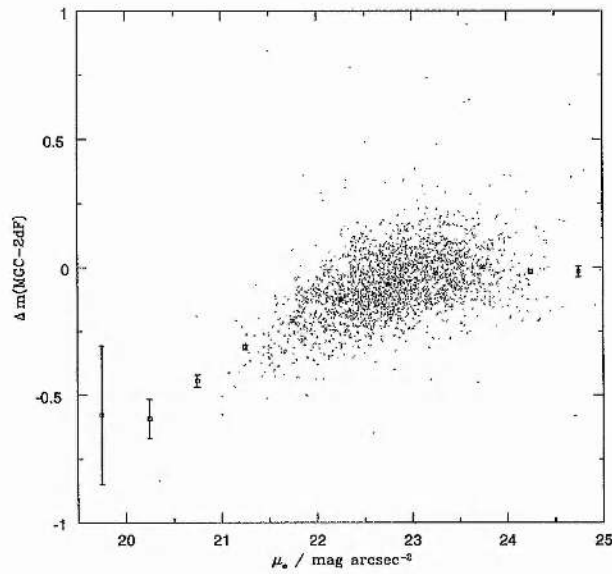


Figure 3.20: The variation of $\Delta m = B_{MGC} - b_{j,APM} - 0.1353$ as a function of μ_e . The points with error bars show the mean Δm at each μ_e .

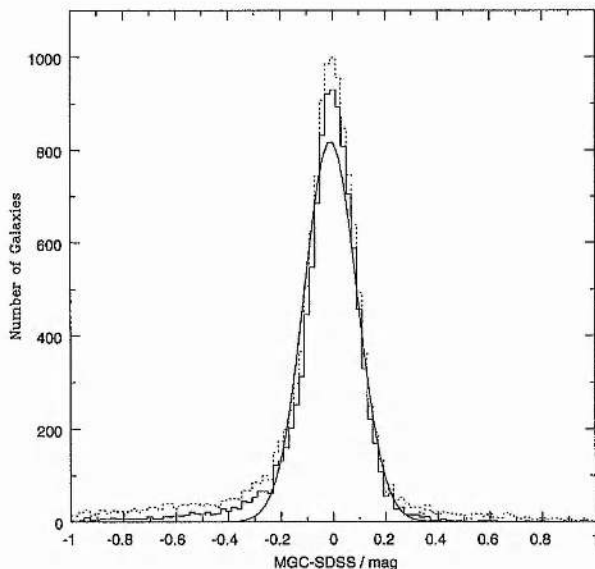


Figure 3.21: Histograms of the difference between the MGC and SDSS-EDR magnitudes, $\Delta m = B_{MGC}(MGC - SDSS)$. The dotted line shows all the matched objects, while the solid line shows the population of good single galaxies. The Gaussian distribution shown represents the $3 - \sigma$ clipped mean and standard deviation.

Again, we only used single component, $14 < B_{MGC} < 20$ galaxies with $M_Q = 1$ to compare the SDSS-EDR and MGC photometry. This gave a total of 10871 objects. The mean and standard deviation were found as before. It was found that $\Delta m(MGC - SDSS) = -0.009 \pm 0.100$. The histogram of the difference between the MGC and SDSS-EDR magnitudes is shown in Fig 3.21.

Variation with Plate no.

The variation in the MGC-SDSS with MGC field number is shown in Fig 3.22. The field to field variation is much smaller than the field-to-field variation between the MGC and 2dFGRS. Even where there is larger variation, e.g. MGC 143 and 144, it appears to be systematic over a few fields and different to the variation with 2dFGRS, suggesting that at least some of the variation is due to errors in the SDSS-EDR. The first 80 fields show very little variation as expected, but then there appears to be a systematic increase in error until field 110, with an overall offset of ~ 0.05 mag. Liske et al. (2002) showed that the field to field photometry is well constrained for the first 80 fields, but then may be prone to systematics of up to 0.05 mag for fields > 80 due to the lack of good photometric standard fields in this range.

Scale Errors

To check for scale errors in the photometry, we looked at how Δm varies as a function of B_{MGC} over all fields, as shown in Fig. 3.23. The best fit line is $\Delta m = -0.0017 + 0.017(B_{MGC} - 19.45)$. However, there is a small non-linearity at the bright end. If the distribution is capped so $B_{MGC} > 16$, $\Delta m = -0.0026 + 0.014(B_{MGC} - 19.45)$. The scale error is small, a 0.06 change

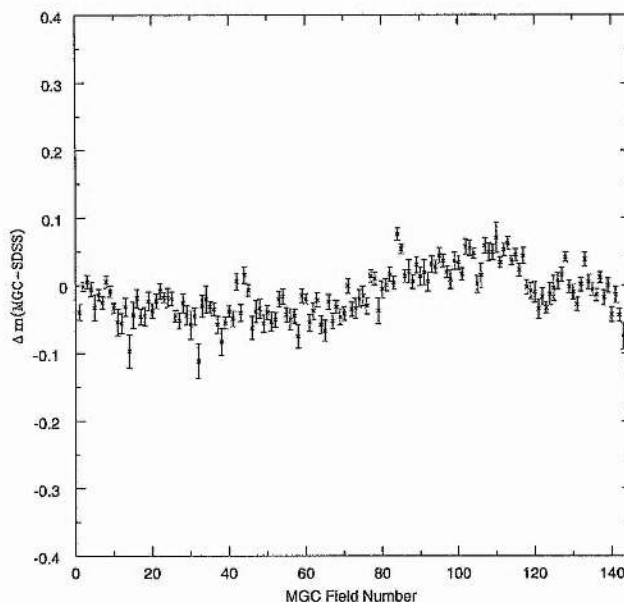


Figure 3.22: The variation of the difference between the MGC and SDSS magnitudes, $\Delta m = B_{MGC}(MGC - SDSS)$ with MGC field.

over the interval $16 < B_{MGC} < 20$

The variation with μ_e is shown in Fig. 3.24. The scale error with μ_e seen in § 3.5.2 is not apparent in the comparison with SDSS-EDR, suggesting that this is a problem with the 2dFGRS data.

3.5.4 Variations with Redshift

Fig 3.25 shows the clustering in the MGC region. These inhomogeneities must be taken into account when calculating the space density of galaxies. Several large clusters appear at $\sim z = 0.1$. The reason that they appear at this redshift is a selection effect. At lower redshifts the volume sampled decreases, so the probability of a large cluster occurring within the survey diminishes. At high redshifts, the probability of a cluster occurring at that redshift increases, but only the very brightest members can be detected, so it will only be picked up as a large group at best.

Fig 3.26 shows the scale error of the 2dFGRS as a function of redshift. There is a strong scale error with the overall population having a best fit line, $\Delta m = a + bz$, with $a = -0.0691$ and $b = 1.096$. $\Delta(\Delta m) = 0.20$ over the range $0.02 < z < 0.2$. The most likely explanation for this change is the saturation of high surface brightness galaxies. The low redshift population will contain galaxies of a variety of surface brightnesses, including many at low surface brightness. To test this out we have plotted the apparent surface brightness distribution of galaxies at $z = 0.02$ and $z = 0.2$ in Fig 3.27.

While there are more $z = 0.02$ galaxies with high surface brightness, the difference in magnitude due to the variation in the surface brightness is ~ 0.05 mag. This only accounts for a quarter of the total change. Another factor could be the reddening of galaxies as a

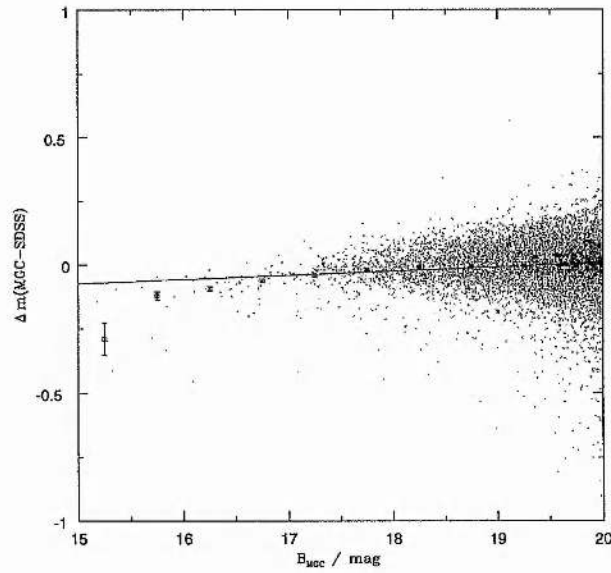


Figure 3.23: This plot shows the variation in $\Delta m(MGC - SDSS)$ with B_{MGC} . The distribution of $\overline{\Delta m}$ is linear for $B_{MGC} > 17.5$, but has a small non-linearity for brighter galaxies.

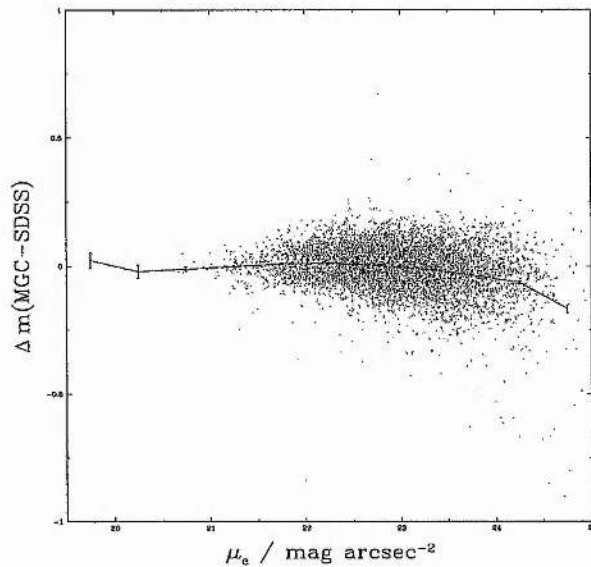


Figure 3.24: The variation of $\Delta m = B_{MGC}(MGC - SDSS)$ as a function of μ_e . The points with error bars show the mean Δm at each μ_e .

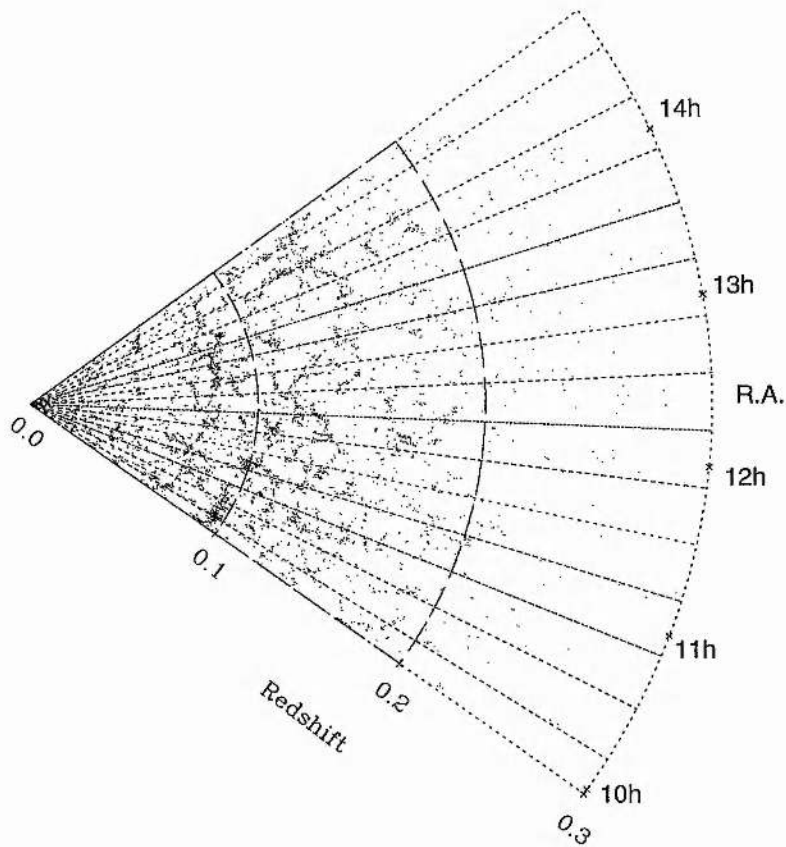


Figure 3.25: Plot showing the distribution of galaxies in Right Ascension and redshift for the MGC-2dFGRS region. The dotted lines show the UKST plate boundaries. There is a lot of substructure: clusters and voids even on the scales of the MGC. A correction for inhomogeneity is therefore essential.

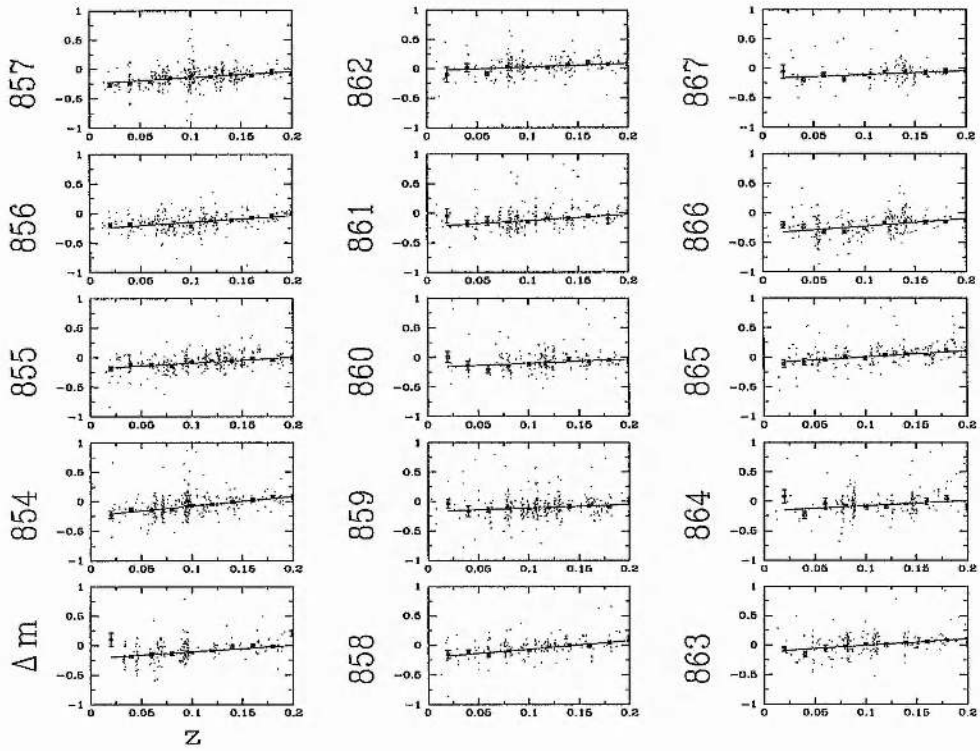


Figure 3.26: The variation of $\Delta m = B_{MGC} - b_{j,APM} - 0.1353$ as a function of z for each UKST plate no. The points with error bars show the mean Δm at each z .

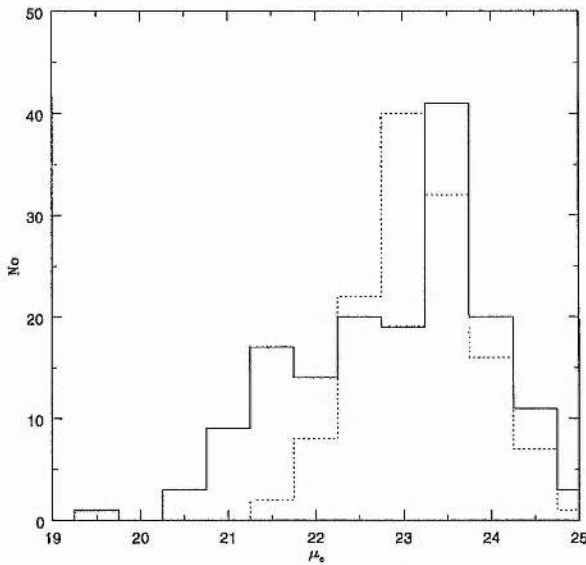


Figure 3.27: This plot shows the distribution of μ_e^{app} at $z = 0.02$ (solid histogram) and $z = 0.2$ (dotted histogram). Both have peaks at $23. < \mu_e < 23.5$, but the $z = 0.02$ distribution is much broader, including more saturated galaxies.

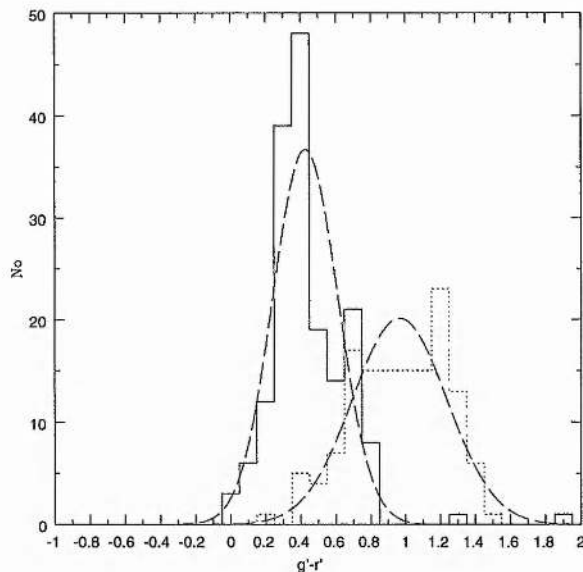


Figure 3.28: This plot shows the distribution of $g^* - r^*$ at $z = 0.02$ (solid histogram) and $z = 0.2$ (dashed histogram). The $z = 0.2$ distribution is both redder and broader. The best fit Gaussians are shown with the mean and standard deviations in the text.

function of redshift. Eqn 3.5 shows that a difference in the mean colour of galaxies equivalent to $\Delta(B - V) = 1.46$ over the range $0.02 < z < 0.2$ would explain the scale error seen in data. There are two effects which increase $(B - V)$ with redshift. The first is the reddening of light, so the spectrum increases in wavelength by a factor of 1.18 over the range $0.02 < z < 0.2$. Coleman, Wu & Weedman (1980) plot the change in $(B - V)$ for 5 types of spiral galaxy. The change in $(B - V)$ varies from 0.3 mag for an Im galaxy to 0.6 mag for a galaxy like M31 or M81.

The second effect is the change due to Malmquist bias. At $z = 0.02$, a wide range of galaxies is seen, with $M_B < -14.5$, assuming a limiting magnitude of $B = 19.5$. At $z = 0.2$, a narrow range of galaxies is seen, with $M_B < -20.0$. The latter range is dominated by ellipticals and S0s which are intrinsically red. Galaxies detected at $z = 0.02$ will contain more late-type spirals and irregulars. Blanton et al. (2001) show a strong correlation between M_{r^*} and $g^* - r^*$ colours.

Fig 3.28 shows the distribution of SDSS-EDR $g^* - r^*$ colours at $z = 0.02$ (solid line) and $z = 0.2$ (dotted line). There is a clear increase in $g^* - r^*$ with redshift, from $\overline{g^* - r^*} = 0.427$ at $z = 0.02$ to $\overline{g^* - r^*} = 0.966$ at $z = 0.2$ accompanied by a broadening of the distribution, from $\Delta(g^* - r^*) = 0.185$ at $z = 0.02$ to $\Delta(g^* - r^*) = 0.272$ at $z = 0.2$. This gives $\Delta(\overline{g^* - r^*}) = 0.54 \pm 0.33$. This gives $\Delta(\overline{B - V}) = 0.57 \pm 0.35$ over the corresponding redshift interval.

This can account for ~ 0.08 mag of the variation seen in $\Delta m(MGC - 2dF)$ with z . There is still an unaccounted $\Delta m = 0.07$. Fig 3.29 shows the variation between the MGC and SDSS-EDR magnitudes as a function of redshift. While there was no significant scale error with magnitude or surface brightness, there is with redshift. The best fit linear relationship is $\Delta m = 0.51z - 0.05$. Over the range $0.02 < z < 0.2$ this adds up to $\Delta(\Delta m) = 0.09$, which

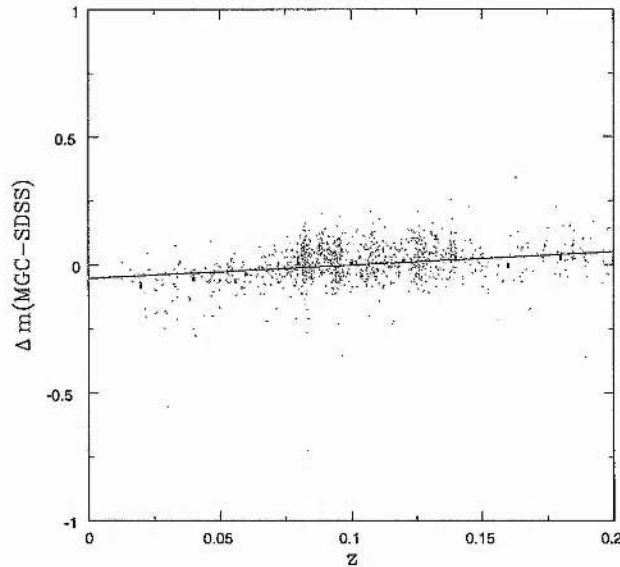


Figure 3.29: The variation of $\Delta m = B_{MGC}(MGC - SDSS)$ as a function of z . The points with error bars show the mean Δm at each z . The line is the best linear fit to these points.

accounts for the remainder of the difference between MGC and 2dF.

The differences could be due to differences in the magnitude types with redshift. This can be tested by comparing the Kron and Gaussian corrected MGC magnitudes to the SDSS-EDR and see if a different relationship is seen. The Kron magnitudes give a best fit $\Delta m = 0.48z - 0.05$ and the Gaussian gives $\Delta m = 0.67z - 0.09$. Kron and Petrosian magnitudes are designed to have low redshift dependence and would be expected to vary by ~ 0.03 mag over this redshift range. They will also vary in the roughly the same direction, so it seems unlikely that this will explain the 0.1 mag variation seen over the range $0.02 < z < 0.2$.

A more likely explanation is a variation in the colour equation Eqn 3.7 with redshift. The magnitude of a galaxy is the spectrum of the galaxy convolved with the instrument efficiency in each filter. The colour equation is the best fit conversion for these filters. It is the average over all galaxy types and across the redshift range observed. At different redshifts, different parts of a galaxies spectrum will be observed through a filter.

Thus the variation between the 2dFGRS and MGC magnitudes with redshift is a combination of the surface brightness error in the 2dFGRS magnitudes, the error caused by assuming a mean $(B - V)$ in the colour equation and the variation in the colour equation with redshift. The variation between the SDSS-EDR magnitudes and the MGC magnitudes with redshift is just due to the variation in the colour equation with redshift.

3.6 MGC bright catalogue

The MGC bright catalogue is described in Liske et al. (2002). After matching it to the 2dFGRS we did the reverse process, by inverting the 2dFGRS matched catalogue and adding in the extra matches found. We then checked to see if any MGC object was matched to more

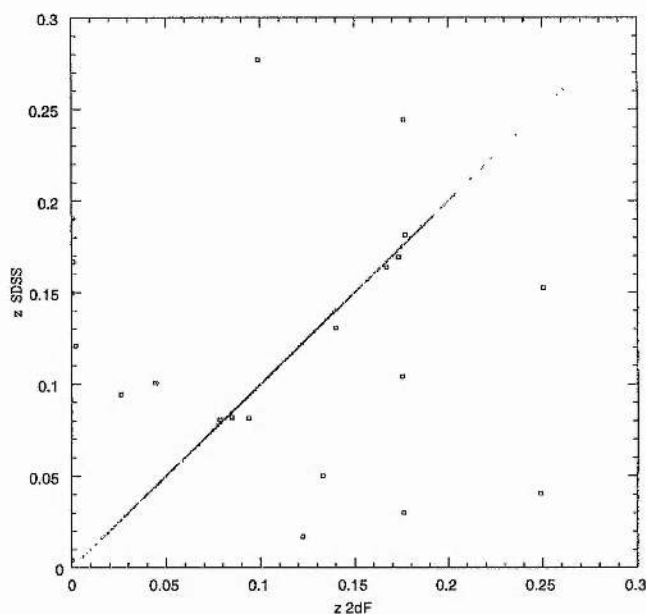


Figure 3.30: The comparison of 2dFGRS and SDSS-EDR redshifts. The scatter is extremely small and there are only 32 blunders (1.3%).

than one 2dFGRS object and found four such objects. These 4 corresponded to 4 of the 13 objects described in § 3.3.2, see Table 3.1, where a 2dFGRS object was missed because it was part of a large galaxy broken up by the APM. The other 9 objects of this type are eyeball rejects in the 2dF.

There are 6499 2dFGRS objects matched to MGC objects. Of these $80.5 \pm 1.5\%$ have good quality redshifts. $88.0 \pm 1.6\%$ are the only match to 2dFGRS objects, $7.4 \pm 0.4\%$ are the main component and $4.6 \pm 0.3\%$ are the secondary component to 2dFGRS objects.

3055 of the SDSS-EDR matches have redshifts and 5903 of all MGC objects have a 2dFGRS or SDSS-EDR redshift. Of these 5577 have SDSS-EDR colours and 5410 objects are galaxies with redshifts and colours. 2384 objects have redshifts from both 2dFGRS and SDSS-EDR. The comparison of redshifts is shown in Fig 3.30. $\Delta z = 4.25 \times 10^{-6} \pm 2.92 \times 10^{-4}$. In terms of velocity this is equivalent to $\Delta v = 1.27 \times 10^3 \pm 8.76 \times 10^4 \text{ms}^{-1}$. Colless et al. (2001) describe a blunder as any object with $|\Delta cz| > 600 \text{kms}^{-1}$. Thus there are 32 blunders, giving a blunder rate of 1.3%. These figures compare well with the comparisons in Colless et al. (2001).

In Chapter 4 we will use the combined catalogue to measure the BBD and the relationship between different variables. The redshifts for each galaxy were measured from the 2dFGRS and SDSS-EDR. If there was only a measurement in one catalogue then it was selected. When there was a redshift measured in both catalogues, and it was not considered a blunder, then the 2dFGRS redshift was selected. For the blunders, if one component had $z < 0.002$ then it was assumed that starlight or moonlight had contaminated the spectra, so the other redshift was used. This was the case for half of the blunders. The rest were checked carefully to see if there were two galaxies close to each other. In five cases there were. In one of them there was clear evidence of a merger event (i.e. tidal tails, see Fig 3.31). The 2dFGRS only targeted this as

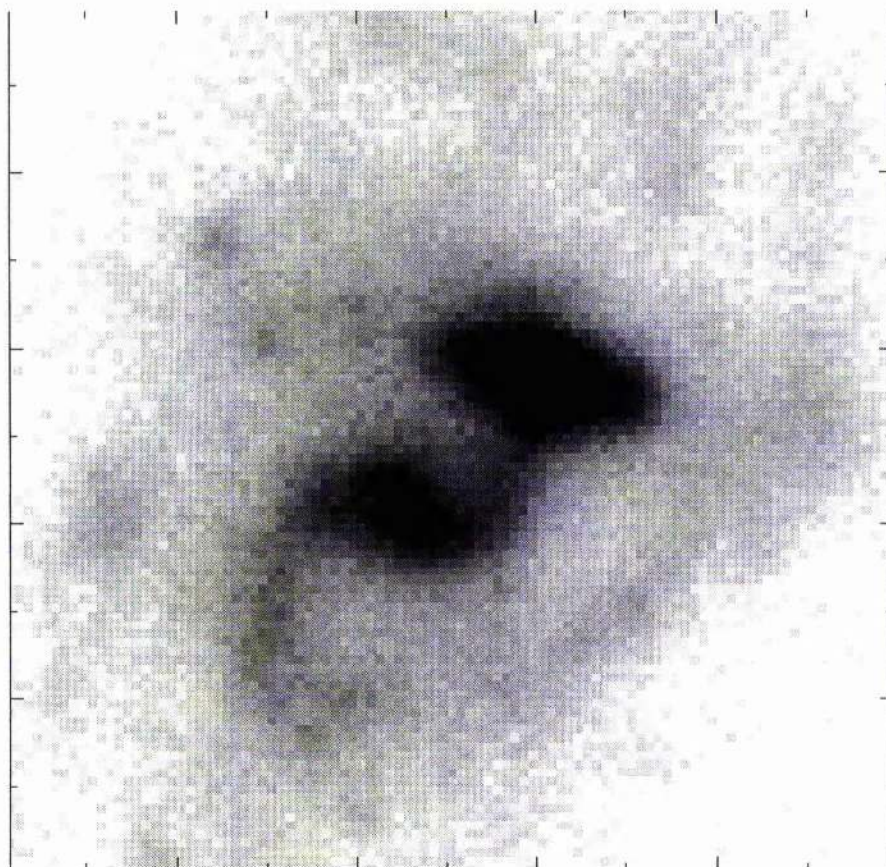


Figure 3.31: MGC11548 is an odd galaxy, with evidence of a merger taking place. The lower galaxy has two spiral arms, one going directly into the upper galaxy and the other forming a stream looping away in the opposite direction. There is other gas and stars surrounding the two galaxies. This is the pattern that you would expect if the upper galaxy was pulling material off the lower galaxy as they were merging. Unfortunately the redshifts from 2dFGRS and SDSS-EDR do not agree. While this would be expected if they were optical doubles (line of sight) rather than a true gravitational held system, the image seems to suggest that they are in the process of merging. The difference in redshift $\Delta z = 0.068$, equivalent to $\Delta v \sim 20000 \text{ km s}^{-1}$, much higher than infall velocities even within clusters.

one galaxy, and although SDSS-EDR targeted it as two, they had only obtained one redshift. Although these galaxies are clearly connected the two redshifts were different by $\Delta z = 0.068$, thus it was decided that there was not enough information to decide which redshift was correct and this galaxy was classified as having no redshift. In the other 4 cases, there was not enough information either, but the redshifts were within 5% of each other so it was decided to take the mean value. For all the other blunders, there was not enough information to decide which value to take, so none were taken. All the secondary components of 2dFGRS objects without an SDSS-EDR redshift were checked for signs of merger events, to tie the redshift of the primary to that of the secondary. No evidence was found of mergers in any of these galaxies, so it is impossible to tie down the redshifts.

3.7 Incompleteness of 2dFGRS

The photometry of objects in the 2dFGRS has been revised since the input catalogues were produced, so there is not a single magnitude limit. In the region of the MGC, the mag limit varies over the range $19.241 < b_{j,limit} < 19.52$. The bright limit corresponds to $B_{MGC} = 19.298 \pm 0.157$, see Fig. 3.20. The survey should be 95% complete at 2σ brighter than this, i.e. at $B_{MGC} = 18.98$. If we exclude all objects with a $b_{j,lim}$ brighter than $b_j = 19.3$, then we can extend the limit to $B_{MGC} = 19.05$. If we exclude all objects with a $b_{j,lim}$ brighter than $b_j = 19.35$, then we can extend the limit to $B_{MGC} = 19.10$ and if we exclude all objects with a $b_{j,lim}$ brighter than $b_j = 19.4$, then we can extend the limit to $B_{MGC} = 19.15$. $b_{j,lim}$ varies plate by plate, but also varies by a small amount within each plate, because the dust correction has been updated since the original limits were defined. For each UKST plate we take the galaxy in the MGC region with the brightest $b_{j,lim}$ as the $b_{j,lim}$ for that region.

We first of all select all galaxies with $M_Q \leq 2$, i.e. those with “good” or “compromised” photometry, see § 3.2.2. We remove all galaxies in regions where there are holes in the 2dFGRS using a code supplied by Gavin Dalton. There are 5510 galaxies in regions defined to have $b_{j,lim} > 19.3$, 3772 galaxies in regions defined to have $b_{j,lim} > 19.35$ and only 400 galaxies in regions defined to have $b_{j,lim} > 19.4$. We can therefore measure the completeness down to a limit of $B_{MGC} = 19.10$.

This gives a catalogue to test the completeness. This was separated into objects with a 2dFGRS match and objects without. Objects that are a member of a multiple system matched to a single 2dFGRS object were placed into the matched bin if they were the principle component and into the non-matched bin if they were a secondary component. The variation of incompleteness with magnitude is shown in Fig. 3.32.

The overall incompleteness to $B_{MGC} = 19.0$ was calculated for the two cases above. When $b_{j,lim} \leq 19.3$, the incompleteness $IC_{19.0} = 0.0815 \pm 0.0051$ and when $b_{j,lim} \leq 19.35$, $IC_{19.0} = 0.0820 \pm 0.0062$. These two cases are consistent.

As can be seen, the incompleteness is worst at the bright and faint ends, reaching a minimum of ~ 0.05 in the range $17.25 < B_{MGC} < 18.0$. It increases linearly with magnitude in the range $18.0 < B_{MGC} < 19.0$, as shown in Fig. 3.32. In Fig 3.32 the incompleteness appears to suddenly increase for $B_{MGC} > 19.1$. This is not the true incompleteness, since galaxies with $B_{MGC} > 19.1$ are within 2 standard deviations of the 2dFGRS magnitude limit, so a significant proportion will have measured APM magnitudes that are slightly too faint to get into the input catalogue for 2dFGRS. This is due to random errors in the measurement of the magnitudes. If the linear increase in incompleteness is extrapolated to $B_{MGC} = b_j + \Delta m = 19.51$, the original faint limit for the 2dFGRS, then the incompleteness will reach 14.0%. There are also some galaxies which have $B_{MGC} > 19.51$, again due to random errors in the measurement of the magnitudes.

The variation with effective surface brightness is shown in Fig. 3.33. For $22.25 < \mu_e < 24.25$ the incompleteness is fairly constant $IC \sim 5\%$. The incompleteness of LSBG increases rapidly beyond $\mu_e = 24.25$ and no 2dFGRS galaxies are seen with $\mu_e > 25.75$, as expected with an isophotal limit $\mu_{lim} = 24.67$ (see Chapter 2). At the bright end, the incompleteness rises steadily.

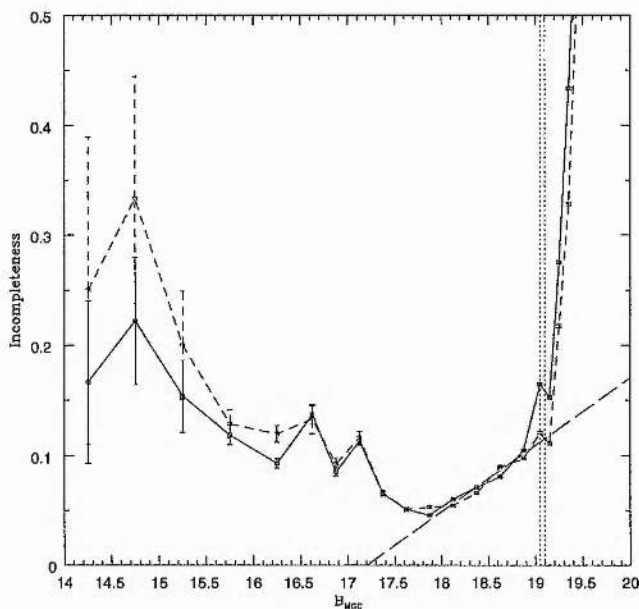


Figure 3.32: The variation of the incompleteness of the 2dFGRS with B_{MGC} . The solid line uses all galaxies to $b_{j,lim} = 19.3$ and the dotted line uses all galaxies to $b_{j,lim} = 19.35$. The vertical dashed lines show the limits at which the data can be believed for each case. The long dashed line represents the incompleteness. When extrapolated to the limit, the incompleteness at the limit is 14%.

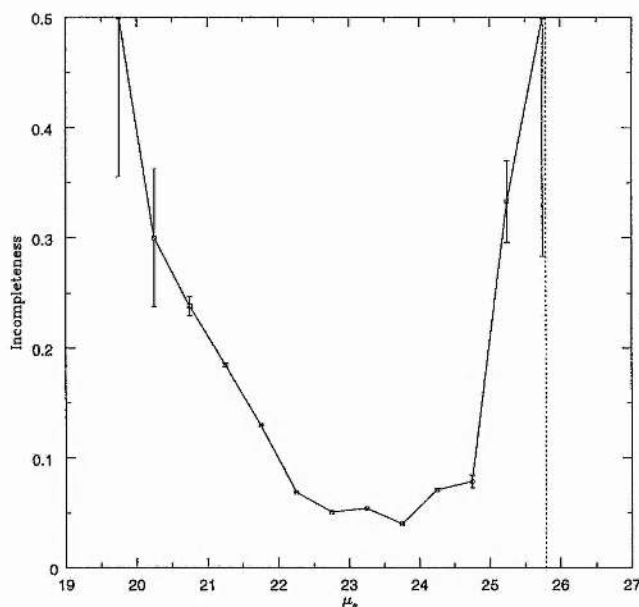


Figure 3.33: The variation of the incompleteness of the 2dFGRS with μ_e . The solid line uses all galaxies to $B_{MGC} = 19.0$. The vertical dashed line shows the effective surface brightness of an exponential galaxy when $\mu_0 = \mu_{lim} = 24.67 \text{ mag arcsec}^{-2}$.

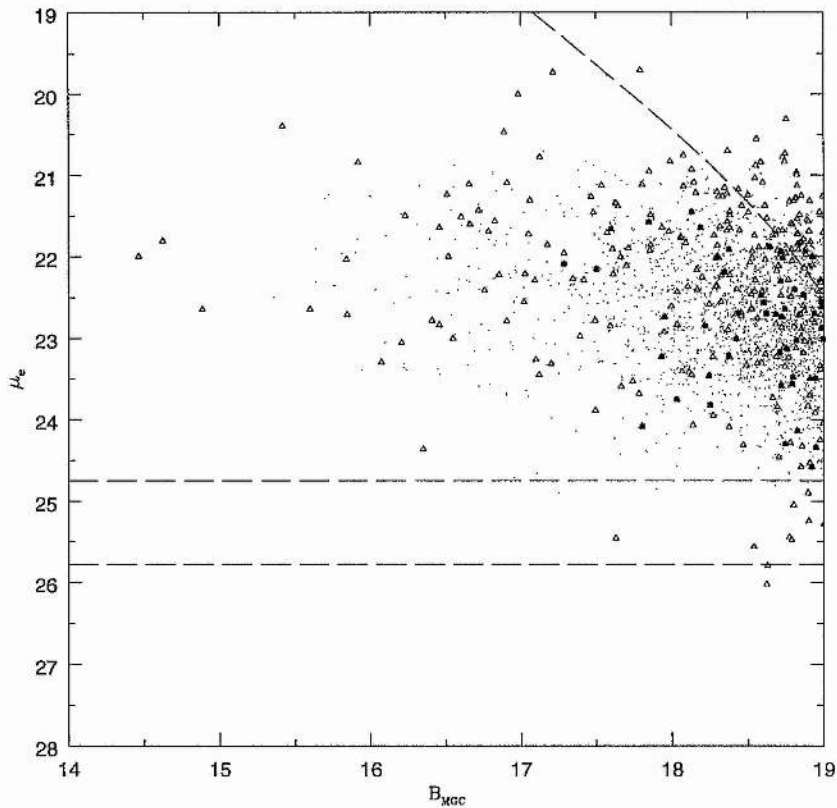


Figure 3.34: Plot of all galaxies $B_{MGC} \leq 19.0$ in the B_{MGC}, μ_e plane. The dots represent galaxies with 2dFGRS matches, the triangles represent those without matches and the squares represent those without matches which are the secondary components of 2dFGRS matches. The lower horizontal line represents the theoretical limit at which 2dFGRS galaxies can be seen. The upper horizontal line represents the limit at which a significant fraction of 2dFGRS galaxies are being missed. Objects below this line are probably missed because of their low surface brightness.

The curved line represents an exponential galaxy with a radius of $3.6''$. More compact objects were excluded because they were classified as stars - see Cross et al. (2001).

3.7.1 Types of Galaxy Missing from 2dFGRS

Fig. 3.34 shows all the galaxies $B_{MGC} \leq 19.0$ plotted in the B_{MGC}, μ_e plane.

The upper horizontal line represents the limit at which low surface brightness galaxies are being missed from the 2dFGRS and the lower horizontal line represents the limit at which they should theoretically be seen to. The percentage of missing galaxies that are LSBGs is $3.0 \pm 1.0\%$. The curved line represents the rough star-galaxy separation line. The curve is the locus of disk galaxies with $r_{iso} = 3.6''$ when $\mu_{lim} = 24.67$. The APM has a cut off in area corresponding to a radius of $3.6''$. $24.0 \pm 3.0\%$ of missing galaxies were missed due to the strict star-galaxy separation. The squares represent objects which are secondary components of 2dFGRS galaxies. These make up $16.3 \pm 2.4\%$ of missing galaxies.

The APM catalogue contains many objects that did not make the final 2dFGRS catalogue. The excluded objects included blended objects, unresolved objects and some normal galaxies.

After looking at these objects, it was discovered that $50.9 \pm 4.8\%$ of missing 2dFGRS objects were classed as blended, or were secondary objects matched to a 2dFGRS object, $24.7 \pm 3.0\%$ were unresolved, $21.1 \pm 2.8\%$ were normal galaxies and $3.0 \pm 1.0\%$ were LSBGs.

Pimblet et al. (2001) have also looked at the completeness of the APM by matching it to Las Campanas / AAT Rich Cluster Survey (LARCS) data for 4 Abell clusters. They found that 10-20% of galaxies were missing at all magnitudes, $b_j \leq 18.85$, with $\sim 20\%$ missing for $b_j < 17.0$. They find that $59 \pm 7\%$ of missing objects are blends, $23 \pm 4\%$ were unresolved galaxies, $11 \pm 3\%$ are normal galaxies and $7 \pm 2\%$ are LSBG. The Pimblet et al. (2001) figures compare well with those presented here for unresolved galaxies and blended galaxies, but not so well for normal galaxies and LSBGs. The differences could be due to the environmental difference - a cluster environment is a much denser environment and is likely to have more blended objects compared to normal galaxies. The denser environment of clusters could also explain why a larger fraction of objects are missing in the LARCS data. However, Pimblet et al. (2001) show that there is no increase in total fraction or blended fraction close to the cluster centres.

Pimblet et al. (2001) also ascertained why these galaxies are missed. While the blended and unresolved objects, and LSBGs are easily understood, those classified as normal are more difficult to understand. However, these objects have been classified as "stellar", "merged" or "noise" on the R-band plates.

3.8 Incompleteness of the SDSS-EDR

We have also made a preliminary test of the SDSS-EDR completeness. Unfortunately the masks for the SDSS-EDR which allow one to remove holes are not publicly available yet. Although we have removed obvious holes, the final incompleteness may be lower than the figures quoted below. However, the trends in magnitude and surface brightness should still be the same.

Fig 3.35 shows the photometric incompleteness of the SDSS-EDR as a function of B_{MGC} . The incompleteness is never greater than 7% at any magnitude. It is $\sim 5\%$ for $B_{MGC} < 17$, reaches a minimum of $\sim 1\%$ at $B_{MGC} = 18$ and then steadily rises to $\sim 3\%$ at $B_{MGC} = 20$.

Fig 3.36 shows the photometric incompleteness of the SDSS-EDR as a function of μ_e . The incompleteness is $\sim 2\%$ for $21.5 < \mu_e < 23.5$. It rises quite steeply when $\mu_e < 21.5$, due to unresolved galaxies and it rises rapidly when $\mu_e > 24.5$ due to LSBGs.

The SDSS-EDR suffers from similar incompleteness problems to the 2dF, but to a much lower extent. Whereas the overall incompleteness of the 2dFGRS is $\sim 8\%$ for $B_{MGC} < 19.0$, the overall incompleteness of the SDSS-EDR is $< 2\%$ over the same range.

3.9 Producing the MGC/2dFGRS/SDSS-EDR BBD.

3.9.1 The Photometric and Redshift Completeness.

In § 3.7 we showed the incompleteness of the 2dFGRS as a function of B_{MGC} and μ_e separately. In this section we will look at both the photometric and redshift completeness of the SDSS-EDR and the overall photometric and redshift completeness of the final catalogue as a function of both B_{MGC} and μ_e .

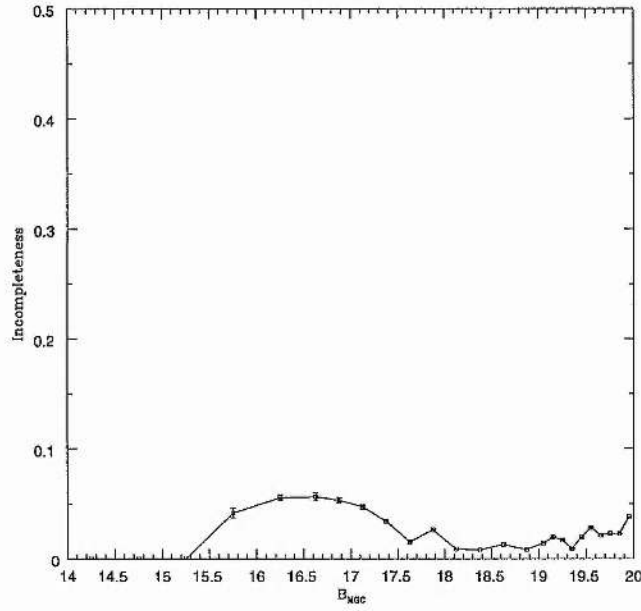


Figure 3.35: This figure shows the photometric incompleteness of the SDSS-EDR as a function of B_{MGC} . The axes are the same as Fig 3.32, so that it is easy to make a direct comparison.

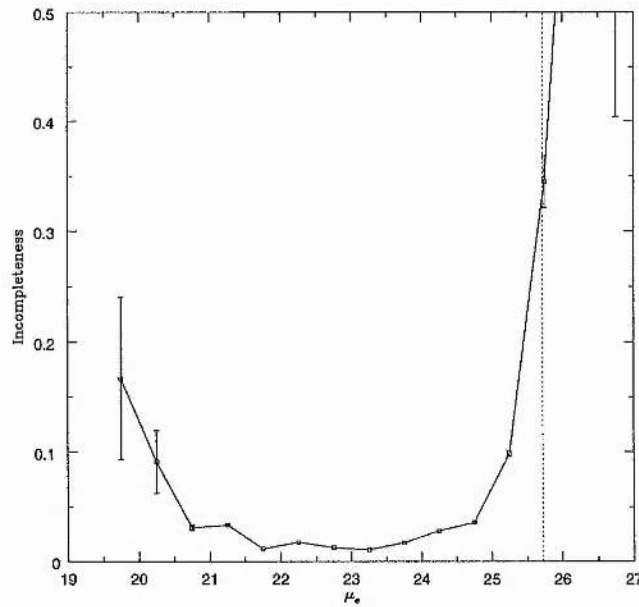


Figure 3.36: This figure shows the photometric incompleteness of the SDSS-EDR as a function of μ_e . This is shown to the same scale as Fig 3.33. The vertical line shows the isophotal detection threshold of the SDSS-EDR.

This is a necessary requirement to selecting a region of parameter space suitable for measuring the BBD. If a region has high photometric incompleteness, then many objects have been missed from the input catalogues, e.g. compact objects that are thought to be stars, LSBGs. We have no information about these objects and can only speculate on their importance to the overall luminosity and mass density. In regions where the photometric incompleteness is high, then the redshift incompleteness will also be high, but there can be additional regions where the photometric incompleteness is low, but the redshift incompleteness is high. This may be for a variety of reasons - low signal to noise in the spectrograph, or objects which are only found in clusters may be missed preferentially because of the minimum separation of fibres.

Thus a BBD will only be robust in regions where both the photometric and the redshift incompleteness are low. In regions where the redshift incompleteness is high, the question is: have the missing objects got the same redshift distribution as those objects with redshifts? This may be a plausible assumption, but objects with spectral lines close to sky lines may be missed preferentially, or objects with weak emission or absorption may be missed in preference to those objects with strong lines. Objects with different spectra may have different redshift distributions. If the photometric incompleteness is high, not only do we have these problems, but we also have to wonder if there is redshift or other bias in the missing objects. As shown in § 3.7.1, there are many blended objects and compact objects missing from the 2dFGRS. These may be preferentially missed from cluster environments where a lot of galaxies have a similar redshift. Thus the redshift distribution seen in that region of parameter space may be less clustered than the true redshift distribution.

Fig 3.37 shows the photometric completeness of the 2dFGRS as a function of both magnitude and surface brightness. There is high incompleteness $> 10\%$ for galaxies in the range $B_{MGC} < 16.5, 21.5 < \mu_e < 23.5$, in the range $B_{MGC} > 18.6$, in the range $\mu_e > 25.0$ and $\mu_e < 21.8, B_{MGC} > 16.0$. The statistically significant ranges are $B_{MGC} > 18.8, \mu_e < 21.8, B_{MGC} > 17.0$ and $\mu_e > 25.3$.

Fig 3.38 shows the photometric completeness of the SDSS-EDR as a function of both magnitude and surface brightness. There is high incompleteness $> 10\%$ for galaxies in the range $\mu_e > 24.8$ and $\mu_e > 23.0, B_{MGC} < 17.5$. There are several other points where the incompleteness rises above 10% , but the only place that the incompleteness is $> 10\%$ of statistical significance is $\mu_e > 25.0, B_{MGC} > 19.5$.

Both surveys appear to suffer from significant photometric incompleteness for $\mu_e > 25$. The surveys have put magnitude limits on the spectroscopic surveys. For the 2dFGRS the original limit was $b_j = 19.45$, but this has now become a variable, with plate number and dust correction. The analysis above showed that the limit for high completeness is $B_{MGC} \sim 18.8$. For the SDSS-EDR, the spectroscopic limit is $r^* = 18.2$ for most galaxies, with a QSO limit $r^* = 19.2$ and luminous red galaxy limit $z = 0.4$. The filter conversion equation is $B = g^* + 0.281(g^* - r^*) + 0.185$ which converts to $B_{MGC} = r^* + 1.281(g^* - r^*) + 0.185$. Using a typical $(g^* - r^*) = 0.7$, $B_{MGC,lim} = 19.2$ for the SDSS-EDR. However, the completeness may drop before this limit or after this limit due to the colours of objects and the higher limits of EROs and QSOs.

Therefore a sample has been selected covering the range $15 < B_{MGC} < 19.1$ and $\mu_e < 25.0$.

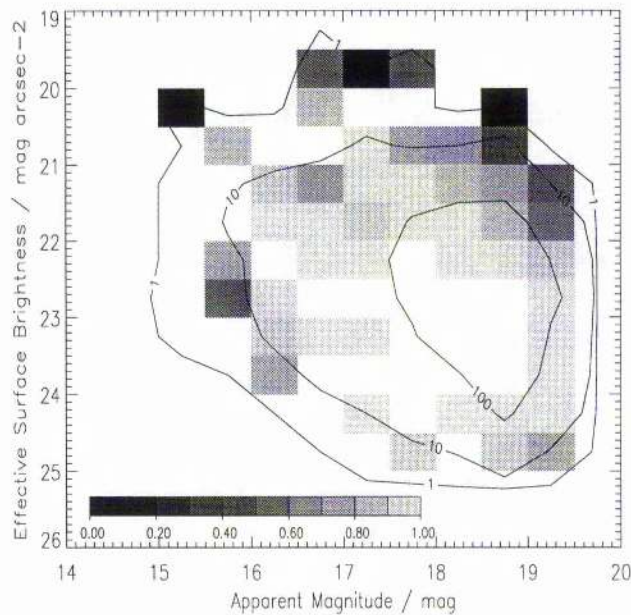


Figure 3.37: This figure shows the photometric completeness of the 2dFGRS as a greyscale plot in B_{MGC} and μ_e , where black is 0% complete and white is 100% complete. The contours represent the number of galaxies.

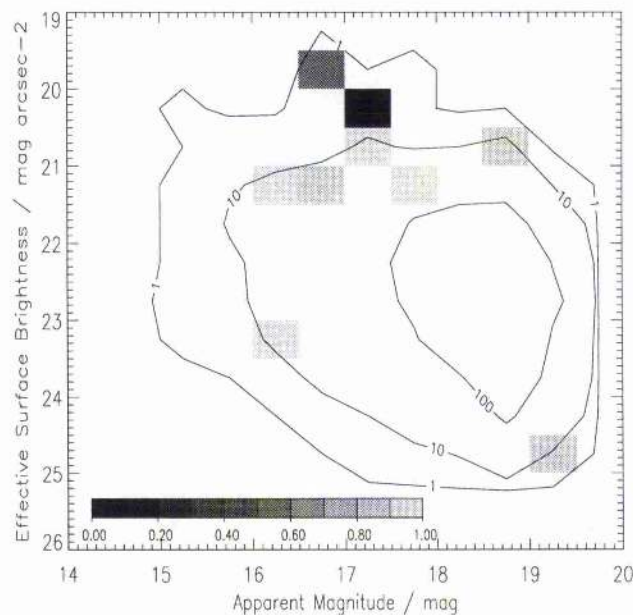


Figure 3.38: This figure shows the photometric completeness of the SDSS-EDR as a greyscale plot in B_{MGC} and μ_e , where black is 0% complete and white is 100% complete. The contours represent the number of galaxies.

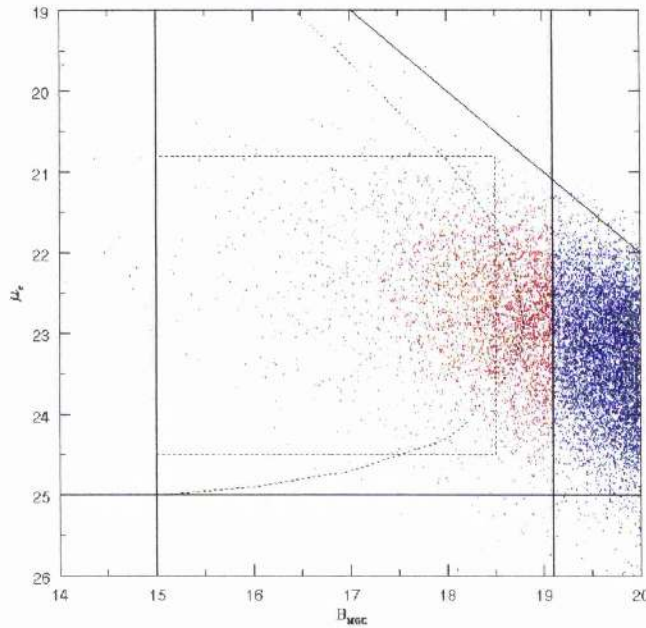


Figure 3.39: This figure shows the distribution of galaxies as a function of B_{MGC} and μ_e . The blue represents the full distribution of MGC galaxies. The red represents the distribution within the initial selected region for the completeness test. The solid lines represent the boundaries of this region. Within this region, there is very high photometric completeness for the combined surveys. They are at $B_{MGC} = 15.0$, $B_{MGC} = 19.1$, $\mu_e = 25.0$ and $r_e = 0.75$. The dotted curve represents the 90% redshift completeness boundary. The dotted horizontal and vertical lines define a region of high redshift completeness.

These limits are chosen to be slightly wider than the limits discussed above, as binning may be a problem. The $B_{MGC} < 19.1$ is just beyond the 2dFGRS limits discussed above, which constitute the majority of the redshifts. The $B_{MGC} < 15.0$ represents the saturation limit. Galaxies brighter than this do not have completely reliable magnitudes (see Liske et al. 2002). A further constraint is added: $r_e > 0.75''$. This is roughly equal to the star galaxy separation criteria. Fig 3.39 demonstrates these constraints.

The combined photometric completeness is even better as is demonstrated in Fig 3.40 where most of the region is over 90% complete.

Fig 3.41 shows the redshift completeness of the 2dFGRS and Fig 3.42 shows the combined redshift completeness of the 2dFGRS and SDSS-EDR. The extra galaxies from the SDSS-EDR increase the redshift completeness significantly, so that rather than just being a few patches where the completeness is greater than 90%, we have a well defined region.

The 90% contour has a pronounced curvature, suggesting that it is dominated by isophotal detection limits. The star-galaxy separation for the 2dFGRS appears to occur at an isophotal radius, $R_{iso} = 3.6''$. While the spectroscopic target selection is carried out using corrected magnitudes for the 2dFGRS, the redshift completeness will depend on adequate signal-to-noise in the spectra. The difference between Fig 3.37 and Fig 3.41 suggests that the signal-to-noise for LSBGs is not adequate. Estimating the isophotal limits for the spectra is not a simple task.

The 80% contour is broader as the SDSS-EDR comes into play. The star galaxy separation

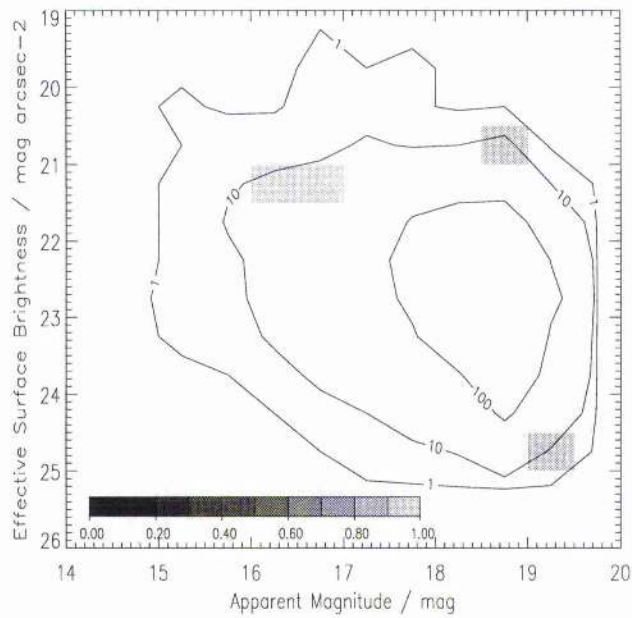


Figure 3.40: This figure shows the photometric completeness of the combined 2dFGRS and SDSS-EDR as a greyscale plot in B_{MGC} and μ_e , where black is 0% complete and white is 100% complete. The contours represent the number of galaxies.

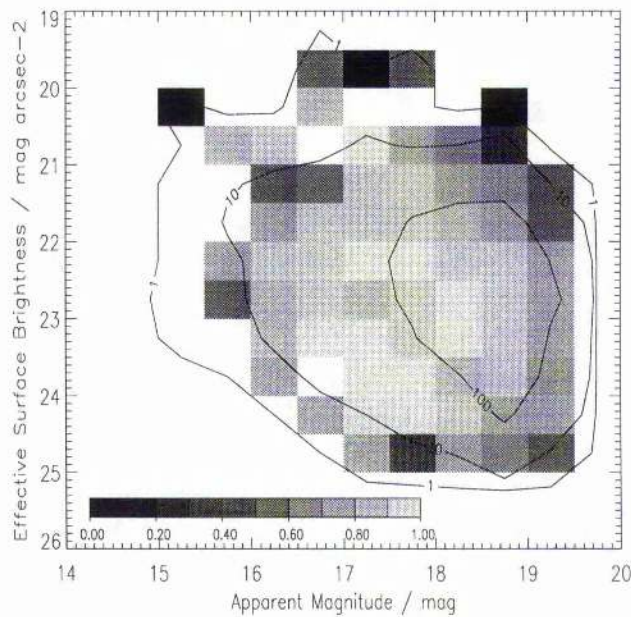


Figure 3.41: This figure shows the redshift completeness of the 2dFGRS as a greyscale plot in B_{MGC} and μ_e , where black is 0% complete and white is 100% complete. The contours represent the number of galaxies.

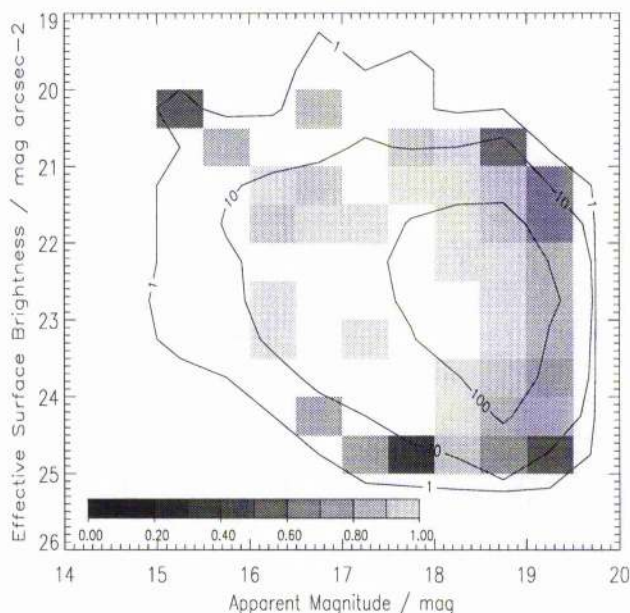


Figure 3.42: This figure shows the combined redshift completeness of the 2dFGRS and the SDSS-EDR as a greyscale plot in B_{MGC} and μ_e , where black is 0% complete and white is 100% complete. The contours represent the number of galaxies.

is not as tough for the SDSS-EDR, although the isophotal limit is shallower. It is possible to define some fairly square boundaries which contain most of the region with $> 80\%$ redshift completeness. These boundaries are $20.8 < \mu_e \leq 24.5$, $B_{MGC} \leq 18.5$, see Fig 3.39.

Beyond these boundaries it becomes increasingly difficult to determine the number density of galaxies.

3.10 Summary.

In this chapter we used a deep wide field CCD imaging survey, the MGC (Liske et al. 2002) to test the photometric accuracy and completeness of the 2dFGRS and SDSS-EDR. We then used a combined catalogue to define a region in B_{MGC}, μ_e parameter space where there is good photometric and redshift completeness.

The MGC is found to have a match for every 2dFGRS galaxy. When SExtractor could not find a match, as was the case for 4.4% of all 2dFGRS galaxies within the MGC CCDs, an object was observed on the images, and a good explanation was readily available. A small number of objects, 0.9%, were first thought to be missing, but were later discovered to be 2dFGRS eyeball rejects, missing from the Digitised Sky Survey (DSS) too, or were seen to be asteroids or other odd objects in the DSS.

However, 8.0% of the 2dFGRS galaxies were matched to more than one MGC object. This was almost certainly due to poor seeing on the nights that the UKST plates were taken. The combined magnitudes of these galaxies are closer to the magnitude of the 2dFGRS galaxy than each component. 7.3% of objects in the 2dFGRS were found to be stars or contain a stellar component. The stars have very poor photometry which is probably due to a combination of

poor dynamic range and non-linearities in photographic plates.

The overall photometry of the 2dFGRS was good, with $B_{MGC} - B_{2dF} = -0.078 \pm 0.157$. The plate-to-plate errors in the 2dFGRS were 0.0643mag, which showed evidence for systematic errors, although these were no greater than 0.1 mag. There is no significant scale error with magnitude, but there is a very significant scale error with surface brightness. High surface brightness objects have their fluxes significantly underestimated in the APM. This is the same problem that affects the stars.

The 2dFGRS has $8.2 \pm 0.5\%$ incompleteness to $B_{MGC} = 19.0$. When this is extrapolated to $b_j = 19.45$, we expect there to be 14% incompleteness at the limit. The missing galaxies can be split into four classes: LSBGs 3.0%; unresolved objects, 25%; blended objects, 51%, of which 16% of the total is made up of secondary components of matches; normal galaxies 21%. This is in line with the findings of Pimblet et al. (2001).

The SDSS-EDR has very good photometry, with a $\Delta m = -0.009 \pm 0.100$. There are no significant scale errors and the mean incompleteness is $< 2\%$.

When combined together, the MGC, 2dFGRS and SDSS-EDR provide a catalogue with ~ 11800 galaxies and ~ 5500 redshifts. While the photometric completeness of the combined 2dFGRS and SDSS-EDR input catalogues is extremely high $> 96\%$ when $B_{MGC} < 19.1, \mu_e < 25.0$, the redshift completeness has a much stronger variation with surface brightness. However, a region with good ($> 80\%$) redshift completeness and excellent ($> 96\%$) photometric completeness can be defined for future work.

In Chapter 4 we will use the measurements of photometric and redshift completeness to derive regions of M, μ_e space where we can measure accurate BBDs using the MGC photometric catalogue combined with 2dFGRS and SDSS-EDR redshifts.

Chapter 4

The MGC Bivariate Brightness Distribution.

In this Chapter, we use the MGC photometry along with 2dFGRS and SDSS-EDR redshifts to produce a Bivariate Brightness Distribution (BBD). In Chapter 3 we showed that the MGC photometry was excellent, and checked the completeness of the 2dFGRS and SDSS-EDR. In this chapter we select subsamples, taking into account completeness, star-galaxy separation and the photometric accuracy of the data. With better photometry and a better understanding of all the selection biases, we find galaxies at all the selection boundaries, apart from the bright, high surface brightness region of the BBD. This was not the case in § 2.6.3.

It proved possible to get a fit to the BBD using the analytic function of Choloniewski (1985). This gave a fit to the distribution with $M_B^* - 5 \log h = -19.48 \pm 0.10$, $\phi^* = (2.34 \pm 0.12) \times 10^{-2} h^3 \text{ Mpc}^{-3}$, $\alpha = -0.96 \pm 0.06$, $\beta_\mu = 0.168 \pm 0.12$, $\mu_e^* = 22.03 \pm 0.10 \text{ mag arcsec}^{-2}$ and $\sigma_\mu = 0.765 \pm 0.005$. This is a shallower and wider distribution than that found in Chapter 2. Good fits were found for the Schechter function to the luminosity function. The bright end is $0.075 \pm 0.025 \text{ mag}$ brighter than the 2dFGRS luminosity function (Norberg et al. 2002). The surface brightness function was found to be flat for $\mu_e > 21.5$.

4.1 Introduction

In this chapter we use the catalogue, prepared in § 3.6, to produce the BBD. This catalogue contains CCD imaging data from the Millennium Galaxy Catalogue (MGC), redshifts and spectral types from the Two-degree Galaxy Redshift Survey (2dFGRS) and colours and redshifts from the Sloan Digital Sky Survey Early Data Release (SDSS-EDR). It is important to take into account all the selection limits on the data, both imaging and spectroscopic. The imaging constraints come from the ability to detect objects, reliably determine their photometric properties and to correctly classify objects as stars or galaxies. The volume over which

a galaxy can be seen, and thus its detectability, is described by visibility theory (see Phillipps, Davies & Disney 1990 and § 2.4). In visibility theory one describes galaxies as a function of absolute magnitude M and effective surface brightness μ_e and places apparent magnitude and diameter constraints. The minimum half light radius and faint magnitude limits have tighter constraints from other factors such as star-galaxy separation and classification of morphological types, see Liske et al. (2002). Spectroscopic limits are often the determining factor on the magnitude limit, since the efficiency of spectrographs is much lower than imaging devices. This reduced throughput in the spectrograph also puts strong limits on the surface brightness of galaxies for which one can get reliable redshifts (Shectman et al. 1994, and § 3.9.1).

By taking into account all these limiting factors and using high quality imaging and spectroscopic data we have produced Bivariate Brightness Distributions and Luminosity Functions with the smallest systematic errors to date, so that random errors should be the dominant error. However, these limits severely reduce the numbers of galaxies in our samples so that it is not practical to measure the BBD of subsamples.

4.2 Producing the MGC BBD.

In § 3.6 we define the MGC bright catalogue, consisting of all MGC objects with $15 < B_{MGC} < 20$ mag. We have matched these objects to both the 2dFGRS and SDSS-EDR as described in Chapter 3. We now use the objects defined as galaxies in this catalogue to produce the BBD. The magnitudes, B_{MGC} , half-light radii r_e , redshifts z and spectral types are all defined in Chapter 3.

We begin by carefully defining the apparent limits of the data set using Fig 3.42 and the known limitations of the MGC data set. The MGC provides some hard limits: the isophotal limit $\mu_{lim,B} = 26.0$ mag arcsec⁻², and the minimum half light radius $r_e = 0.793''$, defined by the average star-galaxy separation, and $r_e = 15.8''$, defined by the size of the postage stamps (small 95×95 pixel images of each galaxy) used to calculate the half light radii.

However, only a very few galaxies (6) have maximum sizes which are greater than $r_e = 15.8''$, so the postage stamp size does not affect the distribution significantly. The sky subtraction process used by SExtractor limits the maximum object size at $\sim 20''$ when a local background is used, which is probably why so few galaxies are seen with $r_e > 15.8''$, within the magnitude limits of the selected sample.

A local background helps to reduce the problem of gradients in the background due to the CCD or other objects such as a bright star, but the local background can be increased by a low surface brightness galaxy (LSBG) such that this galaxy is missed or at least significantly underestimated in size and magnitude. The MGC uses the largest mesh available in SExtractor to measure the local background, a 256×256 pixel mesh, with a 7×7 median filter. An object with $r_e \gtrsim 20''$ would have half of its light spread across $\sim 40''$, which is equivalent to ~ 120 pixels since the pixel size is $0.333''$. This means that $\sim \frac{1}{4}$ of the background is overestimated, a significant amount. While it could be argued that the effect of a LSBG on the background will be small, it only needs a small change in the background to significantly effect the magnitude of an LSBG. Fortunately Figs 3.20 & 3.24 show that the difference in magnitude between the 2dFGRS and MGC and SDSS and MGC is negligible at the low surface brightness end. Both

surveys have independent background estimates, so it would appear that the error caused by the background is negligible. However, a more careful analysis of the background will form part of the future work to be undertaken. For now we will use $r_{e,max} = 15.8''$ as defined by the size of the postage stamps.

The other limits are defined by the completeness, as shown in Fig 3.42. We select two subsamples, one based roughly on the 80% completeness boundary, i.e all the bins have a completeness of 80% or higher and one based roughly on the 70% completeness boundary. The contours in Fig 3.42 have some dependence on the binning procedure and are only useful where there is a statistically significant result, so they are only used as a guide to where the completeness is high.

The first subsample is defined as objects with $15 \leq B_{MGC} \leq 18.5$, $20.8 < \mu_e^{app} < 24.5$ and the second is defined as objects with $15 \leq B_{MGC} \leq 19.0$, $21.0 < \mu_e^{app} < 24.5$. The first catalogue includes 2100 objects, with an overall 95% completeness and the second contains 3700 objects with an overall 92% completeness. The two catalogues are shown in Fig 4.1 with the corresponding selection limits. However, the redshift limits applied in § 4.2.1 reduce these numbers further.

As we discuss in § 3.2.2, MGC “best” magnitudes are closer to total magnitudes than isophotal magnitudes, and have only a small surface brightness dependence. The visibility calculations for total magnitudes, half-light radii and apparent surface brightness are outlined in § 2.4, see Eqns 2.34, 2.35 & 2.36.

4.2.1 The Distribution in the M, μ_e plane

Fig. 4.2 shows Fig. 4.1 with the axes converted to absolute parameter space using the conversions given in § 2.2. Galaxies in different regions of this figure are seen over differing volumes, because of Malmquist bias, hence it is not yet valid to compare the relative numbers in a magnitude limited catalogue. The perimeter of the shaded region is a constant volume line ($V = 5000 \text{Mpc}^3$) derived from visibility theory (Phillipps, Davies & Disney 1990, see § 2.4). The shading shows the region where the volume is less than 5000Mpc^3 and hence where we are insensitive to galaxy densities of $< 8 \times 10^{-3} \text{galaxies Mpc}^{-3} \text{mag}^{-1} (\text{mag arcsec}^{-2})^{-1}$. The equations used to calculate the lines are laid out in § 2.4. The parameters used in the visibility calculations are: $\mu_{lim} = 26.00 \text{ mag arcsec}^{-2}$; $r_{e,min} = 0.793''$, $r_{e,max} = 15.8''$, $m_{bright} = 15.00 \text{ mag}$; $m_{faint} = 18.5 \text{ mag}$; $z_{min} = 0.04$; and $z_{max} = 0.11$, for the 1st subsample. The redshift limits are set so that $N_{clus} N_z$ is maximised, where N_{clus} is the number of galaxies in the volume limited sample used to calculate the clustering correction, see § 2.6.1 and N_z is the total number of galaxies with redshifts.

One important difference between the subsamples selected here, and the subsample selected in Chapter 2 (and Cross et al. 2001) is the luminous, low surface brightness region of Fig 4.2 cf. Fig 2.6. In Fig 2.6 there is a clear gap between the data and the selection limits, suggesting that there are very few luminous, low surface brightness galaxies. In Fig 4.2 there is data up to the selection limits, suggesting that luminous low surface brightness galaxies may be more common than appreciated, because of the difficulties involved in measuring the sizes of large galaxies.

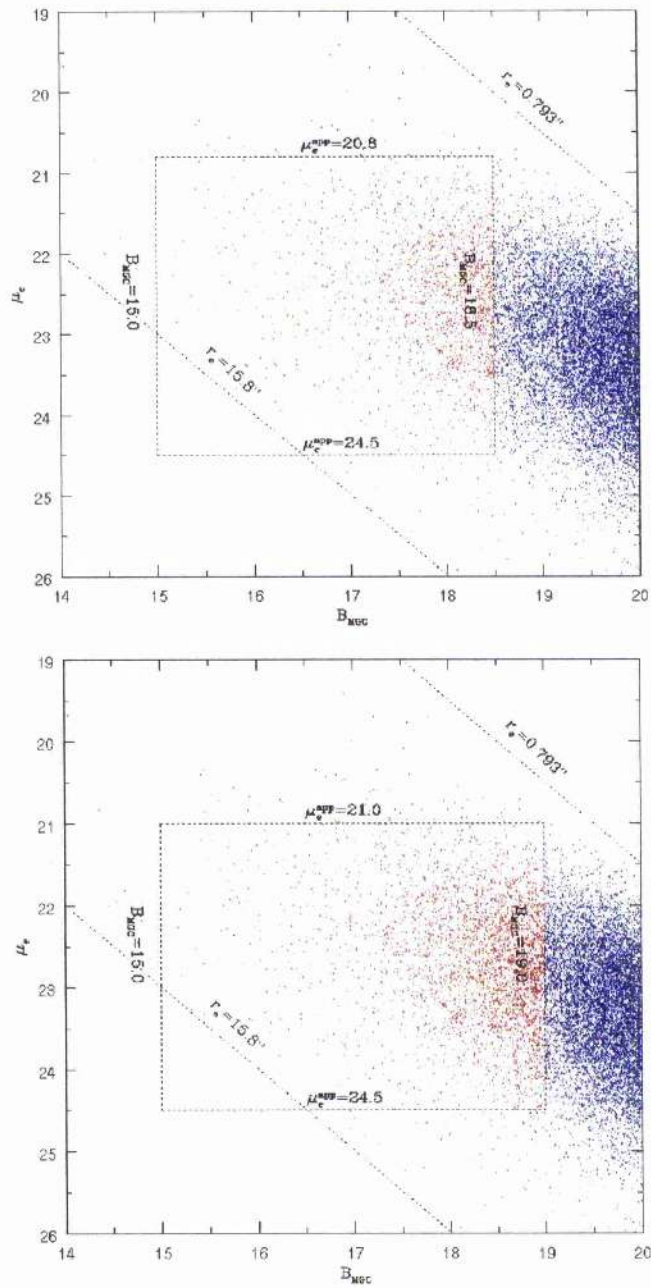


Figure 4.1: This figure shows the distribution of the 2 carefully selected subsamples of MGC galaxies in B_{MGC} and μ_e . The dotted lines represent the selection limits for subsample 1 (upper plot) and subsample 2 (lower plot). The data, marked in red within these limits are the two subsamples. In subsample 1, the data is $\geq 80\%$ complete for all values of B_{MGC} and μ_e . In subsample 2, the data is $\geq 70\%$ complete for all values of B_{MGC} and μ_e .

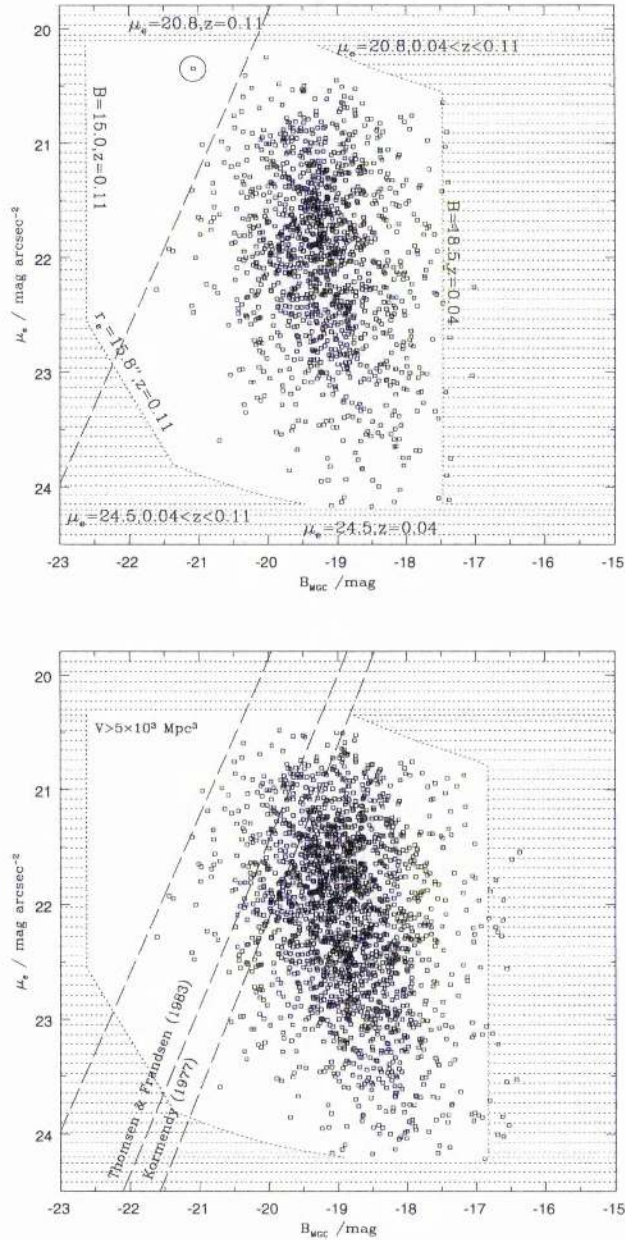


Figure 4.2: This figure shows the distribution of the two carefully selected subsamples of MGC galaxies in M and μ_e . The shaded region represents the region where the volume is less than 5000 Mpc^3 . Notice that there is data right up to the selection boundaries, apart from at the bright end. The top plot highlights the selection boundaries for the first subsample, and the second plot shows the best fit line to the distribution of ellipticals seen in Kormendy (1977) and Thomsen & Frandsen (1983). The dashed line marking the edge of the data set in both cases is roughly parallel to the elliptical galaxy distribution, and is likely to be a real physical boundary rather than a missed selection effect. The galaxy in subsample 1 marked by the circle is MGC02897, an elliptical galaxy with faint streams of stars projecting from it. The authors speculate that this galaxy, well beyond the dashed line, has recently undergone a major merger resulting in massive star formation. However, follow up work will be needed to support this speculation.

The reasons for the difference between the data in these two figures and Fig 2.6 are an improved understanding of the selection boundaries and improved photometry. The 2dFGRS was not specifically designed for measuring the BBD, so the boundary conditions in Chapter 2 could not be defined as well as these boundary conditions. The measurements of the total magnitude and effective surface brightness are also more robust. Instead of fitting a face-on exponential profile to the galaxy, § 2.5, which depends on knowing the isophotal limit (this varies slightly from plate to plate in the 2dFGRS and is therefore not well defined), the half light radii were measured directly from the data and are corrected for inclination (see § 3.2.2). Assuming a face on exponential profile is clearly wrong for elliptical galaxies, and can give errors in both the magnitude ~ 0.1 mag and the effective surface brightness ~ 0.55 mag arcsec $^{-2}$, see Cross & Driver (2001).

Fig 4.2 shows that there is a straight edge to the galaxies at the bright high surface brightness end of the distribution. This line is described by Eqn 4.1.

$$M = (-0.73 \pm 0.1)\mu_e - (5.5 \pm 1.5) \quad (4.1)$$

This is similar to the relationship seen between μ_e and r_e for elliptical galaxies by (Kormendy 1977) and Thomsen & Frandsen (1983). When converted to M and μ_e their relationships become:

$$\begin{aligned} M &= -0.66\mu_e - 5.4 \\ M &= -0.69\mu_e - 5.2 \end{aligned} \quad (4.2)$$

These lines are plotted on Fig 4.2 and have the same gradient, but are offset by 1.25 mag & 1.75 mag respectively. The offset will depend primarily on the selection limits of the Kormendy and Thomsen & Frandsen datasets. Eqn 4.1 may describe an unknown selection line or some aspect of the physics of galaxy formation, such as the accretion time scale of galaxies. The top plot of Fig 4.2 shows a galaxy at $M = -21.08$, $\mu_e = 20.35$, ~ 0.75 mag brighter than the line described by Eqn 4.1. This galaxy is marked by a circle. The models of Larson & Tinsley (1978) imply that galaxies should brighten by 0.75 mag when a starburst takes place after a major merger. On closer inspection it appears to be a bulge dominated galaxy with loops of gas or stars coming off the sides, see Fig 4.3. This galaxy has $\eta = -2.815$ (Type 1) and $g' - r' = 0.751$ ($(B - V) = 0.93$). The spectral type marks it as an elliptical galaxy and the $u' - g'$ versus $g' - r'$ colours are typical of η -type 1 galaxies or elliptical galaxies, see Fig 4.4. Although the image suggests that this is an odd galaxy, and the position in the M , μ_e plane suggests this is a merger remnant, the spectral type and colours do not. More information is needed before this galaxy can be classified as unusual.

Considering the position and possible nature of MGC02897 and the fact that Kormendy (1977) and Thomsen & Frandsen (1983) both get similar results with independent datasets, with different selection limits, it seems unlikely that Eqn 4.1 is an unknown selection line. Instead it seems more likely that this line represents a real physical limit.

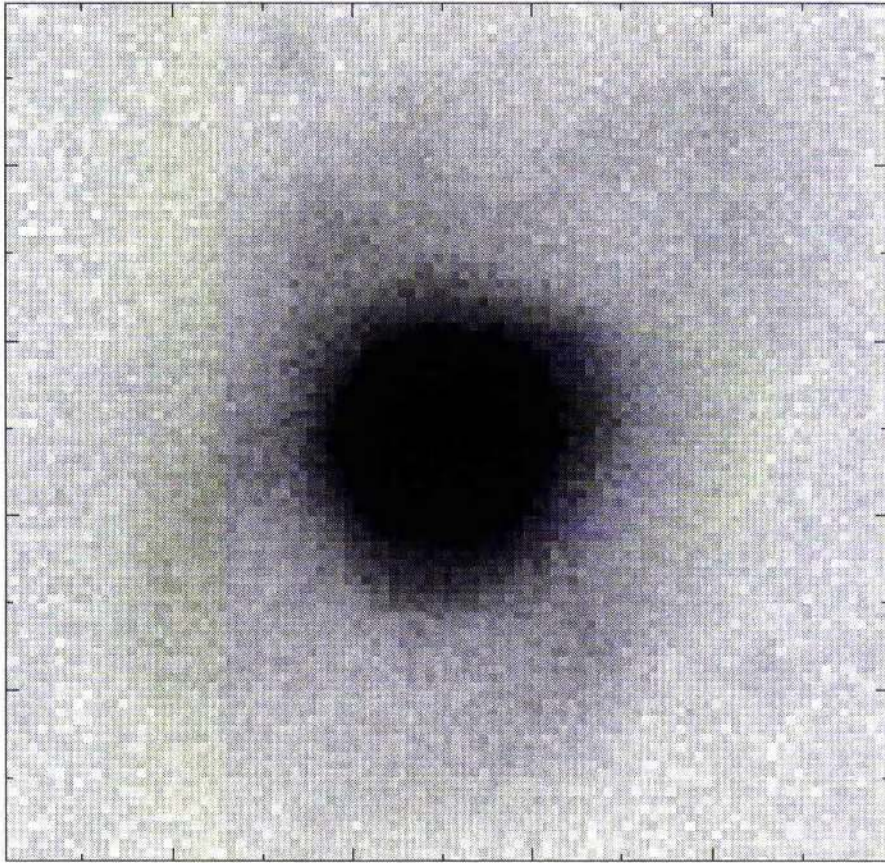


Figure 4.3: MGC02897 is situated in an unusual position in the Bivariate Brightness Distribution. It is extremely bright and high surface brightness. It was picked up because it was clearly beyond a line of bright high surface brightness galaxies which may indicate unknown selection effects, or some of the physics behind the BBD. This galaxy shows clear signs of a major merger, which would be likely to put it beyond the normal limits of passively evolving galaxies.

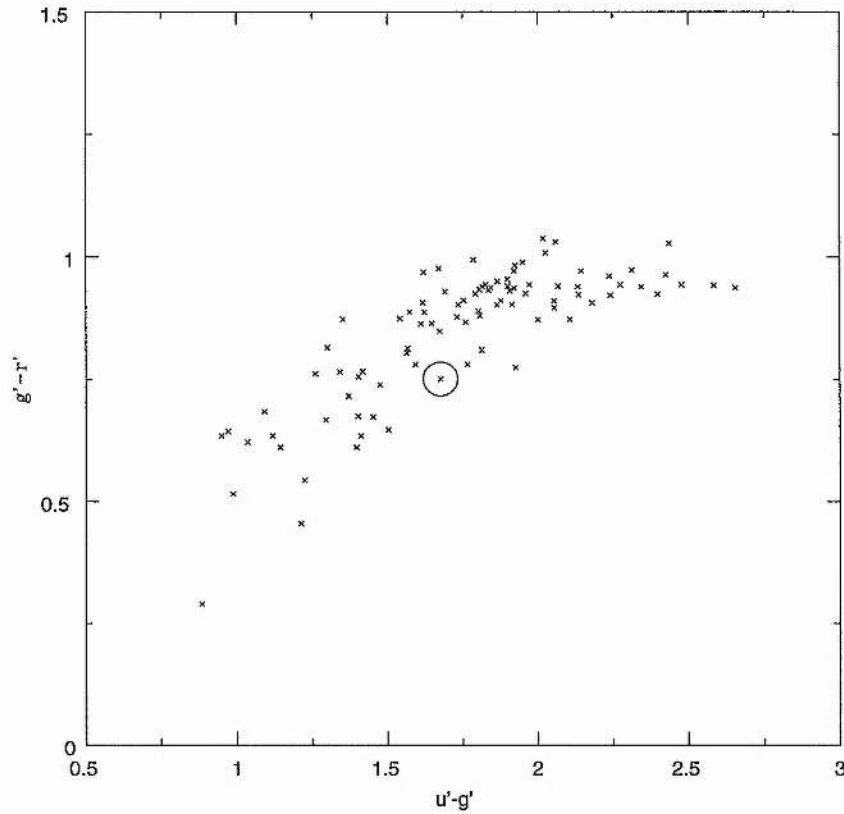


Figure 4.4: This plot shows the colours of η -type 1 galaxies in subsample 1. The position of MGC02897, $M = -21.08$, $z = 0.0965$ is marked by a blue circle. These galaxies were chosen to have a small redshift range ($0.09 < z < 0.10$), so that the colours could be compared. They were also selected to have $B_{MGC} < 18$, equivalent to $M_{B_{MGC}} < -19.5$ at $z = 0.095$, so that only bright η -type 1s - giant elliptical and lenticular galaxies would be compared. MGC02897 has typical colours for an η -type 1 at $z = 0.0965$, although it has a low value of $g' - r'$ for the particular $u' - g'$.

When we measure the BBD using the stepwise maximum likelihood (SWML) method, see § 2.6.2, we use the same subsamples, except that we can widen the redshift limits. In the previous section, the redshift limits were very important in getting the best statistics for the clustering correction as well as the overall BBD. However the clustering correction in SWML does not need a volume limited subsample between the full limits of the dataset. Therefore we do not have to limit the redshift range, as we do when we use the empirical method. We use a minimum redshift limit of $z = 0.01$ to avoid galaxies with significant peculiar velocities and a maximum redshift of $z = 0.2$ since there are no η values beyond this redshift. Since random velocities of galaxies are of the order of 100s kms^{-1} , a limit of $z = 0.01$ will only contain galaxies with a maximum 10% contribution from the peculiar velocity. This allows us to sample a larger region of parameter space, and more importantly get better statistics for bins where we already have numbers, especially at the faint end.

The distribution of galaxies with the new selection boundaries is shown in Fig 4.5. Again there is data right up to the selection boundary except at the bright, high surface brightness end. What is particularly interesting are the galaxies brightwards of the dashed line. Like MGC02897, they appear to be bright ellipticals. Several appear to have streams of stars or have very close companions, see Fig 4.6, suggesting that these may be undergoing mergers. At $M = -21, \mu_e = 20.25$, the centre of this distribution, the volume over which galaxies are seen using the redshift limits of the sample in Fig 4.2 defined by the needs of empirical method is $V = 33,000\text{Mpc}^3$. Using the redshift limits of the SWML method, $V = 400,000\text{Mpc}^3$, thus the increase in numbers of galaxies occupying this parameter space is due to a simple increase in volume. These galaxies are exceedingly rare, the number density $\phi(M, \mu) \sim 2.5 \times 10^{-5} h^3$ galaxies Mpc^{-3} .

In Fig 4.7 we display a selection of galaxies from the MGC, positioned in the correct places in the M, μ_e plane. The brightest galaxies are ~ 1500 times brighter than the faintest galaxies, and the effective surface brightnesses cover a dynamic range of 100. There is a big contrast in the morphologies of the galaxies across the BBD. Bright low surface brightness galaxies are predominantly spirals whereas the bright high surface brightness galaxies are predominantly ellipticals. At the faint end, this still appears to be true, but very little structure can be seen, due to the poor resolution.

4.3 The MGC BBD

The methods outlined in § 2.6.1 and § 2.6.2 were used to calculate the BBD for the two datasets. The arrays $O(M, \mu)$, $I(M, \mu)$, $V(M, \mu)$ and $W(M, \mu)$, representing the distribution of observed galaxies with redshifts, the incompleteness distribution, the volume over which these galaxies can be seen and the weight of each bin due to inhomogeneities (see § 2.6.1), are calculated via the empirical method and displayed in Figs 4.8 & 4.9 for subsamples 1 and 2, respectively. These arrays are displayed in the top left, top right, bottom left and bottom right as both surface and contour plots, respectively. Note that bins containing fewer than 10 galaxies are not shaded.

Compared to $O(M, \mu)$, $I(M, \mu)$ is biased towards both high surface brightness galaxies due to the strict star-galaxy separation in the 2dFGRS and low surface brightness galaxies due to

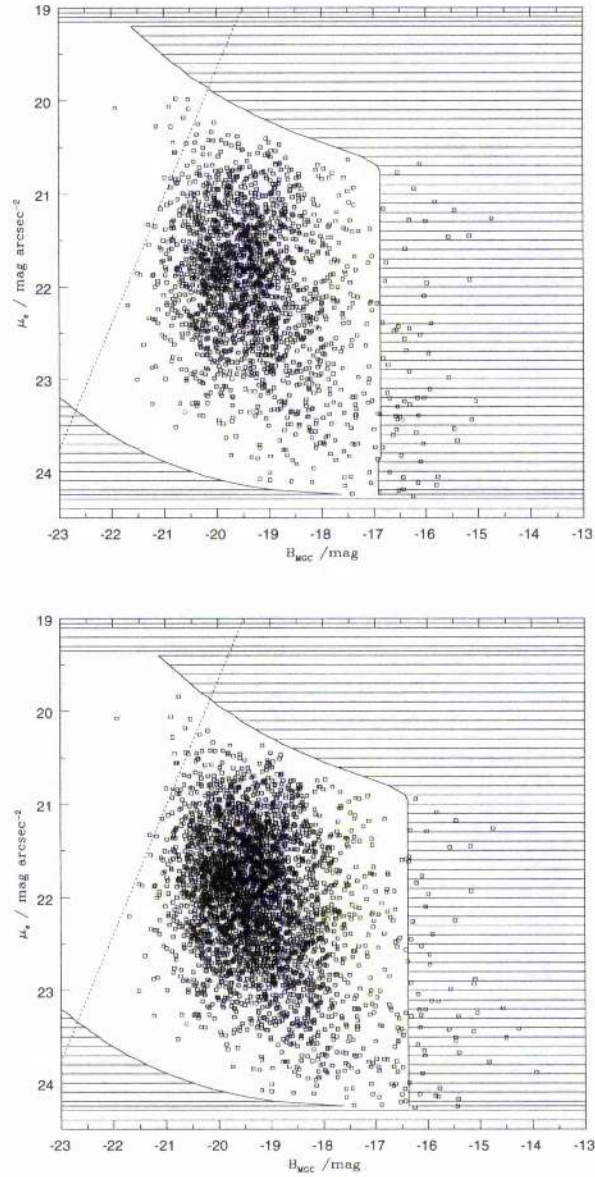


Figure 4.5: This plot shows the data from dataset 1 (upper panel) and dataset 2 (lower panel) used to produce the BBDs via the SWML method. The only differences between these plots and those in Fig 4.2 are the redshift limits. The redshift limits in this diagram are $z_{\min} = 0.01$ and $z_{\max} = 0.2$. These are applied to both the selection limits and the data.

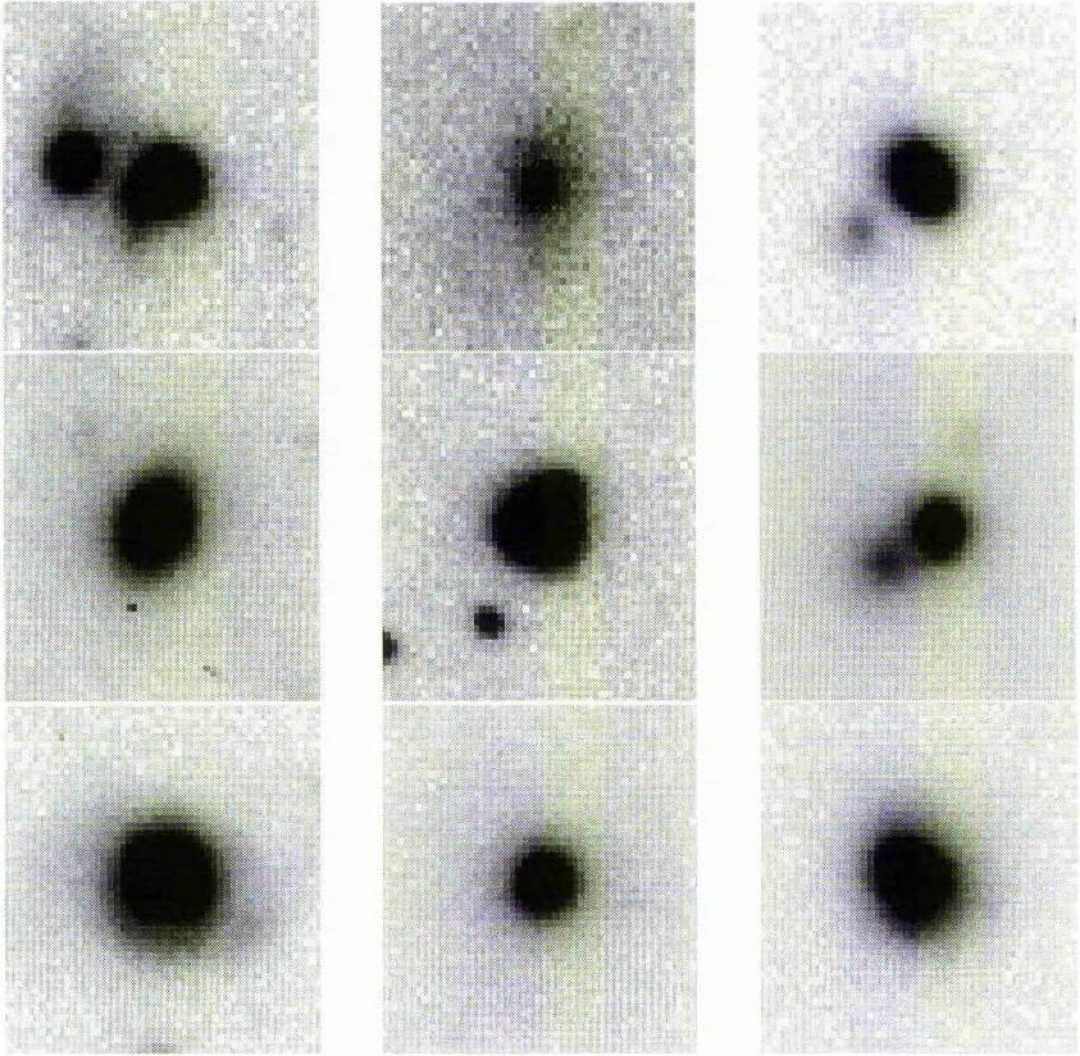


Figure 4.6: This plot shows 9 bright HSBGs which are thought to be undergoing mergers. Several have close companions (top left, top right, central, centre right), or tidal streams (top left, top centre, bottom left). However, the centre left, bottom centre and bottom right galaxies appear to be normal ellipticals.

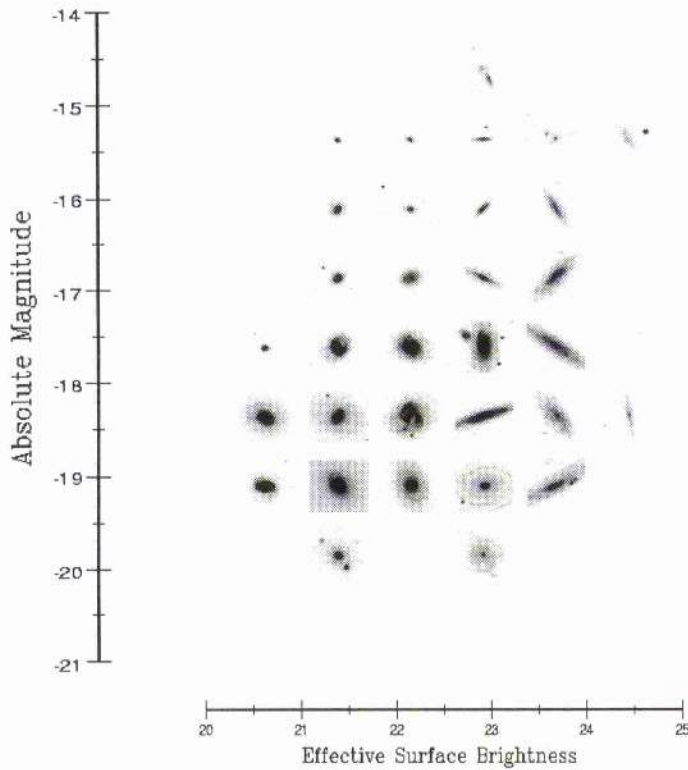


Figure 4.7: We demonstrate the BBD using 32 galaxies selected from the MGC. The top row of galaxies have $M_B \sim -14$ mag, with each row increasing in brightness by 1.0 mag until the bottom row have $M_B \sim -21$ mag. The left hand column galaxies are high surface brightness galaxies $\mu_e \sim 20.0$ mag arcsec $^{-2}$. Each column becomes fainter in surface brightness by 1.0 mag arcsec $^{-2}$ until the right hand column which has $\mu_e \sim 25.0$ mag arcsec $^{-2}$. Each galaxy is shown between the 22 mag arcsec $^{-2}$ and 26 mag arcsec $^{-2}$ isophote. Since no redshift range spans the whole distribution, we have selected galaxies in 4 redshift ranges. The faintest galaxies all have redshifts $0.017 < z < 0.023$, the faint-medium galaxies have $0.027 < z < 0.033$, the medium-bright galaxies have $0.047 < z < 0.053$, and the brightest galaxies have $0.097 < z < 0.103$. Therefore the brightest galaxies appear fainter in comparison to the faintest galaxies than they are in reality. There are gaps where we did not have any galaxy with the correct intrinsic parameters within these redshift ranges.

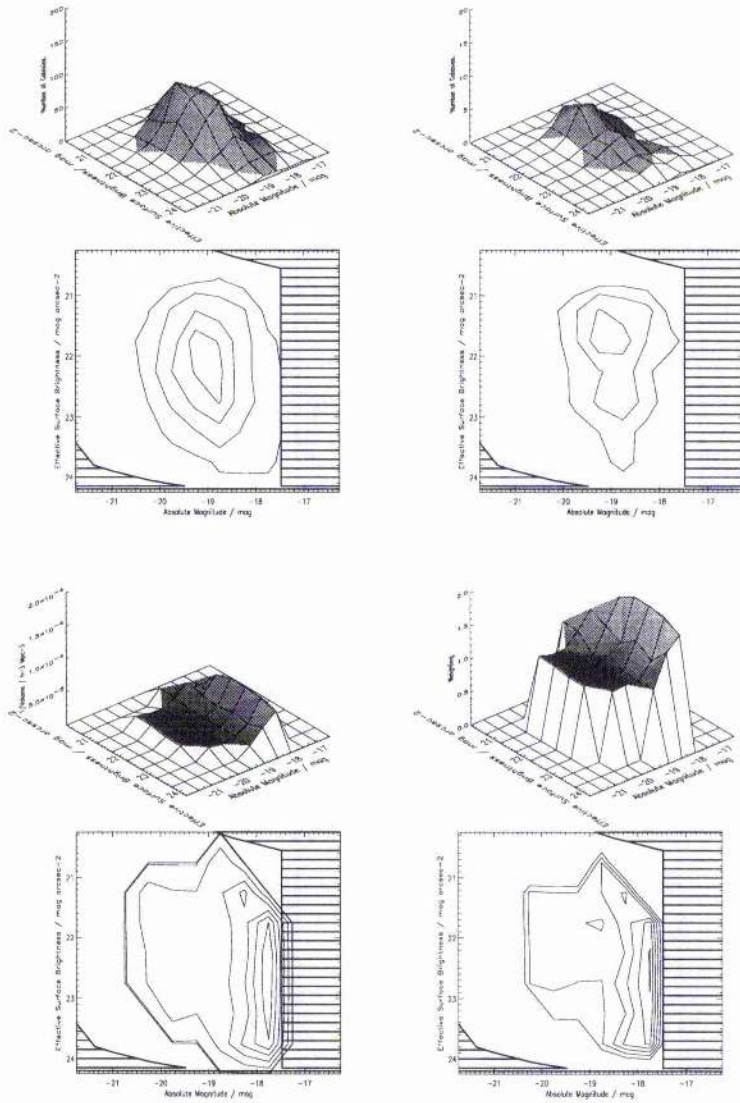


Figure 4.8: The arrays $O(M, \mu)$, $I(M, \mu)$, $\frac{1}{V(M, \mu)}$ and $W(M, \mu)$ for subsample 1. These are displayed in the top left, top right, bottom left and bottom right, respectively. The shading on the contour plots represents parameter space where $V < 5000 \text{ Mpc}^3$.

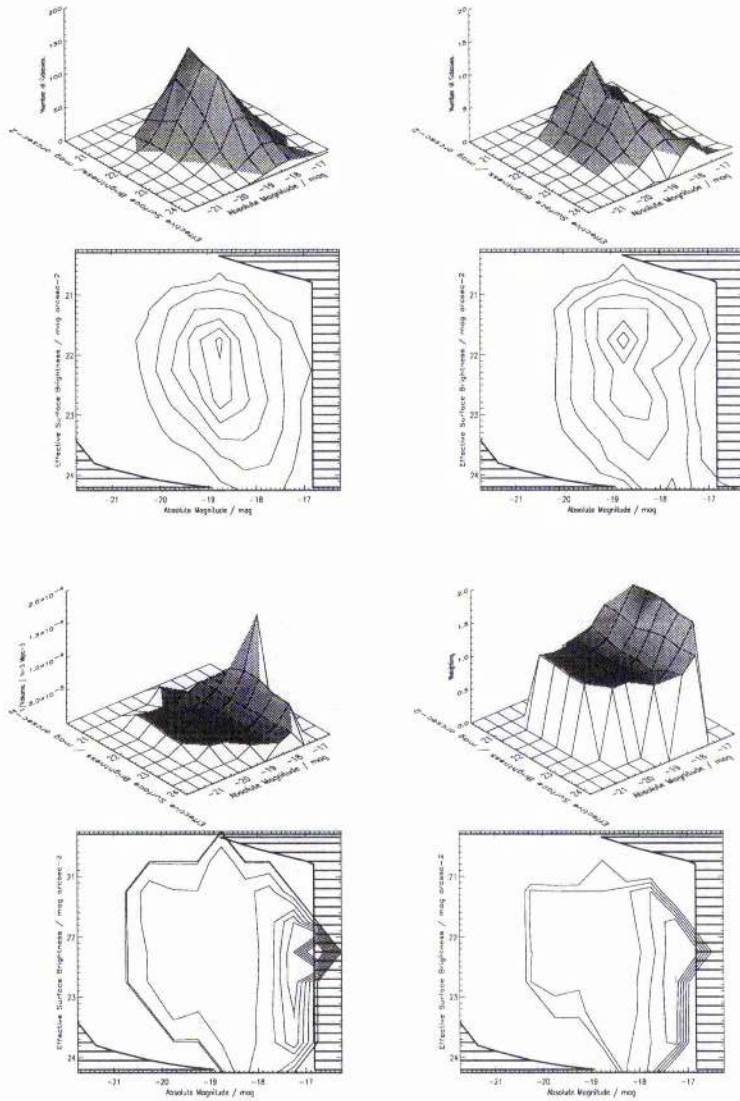


Figure 4.9: The arrays $O(M, \mu)$, $I(M, \mu)$, $\frac{1}{V(M, \mu)}$ and $W(M, \mu)$ for subsample 2. These are displayed in the top left, top right, bottom left and bottom right, respectively. The shading on the contour plots represents parameter space where $V < 5000 \text{Mpc}^3$.

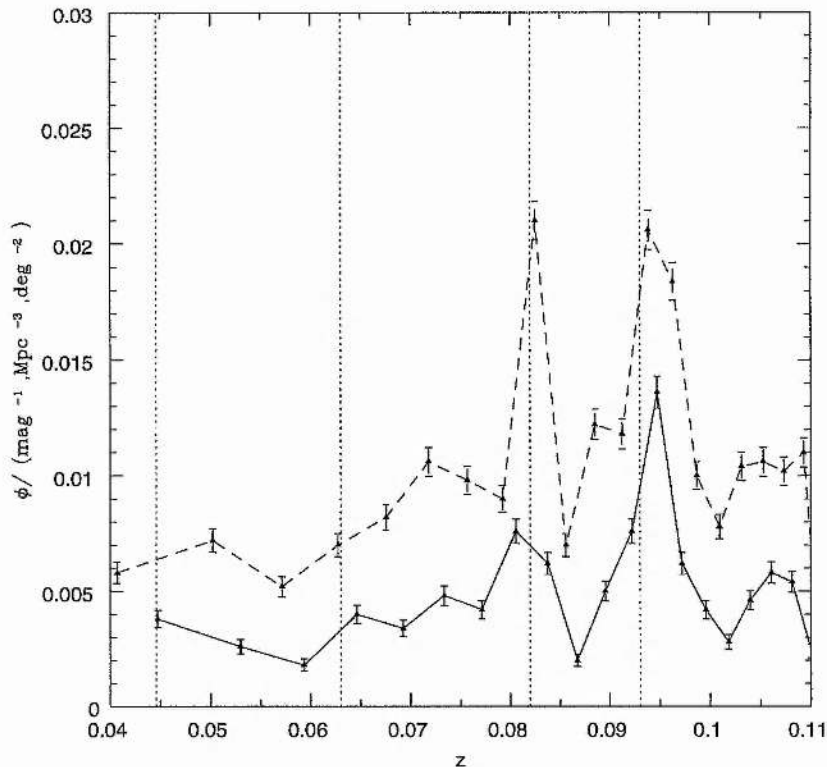


Figure 4.10: The clustering map. This shows the number density of giant galaxies as a function of redshift for the two subsamples. The points are spaced equally in volume at intervals of $5000 \text{ h}^3 \text{ Mpc}^3$ starting at $10000 \text{ h}^3 \text{ Mpc}^3$. The solid line shows dataset 1, and the dashed line shows dataset 2. The volume limited subsample from dataset 1 used to produce this plot is at brighter absolute magnitudes than the volume limited subsample from dataset 2 and therefore has a lower average space density. Known clusters within the MGC region are marked with vertical dotted lines. The two largest show up well at $z = 0.082$ (RXJ 13 20.3 +00 13 10) and $z = 0.093$ (Abell 0954), but [AT2 98] C010 ($z = 0.063$) and Abell 0912 ($z = 0.0446$) are not so obvious.

the detection limits of the spectrographs, particularly the 2dF (see § 3.9.1).

The $\frac{1}{V(M, \mu)}$ is flat-bottomed due to the cutoff at z_{max} , although $V(M, \mu)$ is slightly reduced for the very brightest bins as the bright magnitude and maximum half light radius increase the value of z_{min} . $V(M, \mu)$ shows a strong dependency upon magnitude (i.e. classical Malmquist bias as expected) but very little or no dependence on surface brightness. This indicates that the MGC magnitudes have very little surface brightness dependence, and that the completeness of the MGC is not significantly effected by surface brightness. It is worth comparing these plots to Fig 2.7, where there was an obvious surface brightness dependence in $V(M, \mu)$ which had the same curvature as the visibility curve.

Fig 4.10 shows that clustering is severe with a factor of ~ 5 variation in density between the low density and high density regions. For instance, there appears to be strong clustering at $z = 0.095$. In Fig 3.25 there is a large cluster at $z \sim 0.093$ and at R.A. 10h13m; this is Abell 0954. A reliable measure of the BBD needs to correct for this clustering-bias. Here we adopt

a strategy which implicitly assumes, firstly, that clustering is independent of either M or μ , and secondly, that evolutionary processes to $z = 0.11$ are negligible. Fig 4.10 does not have any overall gradient which would suggest evolution or an error in the cosmology. However, there is a sharp increase in $W(M, \mu)$ when $M > -18.5$ and $M > -18.0$ for subsamples 1 and 2 respectively. These absolute magnitudes correspond to galaxies at $z = 0.08$ and at the apparent limits of each subsample, so galaxies with an absolute magnitude brighter than $M > -18.5$ or $M > -18.0$ are seen in the clusters at $z = 0.082$ and galaxies with an absolute magnitude brighter than $M > -18.5$ or $M > -18.0$ are not.

Producing the Stepwise Maximum Likelihood BBD.

It is important to fully understand the selection limits when using SWML, see § 2.6.2, because they are necessary to calculate H_{ijk} at each point. In the empirical method the volumes are calculated using the data, so any selection limits are automatically taken into account. The lower value of z_{min} lets us probe further into the faint end of the galaxy distribution, $M < -16.9$ and $M < -16.4$ in comparison to $M < -17.4$ and $M < -16.8$ for the empirical method.

Figs 4.11 shows the redshift incompleteness function, $1 - C_z(M, \mu_e)$ where C_z is defined as the number of galaxies with redshifts divided by the total number of galaxies, see § 2.6.2, for each subsample. There is high incompleteness amongst both the high and low surface brightness galaxies, but little variation with absolute magnitude.

Normalisation.

The BBDs are normalised by fitting the luminosity function found by summing the BBD in surface brightness to the number counts (Liske et al. 2002). The number counts are calculated using $K + e = 2.5z + 2.5 \log(1 + z)^{0.75}$, which gives similar results to the Norberg et al. (2002) (K+e) correction, but gives more realistic results beyond $z = 0.3$.

In Norberg et al. (2002) the SDSS-EDR, which overlaps with the MGC was shown to be overdense by $\sim 5\%$. In Liske et al. (2002), a similar comparison has shown that the MGC is indeed over dense by $\sim 5\%$ compared to the overall 2dF number counts. This is taken into consideration when normalising the BBD.

4.4 The Space Density of Galaxies

Finally we can combine the four arrays, $O(M, \mu)$, $I(M, \mu)$, $V(M, \mu)$ and $W(M, \mu)$, to generate the 2dFGRS bivariate brightness distribution, $\phi(M, \mu)$, see Eqn 2.40. This is shown in the top-left hand plot of Figs 4.12 & 4.13. This depicts the underlying local galaxy number-density distribution inclusive of surface brightness selection effects. Only those bins which contain 10 or more galaxies are shown. The top right plots show the errors for this BBD as determined using Eqn 2.45.

The bottom left plots on Figs 4.12 & 4.13 are the number densities calculated using the SWML method. The bottom right plots show the errors for this BBD as determined in Eqn 2.45.

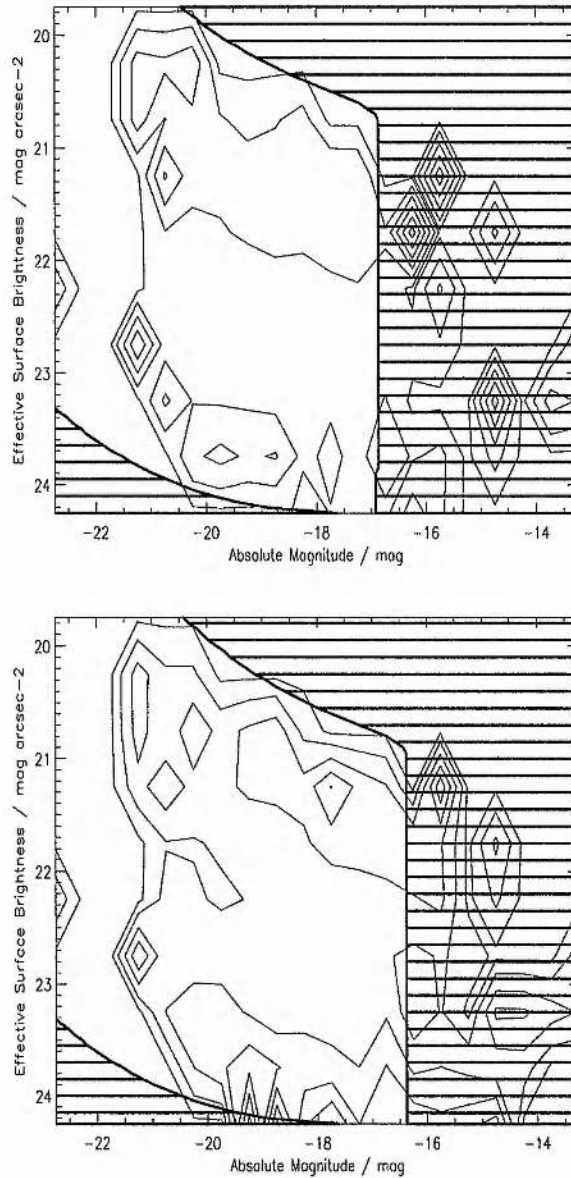


Figure 4.11: This plot shows the array $1 - C_z(M, \mu_e)$ for dataset 1 (upper panel) and dataset 2 (lower panel) used to produce the SWML BBD. The contour lines are set at 0.01, 0.05, 0.10, 0.15, 0.20 and 0.25. There is high incompleteness at high surface brightness (due to the star-galaxy separation) and low surface brightness (due to the capabilities of the spectrograph). There is very little variation in incompleteness with absolute magnitude.

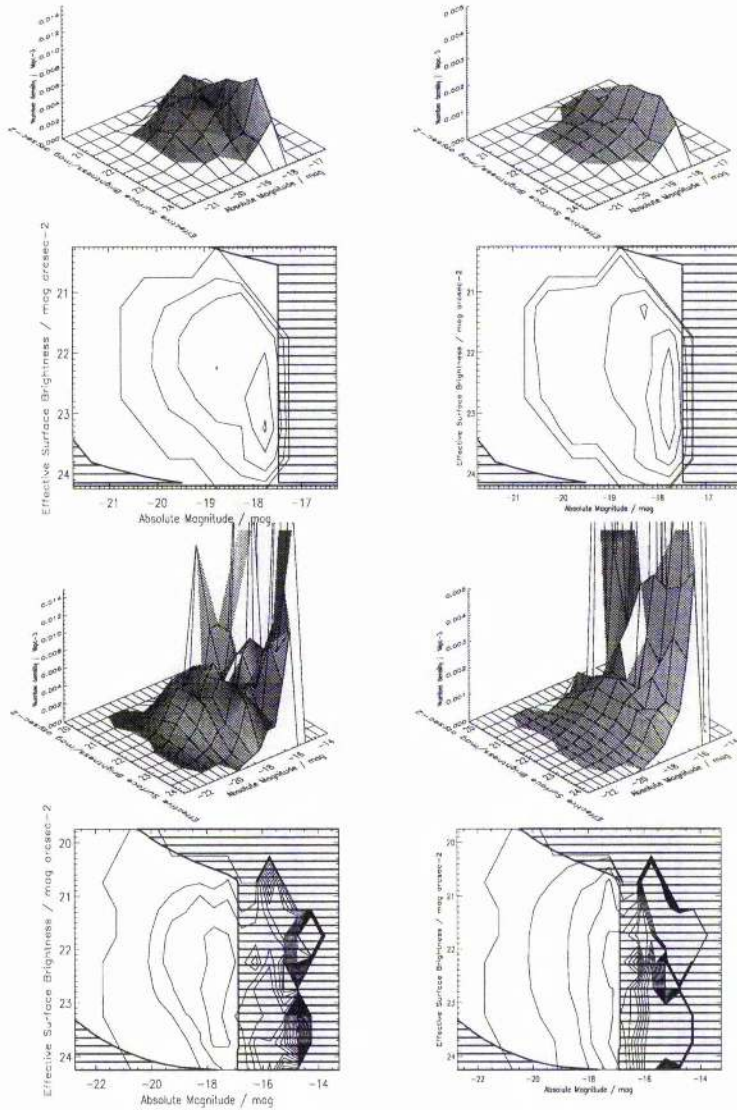


Figure 4.12: The MGC Bivariate Brightness Distribution for subsample 1. The top left hand plot shows the BBD produced via the empirical method with the errors for this plot shown in the top right plot. The bottom left hand plot shows the BBD produced via the SWML method with the errors for this plot shown in the bottom right plot. The contour lines for the BBDs are set at 1.0×10^{-7} , 1.0×10^{-3} , 2.5×10^{-3} , 5.0×10^{-3} , 7.5×10^{-3} , 1.0×10^{-2} , 1.25×10^{-2} , 1.5×10^{-2} , 1.75×10^{-2} , 2.0×10^{-2} , and 2.25×10^{-2} galaxies Mpc^{-3} . The contour lines for the errors are set at 1.0×10^{-7} , 1.0×10^{-4} , 5×10^{-4} , 1.0×10^{-3} , 1.5×10^{-3} , 2.0×10^{-3} , 2.5×10^{-3} , 3.0×10^{-3} , and 3.5×10^{-2} galaxies Mpc^{-3} . The shading represents the regions where $V \leq 5000 \text{Mpc}^3$.

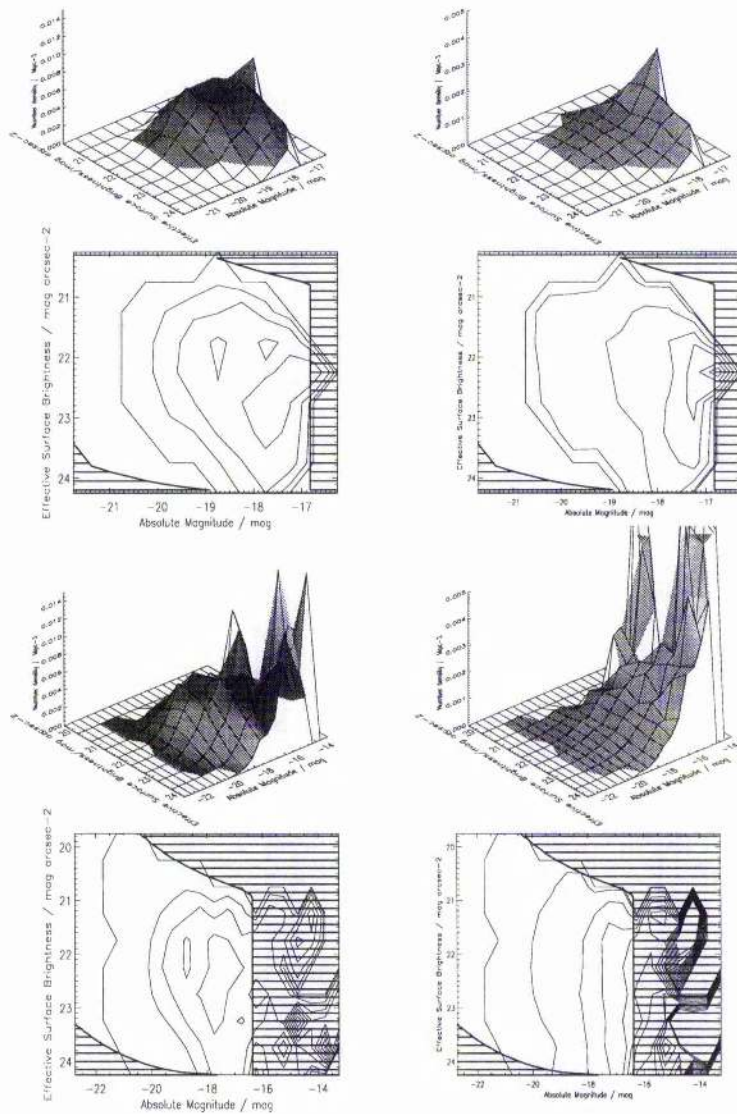


Figure 4.13: The MGC Bivariate Brightness Distribution for subsample 2. The top left hand plot shows the BBD produced via the empirical method with the errors for this plot shown in the top right plot. The bottom left hand plot shows the BBD produced via the SWML method with the errors for this plot shown in the bottom right plot. The contour lines for the BBDs are set at 1.0×10^{-7} , 1.0×10^{-3} , 2.5×10^{-3} , 5.0×10^{-3} , 7.5×10^{-3} , 1.0×10^{-2} , 1.25×10^{-2} , 1.5×10^{-2} , 1.75×10^{-2} , 2.0×10^{-2} , and 2.25×10^{-2} galaxies Mpc^{-3} . The contour lines for the errors are set at 1.0×10^{-7} , 1.0×10^{-4} , 5×10^{-4} , 1.0×10^{-3} , 1.5×10^{-3} , 2.0×10^{-3} , 2.5×10^{-3} , 3.0×10^{-3} , and 3.5×10^{-2} galaxies Mpc^{-3} . The shading represents the regions where $V \leq 5000 \text{Mpc}^3$.

4.4.1 The Bivariate Brightness Function.

The first task is to fit a function to the BBD, as in § 2.7.1. We will use the Chołoniewski (1985) function shown in § 2.7.1, Eqn 2.56.

The best fit parameters for subsample 1, using the BBD produced by empirical method are $M_{B_{MGC}}^* - 5 \log h = -21.29 \text{mag}$, $\phi^* = 3.82 \times 10^{-3} h^3 \text{Mpc}^{-3}$, $\alpha = -1.10$, $\beta_\mu = -0.479 \text{mag arcsec}^{-2}$, $\mu_e^* = 23.27$ and $\sigma_\mu = 1.34$ with $\chi^2 = 387$ for $\nu = 26$ degrees of freedom. The best fit parameters for subsample 2, using the BBD produced by empirical method are $M_{B_{MGC}}^* - 5 \log h = -20.95 \text{mag}$, $\phi^* = 1.12 \times 10^{-2} h^3 \text{Mpc}^{-3}$, $\alpha = -0.831$, $\beta_\mu = 0.136 \text{mag arcsec}^{-2}$, $\mu_e^* = 22.15$ and $\sigma_\mu = 1.43$ with $\chi^2 = 513$ for $\nu = 35$ degrees of freedom.

The fits are poor, and the best fit parameters are very different to previous estimates. Either Eqn 2.56 is not a good model, or there is not enough data to determine the parameters of the bivariate brightness function (BBF). As Figs 4.12 & 4.13 show, the errors are a significant (> 0.2) fraction of the data brightwards of $M \sim -20$ and faintwards of $M \sim -18$, and at the low surface brightness and high surface brightness extremes.

When the BBDs produced via SWML are fitted the likelihood of a good fit is higher. Subsample 1 has a best fit of $M_{B_{MGC}}^* - 5 \log h = -19.28 \text{mag}$, $\phi^* = 2.30 \times 10^{-2} h^3 \text{Mpc}^{-3}$, $\alpha = -0.846$, $\beta_\mu = 0.156 \text{mag arcsec}^{-2}$, $\mu_e^* = 21.99$ and $\sigma_\mu = 0.766$ with $\chi^2 = 152$ for $\nu = 92$ degrees of freedom. The best fit for subsample 2 is $M^* = -19.24$, $\phi^* = 2.47 \times 10^{-2}$, $\alpha = -0.796$, $\beta_\mu = 0.180$, $\mu_e^* = 22.06$ and $\sigma_\mu = 0.765$ with $\chi^2 = 220$ for $\nu = 101$ degrees of freedom.

Comparing with the Cross & Driver (2001) result we find that μ_e has decreased by $\sim 0.55 \text{mag arcsec}^{-2}$ (from $\mu_{e B_{MGC}} = 22.58$ to $\mu_{e B_{MGC}} = 22.03$). This is exactly the value found before corrections to take into account the variable profiles and inclinations were added. However the value of μ_e^* is dependent on the value of M^* . The change in μ_e with M depends on the value of the luminosity-surface brightness gradient β_μ . If β_μ does change significantly from ellipticals to spirals then it will be difficult to predict exactly how μ_e changes. We will examine this question in Chapter 5, when we deal with galaxies of different spectral type.

We also find that β_μ has reduced by a factor of 2 and σ_μ has increased by 50%. The luminosity surface brightness gradient β_μ appears to get steeper changing from subsample 1 to subsample 2 and from the empirical method to the SWML. In each case the effective limit of the survey (where the volume drops below $V \sim 5000 \text{Mpc}^3$), shown by the shaded region in Figs 4.12 & 4.13 moves to a fainter absolute magnitude ($M \sim -17.5$ to $M \sim -16.2$). Many previous surveys have shown that the luminosity surface brightness correlation for bright elliptical galaxies has a negative value of β_μ (see e.g. Kormendy 1977, Thomsen & Frandsen 1983, Chołoniewski 1985, Sodr  & Lahav 1993), whereas spirals have a positive value of β_μ (e.g. Driver 1999, de Jong & Lacey 2000). Ellipticals and S0s are found in equal numbers to spirals at bright absolute magnitudes and spirals and irregulars become more dominant at the faint end (Marzke et al. 1998), thus β_μ increases with absolute magnitude. For the two samples calculated via the empirical method, the change in β_μ from negative to positive occurs where the errors are smallest, so that the BBF is fitted to a distribution which is composed of two very different distributions, neither dominating. The SWML samples probe a little fainter, and are dominated by the spirals. Cross et al. (2001) probed even fainter, into the regime dominated by spirals, and therefore saw a clearer correlation. Considering that

Cross et al. (2001) modelled all their objects as exponential profile galaxies, so the surface brightness estimates of the ellipticals were poor, it is not surprising that a distribution close to that of spirals was measured. Unfortunately the subsamples are too small to break down into morphological or spectral types to measure the luminosity- surface brightness correlations per type. This will be addressed in Chapter 5.

There are several reasons why the width, σ_μ of the BBD is significantly larger than the Cross et al. (2001) result. One reason is the bright absolute limits, and the significant contamination by ellipticals. If the ellipticals follow the Kormendy (1977) result, with a negative β_μ then the width of the population, measured along a positive β_μ direction will be greater.

Another possible reason, is the improved measurement of surface brightness, see § 2.3. § A.1.2 discusses the error caused by assuming that an optically thin disk galaxy is viewed face-on and § A.1 discusses the errors in μ_e due to the assumption that the galaxy is an exponential and not taking into account seeing. While we have not taken seeing into account, the direct measurement of surface brightness is profile independent. The incorrect measurement not only causes a measurement error in μ_e^* equal to ~ 0.55 (Cross & Driver 2001), it is also likely to affect the width.

We see data right up to the selection boundaries, see Fig 4.1, and we see a luminosity surface brightness correlation, but with a shallower gradient. The space density does fall away before the boundaries in Figs 4.12 & 4.13, and so the density of giant LSBGs is significantly lower than the density of normal giant galaxies.

4.4.2 The Luminosity Function, Surface Brightness Function and Luminosity Density.

Fig 4.14 shows the BBDs summed to produce luminosity functions (LFs). There is good agreement between the four MGC luminosity functions for $M < -17.5$. Beyond that, the volume over which galaxies can be seen becomes tiny, see Figs 4.2 & 4.5. The dotted lines show the Schechter function fits to the data. While the bright end is well determined, there is a large variation in the faint end slope ($-0.770 > \alpha > -1.00$). The dashed line shows the Norberg et al. (2002) line calculated using Einstein-de Sitter cosmology. The bright end is slightly fainter 0.075 ± 0.025 mag, and the faint end slope is much steeper. From Fig 2.15 we would expect the bright end to be slightly fainter, and there to be a slight steepening of the faint end slope, if the 2dF magnitudes used by Norberg are not as close to total magnitudes as the MGC magnitudes. Since the 2dFGRS uses Gaussian corrected magnitudes that are then calibrated to deeper CCD photometry, we expect that the offsets for corrected magnitudes at $\mu_{lim} \sim 26.0 \text{ mag arcsec}^{-2}$ in Table 2.3 will match the difference between our results and the Norberg results. Thus we predict a decrease in M^* of 0.06 mag and a decrease in ϕ^* of 5.5% and no significant change in α . However, since the Norberg et al. (2002) LF is normalised to the number counts, their value of ϕ^* is reliable. This accounts for the small error in M^* .

In Norberg et al. (2002), the luminosity function is shallower in the Northern Galactic Pole (NGP) region than the Southern Galactic Pole (SGP) region. For the Λ -CDM case the NGP has a faint end slope gradient $\alpha = -1.14$ and the SGP has $\alpha = -1.28$ (Norberg, private communication). Since there is little variation between the values of α in the different

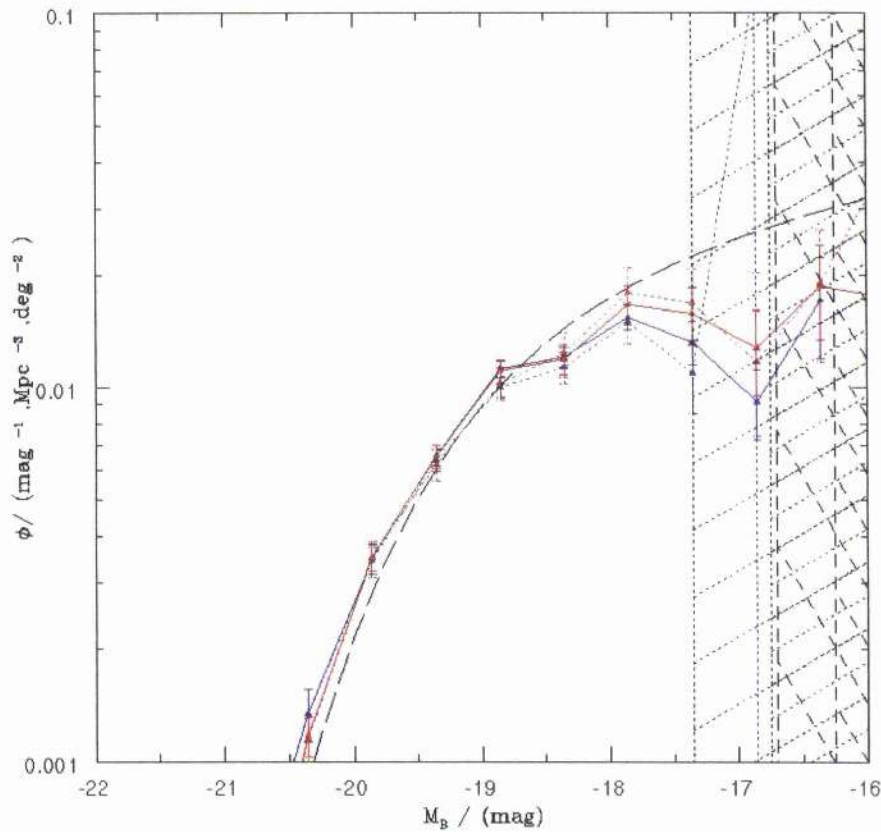


Figure 4.14: This plot shows 4 LFs produced using the MGC data. The blue lines show the LFs produced using the empirical method, with subsample 1 shown as a dotted line and subsample 2 as a solid line. The red lines show LFs produced using the SWML method. There is good agreement within the selection limits. The shaded regions show the limits for each subsample and method. Subsample 1, with the empirical method is valid for $M < -17.5$, and with SWML it is valid to $M < -16.9$. The equivalent limits for subsample 2 are $M < -16.85$ and $M < -16.4$. The Norberg et al. (2002) result is shown by the dashed line.

cosmologies, this difference is true for the Einstein-de Sitter cosmology. The MGC is located in the NGP, so this difference could explain some of the variation seen between the Norberg et al. (2002) results and the MGC LFs. Finally, the faint end slope is dominated by an apparent dip in the LF at $M = -17$, which is very close to the limits of the survey. In Chapter 5 we will probe deeper into the faint end of the LF, so we will be able to test whether this is real substructure or not. This substructure may well have been missed by Norberg et al. (2002) because of the errors in magnitudes. While they corrected their magnitudes for the overall offset compared to the SDSS-EDR, they did not correct for the non-linearities in surface brightness. This will underestimate the magnitudes of high surface brightness galaxies, but will overestimate the magnitudes of low-surface brightness galaxies, or galaxies at high redshift.

The parameters and fits are detailed in Table 4.1. The fits are very good apart from subsample 2 calculated by the empirical method. The errors are a combination of the random errors and the errors in the K+e corrections listed in Norberg et al. (2002). The errors in our result are of the same order of magnitude as those quoted in Norberg et al. (2002). Their error

Table 4.1: A comparison of the fits found both subsamples using both methods. All results are converted to Johnson B and are calculated for an Einstein-de Sitter cosmology, unless stated.

Method/Sample	$M_B^* - 5 \log h$	$\phi^*/10^{-2}h^3$	α	χ^2	ν	$j/10^8 hL_\odot \text{Mpc}^{-3}$
EMP/Sub1	-19.30 ± 0.07	(2.02 ± 0.09)	-0.940 ± 0.04	6.81	7	(1.64 ± 0.17)
EMP/Sub2	-19.08 ± 0.07	(2.66 ± 0.09)	-0.770 ± 0.04	16.25	8	(1.61 ± 0.16)
SWML/Sub1	-19.24 ± 0.07	(2.15 ± 0.09)	-1.00 ± 0.04	5.50	12	(1.66 ± 0.19)
SWML/Sub2	-19.18 ± 0.07	(2.36 ± 0.09)	-0.922 ± 0.04	5.63	15	(1.66 ± 0.18)
2dF*	-19.20 ± 0.07	(2.15 ± 0.09)	-1.18 ± 0.02			(1.83 ± 0.17)
ESP* ²	-19.33 ± 0.08	(2.00 ± 0.04)	-1.22 ± 0.06			(1.99 ± 0.20)
SDSS* ³	-19.42 ± 0.04	(2.69 ± 0.34)	-1.22 ± 0.05			(2.91 ± 0.40)
EMP/Sub2/ ¹	-18.98 ± 0.07	(2.84 ± 0.09)	-0.72 ± 0.02	13.76	8	(1.56 ± 0.17)
SWML/Sub2/ ¹	-19.32 ± 0.07	(1.91 ± 0.09)	-0.977 ± 0.02	3.84	13	(1.56 ± 0.17)
Sim/Sub2/**, ¹	-18.96 ± 0.07	(2.88 ± 0.09)	-0.956 ± 0.02	25.8	15	(1.68 ± 0.17)
2dF* ¹	-19.38 ± 0.07	(1.68 ± 0.09)	-1.21 ± 0.02			(1.74 ± 0.17)
SDSS* ⁴ ¹	-19.40 ± 0.07	(1.63 ± 0.09)	-1.26 ± 0.02			(1.81 ± 0.40)

* Norberg et al. (2002). ² Zucca et al. (1997) ³ Blanton et al. (2001) ⁴ Modified as in Norberg et al. (2002). ** In this case a luminosity function, without surface brightness corrections was calculated, using the SWML methodology. ¹ Λ -CDM cosmology. $\Omega_m = 0.3$, $\Omega_v = 0.7$.

is dominated by errors in the zero point and the completeness whereas our error is dominated by random errors due to the sample size.

In Table 4.1 and Fig 4.15 we compare 3 recent LFs to the MGC LFs. We compare the 2dFGRS LF (Norberg et al. 2002), the ESP LF (Zucca et al. 2001) and the SDSS LF (Blanton et al. 2001). As we discussed above the MGC does not penetrate far into the faint end of the LF, so we will concentrate on the bright end, where the deep CCD photometry using Kron magnitudes (see § A.1 for a comparison of magnitude systems) will provide tight constraints. The ESP gives the best fit to the bright end of the MGC while the SDSS gives the worst fit. Only the ESP fits the MGC within the error bars at the bright end. It would be expected that the SDSS would give a close fit, as it is based on Petrosian CCD magnitudes in 5 colours, and gives an excellent match to the MGC magnitudes, see § 3.5.3. Norberg et al. (2002) have analysed the SDSS LF and conclude that when the correct colour equation is applied to the g' LF, the over-density in the LF within the SDSS region is taken into account and pure luminosity evolution is factored in, the 2dFGRS and SDSS LF are consistent. Norberg et al. (2002) did the analysis of the two surveys using a Λ -CDM cosmology, and so we will compare the Norberg calibrated SDSS LF with a MGC LF generated assuming a Λ -CDM cosmology.

The luminosity density calculated for the MGC LFs is consistent compared to each other. There are no noticeable differences between the two subsamples. The mean value is $j_B = (1.64 \pm 0.17) \times 10^8 hL_\odot \text{Mpc}^{-3}$ for the Einstein-de Sitter cosmology. This compares with the 2dFGRS value $j_B = (1.83 \pm 0.17) \times 10^8 hL_\odot \text{Mpc}^{-3}$. The ESP which fits the MGC better at the bright end gives a higher value $(1.99 \pm 0.20) \times 10^8 hL_\odot \text{Mpc}^{-3}$.

The surface brightness functions are shown in Fig 4.16. While the new LFs are similar to the Cross et al. (2001) luminosity function, the surface brightness functions are significantly wider and flatter. This is likely to be due to the improved measurement of surface brightness, allowing for different profile shapes and inclination. In § A.1.2 and Fig. A.6 we discuss the effects of inclination and profile type respectively. Fitting an exponential profile will underestimate the

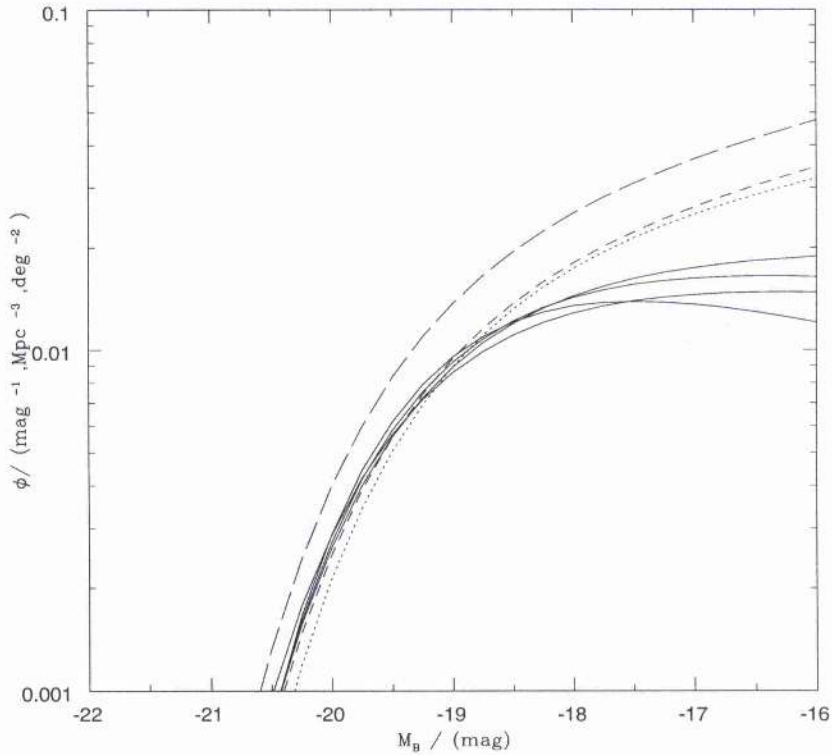


Figure 4.15: This plot shows 4 Schechter Function fits to the MGC subsamples in Fig 4.14 compared to 3 recent surveys. The solid lines are the MGC LFs, the dotted line is the 2dFGRS LF (Norberg et al. 2002), the short dashed line is the ESP LF (Zucca et al. 1997) and the long dashed line is the SDSS LF (Blanton et al. 2001). While the MGC cannot probe the faint end due to the redshift incompleteness and small survey area, it gives excellent constraints on the bright end. The ESP LF fits the bright end best, and the SDSS fits it worst.

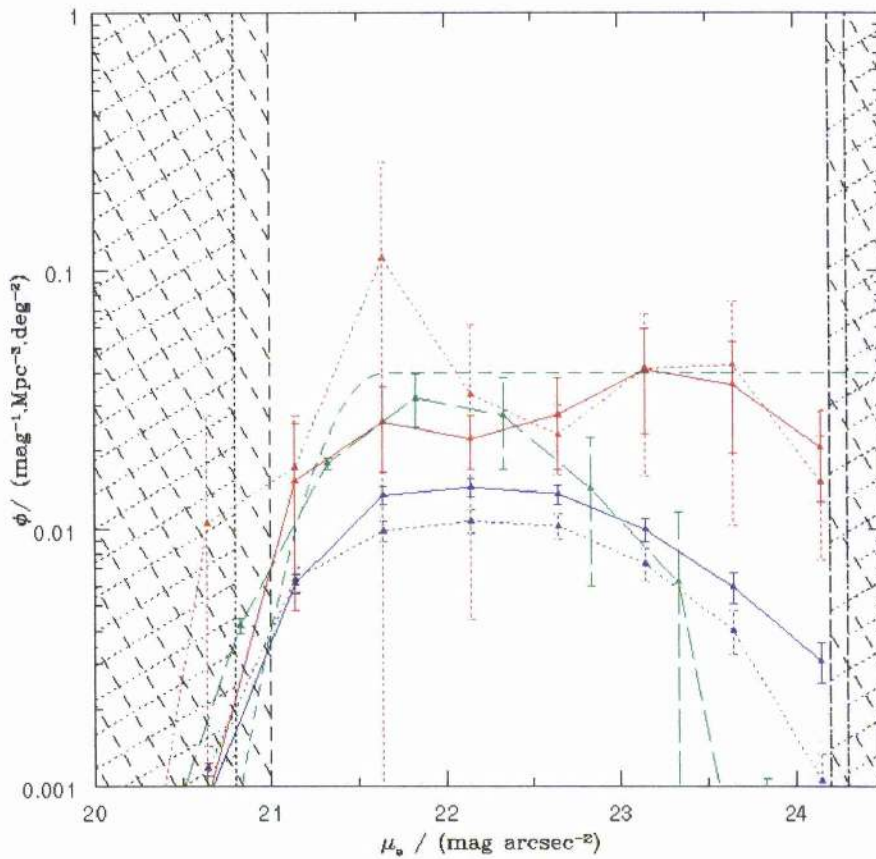


Figure 4.16: This plot shows 4 SBFs produced using the MGC data. The blue lines show the LFs produced using the empirical method, with subsample 1 shown as a dotted line and subsample 2 as a solid line. The red lines show LFs produced using the SWML method. The higher values for the SWML reflect the fact that these contain more intrinsically faint galaxies. The green dashed lines show previous results. The green dashed line with points is the Cross et al. (2001) result, and the green dashed line without points is the O'Neil & Bothun (2000) result. The O'Neil & Bothun have been normalised so that $\phi(\mu_e = 21.65) = 0.04$. The MGC seems to support the O'Neil & Bothun (2000) result. The black shaded regions are the limits where the volume falls below 5000Mpc^3 .

effective surface brightness of ellipticals while overestimating the effective surface brightness of early type spirals. Thus if both types of galaxy had the same surface brightness when measured using a fitted exponential profile, the elliptical would in reality have a higher surface brightness than the spiral. The surface brightness distribution can become wider or narrower when the surface brightness is calculated from the half-light radius measurement, rather than the method used in Chapter 2.

The inclination correction will reduce the surface brightness of highly inclined galaxies, since a highly inclined, optically thin spiral galaxy will appear to have a higher surface brightness than the same galaxy viewed face on.

The surface brightness distribution appears to be consistent with a flat distribution, as O'Neil & Bothun (2000) found. However brighter than the Freeman value ($\mu_e < 21.65$), where the space density is usually found to significantly decrease, is where the star galaxy separation line limits the volume over which these galaxies can be seen. The difference between the

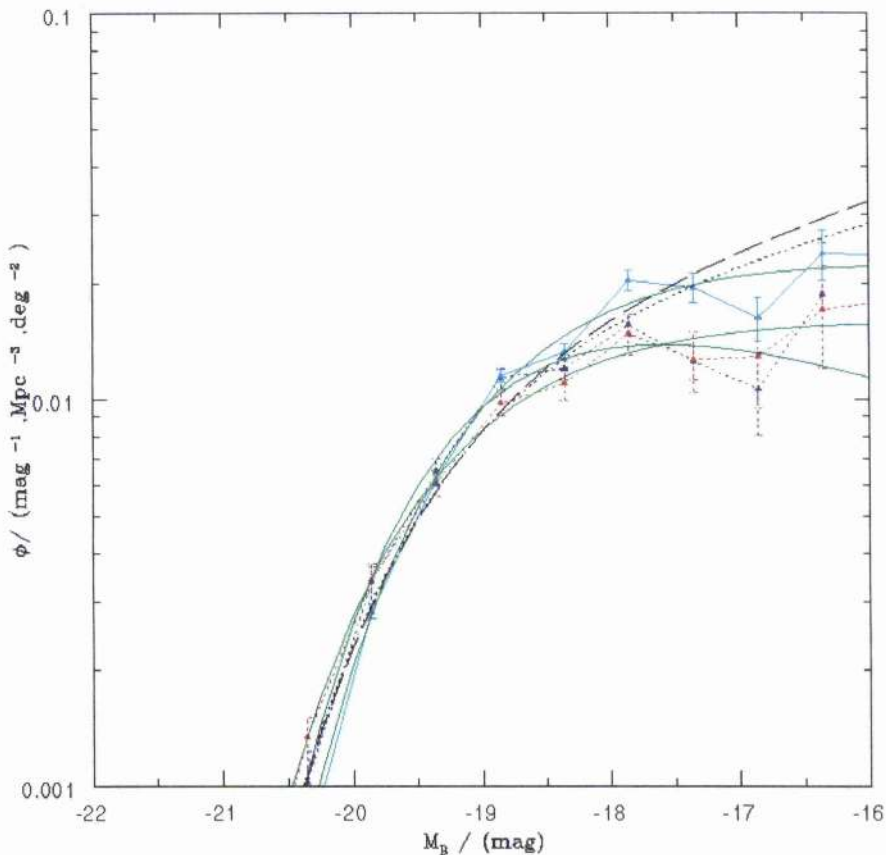


Figure 4.17: This plot shows 2 LFs produced using the MGC data and Λ -CDM cosmology. The blue line shows the LF produced using the empirical method, and the red lines shows the LF produced using the SWML method. There is good agreement within the selection limits. The cyan curve shows a LF calculated using the traditional SWML of Efstathiou, Ellis & Peterson (1988). The shaded regions show the limits for each subsample and method. The solid curves are the Schechter function fits to the MGC LFs. The dotted line shows the best fit 2dFGRS LF (Norberg et al. 2002) and the dashed line shows the best fit SDSS LF, modified by Norberg et al. (2002).

results from the empirical method and the SWML is due to the magnitude range that they sum galaxies over. The SWML BBDs are summed to $M = -13$, whilst the empirical BBDs are only summed to $M = -16$ due to the different z_{min} limits. The surface brightness distribution appears to get flatter as the magnitude range over which it is summed increases.

4.4.3 Λ -CDM Cosmology.

For completeness we calculate the LF and j for the standard Λ -CDM, using subsample 2 only. The relevant Schechter function parameters are in Table 4.1.

The modified SDSS LF is a good fit to the 2dFGRS, but underestimates the bright end compared to the MGC. When the LF is calculated from the MGC using a traditional SWML Luminosity function without any surface brightness information and therefore visibility, the bright end is underestimated, but the faint end is overestimated, and becomes comparable to the 2dFGRS LF. This suggests that a selection bias rather than a magnitude error is

responsible. The most likely bias is either the incompleteness correction or the effects of the maximum half light radius limit at the bright end. Norberg et al. (2002) assume a constant incompleteness, as do we for this simple LF, but we have shown, Fig 4.11, that the incompleteness is a strong function of surface brightness. At the bright end, the volume over which low surface brightness galaxies can be seen is severely affected by the maximum half-light radius, see Fig 4.2. Since the maximum size of a galaxy has not been rigorously defined for the 2dFGRS or SDSS it is difficult to test whether this is the cause or not.

4.5 Summary

In this chapter we have set out to reduce the systematic error in the BBD by using deep CCD data in our input catalogue rather than the APM catalogue. We have also carefully selected a sample for accurate magnitudes, surface brightnesses and high completeness.

We find that the data covers the parameter space right up to the selection limits except at the bright end, where a line of galaxies with the same slope as the absolute magnitude - effective surface brightness correlation of elliptical galaxies forms a boundary. However, there appear to be several extremely bright high surface brightness objects beyond this line. A large fraction of these have evidence of recent mergers and so the extreme nature of these galaxies is likely to be due to star burst activity.

The BBD was measured using two subsamples, one with an average 95% completeness and the other with 92% completeness. The BBDs produced using the empirical method could not be fitted well with the Choloniewski function, but the SWML BBDs could, giving a BBF that is significantly broader and shallower than the BBF in Cross et al. (2001). Since the limits in M are brighter than the Cross et al. (2001) sample this is most likely to be due to a distribution of elliptical galaxies, with a negative gradient luminosity- surface brightness relation at the bright end, distorting the spiral galaxy distribution. The BBD was summed to produce luminosity functions which were well fit by Schechter functions. The LFs are completely consistent for $M < -17.5$, and give a mean value of $j_B = 1.64 \pm 0.17 \times 10^8 h L_\odot \text{Mpc}^{-3}$. When compared to recent LFs the MGC matched the ESP well at the bright end, but finds a much flatter distribution than the 2dFGRS, ESP or SDSS. The difference between the 2dFGRS and MGC LFs $\Delta M_B = 0.075 \pm 0.025$ is consistent with a combination of magnitude errors and surface brightness selection effects in the 2dFGRS at the bright end. The initial SDSS LF overestimates the space density at every magnitude interval, but the modified version produced by Norberg et al. (2002) closely matches the 2dFGRS and has the same discrepancies with the MGC. The surface brightness function calculated is flat at faint absolute magnitudes and therefore consistent with the O'Neil & Bothun (2000) result. The surface brightness function appears to get flatter as the population is summed to fainter absolute magnitude limits. If it is summed to even fainter limits, the space density of galaxies may start to increase as one moves to lower surface brightnesses. The surface brightness distribution is significantly broader than the Cross et al. (2001) surface brightness distribution implying a high density of low surface brightness galaxies.

The greatest limits on the subsamples selected above were the redshift incompleteness and the clustering correction. The clustering correction can be significantly improved by

using brighter catalogues and the NASA Extragalactic Database (NED) to provide accurate magnitudes surface brightnesses and redshifts for galaxies with $B_{MGC} < 15$. To improve the redshift completeness and therefore improve the random errors and probe intrinsically fainter regions of the MGC, we intend to measure redshifts for all objects to $B_{MGC} = 20$. This will increase the sample size from 1500 – 2000 galaxies to ~ 12000 galaxies, with good photometry. The small sample size at present means that it is impossible to look at the BBD/LF as a function of spectral type, morphological type colour, or redshift.

Using the information gained here about the selection criteria, and using the much larger 2dFGRS data base with magnitudes and surface brightnesses corrected using the MGC data, it should be possible to improve the numbers of galaxies significantly. Using just the data from the 15 UKST plates containing MGC data, on which corrections will be valid, will give a dataset of 60,000 galaxies. It will then be possible to measure the BBD for subsamples.

In Chapter 5, we will measure the BBD using 2dFGRS data from the 15 plates that overlap with the MGC. We will correct the 2dFGRS magnitudes so that they do not have the scale errors seen in Chapter 3. The sample size will increase by a factor of ~ 10 , so we will be able to measure the faint end more reliably and separate the BBD into spectral types. Since spectral type 1 galaxies are typically Ellipticals/S0s and Types 2-4 are typically spirals and irregulars, we will be able to crudely test the luminosity surface brightness relationship for ellipticals and spirals separately.

Chapter 5

Using the 2dFGRS to measure the the BBD as a Function of Spectral Type.

In this chapter, we use the much larger data set available on the 15 Two degree field galaxy redshift survey (2dFGRS) plates that overlap with the Millennium Galaxy Catalogue (MGC) to measure the faint end of the Bivariate Brightness Distribution (BBD) and to measure the BBD as a function of the spectral types defined by Madgwick et al. (2001).

To use these data, we must first make corrections for the discrepancies between the 2dFGRS magnitudes and the MGC magnitudes, discussed in Chapter 3. These are corrected (on a plate by plate basis) by fitting a model of the magnitude errors to the 2dFGRS magnitudes and mean surface brightnesses. The corrected magnitudes have an offset $\Delta m(MGC - 2dF) = -0.003 \pm 0.124$, an improvement on $\Delta m(MGC - 2dF) = -0.078 \pm 0.157$ for the uncorrected magnitudes, measured in Chapter 3. New estimates of the effective surface brightness have also been obtained by fitting a model of the differences between MGC effective surface brightness and 2dFGRS mean surface brightness to 2dFGRS magnitudes and mean surface brightnesses. The comparison between the new 2dFGRS μ_e and the MGC μ_e gives $\Delta \mu_e(MGC - 2dF) = 0.005 \pm 0.515 \text{ mag arcsec}^{-2}$.

When the faint end of the luminosity function is probed, we find that the faint end slope becomes significantly steeper fainter than $M = -17$, confirming the Abell cluster result (Driver et al. 1994) and the ESO Slice Project (ESP) result for field galaxies (Zucca et al. 1997). The η -type 1 galaxies (strong absorption features, mainly elliptical and S0 galaxies) BBD turns over at $M = -18.5$ and does not have a clear luminosity-

surface brightness correlation. The η -type 2-4 galaxies (galaxies with increasingly strong emission features; Sa-Sd/Im galaxies) have a strong luminosity-surface brightness correlation that does not vary much in gradient or width between types. However, the value of M^* , and the faint end slope vary enormously between types; the faint end slope becomes rapidly steeper and the M^* point becomes fainter as one moves from η -type 2 to η -type 4.

5.1 Introduction

In Chapter 4, we showed that the BBD produced using the MGC data was significantly broader in surface brightness and had a shallower luminosity-surface brightness relationship than the BBD produced using the 2dFGRS data, given in Chapter 2 and Cross et al. (2001). In Chapter 3, we showed that the 2dFGRS data, which had already been recalibrated since Cross et al. (2001), has a small zeropoint error and considerable non-linearities at the bright end. The MGC allows a measurement of the effective surface brightness, the mean surface brightness within the half light radius, directly from the data, rather than a fit assuming a face on exponential profile, as in Cross et al. (2001).

The BBDs produced in Chapter 4 provided a good measurement of the bright end of the BBD and of the luminosity function. We demonstrated that the ESP gives the best fit of the previous surveys to the bright end, but that the 2dFGRS and the Sloan Digital Sky Survey (SDSS), modified by Norberg et al. (2002), are fainter by 0.075 ± 0.025 mag, probably because they do not take the selection limits into account properly.

However, the random errors in the MGC BBD are large since the careful selection of data meant that the subsamples chosen to meet our stringent criteria contained only 1000-2000 galaxies. Therefore it is impossible to subdivide further to measure the BBD of smaller subsamples, e.g. the η -type 1 galaxies, with the present MGC dataset.

The 2dFGRS contains $\sim 200,000$ galaxies with redshifts, more than enough to get good statistics. However, there are systematic errors in the photometry and poorly understood selection limits. To use this larger data set, we correct the 2dFGRS photometry on plates containing the MGC, significantly increasing the numbers of galaxies in each subsample. We can also use the MGC selection limits. Since the empirical and stepwise maximum likelihood (SWML) methods, defined in § 2.6.1 and 2.6.2 give the same result, the selection limits are well defined.

It is only possible to use the 15 2dFGRS plates containing the MGC galaxies, because the limiting isophote and therefore the corrections vary on a plate by plate basis, as can be seen by looking at Fig. 13 of Colless et al. (2001). These plates contain 66705 objects in the 2dFGRS, although $\sim 6\%$ of these are stars.

In this chapter we will use the larger data set to probe the faint end $M > -17$ and to look at the BBD for different η -types separately. We will use the additional information gained from these separate η -type BBDs to understand subtleties in the overall BBD.

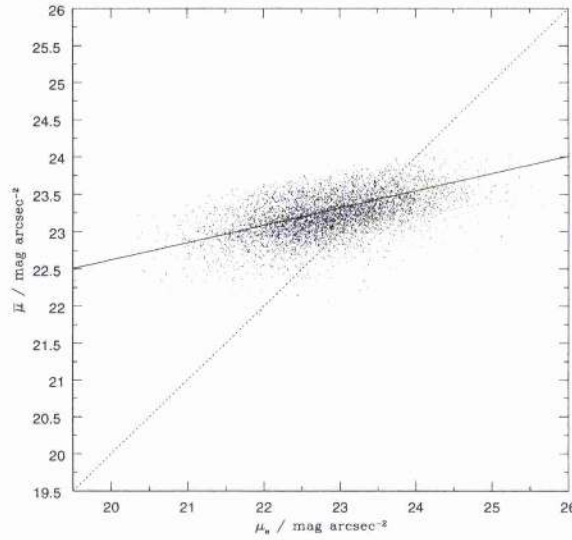


Figure 5.1: This plot shows the variation in the 2dF mean surface brightness $\bar{\mu}$ with the MGC effective surface brightness μ_e . The variation is linear.

5.1.1 Photometric Corrections

Using a subsample of MGC galaxies which are single components of 2dFGRS galaxies with good photometry, as discussed in Chapter 3, we used the 2dFGRS magnitudes (b_j) and mean surface brightness ($\bar{\mu}$) to calculate pseudo-MGC magnitudes ($B_{MGC,psd}$) and effective surface brightnesses ($\mu_{e,psd}$). We use the values of b_j discussed in Chapter 3, i.e. those derived from calibration with 2MASS and other CCD data, but not calibrated using the MGC.

The form of the correction can be estimated by looking at the variation in b_j with B_{MGC} and μ_e and the variation in $\bar{\mu}$ with B_{MGC} and μ_e . $\Delta m = B_{MGC} - b_j - 0.1353$ vs B_{MGC} is shown in Fig 3.18 and Δm vs μ_e is shown in Fig 3.20. The variation in b_j with B_{MGC} has a small linear component, with gradient $0.0221 \text{ mag mag}^{-1}$, see § 3.5.2. The variation with μ_e is flat at the low surface brightness end, but non-linear at the high surface brightness end.

Fig 5.1 shows the variation in $\bar{\mu}$ with μ_e and Fig 5.2 shows the variation in $\bar{\mu}$ with B_{MGC} . In both cases the variation is very close to linear. Using the above information, a fit is given in Eqns 5.1 and 5.2.

$$B_{MGC,psd} = b_j + a + b(b_j - 19.45) + c(\bar{\mu} - 25) + d(\bar{\mu} - 25)^2 \quad (5.1)$$

$$\mu_{e,psd} = \bar{\mu} + e + f(\bar{\mu} - 25) + g(b_j - 19.45) \quad (5.2)$$

where $B_{MGC,psd}$ and $\mu_{e,psd}$ are pseudo- B_{MGC} and pseudo- μ_e values respectively. a, b, \dots, g are parameters which are fitted on a plate-to-plate basis. The best fit universal parameters are $a = 0.428$, $b = -0.0271$, $c = 0.273$, $d = 0.0290$, $e = 0.738$, $f = 0.672$ and $g = -0.124$. The values of a to g for each plate are given in Table 5.1

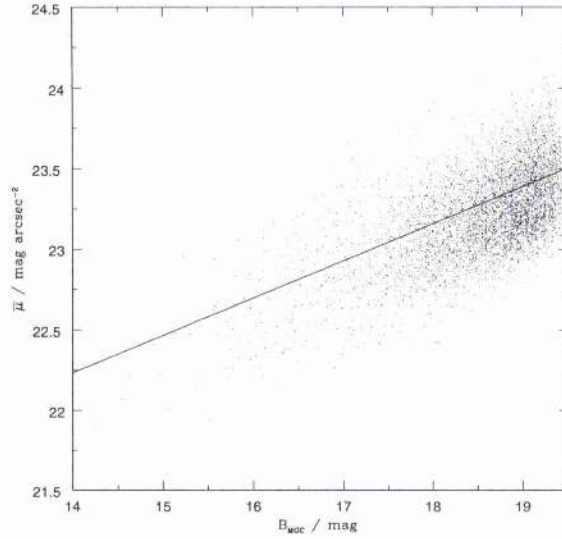


Figure 5.2: This plot shows the variation in the 2dF mean surface brightness $\bar{\mu}$ with the MGC B_{MGC} -band magnitude B_{MGC} . The variation is linear.

Table 5.1: A comparison of the solutions found to convert the 2dFGRS b_j magnitudes and mean surface brightnesses to MGC magnitudes and effective surface brightnesses.

UKST plate	a	b	c	d	χ^2/ν	e	f	g	χ^2/ν
853	1.243	-0.134	1.111	0.157	251/272	1.53	1.52	-0.280	154/273
854	0.456	-0.043	-0.156	-0.083	395/399	1.96	2.02	-0.372	214/400
855	0.358	-0.025	0.105	-0.037	288/383	3.03	2.01	-0.406	146/384
856	1.053	-0.068	0.648	0.036	304/310	4.88	2.88	-0.536	97/311
857	-0.443	-0.053	-0.760	-0.297	288/395	3.30	2.31	-0.454	118/396
858	-0.543	-0.006	-0.911	-0.303	200/244	4.60	2.64	-0.392	92/245
859	1.445	-0.165	1.101	0.147	450/402	4.83	3.03	-0.805	146/403
860	0.645	-0.183	0.516	0.023	210/253	2.33	2.39	-0.880	126/254
861	0.855	-0.150	0.740	0.092	311/268	2.66	2.39	-0.701	133/269
862	0.369	-0.168	-0.096	-0.147	212/286	4.31	2.86	-0.844	112/287
863	1.168	-0.017	0.797	0.120	386/322	3.73	2.43	-0.442	181/323
864	1.286	-0.185	1.021	0.141	245/262	3.01	2.25	-0.766	95/262
865	-0.061	-0.0579	-0.473	-0.191	558/341	3.93	2.14	-0.416	104/342
866	0.584	-0.096	0.388	-0.014	306/290	2.96	2.12	-0.546	126/291
867	1.234	-0.075	0.892	0.121	169/165	4.53	2.81	-0.661	53/166

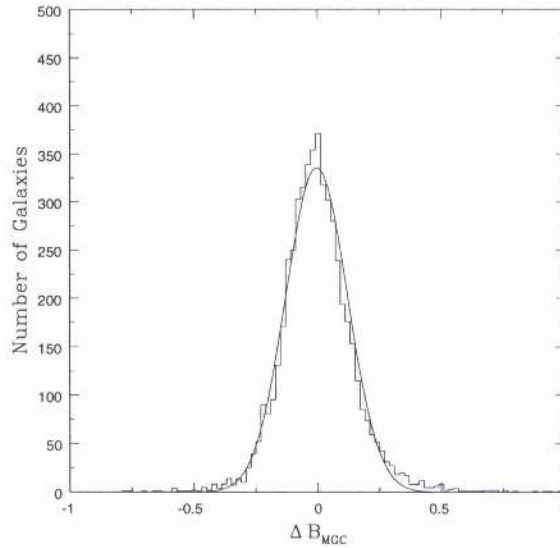


Figure 5.3: This plot shows the histogram of $\Delta m = B_{MGC} - B_{MGC,psd}$. The histogram is well fitted by a Gaussian with mean -0.005 mag and standard deviation 0.124 mag.

The minimum χ^2 was calculated using the Levenberg-Marquardt method, using an error $\Delta b_j = 0.145$, calculated from the comparison of MGC with 2dFGRS, SDSS-EDR with 2dFGRS and MGC with SDSS-EDR. The error in $\bar{\mu}$ does not vary with the varying isophotal limit because the fit is done plate by plate. However it will depend on the seeing, which will affect smaller galaxies but not larger galaxies, on sky subtraction and the presence of nearby objects which can affect the local background. The error in $\bar{\mu}$ is calculated from the scatter about the best fit line between $\bar{\mu}$ and μ_e . This scatter is $\Delta\bar{\mu} \sim 0.85 \text{ mag arcsec}^{-2}$.

When minimised plate by plate the χ^2 values for the fit to Eqn 5.1 were generally good, with typical values $\chi^2 = 387$ for $\nu = 345$ degrees of freedom. When $B_{MGC,psd}$ is compared with B_{MGC} , $\Delta m(B_{MGC} - B_{MGC,psd}) = -0.005 \pm 0.124$, an improvement on $\Delta m(MGC - 2dF) = -0.078 \pm 0.157$, measured in Chapter 3. The scatter varies from 0.110 to 0.151 across the plates. The overall distribution is shown in Fig 5.3.

The χ^2 values for the fit to Eqn 5.2 are also good with a typical $\chi^2 = 100$ for $\nu = 300$ degrees of freedom. These values seem too good, suggesting that the error in $\mu_{e,psd}$ was overestimated. We can use the new values of $\mu_{e,psd}$ to calculate the error in μ_e . $\Delta\mu_e(\mu_e - \mu_{e,psd}) = -0.003 \pm 0.515$. The scatter varies from 0.41 to 0.63 across the plates. Again the scatter is significantly reduced. The difference between μ_e and $\mu_{e,psd}$, $\Delta\mu_e$ is displayed in Fig 5.4.

The apparent distribution in $B_{MGC,psd}$ and $\mu_{e,psd}$ is shown in Fig 5.5. Henceforth $B_{MGC,psd}$ and $\mu_{e,psd}$ will be referred to as B_{MGC} and μ_e , unless stated otherwise. We also show the apparent distribution for each spectral type. Since there was no significant difference between the BBDs produced using subsample 1 or 2 (defined in Chapter 4) we have decided to use the selection limits from subsample 2, the larger of the two subsamples.

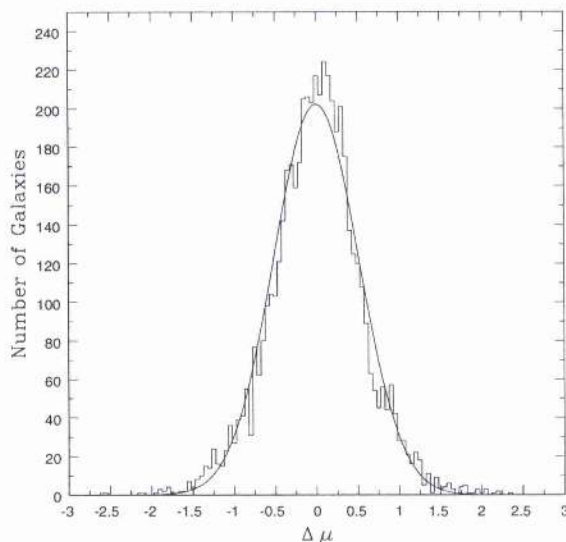


Figure 5.4: This plot shows the histogram of $\Delta\mu_e = \mu_e - \mu_{e,psd}$. The histogram is well fitted by a Gaussian with mean $-0.003 \text{ mag arcsec}^{-2}$ and standard deviation $0.515 \text{ mag arcsec}^{-2}$.

5.1.2 Incompleteness and Stellar Contamination

In Chapter 4, we produced the BBD using the MGC which has high photometric completeness and has been carefully eyeball classified to remove unresolved objects. The 2dFGRS has $\sim 8\%$ photometric incompleteness to $B_{MGC} = 19$ and $\sim 6.0\%$ of objects are stars. We can use the MGC to measure the stellar fraction and photometric incompleteness in the overlap regions and extrapolate over the rest of the survey.

The redshift completeness is corrected as before, but now photometric incompleteness and stellar contamination must be factored in. We measure the photometric incompleteness and stellar contamination as a function of (B_{MGC}, μ_e) , calculating the matrices $f_{st}(B_{MGC}, \mu_e)$ and $C_{ph}(B_{MGC}, \mu_e)$.

$$\begin{aligned}
 N_{gal}(B_{MGC}, \mu_e) &= N_{2dF}(B_{MGC}, \mu_e) \frac{N_{gal,2dF}(B_{MGC}, \mu_e)}{N_{2dF}(B_{MGC}, \mu_e)} \frac{N_{gal}(B_{MGC}, \mu_e)}{N_{gal,2dF}(B_{MGC}, \mu_e)} \\
 N_{gal}(B_{MGC}, \mu_e) &= N_{2dF}(B_{MGC}, \mu_e) \frac{1 - f_{st}(B_{MGC}, \mu_e)}{C_{ph}(B_{MGC}, \mu_e)}
 \end{aligned} \tag{5.3}$$

The photometric completeness correction should be applied to all galaxies whether they have a redshift or not, assuming that the population of galaxies missed in the input catalogue is not particularly biased in terms of the ease of measuring the redshift. Objects unresolved in the 2dFGRS, or normal galaxies that were missed for one reason or another (e.g. they overlapped with a satellite trail) are unlikely to have a biased redshift distribution. However, blended galaxies will be underrepresented because of the minimum separation of fibres, and the confusion between the two spectra. The minimum separation of fibres is $\sim 30''$, see § 3.2.1, which corresponds to $\sim 50\text{kpc}$ at $z = 0.11$, the median redshift. This is roughly the distance

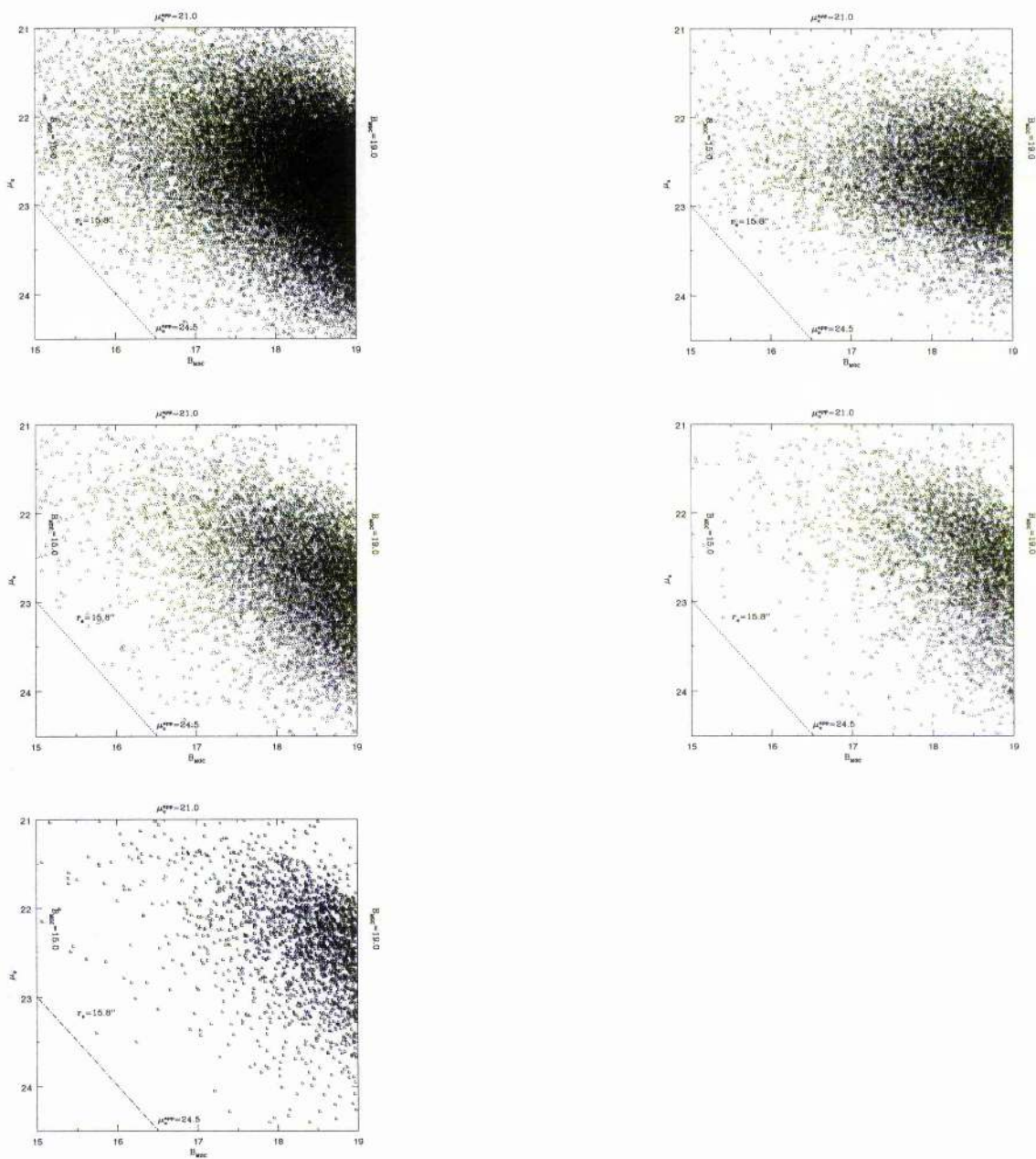


Figure 5.5: This figure shows the distribution of the galaxies in B_{MGC} and μ_e . The top left plot contains all the galaxies, the top right contains only η -type 1 galaxies, the centre left shows η -type 2 galaxies, the centre right only η -type 3 galaxies and the bottom left contains only η -type 4 galaxies. The dotted lines represent the selection limits.

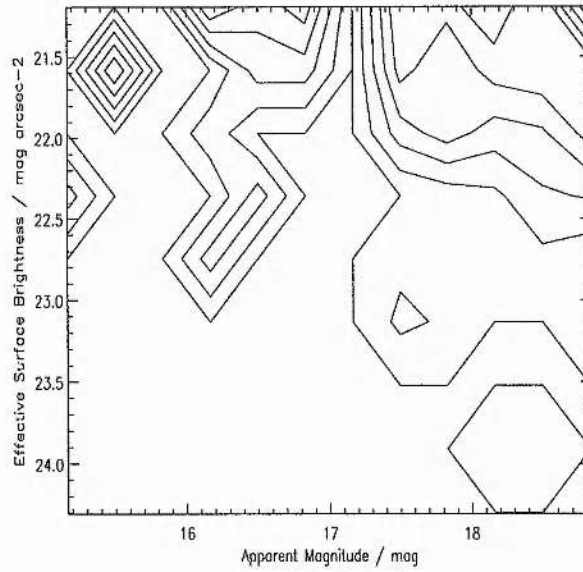


Figure 5.6: This shows the fraction of 2dF objects without redshifts that are stars. The contour lines represent the following fractions: 0.2, 0.4, 0.6, 0.8 and 1.0. There are no stars in the bright, low surface brightness region. The nonlinearities in the UKST plates are particularly bad for stars, so the measured magnitudes and surface brightness do not separate the stars and galaxies very well.

between the Milky Way and the Magellanic Clouds, i.e. a typical distance between satellite galaxies and the main galaxy. Low surface brightness galaxies have poor signal-to-noise, so will again be unrepresented. However, the amount of bias is difficult to estimate, and low surface brightness galaxies only represent 5% of all missing objects.

The fraction of stars correction should only be applied to galaxies without redshifts, as galaxies with redshifts are defined as ones with $z \geq 0.002$ and $Q \geq 3$. Thus any stars with good quality spectra will be placed with objects without redshifts. The definition of the fraction of stars must be modified slightly.

$$f_{st}(B_{MGC}, \mu_e) = \frac{N_{st,2dF}(B_{MGC}, \mu_e)}{N_{nz,2dF}(B_{MGC}, \mu_e)} \quad (5.4)$$

$f_{st}(B_{MGC}, \mu_e)$ is shown in Fig 5.6. $C_{ph}(B_{MGC}, \mu_e)$ is shown in Fig 3.37. $f_{st}(B_{MGC}, \mu_e)$ is calculated from the 2dF data using the pseudo-MGC magnitudes calculated above. The stars are not separated from the galaxies in the apparent BBD partly because of poor seeing, but mainly because of non-linearities in the photometry. Since stars are point sources convolved with a point spread function, they will have higher surface brightnesses than galaxies at the same magnitude, so they are particularly badly affected by the non-linearities in the plates, see § 3.5.1 and in particular Fig 3.14.

The overall redshift incompleteness (24.4%) is higher for the 15 plates than for the MGC region (8%) within the selection limits, because the survey has not been completed yet. However, where fields have not been completed there should not be any bias in redshift, magnitude or surface brightness. The redshift incompleteness code will take care of any magnitude/ surface

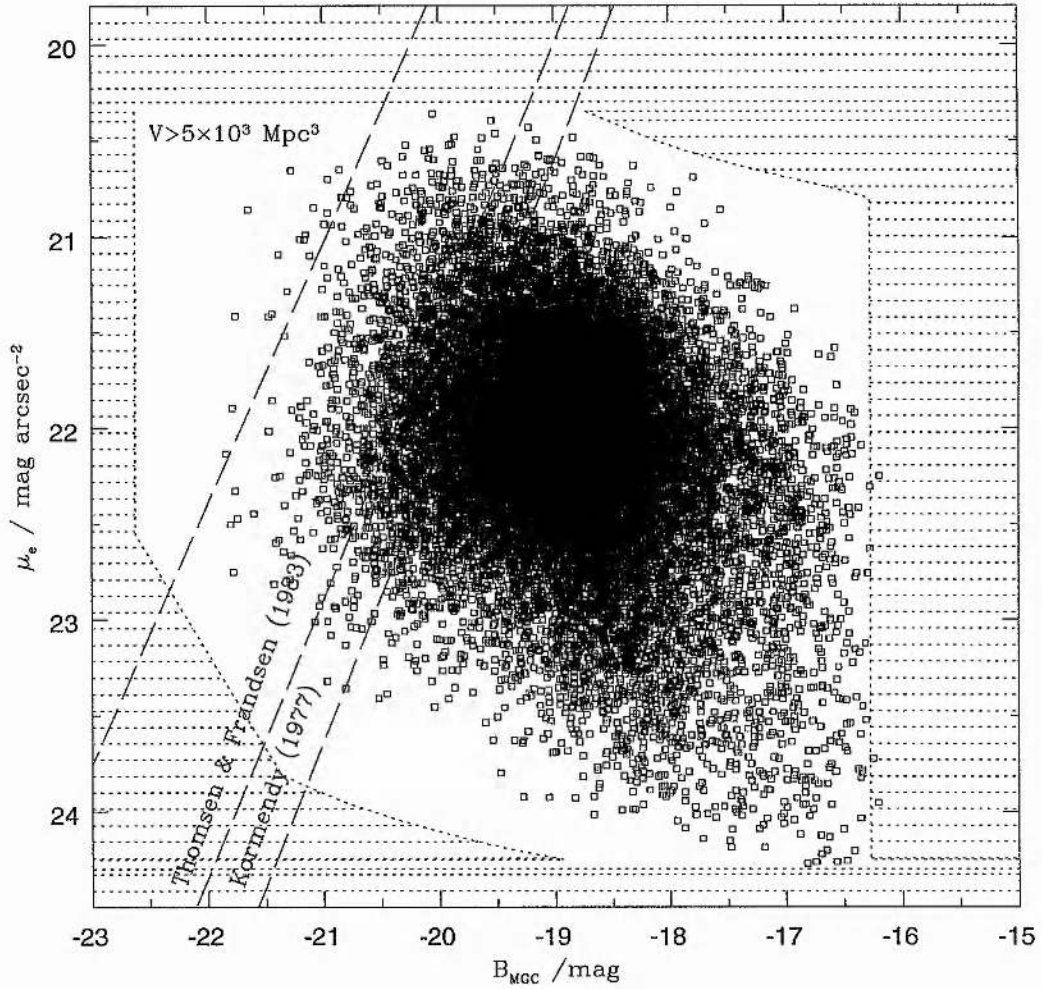


Figure 5.7: This plot shows the distribution in M, μ_e of 18180 2dFGRS galaxies covering the 15 plates which overlap with the MGC data. These galaxies have been selected using the criteria for subsample 2 in Chapter 4.

brightness bias. Therefore there will not be any additional systematic effects in incompleteness and stellar contamination.

Finally, when we look at subsamples of different η -type, it is necessary to correct for the fact that not all galaxies without redshifts are of the same type. As Fig 5.5 demonstrates, the fraction of each type varies in both B_{MGC} and μ_e . We multiply Eqn 5.3 by an extra factor $\frac{N_{type,z}}{N_z}$. Like the stellar contamination correction, this is only applied to galaxies without redshifts.

5.2 Overall BBD

Fig 5.7 shows the distribution of the 2dFGRS galaxies in the M, μ_e plane, for the redshift limits used in the empirical method. Faint low surface brightness galaxies can be seen right up to the limits, but for the rest of the galaxies, there is either a clear gap or a substantial

Table 5.2: A comparison of the fits found both subsamples using both methods. All results are converted to Johnson B and are calculated for an Einstein-de Sitter cosmology, unless stated

Sample	M_B^*	$\phi^*/10^{-3}$	α	β_μ	μ_e^*	σ_μ
EMP						
All	-18.93 ± 0.1	(12.6 ± 1.2)	-0.641 ± 0.03	-0.192 ± 0.02	22.55 ± 0.1	0.431 ± 0.005
Type 1	-20.20 ± 0.1	(8.80 ± 1.3)	-0.45 ± 0.05	-0.500 ± 0.05	23.57 ± 0.15	0.592 ± 0.007
Type 2	-18.63 ± 0.1	(6.46 ± 1.3)	-0.82 ± 0.05	0.304 ± 0.05	22.70 ± 0.15	0.797 ± 0.007
Type 3	-19.27 ± 0.1	(0.690 ± 1.3)	-1.47 ± 0.05	0.276 ± 0.05	22.34 ± 0.15	0.688 ± 0.007
Type 4	-18.28 ± 0.1	(2.89 ± 1.3)	-1.25 ± 0.05	0.0857 ± 0.05	22.72 ± 0.15	0.615 ± 0.005
SWML						
All	-19.30 ± 0.1	(19.3 ± 1.2)	-0.99 ± 0.05	0.132 ± 0.03	22.00 ± 0.15	0.565 ± 0.005
Type 1	-19.20 ± 0.1	(10.9 ± 1.3)	-0.39 ± 0.05	0.012 ± 0.05	21.99 ± 0.1	0.498 ± 0.005
Type 2	-18.85 ± 0.1	(9.36 ± 1.3)	-0.71 ± 0.05	0.219 ± 0.05	22.22 ± 0.15	0.570 ± 0.007
Type 3	-18.94 ± 0.1	(3.98 ± 1.3)	-1.15 ± 0.05	0.265 ± 0.05	21.95 ± 0.15	0.565 ± 0.007
Type 4	-19.17 ± 0.1	(1.60 ± 1.3)	-1.48 ± 0.05	0.215 ± 0.05	21.67 ± 0.15	0.549 ± 0.007
dJL ^{*1}	-19.39 ± 0.17	—	-0.93 ± 0.1	0.49 ± 0.04	22.82 ± 0.19	0.61 ± 0.04
C85 ^{*1}	-20.2 ± 0.2	—	-1.35 ± 0.15	-0.080 ± 0.005	20.8 ± 0.15	0.725 ± 0.05

^{*1} de Jong & Lacey (2000) and Choloniewski (1985). These have been converted from luminosity and diameter to luminosity and surface brightness, see text for details.

reduction in numbers before the limits are reached. The relationship (Eqn 4.1) seen at the bright, high surface brightness edge of the distribution for MGC galaxies is not as well defined in this sample. However, this can be readily explained by the ~ 0.5 mag arcsec⁻² error in μ_e .

The BBD produced via the empirical method is shown in the top left hand corner of Fig 5.8. The BBD produced via the stepwise maximum likelihood method (SWML) is shown in the bottom left hand corner, and the errors for each BBD are shown in the corresponding corners on the right hand side.

The best fit parameters for the bivariate brightness function (BBF) are given in Table 5.2. The BBFs calculated for whole distribution of galaxies via the empirical method agrees with the BBF calculated via the SWML for the 3 Schechter parameters (M^* , ϕ^* and α) and for the width of the Gaussian distribution (σ_μ). However, the gradient of the luminosity surface brightness correlation (β_μ) does not agree. As in Chapter 4, the gradient of the correlation is steeper for the sample with the faintest absolute magnitude limit.

When the whole distribution is summed to produce a luminosity function, the result is shown in Fig 5.9. The best fit Schechter parameters are given in Table 5.3. The luminosity function appears to rapidly steepen at $M_B \sim -17$, which means that the result derived via SWML has a steep faint end slope $\alpha = -1.13$, whereas the empirical method which only has data to $M \sim -16$ has a very flat faint end slope $\alpha = -0.994$. The SWML value for α tallies well with the 2dFGRS value for the NGP ($\alpha = -1.136$; Norberg, private communication). A steepening of the faint end slope was also observed in the ESP data (Zucca et al. 1997) and in Abell clusters (Driver et al. 1994). This would explain the discrepancy in the faint end of the luminosity function for surveys with bright limits such as Stromlo APM, EEP, CfA and Durham UKST which produce essentially flat LFs and the deeper surveys such as Autofib, ESP, 2dFGRS and SDSS which find $\alpha \sim -1.2$, see Fig 1.1. Driver et al. (1994) and Zucca et al. (1997) suggested that the luminosity function would be better fitted by a combination of functions. Zucca et al. (1997) suggested that fainter than $M = M_c$, the function should be

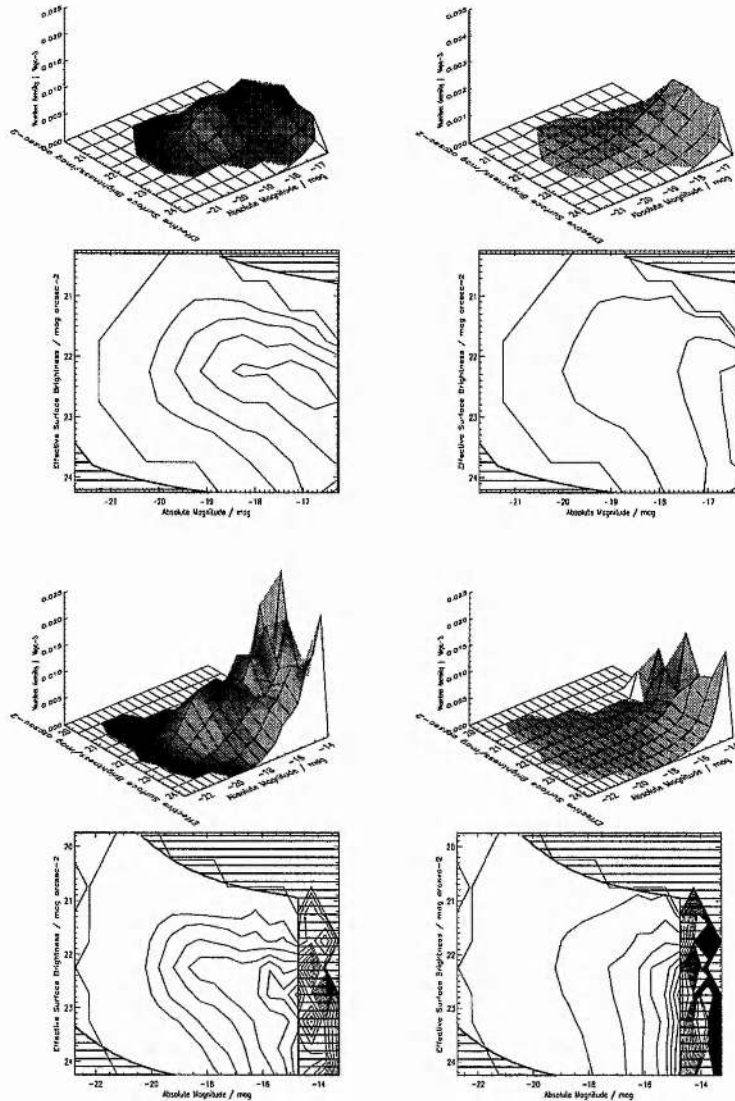


Figure 5.8: The 2dFGRS Bivariate Brightness Distribution. The top left hand plot shows the BBD produced via the empirical method with the errors for this plot shown in the top right plot. The bottom left hand plot shows the BBD produced via the SWML method with the errors for this plot shown in the bottom right plot. The contour lines for the BBDs are set at 1.0×10^{-7} , 1.0×10^{-3} , 2.5×10^{-3} , 5.0×10^{-3} , 7.5×10^{-3} , 1.0×10^{-2} , 1.25×10^{-2} , 1.5×10^{-2} , 1.75×10^{-2} , 2.0×10^{-2} , and 2.25×10^{-2} galaxies Mpc^{-3} . The contour lines for the errors are set at 1.0×10^{-7} , 1.0×10^{-4} , 5×10^{-4} , 1.0×10^{-3} , 1.5×10^{-3} , 2.0×10^{-3} , 2.5×10^{-3} , 3.0×10^{-3} , and 3.5×10^{-2} galaxies Mpc^{-3} . The shading represents the regions where $V \leq 5000 \text{Mpc}^3$.

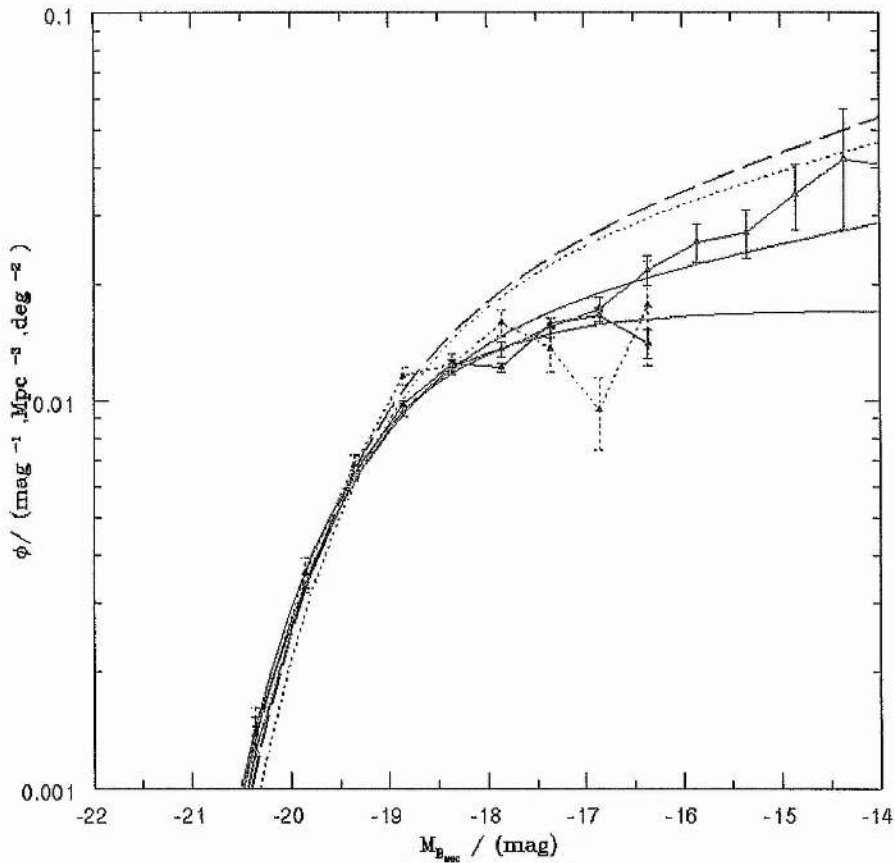


Figure 5.9: This plot shows the luminosity function calculated using the empirical method (blue solid line) and the SWML method (red solid line) and the MGC calculated via the SWML (blue dashed line). The solid green lines represent Schechter Function fits to the two methods. The dotted green line represents the 2dFGRS (Norberg et al. 2002) and the short dashed line is the ESP LF (Zucca et al. 1997). The two methods give identical results at the bright end, and up to the point where the empirical method runs out of data. However, the faint end slope rapidly steepens for $M > -17$. This explains why all the MGC LF's were flat. The dip at $M \sim -17$ seen in the MGC is not apparent when data from all 15 plates are used.

replaced by a power law with index β . The best fit values are $M_{c,B} = -16.71$ and $\beta = -1.57$, with $\alpha = -1.16$ and $M_B^* = -19.29$. Driver et al. (1994) use a combination of 3 Schechter functions, one for ellipticals and spirals, a second for dwarf ellipticals and S0s and a third for dwarf irregulars. The Schechter functions for each group are: $M^* = -19.49$, $\phi^* = 0.016$, $\alpha = -1.1$ (ellipticals and spirals); $M^* = -16.49$, $\phi^* = 0.032$, $\alpha = -1.8$ (dwarf ellipticals and dwarf S0s); $M^* = -16.49$, $\phi^* = 0.064$, $\alpha = -1.8$ (dwarf irregulars).

5.3 The BBD as a Function of Spectral Type

In Fig 5.10 we display the distribution of galaxies of each spectral type (see Madgwick et al. 2001) in the M, μ_e plane. In Fig. 4 of Madgwick et al. (2001), there is a comparison of 2dFGRS spectral type and morphological types from the Kennicutt Atlas (Kennicutt 1992). η -type 1 galaxies correlate with ellipticals and S0 galaxies, η -type 2 galaxies correlate with Sa/Sb galaxies, η -type 3 galaxies correlate with Sb/Scd galaxies and η -type 4 galaxies correlate with

Table 5.3: A comparison of the fits found both subsamples using both methods. All results are converted to Johnson B and are calculated for an Einstein-de Sitter cosmology, unless stated

Method/Sample	$M_B^* - 5 \log h$	$\phi^*/10^{-3}h^3$	α	χ^2	ν	$j/10^8 h L_\odot \text{Mpc}^{-3}$
EMP/All	-19.36 ± 0.06	(19.1 ± 0.8)	-0.994 ± 0.02	62.3	9	(1.64 ± 0.12)
EMP/Type 1	-19.18 ± 0.07	(11.1 ± 0.9)	-0.392 ± 0.03	49.7	9	(0.73 ± 0.08)
EMP/Type 2	-19.14 ± 0.07	(7.07 ± 0.9)	-0.827 ± 0.03	10.75	8	(0.46 ± 0.05)
EMP/Type 3	-18.88 ± 0.07	(4.46 ± 0.9)	-1.120 ± 0.03	12.75	7	(0.27 ± 0.03)
EMP/Type 4	-18.72 ± 0.07	(2.02 ± 0.9)	-1.433 ± 0.03	13.7	7	(0.15 ± 0.02)
SWML/All	-19.44 ± 0.06	(16.7 ± 0.8)	-1.126 ± 0.02	30.7	16	(1.69 ± 0.12)
SWML/Type 1	-19.30 ± 0.07	(10.5 ± 0.9)	-0.497 ± 0.03	18.0	14	(0.76 ± 0.08)
SWML/Type 2	-18.92 ± 0.07	(9.01 ± 0.9)	-0.830 ± 0.03	15.9	13	(0.48 ± 0.05)
SWML/Type 3	-18.98 ± 0.07	(3.96 ± 0.9)	-1.215 ± 0.03	11.2	13	(0.29 ± 0.03)
SWML/Type 4	-19.06 ± 0.07	(1.97 ± 0.9)	-1.470 ± 0.03	8.0	13	(0.22 ± 0.02)

Scd galaxies. As one moves from η -type 1 to η -type 4 galaxies, one moves from early to late type galaxies. Spectral type 1 galaxies are bounded within the selection limits and contain many bright, high surface brightness galaxies. In contrast types 2-4 show a strong luminosity-surface brightness correlation and are found right up to the boundaries at the faint, low surface brightness end.

When the distributions used to produce the BBD via the SWML methodology are displayed, many more outliers are seen amongst the type 1 galaxies, Fig 5.11. Types 2-4 show a very similar distribution as that in Fig 5.10.

The BBDs produced for each type are displayed in Fig 5.12 and Fig 5.13. The fitting parameters are shown in Table 5.2. The fit to η -type 1 galaxies produces different parameters when the SWML method is used compared with the parameters derived via the empirical method. The empirical method finds a tightly bounded distribution, centred on $M = -18.5$, $\mu_e = 22.2$ with a high degree of circular symmetry. The best fit gives a luminosity-surface brightness correlation with $\beta_\mu = -0.5$, close to the gradient of the Kormendy relationship given in Eqn 4.2. However, the BBD produced via SWML has a double peaked distribution, with a second peak at $M = -16$, $\mu_e = 23$. Madgwick et al. (2001) also saw an increase in $\phi(M)$ at the faint end for η -type 1 galaxies. Since the Choloniewski function is not designed for double peaked distributions, the fit is poor and any correlations between M and μ_e are lost since the main axis of the function is forced to fit along the direction between the two peaks. This second peak probably corresponds to dwarf elliptical galaxies.

η -types 2-4 all have a similar value of β_μ , $0.215 < \beta_\mu < 0.30$ apart from the η -type 4 BBD derived via the empirical method. However, in this case it is impossible to get a good fit since there are only 17 bins with which contain more than 10 galaxies, so the constraints are not very good. The width of the distribution σ_μ varies over a small range too. $0.549 < \sigma_\mu < 0.570$ via the SWML and $0.615 < \sigma_\mu < 0.797$ via the empirical method. The gradients of the BBDs produced via the empirical method are also steeper. These parameters correlate, so variations in one will produce variations in the other. Again, the SWML is better constrained at the faint end, assuming that we have not missed any selection effects. If we just use the SWML fits, then types 2-4 have a width $\sigma_\mu = 0.56 \pm 0.01$ and types 2 and 4 have the same luminosity surface brightness relationship $\beta_\mu = 0.217 \pm 0.002$, but the type 3 BBD is steeper $\beta_\mu = 0.265$. While,

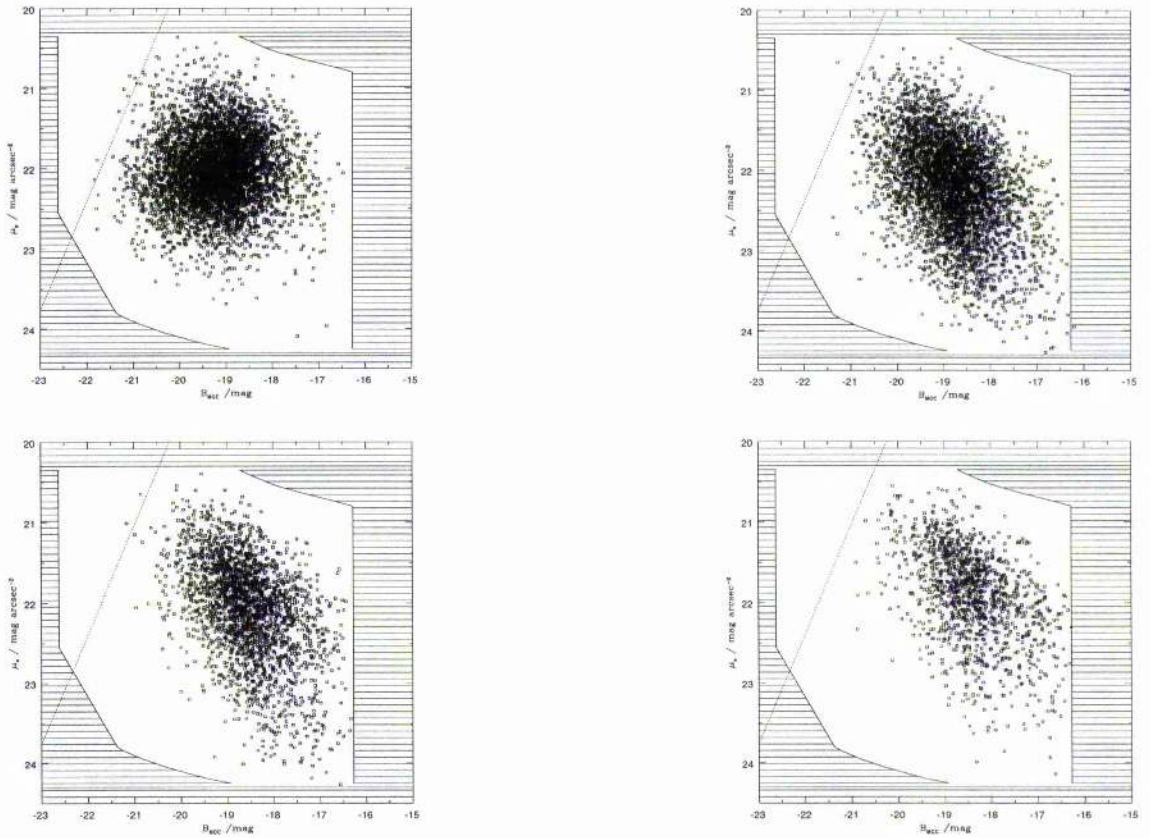


Figure 5.10: This figure shows the distribution of the 4 spectral types of galaxy defined by Madgwick et al. (2001) in M and μ_e . This shows the subsamples used to calculate the BBD via the empirical method. The type 1 distribution is shown in the top left corner, the type 2 distribution is shown in the top right, type 3s in the bottom left and type 4s in the bottom right. The shaded region represents the region where the volume is less than 5000Mpc^3 . The distribution of type 1 galaxies is well within the selection boundaries, and is centred on $M = -19, \mu_e = 22$. Types 2-4 all have a noticeable luminosity- surface brightness correlation, and reduce significantly in numbers before the bright, low surface brightness boundary.

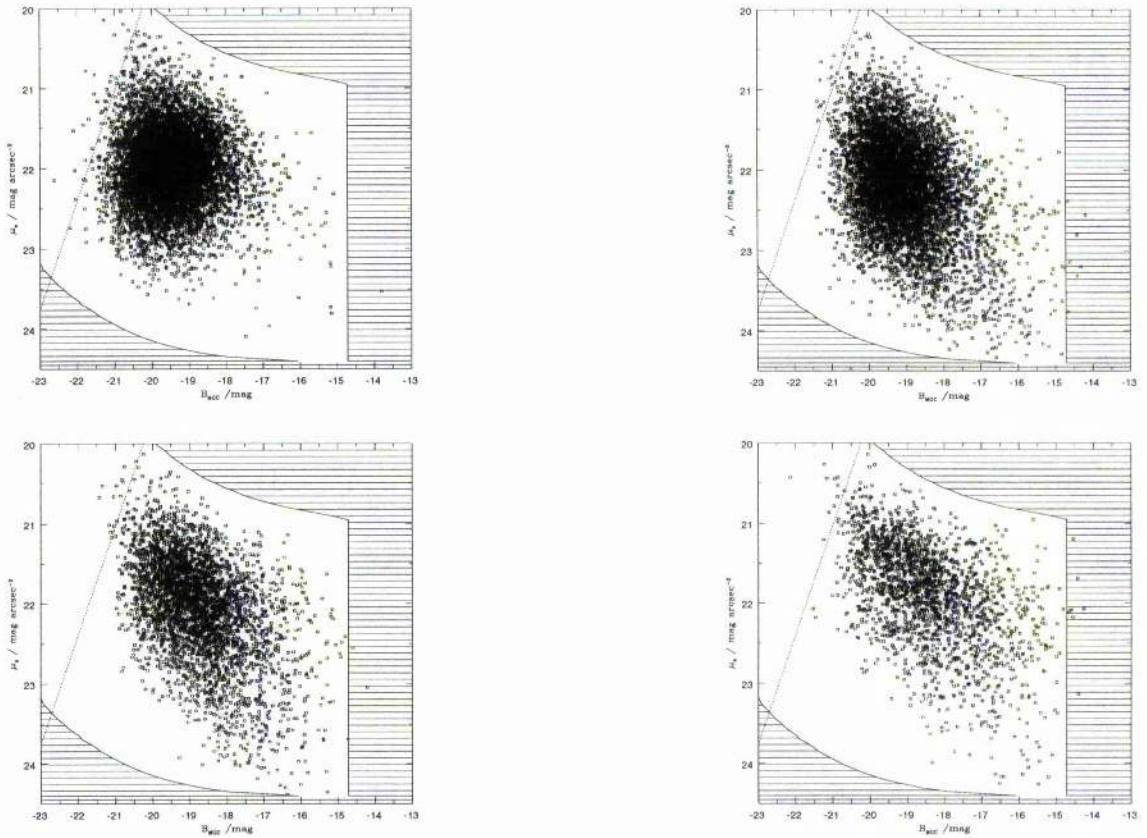


Figure 5.11: This figure shows the distribution of the 4 spectral types of galaxy defined by Madgwick et al. (2001) in M and μ_e . This shows the subsamples used to calculate the BBD via the SWML method. The type 1 distribution is shown in the top left corner, the type 2 distribution is shown in the top right, type 3s in the bottom left and type 4s in the bottom right. The shaded region represents the region where the volume is less than 5000Mpc^3 . The distribution of type 1 galaxies is well within the selection boundaries, and is centred on $M = -19, \mu_e = 22$. Types 2-4 all have a noticeable luminosity- surface brightness correlation, and reduce significantly in numbers before the bright, low surface brightness boundary.

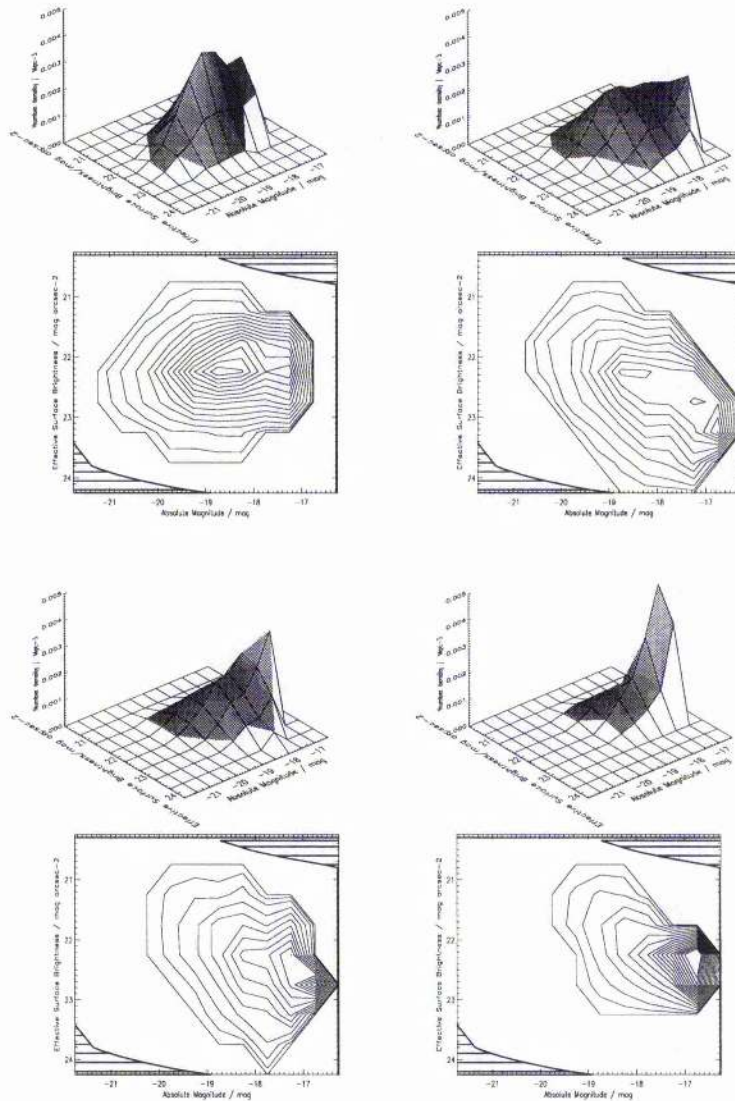


Figure 5.12: The 2dFGRS Bivariate Brightness Distribution as a function of spectral type, all produced via the empirical method. The top left hand plot shows the BBD for η -type 1 galaxies, the top right plot shows the BBD for η -type 2 galaxies, the bottom left hand plot shows the BBD for η -type 3 galaxies and the bottom right hand plot shows the BBD for η -type 4 galaxies. The contour lines for the BBDs are set at 1.0×10^{-7} , 1.0×10^{-4} , 2.5×10^{-4} , 5.0×10^{-4} , 7.5×10^{-4} , 1.0×10^{-3} , 1.25×10^{-3} , 1.5×10^{-3} , 1.75×10^{-3} , 2.0×10^{-3} , and 2.25×10^{-3} galaxies Mpc^{-3} . The shading represents the regions where $V \leq 5000 \text{Mpc}^3$.

μ_e^* appears to get brighter as one moves from type 2 to type 4, it is important to be cautious. μ_e^* correlates with M^* , and while the distributions get significantly fainter going from type 2 to type 4, M^* gets brighter. The 3 parameters μ_e^* , β_μ and σ_μ are similar to those found in Cross & Driver (2001) for the original 2dFGRS data, $\beta_\mu = 0.281 \pm 0.007$, $\mu_e^* = (21.90 \pm 0.01)$ mag arcsec $^{-2}$ and $\sigma_\mu = 0.517 \pm 0.006$, see § 2.7.2.

5.3.1 Comparison with Theory

Since η -type 1 galaxies correlate with early type galaxies, ellipticals and S0s, and η -type 2-4 galaxies correlate with late type galaxies, spirals and irregulars, the luminosity-surface brightness correlation appears to relate to the morphology of the galaxy. de Jong & Lacey (2000) use the Fall & Efstathiou (1980) disk galaxy formation model to predict the BBD. This assumes a dissipational collapse of a gas cloud to form a disk, with angular momentum conserved. Disks are supported by the rotation of the disk. Disks have constant (complete) dissipation but a range of angular momenta. Faint, low surface brightness disks have high angular momentum, and bright, high surface brightness disks have low angular momentum.

Wyse & Jones (1984) discuss the relationships between the rotational parameter (v/σ) to surface brightness and absolute magnitude. The rotational parameter is defined as the ratio of maximum rotational velocity to mean velocity dispersion within half the de Vaucouleurs radius. Brighter and lower surface brightness galaxies tend to have lower rotational parameters, although the correlation is stronger in surface brightness. They argue that dissipation is the key to understanding this correlation since dissipation increases both the surface brightness and the importance of rotational velocities. de Zeeuw & Franx (1991) discuss the dynamics of elliptical galaxies and point out that only the centres will have had time to come into dynamical equilibrium, since the dynamical timescale in the outer parts of elliptical galaxies is similar to the Hubble time ($\gg 10^9$ yrs). Thus elliptical galaxies can be thought of as systems with constant angular momentum but different amounts of dissipation. Fainter, high surface brightness ellipticals have smaller dynamical time scales, since the dynamical time is proportional to $(r^{3/2}/M^{1/2})$, where r is radius, and M is the enclosed mass. Smaller ellipticals will have dissipated more, and be closer to equilibrium. Larger, lower surface brightness ellipticals have had much less dissipation and are further from equilibrium.

Zhang & Wyse (2000) have used these models to discuss the formation of the Hubble sequence for spiral galaxies. They suggest that disks form first, through the dissipational evolution discussed above. Bulges then form from bar instabilities. This gives the variety of bulge-to-disk ratios seen throughout spiral galaxies.

As one moves from η -type 1 to η -type 4, the faint end slope α steepens significantly. η -type 1s represent a distribution that may be better represented by a double Gaussian for the bright population, η -type 2s have $\alpha \sim -0.8$, η -type 3s have $\alpha \sim -1.2$ whereas η -type 4 galaxies have a faint end slope $\alpha = -1.45$. The population becomes intrinsically fainter with each η -type too, although the shape of the functions is such that M^* can actually get brighter. We will discuss the Schechter parameters more in the context of the luminosity function.

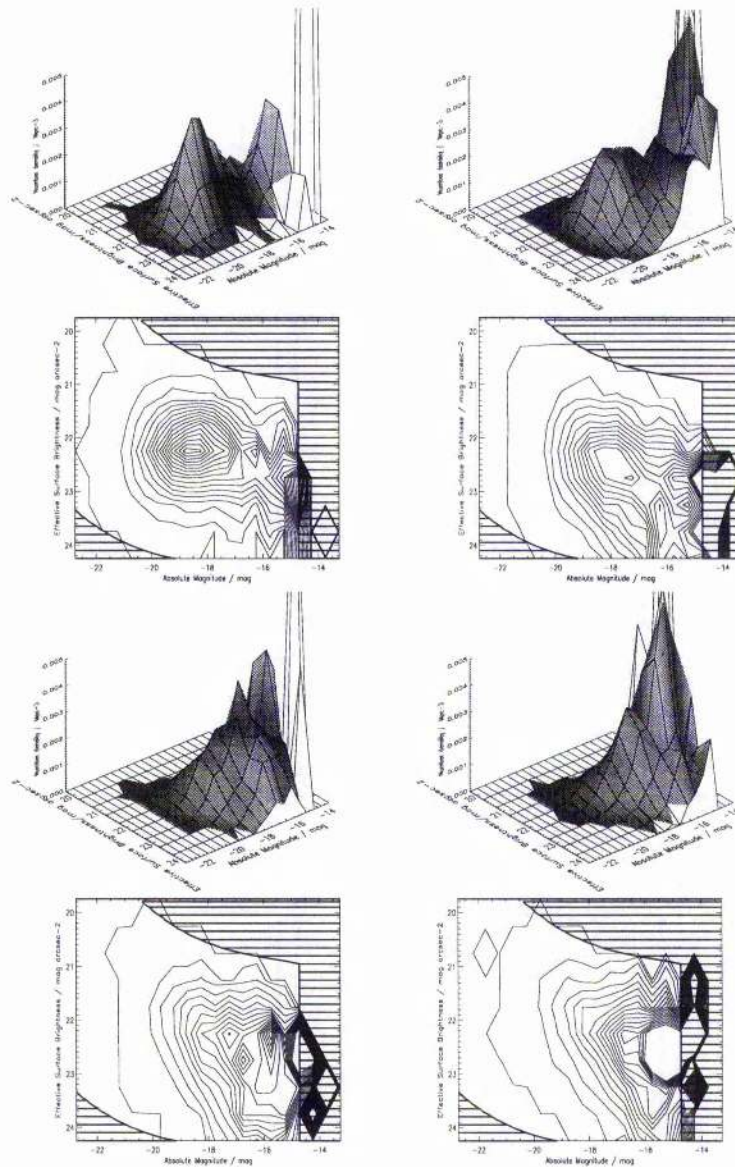


Figure 5.13: The 2dFGRS Bivariate Brightness Distribution as a function of spectral type, all produced via the SWML method. The top left hand plot shows the BBD for η -type 1 galaxies, the top right plot shows the BBD for η -type 2 galaxies, the bottom left hand plot shows the BBD for η -type 3 galaxies and the bottom right hand plot shows the BBD for η -type 4 galaxies. The contour lines for the BBDs are set at 1.0×10^{-7} , 1.0×10^{-4} , 2.5×10^{-4} , 5.0×10^{-4} , 7.5×10^{-4} , 1.0×10^{-3} , 1.25×10^{-3} , 1.5×10^{-3} , 1.75×10^{-3} , 2.0×10^{-3} , and 2.25×10^{-3} galaxies Mpc^{-3} . The shading represents the regions where $V \leq 5000 \text{Mpc}^3$.

5.3.2 Comparison with other Observers

In Table 5.2 we have also listed the parameters obtained by Choloniewski (1985) for elliptical and lenticular galaxies and de Jong & Lacey (2000) for Sb-Sdm spirals. The Choloniewski (1985) data are a sample of 233 galaxies from Sadler (1984), with $m_{est} \leq 14$, $D(ESO) \geq 1'$, and can be compared to η -type 1 BBD. m_{est} is the estimated total brightness and $D(ESO)$ is the maximal isophotal diameter. The data are in the B-band and the parameters have been converted to $H_o = 100 \text{ kms}^{-1}\text{Mpc}^{-1}$. We have converted the absolute magnitude and half light radii values to the absolute magnitude and effective surface brightness parameters using Eqn 2.22. Choloniewski uses Eqn 5.5 to express the luminosity-scalesize correlation:

$$\log r = aM + b \quad (5.5)$$

The conversions from a , b and the width σ_{r_e} to β_μ , μ_e^* and σ_μ are given as:

$$\begin{aligned} \beta_\mu &= 1 - 5a \\ \mu_e^* &= (1 - 5a)M^* - 5b + 38.567 \\ \sigma_\mu &= 5\sigma_{r_e} \end{aligned} \quad (5.6)$$

The Choloniewski (1985) BBF gives a β_μ value close to the SWML value; a flat distribution. However the value of σ_μ and μ_e^* are very different to either the empirical or the SWML values. The value of α that Choloniewski finds is much steeper ($\alpha = -1.35$) although M^* agrees well with the empirical method result.

The de Jong & Lacey sample was also converted to absolute magnitude and effective surface brightness parameters and has been converted from the I-band, see § 2.7.3. In Chapter 2, we compared it to the preliminary 2dFGRS BBD and found that while σ_μ and μ_e^* corresponded, the gradient β_μ was significantly steeper. The increased gradient in the de Jong & Lacey sample could be due to contamination by ellipticals/S0s in the Cross et al. (2001) sample or the colour-luminosity correlation seen by e.g. Marzke et al. 1997, Blanton et al. (2001), Brown et al. (2001), and the colour-surface brightness correlation, Brown et al. (2001). This is discussed in § 2.7.3. However, we can now use the η -type 3 BBD to test whether contamination by ellipticals is the reason for the discrepancy. The η -type 3 sample is mainly composed of Sb-Scd galaxies (see Madgwick et al. 2001) and so it is a straight forward comparison to de Jong & Lacey. The only difference, apart from the selection boundaries which are dealt with by the methodology, is the colour. Again we find that the de Jong & Lacey (2000) sample has a much larger β_μ . The values of μ_e^* and σ_μ lie between the values for the empirical method and the SWML method, so give a good match. However M^* is significantly brighter and α significantly flatter. Blanton et al. (2001) finds no significant change in α with filter for the SDSS luminosity function and finds $\alpha = -1.25$ in the Sloan i^* filter. Since the de Jong & Lacey (2000) sample is quite bright, this effect could be due to a more complicated luminosity function, which starts off flat before rapidly steepening.

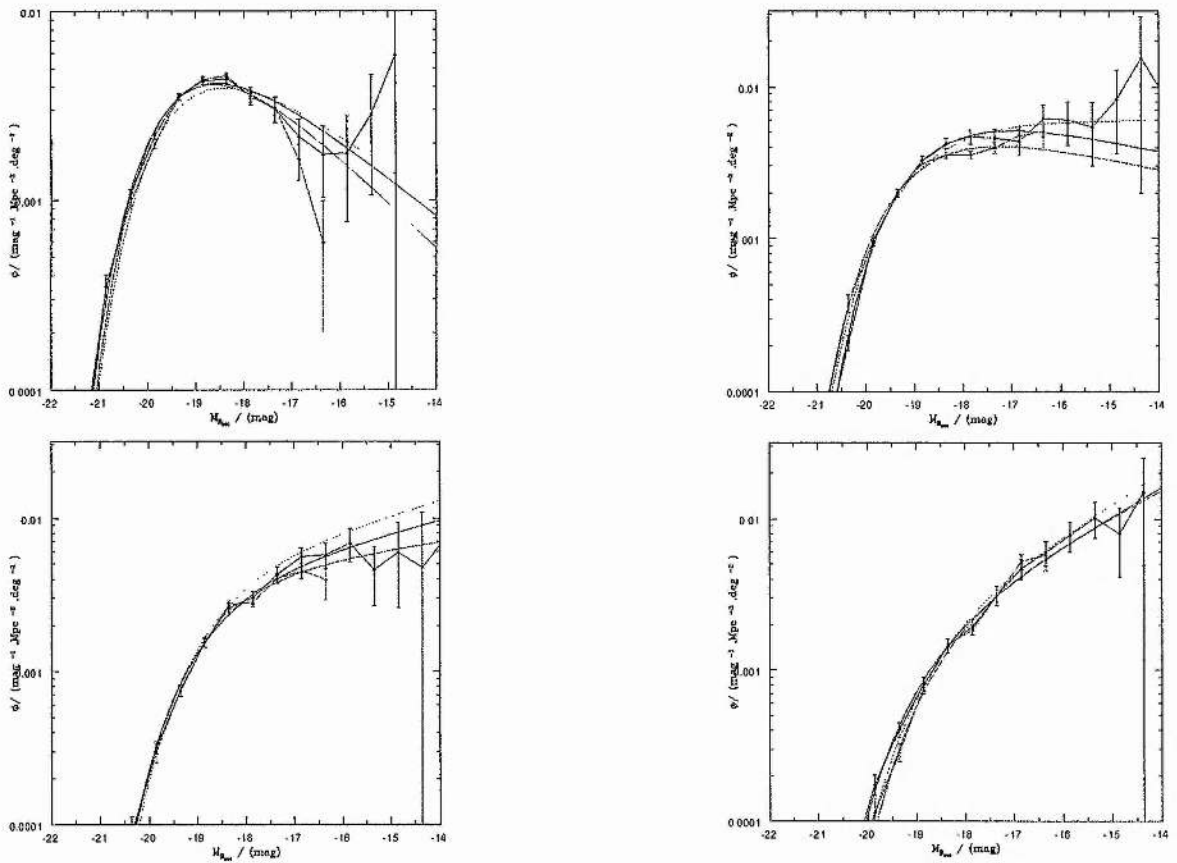


Figure 5.14: The top left hand corner shows the LF for η -type 1 galaxies, the top right shows the LF for η -type 2 galaxies, the bottom left shows the LF for η -type 3 galaxies and the bottom right η -type 4 galaxies. In each the red lines show the LF's produced via the empirical method and the blue lines via the SWML method, with the Schechter function fits shown as the solid curves. The dotted curves show the Madgwick et al. (2001) Schechter function fits.

5.3.3 Luminosity Functions of η -types.

The Madgwick et al. (2001) LF's were produced using a type-dependent K-correction, but not the (K+e) correction derived by Norberg et al. (2002) that we have been using. To compare the results that have a different sets of K-corrections we calculate the difference between the corrections at $z = 0.1$ for each type and apply this offset to the Madgwick LF's. The offset $\Delta M(Norberg - Madgwick) = 0.076$ mag for η -type 1 galaxies, $\Delta M(N - M) = 0.126$ mag for η -type 1 galaxies, $\Delta M(N - M) = 0.016$ mag for η -type 3 galaxies and $\Delta M(N - M) = -0.076$ mag for η -type 4 galaxies.

The η -type 2,3 and 4 luminosity functions calculated above agree well with the Madgwick et al. (2001) LF's. The η -type 1 produced using the bivariate brightness distribution gives a distribution with a slightly brighter M^* .

Since η -type 1 galaxies are predominantly high surface brightness galaxies, they will be most affected by the non-linearities identified in Chapter 3. Thus the magnitudes of many of the η -type 1s will be underestimated, leading to a distribution with a slightly fainter M^* , as observed.

The η -type 2 and η -type 4 luminosity functions produced via the empirical and stepwise methods do not agree with each other. For η -type 2 galaxies, the SWML method produces a luminosity function that is underdense compared to the empirical method at the bright end and overdense at the faint end. The converse is true for η -type 4 galaxies. Fig 5.15 compares the luminosity functions produced by summing each type up with the overall luminosity function using the empirical method and the stepwise method. Using the empirical method, both luminosity functions agree, but using the SWML method, they do not agree. The luminosity function for galaxies without any η -type is unbiased, *i.e. it has the same shape as the overall BBD*, when calculated via the empirical method, but is biased when calculated via SWML.

Norberg et al. (2002) find that their luminosity function gives similar parameters to Madgwick et al. (2001) if they adopt the Madgwick et al. (2001) mean K-correction. We find that the η -type 1s are underestimated, but η -types 1, 2 and 3 are not. Therefore we expect the bright end of LF to be slightly fainter, and this is exactly what we see.

5.4 Missing Galaxies

So far when we have summed the BBD to get the LF we have only summed it over the range $21.0 \lesssim \mu_e \lesssim 24.5$, *i.e.* where the completeness is high. Unfortunately lack of redshifts prevents us measuring the BBD at lower or higher surface brightnesses and thus measuring the LF properly.

Fig 5.13 demonstrates that the completeness is good for $M < -17$, but there is a significant number density of faint low surface brightness galaxies, with $M > -17$, particularly η -type 2 galaxies. Unfortunately, we cannot take these into account properly by just summing in surface brightness. We must extrapolate beyond the limits to estimate the missing contribution of low surface brightness galaxies.

However, the analytical functions can be extrapolated beyond the selection limits. When the Choloniewski function is summed across the whole range of surface brightness, the result is a Schechter function, with the same parameters M^* , ϕ^* and α . Since we have shown that the Choloniewski function gives a very poor fit to the BBD for the whole data set, but gives better fits to each type, we will sum the distributions for each type to give the final luminosity function, which has been corrected for selection effects, includes photometric corrections, redshift incompleteness corrections and photometric incompleteness corrections.

Unfortunately the fits are still not good enough to extract a reliable LF by this method, see Fig 5.16. Separating galaxies into morphological types rather than spectral types and using better fitting functions will improve the results.

5.5 Summary

In this chapter we have used the much larger data set of the 2dFGRS to help to constrain the faint end of the luminosity function and to look at the BBD of the spectral types identified by Madgwick et al. (2001). To be able to use this data set, we first had to correct the 2dFGRS magnitudes and surface brightnesses to the MGC values removing non-linearities. We find that the errors are significantly reduced and are Gaussian.

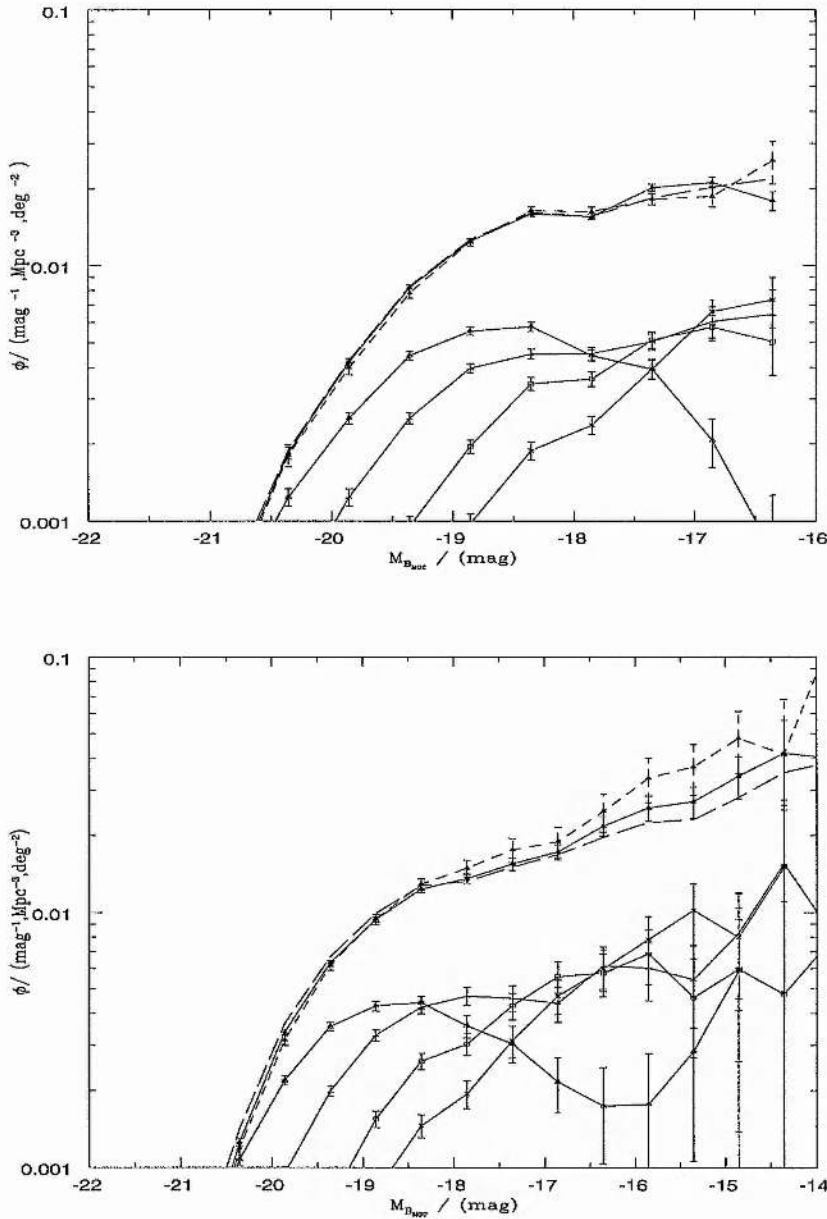


Figure 5.15: Plot showing the LF for all the η -types plotted together. The top plot shows the LFs produced via the empirical method and the bottom plot shows the LFs produced via the SWML method. The open triangles are the η -type 1 LFs, the 3 pointed crosses are the η -type 2 LFs, the open squares are the η -type 3 LFs, and the 4 pointed crosses are the η -type 4 LFs. The combined LFs are also shown. The solid line represents the LF produced from all the galaxies. The short dashed line represents the LF produced from galaxies without a spectral classification and the long dashed line is the sum of the LFs for the four spectral types. The 3 combined LFs agree well for the LFs via the empirical method, suggesting that there is no bias, but do not agree for the SWML, suggesting some bias in the incompleteness correction.

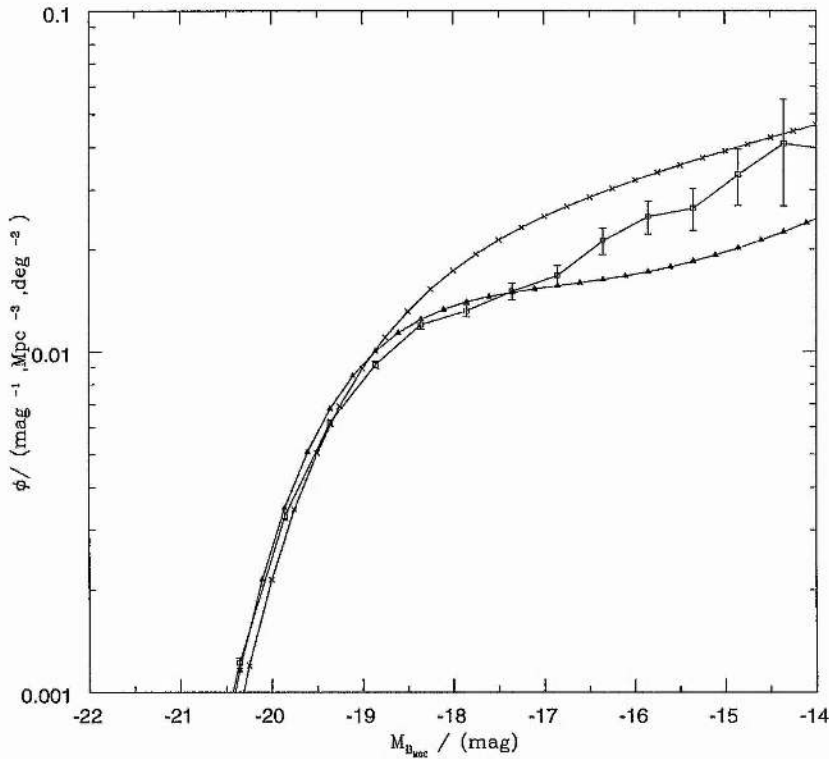


Figure 5.16: This plot shows the final LF (triangles) when the Schechter parameters of the 4 η -type BBFs, from the Empirical method are added up. The LF with squares is the LF found by summing the BBD within the limits. The LF with crosses is the 2dFGRS LF from Norberg et al. (2002). At the bright end the number density increases by $\sim 10\%$, demonstrating the effects of galaxies beyond the selection boundaries. Poor fits to the BBF, particularly by the η -type 1 galaxies leads to an underestimate at the faint end.

When we use the whole 2dFGRS dataset on the 15 plates in common we find that the faint end slope steepens significantly for $M > -17$, consistent with the ESP LF (Zucca et al. 1997) and the Abell cluster LF (Driver et al. 1994).

When we separate the data into the four spectral types we find that the η -type 1 galaxies form a tight puddle of galaxies at the bright, high surface brightness end of the overall BBD, well inside the selection boundaries, with a separate group of galaxies at the faint end which increases up to the selection boundaries. The type 1 BBD is not well fit by the Choloniewski function and the two methods give very different fits. The empirical method gives a fit which has a luminosity surface brightness correlation close to that found by Kormendy (1977). The SWML result, which penetrates to fainter limits picks up this second group of galaxies and gives a flat relationship between luminosity and surface brightness.

The spectral types 2-4, which are closely related to spirals/irregulars show a strong luminosity-surface brightness relationship which is lost in the whole data set by the type 1/elliptical galaxies. The gradient and width do not vary with type, although there is great variation in the luminosity function with type.

Overall, the luminosity functions found by summing the BBDs in surface brightness reproduce the luminosity functions found by Madgwick et al. (2001).

By summing up the BBDs across the whole surface brightness range we can account for galaxies outside the surface brightness limits of the MGC/2dFGRS and get a better estimate of the luminosity function. Unfortunately the BBF is not well fit to the whole distribution. When we apply the BBFs for each type we increase the number density slightly at the bright end, but miss galaxies at the faint end. This is due to the poor fit that the Choloniewski LF has to the η -type 1 galaxies.

Chapter 6

Conclusions

6.1 Conclusions

The focus of this thesis has been two fold: to understand the variation seen in the published values of the luminosity function and the surface brightness distribution; to study the distribution of galaxies in absolute magnitude and effective surface brightness with a view to eventually constraining models of galaxy formation and evolution.

To solve both these problems we have used the bivariate brightness distribution to measure the number density in absolute magnitude (M) and effective surface brightness (μ_e). Using the BBD we test for and remove the surface brightness selection effects described in § 2.4 as well as assess completeness, photometric errors, clustering and the volume over which galaxies can be seen in both M and μ_e . The BBD gives us additional constraints on the formation and evolution of galaxies, see e.g. Dalcanton, Spergel & Summers (1997), de Jong & Lacey (2000) and Zhang & Wyse (2000). In this thesis, we have not developed models, or thoroughly tested models with our data. We have concentrated on calculating the BBD free of surface brightness selection biases.

To calculate the BBDs we have used two methods. The first, published in Cross et al. (2001) is an empirical method, which uses the data as much as possible, to define the selection limits and calculate the necessary corrections. The maximum redshift that a galaxy can be seen to at each M and μ_e is determined from the distribution of galaxies within that bin and a volume limited sample is defined to calculate the amount of clustering as a function of redshift. The incompleteness is also calculated from the data. We describe this method in § 2.6.1. The second method is a more theoretical method, based on the stepwise maximum likelihood method (SWML, Efstathiou, Ellis & Peterson 1988), updated to two dimensions to take into account surface brightness using Sodr  & Lahav (1993) and then modified to take into account visibility theory (Phillipps, Davies & Disney 1990) in § 2.6.2.

We find that both methods give closely matching results for the BBDs calculated in Chapter 4, and for most of the BBDs calculated in Chapter 5. Where there were differences, for η -type 2 and η -type 4 galaxies it appears that the incompleteness correction, which was applied in similar ways for both methods failed when the SWML method was used. Overall the two methods are consistent, demonstrating that our estimators are not causing any systematic errors.

We fitted the Choloniewski (1985) bivariate brightness function (BBF) to a preliminary Two degree Field Galaxy Redshift Survey (2dFGRS) data set, and show that all of the variation at the bright end can be accounted for by the variation in the isophotal detection threshold

($23 < \mu_{lim} < 26$). However, we find that there is greater variation in the faint end than we can account for by surface brightness selection effects alone.

In Chapter 3, we tested the reliability of the 2dFGRS and the Sloan Digital Sky Survey Early data Release (SDSS-EDR) photometry, using a deep wide field CCD survey that covers 36deg^2 of an equatorial strip coincident with both the 2dFGRS Northern Galactic Pole (NGP) region and the SDSS-EDR. This survey, the Millennium Galaxy catalogue (MGC) has a depth of 26 mag arcsec $^{-2}$ and typical seeing of 1.3". The rms scatter between objects in the overlap regions is 0.023 mag (Liske et al. 2002).

We found that the 2dFGRS has 6.0% stellar contamination, which agrees well with the estimate of Maddox et al. (1990b) of 5%, and the measured spectral contamination 6% (Colless et al. 2001). Fig 3.8 shows that there is good agreement between the MGC classification and the spectral classification. We found that 8.4% of 2dFGRS objects had two or more MGC counterparts. As Fig 3.13 demonstrates, the flux of the 2dFGRS object matches the combined flux of these objects, suggesting that these objects were blended on the Schmidt plates, or by the Automated Plate Measuring (APM) machine, rather than one object being too faint or too small to get into the catalogue.

When the photometry of the 2dFGRS was compared to the MGC photometry, we find $\Delta m(MGC - 2dF) = -0.078 \pm 0.157$. However, we find that there are significant non-linearities in the magnitudes at the high surface brightness end, which increase with increasing surface brightness. When we do a similar comparison to the SDSS-EDR we find that $\Delta m(MGC - SDSS) = -0.009 \pm 0.100$, and we do not see any scale error in magnitude or surface brightness. Therefore it appears that it is the 2dFGRS which has the scale errors. Photographic plates, such as the Schmidt plates that the 2dFGRS magnitudes are measured from are non-linear in their response. These are very difficult to correct properly, especially when the flux of photons is high. Modern CCDs, which the MGC and SDSS are based on have a linear response, but have additional problems with readout noise, bleeding and defects. More importantly, CCDs cannot cover such a wide area, and it is only recently that improving sizes have made wide field CCD surveys possible.

We have tested the photometric completeness of the 2dFGRS and SDSS-EDR. We find that while the SDSS is $\lesssim 2\%$ incomplete at $B_{MGC} = 19$, rising to $\lesssim 3\%$ at $B_{MGC} = 20$, the 2dFGRS is $\sim 8.2\%$ incomplete up to $B_{MGC} = 19$, with an extrapolated incompleteness of $\sim 14\%$ at the 2dFGRS limiting magnitude ($b_j = 19.45$, $B_{MGC} = 19.51$). We find that both the SDSS-EDR and the 2dFGRS are missing low surface brightness galaxies (due to the surface brightness limits) and small angular size galaxies (due to star-galaxy separation). However, the 2dFGRS also misses a significant number of blended objects and normal galaxies. Since the brightest component of blended objects was taken to be the match, the missing secondary objects were biased towards the faint end. Only $\sim 5\%$ of missing 2dFGRS galaxies are low surface brightness galaxies (LSBGs). However, the MGC misses objects with $r_e \gtrsim 16''$, so we are incomplete for some bright low surface brightness galaxies. The combined photometric completeness of the 2dFGRS and SDSS is high, see Fig 3.40, with the incompleteness only rising above 10% for the faint, low surface brightness objects.

We also test the redshift incompleteness of 2dFGRS and SDSS and find that the redshift

incompleteness has a strong surface brightness dependence, particularly in the 2dFGRS. This problem was highlighted by Schectman et al. (1994) and Lin et al. (1996) for the Las Campanas Redshift Survey (LCRS). Fig 3.42 demonstrates the redshift completeness in the B_{MGC}, μ_e plane of the combined MGC, 2dFGRS and SDSS-EDR data set that we have produced.

This data set with MGC photometric parameters, 2dFGRS redshifts and spectral types and SDSS-EDR redshifts is used to measure the BBD accurately in Chapter 4. It contains accurate photometry which has been tested against the 2dFGRS and SDSS, and a deep isophote, so it is complete beyond the limits of the 2dFGRS and SDSS. Every $B_{MGC} < 20$ object has been eyeballed for careful star-galaxy separation, which is consistent with spectroscopic estimates. The selection limits are well defined for this data set and the greatest limitations are found to be the redshift incompleteness of the 2dFGRS and SDSS-EDR.

We find that the distribution of galaxies in the M, μ_e plane is seen right up to the selection boundaries, except at the bright high surface brightness end. Some limits were imposed to produce a high completeness sample, with well defined selection limits, and these are not strictly detection limits. However, some limits, such as the maximum half-light radius are detection limits but are not taken into account in most surveys. The problems associated with background estimation and subtraction are potentially the greatest hindrance to finding giant low surface brightness galaxies.

The bright, high surface brightness edge of the galaxy distribution is a fitted by Eqn 4.1. This has the same gradient as the Kormendy (1977) relationship for elliptical galaxies. However, the Kormendy (1977) and similar Thomsen & Frandsen (1983) relation are fainter than this edge by 1.25 mag and 1.75 mag respectively. If the population of elliptical galaxies was bracketed between this edge and bright selection limits, then these relationships will be seen, whether these are true relationships or not.

A few (~ 10) galaxies are seen beyond this edge. The brightest, lowest redshift of these is MGC02897, displayed in Fig 4.3, which has the colours and spectral type of a typical elliptical galaxy. The image reveals that MGC02897 looks like an elliptical, but has some additional disk structure or possibly tidal tails. The simplest explanation is that MGC02897 underwent a merger in the recent past, and the starburst resulting from it significantly increased the magnitude/surface brightness of MGC02897. The Larson & Tinsley (1978) models showed that a typical burst of star-formation typically doubles a galaxies luminosity (the magnitude becomes 0.75 mag brighter - corresponding to the position of MGC02897 and the other candidates) and the objects often (but not always) have anomalous $(U - B)$ and $(B - V)$ colours. Schweizer (1982) demonstrated that the well known merging galaxy NGC 7252 is quite well fitted by a de Vaucouleurs' profile, suggesting that the central parts have relaxed to an equilibrium configuration even though it is clearly irregular at large radii with prominent tidal tails.

One would expect MGC02897 to be much bluer, as the result of a starburst. While hot blue stars do not last long ($\sim 10^7$ yrs), the stellar population can take a long time $\sim 10^{10}$ yrs, Larson & Tinsley (1978), to reach the colours of MGC02897 ($(B - V)=0.93$), in a single star-burst model. Since two colliding galaxies each with magnitudes $M_B \sim -20$ will already have undergone significant star formation and will therefore have lost a significant fraction of their original gas, the effects of a starburst will be small, by dynamical effects such as

tidal tails will still be seen. Features such as tidal tails take $\sim 5 \times 10^8$ yrs, Toomre (1977) to disappear. If MGC02897 is really a merger remnant, then it is likely to be $\sim 10^8$ years old. This illustrates the usefulness of the BBD when it comes to selecting interesting objects for further study, and may eventually lead to an understanding of how galaxies evolve, in the same way as the Hertzsprung-Russell diagram lead to an understanding of stellar evolution. However, a trivariate distribution involving intrinsic colours or other parameters may be needed before this is possible.

The BBDs produced by the MGC data are not well fit by the Choloniewski function. The gradient of the luminosity surface brightness correlation appears to get steeper as the selection boundaries move to fainter absolute magnitudes. As we show in Chapter 5, this is because the population of galaxies is made up of many types, each with a different BBD. The width in surface brightness of the overall MGC BBD is 50% higher than that found in Cross et al. (2001). This is due to the improved measurements of absolute magnitude, and particularly, of surface brightness. The improvements have included using Kron magnitudes rather than fitting exponential profiles, using a direct measurement of the half-light radius to calculate the effective surface brightness rather than extrapolating the profile to get a central surface brightness and finally, taking into account the inclination of galaxies. The fit to the BBD does not appear to depend significantly on the redshift completeness since both subsamples used (subsample 1 with $\gtrsim 80\%$ completeness in all bins and subsample 2 with $\gtrsim 70\%$ completeness in all bins) give the same BBD parameters except for the gradient of the luminosity-surface brightness correlation, when measured via the SWML method. When the empirical method is used, neither subsample gives a good fit. This is due to the smaller subsamples used by this method combined with the difficulty in measuring the BBD when it is changing from an elliptical dominated regime to a spiral dominated regime.

When the BBDs are summed to produce the luminosity function, they give equivalent space densities right up to the selection boundaries. However, while the luminosity functions are equal the fitting function parameters are very different, and diverge rapidly beyond the selection limits. The MGC LFs are brighter than the 2dFGRS LF, Norberg et al. (2002), by ~ 0.1 magnitude, but have a much flatter faint end slope α . This is consistent with the results of Chapter 2, when it was shown that not taking into account surface brightness selection effects would make the M^* value fainter, and reduce the value of ϕ^* , but would only steepen the faint end slope α slightly. Since the 2dFGRS uses corrected magnitudes that are then calibrated to deeper CCD photometry, we expect to see the offset for Gaussian corrected magnitudes at $\mu_{lim} = 26.0 \text{ mag arcsec}^{-2}$. This gives a decrease in M^* of 0.06 mag and a decrease in ϕ^* of 5.5% and no significant change in α . In reality we see a decrease in M^* of 0.075 ± 0.025 mag, no change in ϕ^* and a steepening of α by $\Delta \alpha \sim 0.2$. The change in M^* is as we expect and since the Norberg et al. (2002) LF is normalised to the number counts, their value of ϕ^* should not differ from ours, as seen. The change in α though is unexpected. In Chapter 5, we demonstrated that this difference can be accounted for by a rapid increase in the number density of faint $M_B > -17$ galaxies. The lower value of α measured in the Northern Galactic Pole (NGP) region, $\alpha \sim -1.14$, compared to the SGP, $\alpha \sim -1.28$ by Norberg et al. (2002) is also a contributing factor, since the MGC is in the NGP region. This difference is likely to be

due to local inhomogeneities since the dwarf population can only be observed in small, nearby volumes.

We also compare a few other recent LFs - the ESO Slice Project (ESP, Zucca et al. 1997) and the Sloan Digital Sky Survey (SDSS, Blanton et al. 2001). We find that the SDSS LF is brighter by 0.1 mag and has a significantly higher number density (40% at all magnitudes) than either 2dFGRS or ESP. Norberg et al. (2002) compare overlapping 2dFGRS and SDSS-EDR data and find that the discrepancy is due to a combination of Blanton using the wrong colour equation when converting to b_j , the effects of evolution and a higher number density in the region of sky that Blanton used. We have been careful to take these factors into account when calculating our BBDs and LFs. When these are taken into account the SDSS LF closely matches the 2dFGRS LF. The ESP gives the best fit to the MGC at the bright end, although it is fainter by ~ 0.05 mag.

When the BBD is summed along the luminosity direction to produce the surface brightness function, we find a flat distribution similar to O'Neil & Bothun (2000). We find that the distribution becomes flatter as the magnitude range over which it is summed increases. This is due to the gradient of the luminosity-surface brightness correlation. The distribution is flatter than the Freeman (1970) result and the Cross et al. (2001) result. The number density of galaxies appears to be constant over a wide range of surface brightness, which is an important constraint on galaxy formation models. However, care must be taken, since there are correlations between luminosity and surface brightness, and we are only probing the most luminous galaxies.

The BBD shows a decrease in number density before it reaches the selection boundaries, except at the faint, low surface brightness region. This demonstrates that giant low surface brightness galaxies, such as Malin 1, or faint high surface brightness galaxies, such as M32, do not contribute much to the space density of galaxies. These galaxies are nevertheless important since a model of galaxy formation and evolution that could not account for these objects would be incomplete. The rising population at the faint end demonstrates that we may still not be seeing the majority of galaxies, even though, as we demonstrated in Chapter 2, we account for $\sim 98\%$ of the luminosity density, unless the faint end becomes significantly steeper. The faint end slope would have to have $\alpha \sim -2.0$ for dwarf galaxies to contribute significantly to the luminosity density. Zucca et al. (1997) found a faint end slope $\alpha = -1.57$ and Driver et al. (1994) found a faint end slope $\alpha = -1.8$ for dwarfs. This suggests that there are not enough dwarf galaxies for them to dominate the luminosity density of the universe.

We measure the luminosity density of the universe to be $j_B = (1.64 \pm 0.17) \times 10^8 h L_\odot \text{Mpc}^{-3}$ using an Einstein-de Sitter cosmology and $j_B = (1.56 \pm 0.17) \times 10^8 h L_\odot \text{Mpc}^{-3}$ using a Λ -CDM cosmology. The 2dFGRS results (Norberg et al. 2002) are $j_B = (1.83 \pm 0.17) \times 10^8 h L_\odot \text{Mpc}^{-3}$ and $j_B = (1.74 \pm 0.17) \times 10^8 h L_\odot \text{Mpc}^{-3}$ for the two cosmologies. The ESP result (Zucca et al. 1997) is $j_B = (1.99 \pm 0.20) \times 10^8 h L_\odot \text{Mpc}^{-3}$ for the Einstein-de Sitter cosmology. Liske et al. (2002) use the MGC number counts to constrain j_B and find that $(1.59 \leq j_B \leq 1.77) \times 10^8 h L_\odot \text{Mpc}^{-3}$. The ESP, and 2dFGRS are overestimating the medium to faint end of the luminosity function, as well as underestimating the very bright end.

Very recent luminosity functions, from the ESP (Zucca et al. 1997), the 2dFGRS (Norberg

et al. 2002) and the MGC agree to within ~ 0.1 mag at the bright end with no difference in the normalisation. While our estimates of α are significantly shallower, the results from Chapter 5 demonstrate that this is caused by a steepening of the LF at $M_B = -17$. The estimates of the luminosity density agree within 20%. This is a significant improvement from Fig 1.1 and Table 1.2.

Given the high redshift incompleteness in many regions of the M, μ_e plane, we are only able to use ~ 3000 of the ~ 6000 MGC galaxies with redshifts. Therefore it has been impossible to break the MGC BBD into subsamples. The 2dFGRS contains many more galaxies, $\sim 200,000$ with redshifts at the time of writing (November 2001), but has biases in the photometry. On the 15 plates that overlap with the MGC, we have calibrated the 2dFGRS magnitudes and mean surface brightnesses to the MGC magnitudes and effective surface brightnesses, correcting for non-linearities. This gives us a data set of 66,000 galaxies, which after the application of the selection limits used in Chapter 4 becomes 31000 galaxies with redshifts, an order of magnitude increase.

Using this much larger data set, we are able to probe the faint end of the BBD and look at the separate distributions for each η -type. When we look at the faint end, we find that it steepens significantly beyond $M = -17$, as seen in the ESP (Zucca et al. 1997) and Abell cluster data (Driver et al. 1994). When we look at Fig 1.1 we see that the shallow surveys find flat LFs ($\alpha \sim -1.0$) whereas the deeper surveys find a steeper LF ($\alpha \sim -1.2$). This demonstrates that a change is occurring in the LF between the limits of the bright surveys and the deep surveys and therefore the Schechter function is not a good description of the luminosity function. The Schechter function fits to the deeper surveys lead to an overestimate of the space density in the range $-19 < M_B < -17$, which explains the discrepancy between the estimates of j_B from deeper surveys such as ESP and 2dFGRS compared to the estimates from the number counts, Liske et al. (2001).

When we split the population up into the four spectral types identified by Madgwick et al. (2001) we find that three of these types, η -types 2-4, have similar luminosity surface brightness gradients ($\beta_\mu \sim 0.23$) and widths ($\sigma_\mu = 0.56$). This should be a strong constraint on theories of the formation of spiral galaxies. These 3 spectral types are well correlated with spirals and irregulars. de Jong & Lacey (2000) predict that $\beta_\mu = \frac{1}{3}$, but our results suggests that a theory that predicts $\beta_\mu = \frac{1}{4}$, fits the B-band BBD better. Spectral type 1 galaxies are well correlated with E/SO galaxies and have a flat or negative β_μ value. Hence a combination of all these types is not well fit by a BBF. The width of the η -type 2-4 distributions is significantly less than that derived from the MGC fit, but close to the de Jong & Lacey result, suggesting that it was the combination of types rather than the improved values of surface brightness that increased the width, since the surface brightness measurements used in Chapter 5 are equivalent to the MGC within random errors. The η -type 1 BBD does not give a good match to the Choloniewski (1987) BBD for E/SO galaxies. When the η -type 3 BBD and the de Jong & Lacey BBD are compared, we find a similar width σ_μ to the surface brightness distribution, and a similar μ_e^* point, but we get a shallower gradient β_μ to the luminosity-surface brightness correlation, and we get a fainter, steeper luminosity function. The difference in β_μ is probably due to the variation in the filter, B -band for the MGC, and I -band, for the de Jong & Lacey

sample. The variation in M^* and α could be due to a difference in galaxy types, if η -type 3s correspond to later types than Madgwick et al. (2001) suggest, or it could be that de Jong & Lacey are only sampling intrinsically bright galaxies, where the faint end slope is not as steep.

The luminosity functions produced for each η -type match the Madgwick et al. (2001) LFs, apart from η type 1, galaxies which are brighter by 0.075 ± 0.025 mag. However, there are differences between the luminosity functions derived via the empirical method and SWML method for η -types 2 and 4. These differences appear to be caused by incorrect completeness estimates for different types calculated for the SWML method.

In principle the BBFs can be used to account for galaxies missing beyond the selection limits of the survey. In practice, though, the fits to the BBFs were not good enough to give a sensible result, except at the very bright end. η -type 1 galaxies in particular are poorly fit, and the rising population of dwarf ellipticals is fit by a steadily falling function.

6.2 Summary and Future Work.

We have shown that surveys over the last 10 years have produced a range of luminosity functions which vary by a factor of 2 at the bright end, and a factor of 10 at the faint end. Given the importance of the luminosity functions in testing evolutionary models, this is extremely worrying.

We have shown that the variation at the bright end can be accounted for by surface brightness selection effects. At the faint end, a combination of a steepening faint end slope which is poorly fitted by Schechter functions, uncertainty in the clustering correction as well as surface brightness selection effects give rise to the variation. When we compare very recent surveys with our results, we find that the variance between the luminosity functions has significantly reduced. While there is still an offset in magnitude $\lesssim 0.1$ mag, due to light loss and incompleteness, there is no variation in the normalisation since the results are normalised by the number counts. The bright end of the luminosity function and the luminosity density are now determined to within the random errors of the survey, rather than being dominated by unknown systematics.

The steepening faint end slope comes about from a combination of many different galaxy types. These also present problems when it comes to fitting functions to the bivariate brightness distribution, as different types have different correlations between M and μ_e . The Schechter and Chołoniewski functions need to be updated to fit more complicated distributions which show interesting substructure.

When the distribution of galaxies is plotted in M and μ_e we find that spiral galaxies have a strong correlation between M and μ_e , $M \propto 0.23\mu_e$. This does not change significantly from early type spirals to late type spirals. Elliptical galaxies do not have a strong correlation, but have a sharp edge at the bright, high surface brightness end. This edge has the same gradient as the Kormendy (1977) relation. A few galaxies are found beyond this edge and show tentative signs of recent mergers, demonstrating the possible future use of the BBD to test models of galaxy evolution.

In the future we intend to look at the variation of the BBD with colour to see if the luminosity-surface brightness relation amongst spirals does indeed steepen as one moves to

redder wavelengths. We are also getting morphological classifications for all MGC galaxies with $B_{MGC} < 20$, using code developed by Odewahn et al. (2000). We will produce morphological BBDs and compare them to the spectral type BBDs and improve the comparison between spectral and morphological types, which was done on a few galaxies in both the 2dFGRS and Kennicutt (1992) sample. We intend to use functional forms that give better fits to the BBD, such as Gaussians (Bernardi et al. 2001) in the luminosity direction for η -type 1 galaxies, a combination of Schechter functions and power laws in the luminosity direction for later types (Zucca et al. 1997).

With complete bulge-disk decomposition using GIM2D (Simard et al. 2001) we will be able to get even more reliable magnitudes and surface brightnesses. We will be able to look at the variation in disk parameters only or bulge parameters only which will lead to a greater understanding of how these objects are formed. We will be able to do tests of models such as the Zhang & Wyse (2000) model of how the Hubble sequence formed, especially by doing a similar comparison at high redshift.

The main problem with the MGC bright catalogue is the redshift incompleteness. We intend to measure all the redshifts of galaxies to $B_{MGC} = 20$. This will not only increase the numbers in our subsamples but will also target new types of galaxy missed by the 2dFGRS and SDSS - very low surface brightness galaxies ($\mu_e > 25$ mag arcsec⁻²) and compact galaxies which are misclassified as stars. Using the MGC to select targets for future spectroscopic observations, combined with using the full SDSS database with the techniques developed in this thesis, will significantly increase the parameter space of the low redshift BBD that can be reliably measured. The MGC will be able to probe 1.5 mag arcsec⁻² deeper than the SDSS, and will therefore be able to measure the low surface brightness population. The size of the SDSS means that it will give the most reliable measurements of the faint end of the BBD.

As one moves to higher redshifts, cosmology and evolution become important. Measuring the BBD at $z = 1$, using e.g. the Advanced Camera for Surveys on the Hubble Space Telescope, would put important constraints on the models of formation and evolution. Fortunately, we have time on this instrument. Driver (1999) found evidence for a luminosity-surface brightness correlation at $z = 0.4$, but the sample of 50 galaxies was too small to measure the number density or measure more than the gradient. Does the $z = 1.0$ BBD have the same gradient and width as the $z = 0$ BBD among spirals? Driver (2000) looked at the evolution of ellipticals, spirals and irregulars in the Hubble Deep Field and concluded that there are strong selection biases in the data. When these were removed the sample was too small to get a statistically significant result. In the next few years we would like to address this issue. The techniques developed here will be essential, because cosmological dimming will be a major factor. At $z = 1$, the cosmological dimming reduces the surface brightness by a factor of 16 - 3 mag arcsec⁻². On top of this there are poorly understood K-corrections.

Lastly, we have briefly discussed odd objects, such as MGC02897 and the use of the BBD as the equivalent of the Hertzsprung-Russell diagram, with possible additional axes, such as intrinsic colour. The most important task first is choice of axes. Principle Components Analysis (PCA) or other multivariate methods can be used to find the axes which give the most information. Whitmore (1984) found that 85% of the variation amongst 60 spirals can be

attributed to two components, one the 'scale', a combination of absolute magnitude and radius, and the other 'form', a combination of the blue-infrared colour index and the bulge-to-total ratio. For these methods to work, a wide range of parameters is necessary. The MGC bright catalogue will have magnitudes, surface brightnesses, colours, spectral types, morphological types and the bulge-disk decomposition parameters from GIM2D. These can be converted to intrinsic parameters for the 12000 galaxies. It should be clear which parameters are the most important for a much wider range of galaxies.

Bibliography

- Allen R.J., Shu F.H. 1979, ApJ, 227, 67
- Andredakis Y.C. 1998, MNRAS, 295, 725
- Andreon S., Cuillandre J.-C., Pelló 2000 in IAP Meeting "Constructing the Universe with Clusters of Galaxies", Eds Durret F.& Gerbal D.
- Andreon S., Cuillandre J.-C., 2001, ApJ, submitted
- Babul, A., Rees, M., 1992, MNRAS, 255, 346
- Babul, A., Ferguson, H.C., 1996, ApJ, 458, 100
- Balbi A., Ade P., Bock J., Borrill J., Boscaleri A., de Bernardis P., Ferreira P.G., Hanany S., Hristov V.V., Jaffe A.H., Lee A.T., Oh S., Pascale E., Rabii B., Richards P.L., Smoot G.F., Stompor R., Winant C.D., Wu J.H.P. 2000, ApJL in press (astro-ph 0005124)
- Beijersbergen, M., de Blok, W.J.G., van der Hulst, J.M. 1999, A&A, 351, 903
- Bekki K., Couch W.J., Drinkwater M.J., Gregg M.D., 2001, ApJ, 557, L39
- Bennett A.S. 1962, MmRAS, 68, 163
- Bernardi M. et al. (The SDSS Team), 2000, AJ, submitted
- Bertin E., Arnouts S. 1996. A&AS, 117, 393
- Bertin E., SExtractor v2.0 User's Guide.
- Binggeli, B., Sandage, A., Tammann, G.A., 1988, ARA&A, 26, 509
- Binggeli, B. 1993 in ESO/OHP Workshop on Dwarf Galaxies, Eds Meylan G.,& Prugniel P., (Publ: ESO, Garching), 13
- Bland-Hawthorn J. et al. (The 2dFGRS Team) 2002, in preparation
- Blanton M.R. et al. (The SDSS Team) 2001, AJ, 121, 2358
- Bomans D.J. Habertzettl L. 2001 in "The New Era of Wide Field Astronomy", ASP Conference Series, Vol. 232. eds Clowes R.G., Adamson A.J. & Bromage G.E.
- Bothun, G.D., Impey, C.D., Malin, D.F., Mould, J.R. 1987, AJ, 94, 23
- Boyce P.J. Phillipps S. 1995, A&A, 296, 26
- Bristow, P.D., Phillipps, S., 1994, MNRAS, 267, 13

- Brown W.R., Gellar M.J., Fabricant D.G., Kurtz M.J. 2001, *AJ*, 122, 714
- Bruzual A.G., Charlot S. 1993, *ApJ*, 405, 538
- Capaccioli M. 1989, in Corwin H.G., Bottinelli L. eds, *The World of Halaxies*, Springer-Verlag, Berlin, p.208
- Carlberg, R.G., Yee, H.K.C., Ellingson, E., Abraham, R. Gravel, P., Morris, S. Pritchett, C.J. 1996, *ApJ*, 462, 32
- Carlberg, R.G., Yee, H.K.C., Ellingson, E. 1997, *ApJ*, 478, 462
- Chóloniewski J. 1985, *MNRAS*, 214, 197
- Chóloniewski, J. 1987, *MNRAS*, 226, 273
- Cole S., Lacey C.G., Baugh C.M., Frenk C.S. 2000, *MNRAS*, 319, 168
- Colberg J.M. et al. (The Virgo Consortium) 2000, *MNRAS*, 319, 209
- Coleman G.D., Wu C.C., Weedman D.W. 1980, *ApJS*, 43,393
- Colless M.M. 1999, *Phil.Trans.Roy.Soc.Lond.A*, 357, 105
- Colless M.M. et al. (The 2dFGRS Team) 2001, *MNRAS*, 328, 1039
- Courteau S., de Jong R.S., Brocils A.H. 1996, *ApJ*, 457, 73
- Cross, N.J.G. et al. (The 2dFGRS Team) 2001, *MNRAS*, 324, 825
- Cross N.J.G., Driver S.P., 2002, *MNRAS*, 329, 579
- Dalcanton J.J., Spergel D.N., Summers F.J. 1997, *ApJ*, 482, 659
- Dalcanton J.J., Spergel D.N., Gunn J.E., Smith M., Schneider D.P. 1997, *AJ*, 114, 635
- Dalcanton J.J. 1998a, *ApJ*, 495, 251
- Dalcanton J.J. 1998b, not published, private communication.
- Davies J.I. 1990, *MNRAS*, 244, 8
- Davies J., Phillipps S., Disney M., Boyce P., Evans R. 1994, *MNRAS*, 268, 984
- de Blok, W.J.G., McGaugh, S.S., van der Hulst, J.M., 1996, *MNRAS*, 283, 18
- de Jong R.S. 1996, *A&A*, 118, 557
- de Jong R. & Lacey C. 1999, *Ap&SS*, 269, 569
- de Jong R. & Lacey C. 1999, in *Low Surface Brightness Universe*, ASP Conference Series 170, Eds Davies J.I., Impey C. & Phillipps S., p52
- de Jong R. & Lacey C. 2000, *ApJ*, 545, 781

- de Lapparent, V., Gellar, M.J., Huchra, J.P. 1986, ApJ, 304, 585
- de Propris R., Pritchett C.J., Harris W.E., McClure R.D. 1995, ApJ, 450, 534
- de Vaucouleurs, G. 1948, Ann. Astrophys., 11, 247
- de Zeeuw T., Franx M. 1991, ARA&A, 29, 239
- Disney M. 1976, Nature, 263, 573
- Disney M. Phillipps S. 1983, MNRAS, 205, 1253
- Dressler A. 1980, ApJ, 236, 351
- Drinkwater M.J., Phillipps S., Gregg M.D., Parker Q.A., Smith R.M., Davies J.I., Jones J.B., Sadler E.M. 1999, ApJ 511, L97
- Driver S.P., Phillipps S., Davies J.I., Morgan I., Disney M.J. 1994, MNRAS, 266, 155
- Driver S.P. 1999, ApJL, 526, 69
- Driver S.P. 2000, in Proc. of the ESO/ECF/STSCI workshop on Deep Fields, Garching Oct 2000, (Publ: Springer)
- Driver, S.P., Windhorst, R.A., Griffiths, R.E. 1995, ApJ, 453, 48
- Driver, S.P., Couch, W.J., Phillipps, S., 1998, MNRAS, 301, 369
- Driver, S.P., Cross N.J.G. 2000, in *Mapping the Hidden Universe*, Eds R. Kraan-Korteweg, P. Henning & H. Andernach (Publ: Kluwer), (astro-ph 0004201)
- Driver, S.P. 2002, in *A New Era in Cosmology*, Eds, T. Shanks & N. Metcalfe, ASP Conference Series.
- Efstathiou G., Ellis R., Peterson B. 1988, MNRAS, 232, 431
- Efstathiou G., Bridle S.L., Lasenby A.N., Hobson M.P. Ellis R.S. 1999, MNRAS, 303, 47
- Ellis, R.S., Colless, M., Broadhurst, T., Heyl, J., Glazebrook, K. 1996, MNRAS, 280, 235
- Ellis, R.S., 1997, ARA&A, 35, 389
- Fall S.M., Efstathiou G. 1980, MNRAS, 193, 189
- Felten, J.E., 1985, Com Ap, 11, 53
- Ferguson H.C., Binggeli B. 1994, A&ARv, 6, 67
- Fernández-Soto A., Lanzetta K., Yahil A., 1998, ApJ, 513, 34
- Fish R.A. 1964, ApJ, 139, 284
- Folkes, S. et al. (The 2dFGRS Team) 1999, MNRAS, 308, 459

- Freeman, K. 1970, *ApJ*, 160, 811
- Freedman W. et al. 2001, *ApJ*, 533, 47
- Fukugita M., Hogan C.J., Peebles P.J.E., 1998, *ApJ*, 503, 518
- Fukugita M., Shimasaku K. Ichikawa T. 1995, *PASP*, 107, 945
- Fukugita M, Ichikawa T., Gunn J.E., Doi M., Shimasaku K., Schneider D.P. 1996, *AJ*, 111, 1748
- Gallego J., Zamorano J., Aragon-Salamanca A., Rego M. 1995, *ApJ*, 455, L1
- Gaztañaga, E., Dalton, G.B. 2000, *MNRAS*, 312, 417
- Hogg D.W. et al. 2000, *ApJS*, 127, 1
- Hubble E. 1926, *ApJ*, 64, 321
- Hubble E. 1936a, *ApJ*, 84, 158
- Hubble E. 1936b, *ApJ*, 84, 270
- Hubble E. 1936c, "The Realm of the Nebulae", (New Haven: Yale University Press)
- Impey, C., Bothun, G. 1997, *ARA&A*, 35, 267
- Infante L. 1987, *A&A*, 183, 177
- Jarrett T. H., Chester T., Cutri R., Schneider S., Skrutskie M., Huchra J. P. 2000, *AJ*, 119, 2498
- Jerjen, H. Binggeli, B. 1997, 'The Nature of Elliptical Galaxies', Eds. M. Arnaboldi, G.S. Da Costa & P. Saha, (Canberra: Mt Stromlo Observatory) p. 239
- Kennicutt R.C.Jr 1992, *ApJS*, 79, 255
- Kent S.M. 1985, *ApJS*, 59, 115
- Kent S.M., Ramella M., Nonino M. 1993, *AJ*, 105, 393
- Kiang T. 1961, *MNRAS*, 122, 236
- Kilborn K., Webster R.L., Staveley-Smith L. 1999, *PASA*, 16, 8
- Kirshner R.P., Oemler A., Schechter P.L. 1979, *AJ*, 84, 951
- Kirshner R.P., Oemler A., Schechter P.L., Schectman S.A. 1983, *AJ*, 88, 1285
- Koo D.C., Kron R.G., 1992, *ARA&A*, 30, 613
- Koranyi D.M., Strauss M.A. 1997, *ApJ*, 477, 36
- Kormendy J. 1977, *ApJ*, 218, 333

- Kron R.G. 1980, *ApJS*, 43, 305
- Larson R.B., Tinsley B.M., 1978, *ApJ*, 219, 46
- Lauberts A., Valentijn, E. 1989, *ESO-Uppsala Catalogue*. European Southern Observatory.
- Lilly, S. J., Le Fevre, O., Hammer, F., Crampton, D. 1996, *ApJ*, 460, 1
- Lin C.C., Shu F.H. 1964, *ApJ*, 140, 646
- Lin, H., Kirshner, R., Shectman, S., Landy, S., Oemler, A., Tucker, D., Schechter, P. 1996, *ApJ*, 464, 60
- Liske J., Lemon D.J., Driver S.P., Cross N.J.G., Couch W.J. 2002, in preparation.
- Loveday J., Peterson B.A., Efstathiou, G., Maddox S.J. 1992, *ApJ*, 390, 338
- Loveday, J., 1997, *ApJ*, 489, 29
- Loveday, J., 2000, *MNRAS*, 312, 557
- Lynden-Bell D. 1971, *MNRAS*, 155, 95
- Madau, P., Pozzetti, L., Dickinson, M. 1998, *ApJ*, 498, 106
- Madgwick D.S. et al. 2001, *MNRAS*, submitted
- Maddox, S.J., Sutherland, W.J., Efstathiou, G., Loveday, J. 1990a, *MNRAS*, 243, 692
- Maddox S.J., Efstathiou G. Sutherland W.J. 1990b, *MNRAS*, 246, 433
- Margon, B. 1999, *Phil.Trans.RSoc.*, 357, 105
- Marzke, R., Huchra, J., Gellar, M. 1994, *ApJ*, 428, 43
- Marzke, R., Da Costa, N., Pelligrini, P., Willmer, C., Gellar, M. 1998, *ApJ*, 503, 617
- Mateo, M.L. 1998, *ARA&A*, 36, 435
- Mathewson D.S., Ford V.L., Buchhorn M. 1992, *ApJS*, 81, 413
- Matthews T.A., Morgan W.W., Schmidt M. 1964, *ApJ*, 140, 35
- McCracken H.J., Le Fevre O., Brodwin M., Foucaud S., Lilly S.J., Crampton D., Mellier Y. 2001, *A&A*, 376, 756
- McGaugh, S.S., 1992, PhD Thesis, Univ. Michigan
- McGaugh, S.S., 1996, *MNRAS*, 280, 337
- McGaugh S.S., Bothun G.D., Schombert J.M. 1995, *AJ*, 110, 573
- Metcalfe, N., Shanks T., Fong, R. Jones R.L. 1991, *MNRAS*, 249, 498
- Metcalfe, N., Fong, R. Shanks T. 1995, *MNRAS*, 274, 769

- Minchin R. 1999, PASA, 16, 12
- Morgan W.W., Lesh J.R. 1965, ApJ, 142, 1364
- Nagashima M., Totani T., Gouda N., Yoshii Y., 2001, ApJ, 557, 505
- Norberg P. et al. (The 2dFGRS Team) 2001, MNRAS, 328, 64
- Norberg P. et al. (The 2dFGRS Team) 2002, MNRAS, submitted
- O'Neil K., Bothun G.D., 2000, ApJ, 529, 811
- O'Neil K., Bothun G.D., Impey C.D., 2000, ApJS, 128, 99
- O'Neil K. 2000, AAS, 197, 58/07
- Odehahn S., Cohen S., Windhorst R., 2000, AAS, 197, 77.01
- Paolillo M., Andreon S., Longo G., Puddu E., Gal R.R., Scaramella R., Djorgovski S.G., de Carvallo R. 2001, A&A, 367, 59
- Peacock J.A., 1999, 'Cosmological Physics', Publ: CUP.
- Peacock J.A. et al. (The 2dFGRS Team) 2001, Nature, 410, 169
- Percival W.J. et al. (The 2dFGRS Team) 2001, MNRAS, 327, 1297
- Persic, M., Salucci, P., 1992, MNRAS, 258, 14pp
- Phillipps, S., Driver, S.P., 1995, MNRAS, 274, 832
- Phillipps, S., Driver, S.P., Couch, W.J., Smith, R.M., 1998, ApJL, 498, 119
- Phillipps S., Disney M. 1986, MNRAS, 221, 1039
- Phillipps S., Davies, J.I., Disney M. 1990, MNRAS, 242, 235
- Phillipps S., Drinkwater M.J., Gregg M.D., Jones J.B. 2001, ApJ, 560, 201
- PF95 Pie Y.C., Fall S.M. 1995, ApJ, 454, 69
- Pimblet, K., Smail I., Edge A.C., Couch W.J., O'Hely E., Zabludoff A.I. 2001, MNRAS, 327, 588
- Press, W., Teukolsky, S., Vetterling, W., Flannery, B. 1986 Numerical Recipes in Fortran, The Art of Scientific Computing 2nd Edition.
- Ratcliffe, A., Shanks, T., Parker, Q., Fong R. 1998, MNRAS, 293, 197
- Sandage, A., Tammann, G.A. 1981, 'A Revised Shapley- Ames Catalog of Bright Galaxies.' (Washington DC: Carnegie Institute of Washington).
- Sandage A. 1958, ApJ, 127, 522

- Sandage A., Tammann, G.A., Yahil, A. 1979, ApJ, 232, 352
- Schechter 1976, ApJ, 203, 297
- Schmidt M. 1968, ApJ, 151, 393
- Schwartzberg J.M., Phillipps S., Smith R.M., Couch W.J., Boyle B.J. 1995, MNRAS, 275, 121
- Schweizer F. 1982, ApJ, 252, 455
- Scott E.L. 1957, AJ, 62, 248
- Sersic J.-L. 1968, "Atlas de Galaxias Australes", (Corboda: Obs. Astronomico)
- Shanks, T. 1990, Proc. IAU Symp. 139 on *Extragalactic Background Radiation*, Eds S.C. Bowyer, C. Leinert, (Publ:Kluwer), 139, 269
- Simard L., Willmer C.N.A., Vogt N., Sarajedini V.L., Phillips A.C., Koo D.C., Im M., Illingworth G.D., Faber S.M., 2001, in preparation.
- Smith, R.M., Driver, S.P., Phillipps, S. 1997, MNRAS, 287, 415
- Smoker, J.V., Axon, D.J., Davies, R.D. 1999, A&A, 341, 725
- Sodré, L.(Jr), Lahav, O. 1993, MNRAS, 260,285
- Sprayberry, D., Impey, C.D., Irwin, M.J. 1996, ApJ, 463, 535
- Sprayberry D., Impey C.D., Bothun G.D., Irwin M.J. 1995, AJ, 109, 558
- Springel V., White S.D.M. 1998, MNRAS, 298, 143
- Takeuchi T.T., Yoshikawa K., Ishii, T.T. 2000, ApJS, 129, 1
- Taylor, K., Cannon, R.D., Parker, Q., 1998, in IAU symp. 179, Eds.B.J.,McLean., D.A.Golembek, J.J.E.Haynes & H.E.Payne, (Publ:Kluwer), p 135
- Tegmark, M., 1999, ApJ, 514, 69
- Thomsen B., Frandsen S. 1983, AJ, 88, 789
- Trentham, N., 1998, MNRAS, 294, 193
- Toomre A. 1977, In "The Evolution of Galaxies and Stellar Populations", eds B.M. Tinsley & R.B. Larson, p401. New Haven, Conn: Yale University Observatory.
- Turner E.L. 1979, ApJ, 231, 645
- Turner J.A., Phillipps S., Davies J.I., Disney M.J., 1993, MNRAS, 261, 39
- Tyson J.A. 1988, AJ, 96, 1
- van den Bergh, S., 1998, 'Galaxy Morphology and Classification.' (Publ. CUP)

- van der Kruit P.C. 1987, *A&A*, 173, 59
- Williams R.E., et al. 1996, *AJ*, 112, 1335
- Willmer, C.N.A., 1997, *AJ*, 114, 898
- White, S.D.M. & Rees, M.J. 1978, *MNRAS*, 183, 341
- White, S.D.M., Tully, B. & Davis, M. 1988, *ApJ*, 333, L45.
- Whitmore, B.C. 1984, *ApJ*, 278, 61
- Wyse R.F.G., Jones B.J.T. 1984, *ApJ*, 286, 88
- Yasuda N., et al. 2001, *AJ*, 122, 1104
- York D.G. et al. (The SDSS Team) 2000, *AJ*, 120, 1579
- Zhang B., Wyse R.F.G. 2000, *MNRAS*, 313, 310
- Zucca, E. et al. (The ESP Team) 1997, *A&A*, 326, 477
- Zwicky F. 1957, *Morphological Astronomy*, Springer.

Appendix A

Appendix

A.1 Magnitudes.

Unlike a star, which is essentially a point source and therefore appears as a point-spread function (PSF) unless it is saturated, galaxies are extended sources, with complex surface-brightness profiles, which are then convolved with a point spread function, as shown in Fig. A.1. The sky is not completely dark and the lowest surface-brightness detectable is limited by the isophotal detection threshold.

Measuring the magnitudes of galaxies in a robust and reliable way is difficult, especially when the method must be automated to cope with the massive volumes of data produced by modern surveys. The Sloan Digital Sky Survey (SDSS) intends to get magnitudes and other photometric data for $\sim 10^8$ galaxies in five different filters.

In this section we have tested five different magnitude systems and compare the reliability. The systems are, the isophotal magnitude, fitting a Gaussian profile to the isophotal parameters, fitting an exponential profile to the isophotal parameters, the Kron aperture system and the Petrosian aperture system.

We test these systems on eight different galaxies, from early types to late types. The eight galaxies in question have properties as described in Table A.1. They are placed at redshifts $z = 0.05, 0.10, 0.15, 0.20, 0.25$ & 0.3 . These are typical of galaxies that we expect to find in a survey like the Two degree Field Galaxy Redshift Survey (2dFGRS) or the SDSS.

The simplest definition of magnitude is the total magnitude. This is simply the total amount of light that could be detected from the galaxy by the instrument if there was no background noise. However, because the sky is bright, there is background noise, and the outer parts of the galaxy get lost in this noise. The noise can be reduced by taking longer exposures, thus lowering the threshold, but this is at the expense of the total number of galaxies that can be

Table A.1: A summary of the Properties of the Simulated Galaxies.

Hubble Type	M_{true}	B/T	$\langle \mu \rangle_e$	$\langle \mu \rangle_d$
E	-18.50	0.999	20.4	21.7
S0	-18.50	0.650	19.2	21.7
Sa	-18.50	0.500	19.6	21.7
Sb	-18.50	0.300	20.4	21.7
Sc	-18.50	0.150	21.0	21.7
Sd	-18.50	0.100	21.2	21.7
LSBG	-18.50	0.120	27.7	23.0
Irr	-18.50	0.001	21.5	22.7

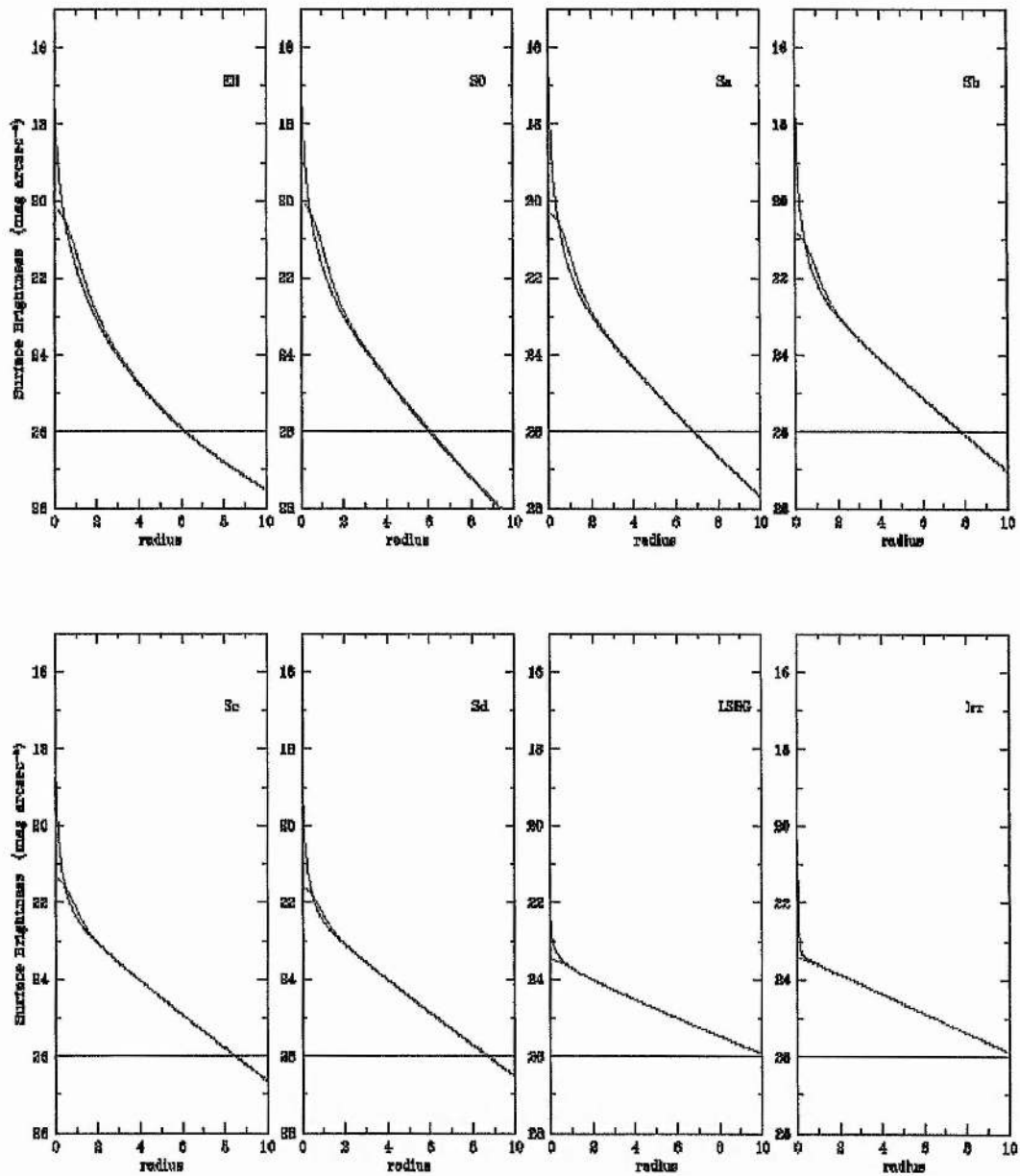


Figure A.1: This plot shows 8 profiles of typical galaxies (blue), with parameters from Table A.1. The profiles in red show the effects of convolving these profiles with a Gaussian point spread function of full width half maximum (FWHM=1.25"). The horizontal line demonstrates the isophotal detection threshold of the Millennium Galaxy Catalogue.

imaged within the limited observing time available.

Another simple definition of magnitude is isophotal magnitude. This is simply the total amount of light that is emitted by connected parts of the galaxy above the threshold. This is the easiest magnitude to measure and has often been used. However, the isophotal magnitude is a meaningless measurement (in terms of the intrinsic properties of the galaxy) that can differ from the total magnitude by large and difficult to calculate factors. It is dependent on the apparent profile of the galaxy and the threshold that this profile is measured at. The apparent profile of the galaxy depends on the intrinsic profile and the redshift.

Consider for example a simple disk galaxy. A galaxy with the Freeman surface brightness of $21.65 \text{ mag arcsec}^{-2}$ (Freeman 1970), has an isophotal magnitude that depends on the threshold of the survey. The isophotal magnitude is related to the total magnitude by:

$$m_{iso} = m_{tot} - 2.5 \log_{10} f(\mu_{lim}, \mu_o) \quad (\text{A.1})$$

$$f(\mu_{lim}, \mu_o) = 1 - [1 + 0.4 \ln(10)(\mu_{lim} - \mu_o)] \exp[-0.4 \ln(10)(\mu_{lim} - \mu_o)] \quad (\text{A.2})$$

where μ_{lim} is the isophotal threshold, and μ_o is the central surface brightness of the disk. $f(\mu_{lim}, \mu_o)$ is the fraction of light above the isophote.

Consider a medium depth survey that has a threshold of $25 \text{ mag arcsec}^{-2}$. The fraction of light above the isophote is 0.813 and the difference between total and isophotal magnitudes is 0.224 mag. If you have a shallower survey, say to $24 \text{ mag arcsec}^{-2}$, the difference becomes much greater, 0.49 mag, whereas a deeper survey, e.g. $26 \text{ mag arcsec}^{-2}$ has a small difference, of only 0.10 mag.

The profile can make a big difference too. Considering only disk galaxies at first, with varying surface brightnesses. Eqn A.2 still works, but μ_o varies rather than μ_{lim} . A high surface brightness galaxy with $\mu_o = 20.0$ will lose only 5.6% of its luminosity - fainter by 0.06mag, at a threshold of $25 \text{ mag arcsec}^{-2}$. However a low surface brightness galaxy with $\mu_o = 23.0$ will lose 45% of its flux and will be fainter by 0.65mag.

Galaxies are more complicated than simple disks. The Milky Way has a bulge and halo too, and the disk is a composite, made up of a thick disk, and a thin disk. The disk can have various inclinations, and the bulge may have various ellipticities. There are a variety of additional problems, such as internal dust, bars, spiral arms, HII regions which can change both the profile and optical thickness of the galaxy. Fortunately, to first order, the overall photometry can usually be fitted well by a two profile system, a bulge with a Sersic (1968, see Eqn 2.12) profile and a disk with an exponential profile, all convolved with a PSF. For bright galaxies, the Sersic profile usually has $\beta = 4$, becoming equivalent to a de Vaucouleurs profile. Our simulated galaxies use a simple bulge and disk model, with a de Vaucouleurs profile for the bulge and a Gaussian PSF. All our objects are face on, although we briefly consider the effects of inclination.

Before considering these more complicated profiles, it is worth considering the effect of redshift on isophotal magnitudes. Consider a disk galaxy with a central surface brightness

of 21.65 mag arcsec⁻² as before. If this galaxy is moved away to a redshift of 0.1, a typical redshift for today's large redshift surveys, its surface brightness will change. First there is a cosmological dimming, by a factor of $(1+z)^4$ and then there is a K-correction term, which depends on the filter and the galaxy type as well as the redshift, see § 2.2.

Isophotal magnitudes are not very useful, but are simple to measure. Total magnitudes, on the other hand are useful, but are difficult, if not impossible to measure. Are there simple ways of estimating total magnitudes from the image data? There are two main methods. The first is to fit a profile to the image data, The second is to measure all the light within an aperture, which depends on the image data. Both methods have their strong points and weak points.

There are many profiles that can be fitted to objects. The complexity of the fit that can be achieved will depend on the quality of data available. However, fitting functions to the data can take a lot of computational time. Simple profiles include a Gaussian profile (Maddox et al. 1990b) and an exponential profile (Cross et al. 2001). The Gaussian profile fits a PSF well, and so is ideal for stars. Small angular size galaxies, close to the seeing limit will also be well fitted by a Gaussian. An exponential profile fits disk galaxies, much larger than the seeing disk, well. An exponential profile gives better magnitudes for galaxies with bulges too, apart from ellipticals, in the absence of seeing (see Table A.2). However, the effective surface brightness of galaxies is overestimated by both fits. The exponential fit gives the best estimate of μ_e for very low bulge-to-total ratios but is very poor for high values. The surface brightness measurements come from the central surface brightness of each fitted profile and are then converted to effective surface brightness using the following formulae.

$$\begin{aligned} \langle \mu \rangle_e &= \mu_{o,G} + 0.355 \\ &= \mu_{o,e} + 1.124 \end{aligned} \tag{A.3}$$

Both these fits can be done with the bare minimum of data. They only require the isophotal magnitude, the isophotal area and the isophotal detection threshold. The isophotal area can be converted to an isophotal radius, assuming that the object is circular.

For the Gaussian profile.

$$\Sigma(r) = \Sigma_o \exp\left(-\frac{r^2}{2\sigma^2}\right) \tag{A.4}$$

$$\begin{aligned} m_{iso} &= \mu_o - 2.5 \log_{10} \left[2\pi \sigma^2 \left(1 - e^{-\frac{r_{iso}^2}{2\sigma^2}} \right) \right] \\ \mu_{lim} &= \mu_o + \frac{2.5}{\ln(10)} \frac{r_{iso}^2}{2\sigma^2} \end{aligned} \tag{A.5}$$

Eqn A.5 can be solved to get μ_o and σ . These can be used to get the corrected magnitude m_{cor} .

$$m_{cor} = \mu_o - 2.5 \log_{10} [2\pi \sigma^2] \tag{A.6}$$

Table A.2: Comparison of Gaussian and Exponential Profiles in the Absence of Seeing.

Type	B/T	z	$\Delta_{M,Gaus-Tot}$	$\Delta_{M,Exp-Tot}$	$\Delta_{\mu,Gaus-Tot}$	$\Delta_{\mu,Exp-Tot}$
Ell	0.999	0.05	-0.023	-0.040	1.430	0.870
Ell	0.999	0.15	-0.028	-0.050	1.014	0.499
Ell	0.999	0.25	-0.034	-0.059	0.588	0.112
S0	0.650	0.05	0.031	0.019	-0.037	-0.669
S0	0.650	0.15	0.052	0.036	-0.309	-0.871
S0	0.650	0.25	0.086	0.064	-0.644	-1.151
Sa	0.500	0.05	0.041	0.021	0.107	-0.424
Sa	0.500	0.15	0.070	0.041	-0.135	-0.583
Sa	0.500	0.25	0.118	0.077	-0.433	-0.811
Sb	0.300	0.05	0.053	0.019	0.271	-0.149
Sb	0.300	0.15	0.090	0.037	0.069	-0.249
Sb	0.300	0.25	0.151	0.075	-0.173	-0.398
Sc	0.150	0.05	0.059	0.012	0.381	0.034
Sc	0.150	0.15	0.100	0.025	0.211	-0.017
Sc	0.150	0.25	0.167	0.053	0.017	-0.096
Sd	0.100	0.05	0.061	0.009	0.393	0.069
Sd	0.100	0.15	0.102	0.018	0.234	0.034
Sd	0.100	0.25	0.170	0.039	0.057	-0.019
LSBG	0.120	0.05	0.176	0.048	-0.268	-0.351
LSBG	0.120	0.15	0.313	0.119	-0.518	-0.478
LSBG	0.120	0.25	0.577	0.318	-0.867	-0.738
Irr	0.001	0.05	0.138	0.002	0.066	0.003
Irr	0.001	0.15	0.232	0.002	-0.091	0.002
Irr	0.001	0.25	0.388	0.002	-0.253	0.000

Similarly for the exponential profile.

$$\Sigma(r) = \Sigma_o \exp\left(-\frac{r}{\alpha}\right) \quad (\text{A.7})$$

$$\begin{aligned} m_{iso} &= \mu_o - 2.5 \log_{10}\left[2\pi \alpha^2 \left(1 - \left(1 + \frac{r_{iso}}{\alpha}\right)e^{-\frac{r_{iso}}{\alpha}}\right)\right] \\ \mu_{lim} &= \mu_o + \frac{2.5}{\ln(10)} \frac{r_{iso}}{\alpha} \end{aligned} \quad (\text{A.8})$$

Eqn A.8 can be solved to get μ_o and σ . These can be used to get the corrected magnitude m_{cor} .

$$m_{cor} = \mu_o - 2.5 \log_{10}[2\pi \alpha^2] \quad (\text{A.9})$$

Table A.2 shows how well the Gaussian and exponential fits do for a variety of galaxies at different redshifts.

Aperture magnitudes can be calculated by summing up all the light within an aperture. The radius of the aperture is defined by the parameters of each galaxy. We discuss two types of aperture magnitudes, Kron and Petrosian.

Kron magnitudes are defined as the sum of all the light within a radius kr_1 , where r_1 is the first moment and k is a constant, usually set at 2.5. The first moment is calculated below.

$$r_1 = \frac{\int_1^{kr_1} r g(r) dr}{\int_1^{kr_1} g(r) dr} \quad (\text{A.10})$$

where $g(r)$ is the amount of flux emitted from an annulus of constant width. $g(r) = 2\pi r \Sigma(r)$, where $\Sigma(r)$ is the surface brightness profile. The range 1 pixel to kr_1 , but integrating from 0 to ∞ will give much the same result (Kron 1980, Infante 1987).

The solution to this is $r_1 \sim 2\alpha$ for an exponential profile, $\Sigma(r) = I_o \exp(-r/\alpha)$, where α is the scale-length of the galaxy. Thus the Kron radius is equal to 5α if the galaxy has an exponential profile. 96% of the flux is within this radius, regardless of redshift. For elliptical galaxies, the result is 91%.

Petrosian magnitudes are defined using the following equation.

$$R_P(r) = \frac{\int_{\alpha_{lo} r}^{\alpha_{hi} r} 2\pi r \Sigma(r) dr / [\pi(\alpha_{hi}^2 - \alpha_{lo}^2)r^2]}{\int_0^r \Sigma(r) dr / [\pi r^2]} \quad (\text{A.11})$$

where α_{lo} and α_{hi} define an annulus at distance r . The Petrosian radius r_P is defined as the radius when $R_P(r_P)$ is equal to some specified limit. For instance Blanton et al. (2001) use the values $\alpha_{lo} = 0.8$, $\alpha_{hi} = 1.25$ and $R_P(r_P) = 0.2$. The Petrosian magnitude is then defined as the flux within $N_P r_P$, where N_P is an integer number. $N_P = 2$ in Blanton et al. (2001).

Now is a good time to consider more complicated profiles. Codes have been written, such as GIM2D, Simard et al. (2001), which model more complicated profiles for galaxies. GIM2D

fits a combined Sersic and exponential profile, convolved with a PSF measured from stars on the same CCD and gives 17 parameters associated with the best fit. It uses a Metropolis algorithm to find the best fit in a complicated parameter space. While the Metropolis routine will find the best fit, it can take a long time to do so. Unfortunately it takes several minutes for an average galaxy on a fairly fast computer. For a small survey of 1000 galaxies this would take a week to calculate. For a large redshift survey such as the 2dFGRS (250,000 galaxies) or SDSS (1,000,000 galaxies) it could take more than a year to compute the best profiles on an equivalent computer. SDSS also contains $\sim 10^8$ galaxies fainter than the redshift survey limits and has five colours for each galaxy, so the task is enormous. While there are faster computers and more than one computer can be employed to run through the data set, these codes are extremely expensive computationally.

The main concern is the effect of the seeing disk. The simplest PSF is a Gaussian. To compare different magnitude types, we have calculated the magnitudes for a set of galaxies, with different Bulge to total ratios and surface brightnesses, representing typical galaxies: an Elliptical, an S0, an Sa, Sb, Sc, Sd, Irregular and an LSBG, see Table A.1. These have been placed at a variety of redshifts and convolved with a seeing disk. They are detected at an isophote. This is an extension of the work carried out in Appendix A of Cross et al. 2001 and Appendix A of Cross & Driver (2001). The bulge is represented using a de Vaucouleur's profile (de Vaucouleurs 1948).

$$\mu_{bulge}(r) = \mu_e + 1.40 + 8.327[(r/r_e)^{1/4} - 1] \quad (\text{A.12})$$

where r_e is the half-light radius of the bulge, μ_e is the effective surface brightness of the bulge. Here we define it as the mean surface brightness within r_e ¹.

The disk is represented by an exponential profile.

$$\mu_{disk}(r) = \mu_o + 1.086(r/\alpha) \quad (\text{A.13})$$

The magnitude of a galaxy and the bulge-disk ratio can be found in terms of the above parameters, by:

$$\begin{aligned} M &= -2.5 \log_{10}[10^{-0.4B} + 10^{-0.4D}] \\ B/T &= \frac{B}{B+D} = \frac{1}{1 + 1/(\frac{B}{D})} \\ B &= \mu_e + 1.40 - 2.5 \log_{10}[7.215\pi r_e^2] \\ D &= \mu_o - 2.5 \log_{10}[\pi \alpha^2] \end{aligned} \quad (\text{A.14})$$

where B is the magnitude of the bulge and D is the magnitude of the disk. B/T is the bulge-to-total ratio. Given the parameters M , B/T , μ_e and μ_o , a galaxy's light profile is fully defined. First all the properties were converted from intrinsic to apparent, using the redshift.

¹Note that the term "effective surface brightness" is sometimes defined as the surface brightness at r_e ; for Ellipticals the correction between the surface brightness at r_e and the effective surface brightness definitions is 1.40.

$$\begin{aligned}
m &= M + 5 \log_{10} d_L + 25 + K(z) \\
\mu_{app} &= \mu + 10 \log_{10}(1+z) + K(z)
\end{aligned}
\tag{A.15}$$

where d_L is the luminosity distance.

Next the galaxy profile is convolved with a Gaussian PSF:

$$I_s(r, \theta) = \frac{1}{2\pi\sigma^2} \int_0^\infty \int_0^{2\pi} I_{act}(r', \theta') \exp\left(-\frac{[r'^2 + r^2 - 2rr' \cos(\theta' - \theta)]}{2\sigma^2}\right) r' d\theta' dr'
\tag{A.16}$$

where $I_s(r, \theta)$ is the apparent profile after convolution, and $I_{act}(r', \theta')$ is the actual profile before seeing.

Now that both $I_s(r, \theta)$ and $I_{act}(r, \theta)$ are known, it is possible to calculate the magnitude determined by each system above, before and after seeing, and the surface brightnesses.

To calculate the Gaussian and Exponential corrections it is necessary to find the isophotal magnitude and radius, see Eqn A.5 and Eqn A.8. The isophotal radius is the point when the $\mu(r) = \mu_{lim}$. The isophotal radius is slightly larger for the galaxy profile convolved with the PSF. The isophotal magnitude is calculated by integrating the profile out to r_{iso} . Table A.3 shows isophotal magnitudes and radii for different galaxies. The Kron and Petrosian are calculated straight from the profiles, see Eqn A.10 and Eqn A.11.

Fig. A.2 demonstrates differences between Kron and Petrosian magnitudes, for $\mu_{lim} = 26.0$ and a seeing of $1.25''$. They both show a similar dependency on the bulge-to-total ratio, although the Kron magnitudes have a smaller dependence. They both have a very weak redshift dependency. The Petrosian magnitudes are closer to total for small bulge-to-total ratios.

A.1.1 Comparison of Magnitude Systems.

Figs A.3- A.14 show how the different magnitude systems behave as functions of z , μ_d , FWHM, μ_{lim} and M .

The error in magnitude as a function of redshift is shown in Fig. A.3 for galaxies with no seeing effects, and in Fig. A.4 for galaxies measured with a seeing of $1.25''$. When there is no seeing, all magnitudes get worse as the redshift increases. There is also a tendency for those which are worst at low redshift to get worse fastest. The errors in aperture magnitudes have an almost linear dependence on redshift for all profile types, whereas the errors in isophotal, Gaussian corrected and exponentially corrected magnitudes have a much stronger redshift dependence. For late types, in particular, isophotal and Gaussian corrected magnitudes are poor fits to the profile and miss a great deal of the light. The exponential profile does much better than either the isophotal or the Gaussian corrected magnitude for all galaxy types apart from ellipticals. When seeing is taken into the exponential profile is actually better than either the isophotal or Gaussian corrected for all galaxy types. However, at higher redshifts, when the isophotal radius of the galaxy is much smaller than the FWHM, then the Gaussian correction should give a perfect fit. It should give a good fit to faint compact galaxies.

Table A.3: Isophotal Magnitudes and Radii of Galaxies.

Type	B/T	z	σ	r_{iso}	m_{iso}	$r_{iso,s}$	$m_{iso,s}$
EII	0.999	0.05	1.25	8.03	17.53	8.08	17.68
EII	0.999	0.10	1.25	3.91	19.19	3.98	19.36
EII	0.999	0.15	1.25	2.53	20.22	2.63	20.41
EII	0.999	0.20	1.25	1.83	20.99	2.03	21.21
EII	0.999	0.25	1.25	1.41	21.62	1.68	21.87
EII	0.999	0.30	1.25	1.13	22.16	1.43	22.45
SO	0.001	0.05	1.25	13.73	17.83	13.73	17.83
SO	0.001	0.10	1.25	6.63	19.58	6.63	19.58
SO	0.001	0.15	1.25	4.20	20.72	4.23	20.72
SO	0.001	0.20	1.25	2.94	21.63	2.98	21.64
SO	0.001	0.25	1.25	2.15	22.45	2.18	22.47
SO	0.001	0.30	1.25	1.59	23.23	1.58	23.31
Sa	0.120	0.05	1.25	13.30	17.86	13.68	17.95
Sa	0.120	0.10	1.25	6.33	19.61	6.53	19.71
Sa	0.120	0.15	1.25	3.94	20.76	4.08	20.88
Sa	0.120	0.20	1.25	2.70	21.68	2.83	21.83
Sa	0.120	0.25	1.25	1.91	22.50	1.98	22.73
Sa	0.120	0.30	1.25	1.35	23.28	1.43	23.60
Sb	0.650	0.05	1.25	6.86	17.58	7.68	17.59
Sb	0.650	0.10	1.25	3.41	19.25	3.88	19.26
Sb	0.650	0.15	1.25	2.25	20.29	2.68	20.31
Sb	0.650	0.20	1.25	1.65	21.08	2.03	21.11
Sb	0.650	0.25	1.25	1.27	21.73	1.68	21.77
Sb	0.650	0.30	1.25	1.01	22.30	1.48	22.34
Sc	0.500	0.05	1.25	8.20	17.60	8.68	17.61
Sc	0.500	0.10	1.25	4.08	19.27	4.38	19.28
Sc	0.500	0.15	1.25	2.68	20.32	2.93	20.34
Sc	0.500	0.20	1.25	1.97	21.12	2.23	21.14
Sc	0.500	0.25	1.25	1.52	21.79	1.83	21.81
Sc	0.500	0.30	1.25	1.21	22.37	1.53	22.40
Sd	0.300	0.05	1.25	9.70	17.63	9.93	17.63
Sd	0.300	0.10	1.25	4.83	19.31	4.98	19.32
Sd	0.300	0.15	1.25	3.18	20.37	3.33	20.38
Sd	0.300	0.20	1.25	2.33	21.18	2.48	21.20
Sd	0.300	0.25	1.25	1.80	21.86	1.98	21.89
Sd	0.300	0.30	1.25	1.43	22.46	1.63	22.50
LSBG	0.150	0.05	1.25	10.69	17.65	10.78	17.65
LSBG	0.150	0.10	1.25	5.32	19.34	5.43	19.34
LSBG	0.150	0.15	1.25	3.50	20.41	3.58	20.42
LSBG	0.150	0.20	1.25	2.56	21.23	2.68	21.24
LSBG	0.150	0.25	1.25	1.98	21.92	2.08	21.95
LSBG	0.150	0.30	1.25	1.58	22.54	1.68	22.59
Irr	0.100	0.05	1.25	11.00	17.66	11.03	17.66
Irr	0.100	0.10	1.25	5.47	19.35	5.53	19.35
Irr	0.100	0.15	1.25	3.60	20.42	3.68	20.43
Irr	0.100	0.20	1.25	2.64	21.25	2.73	21.26
Irr	0.100	0.25	1.25	2.04	21.95	2.13	21.97
Irr	0.100	0.30	1.25	1.62	22.57	1.73	22.61

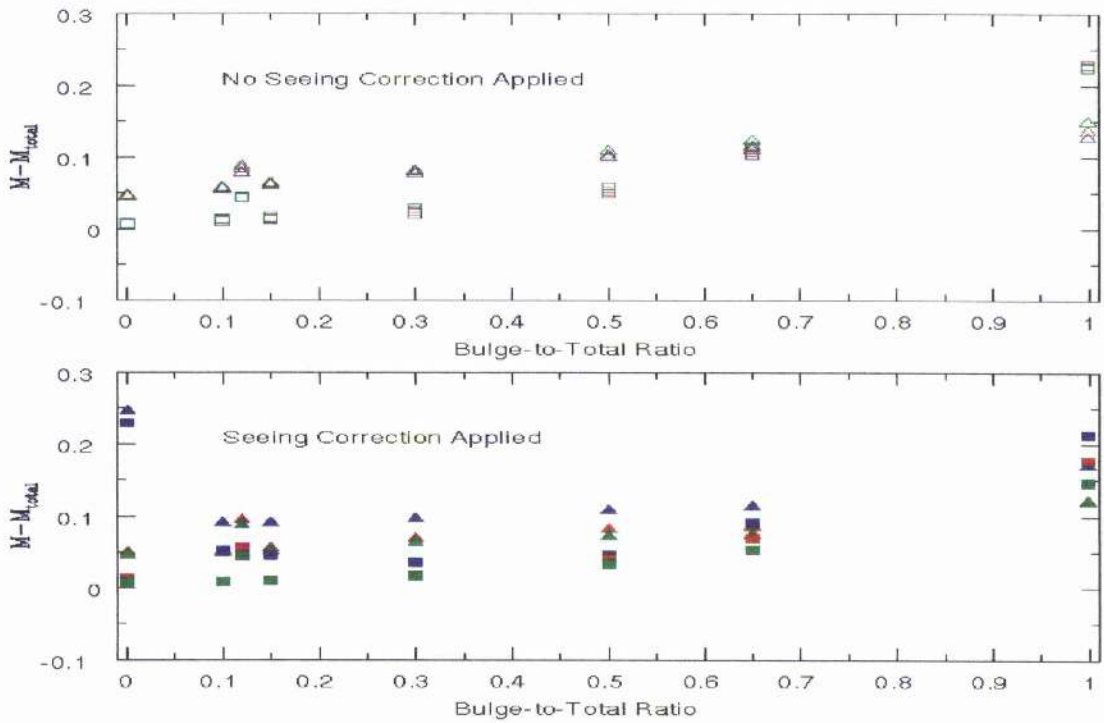


Figure A.2: This plot shows the bias in absolute magnitude for Kron and Petrosian magnitudes as a function of bulge-to-total ratio. The triangles represent Kron magnitudes and the squares represent Petrosian magnitudes. The blue points are $z = 0.05$, the red are $z = 0.15$ and the green are $z = 0.25$ galaxies. There is a weak dependence on redshift. The top plot is with a seeing correction, the bottom plot is without a seeing correction.

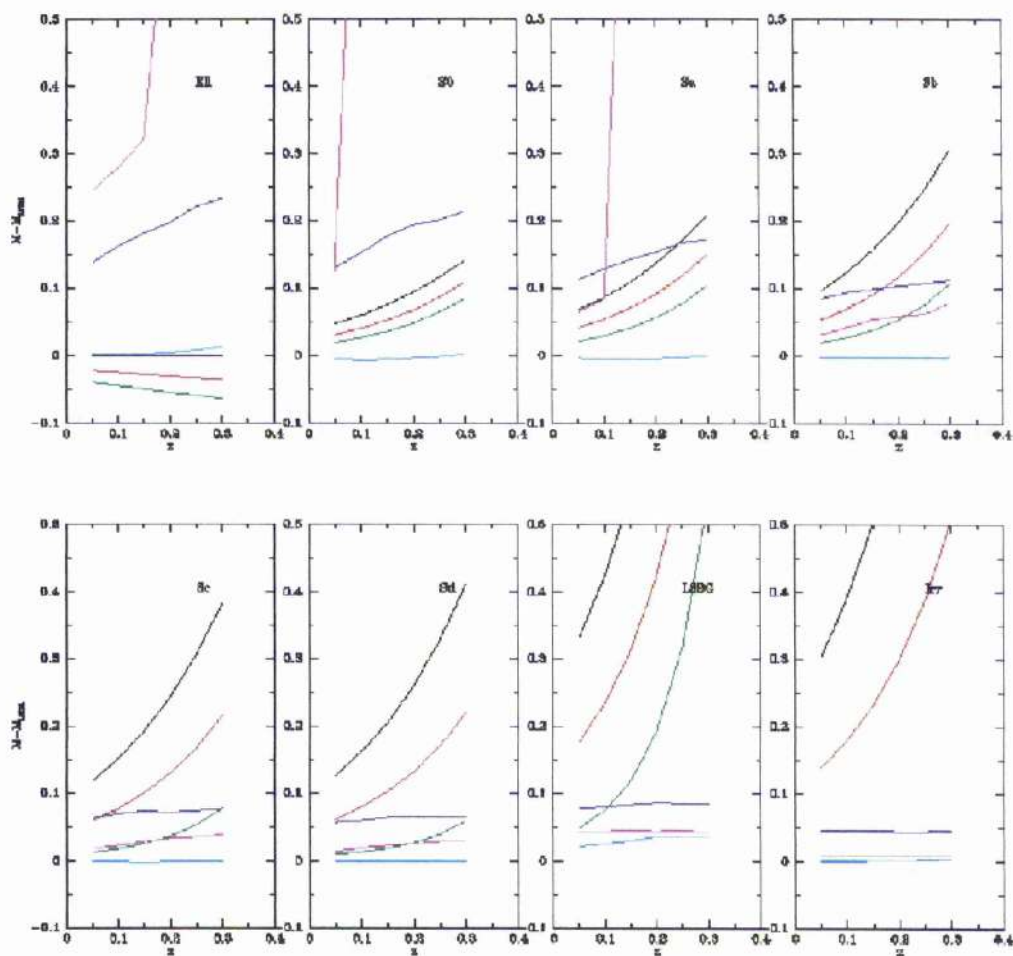


Figure A.3: This plot shows the bias in total magnitude as a function of redshift for each type of galaxy in the absence of seeing. The black line represents the isophotal magnitude, the red line represents the Gaussian corrected magnitude, the green represents the exponentially corrected magnitude, the blue represents the Kron magnitude and the magenta represents the Petrosian magnitude. The cyan line is simply the sum of the profile out to the limits of the array used, minus the total magnitude. This should always have a value of zero. If it does not then the bias in this line will be present in all the other magnitude estimates. The profiles are derived from the numbers in Table A.1. The isophotal limit is $26 \text{ mag arcsec}^{-2}$. The redshift varied from $z = 0.05$ to $z = 0.3$ in intervals of 0.05.

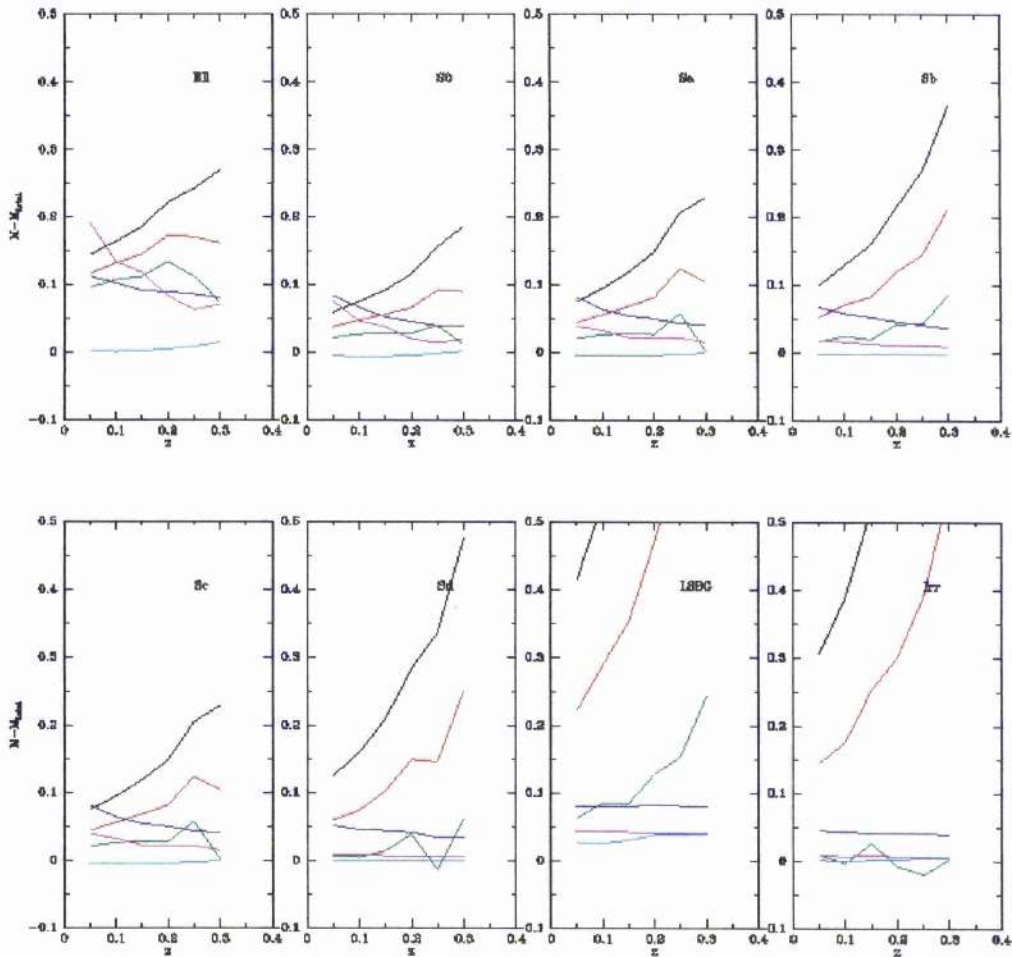


Figure A.4: This plot shows the bias in total magnitude as a function of redshift for each type of galaxy in the presence of seeing. The black line represents the isophotal magnitude, the red line represents the Gaussian corrected magnitude, the green represents the exponentially corrected magnitude, the blue represents the Kron magnitude and the magenta represents the Petrosian magnitude. The profiles were derived from the numbers in Table A.1. The isophotal limit was $26 \text{ mag arcsec}^{-2}$ and the FWHM of the seeing profile was $1.25''$. The redshift varied from $z = 0.05$ to $z = 0.3$ in intervals of 0.05.

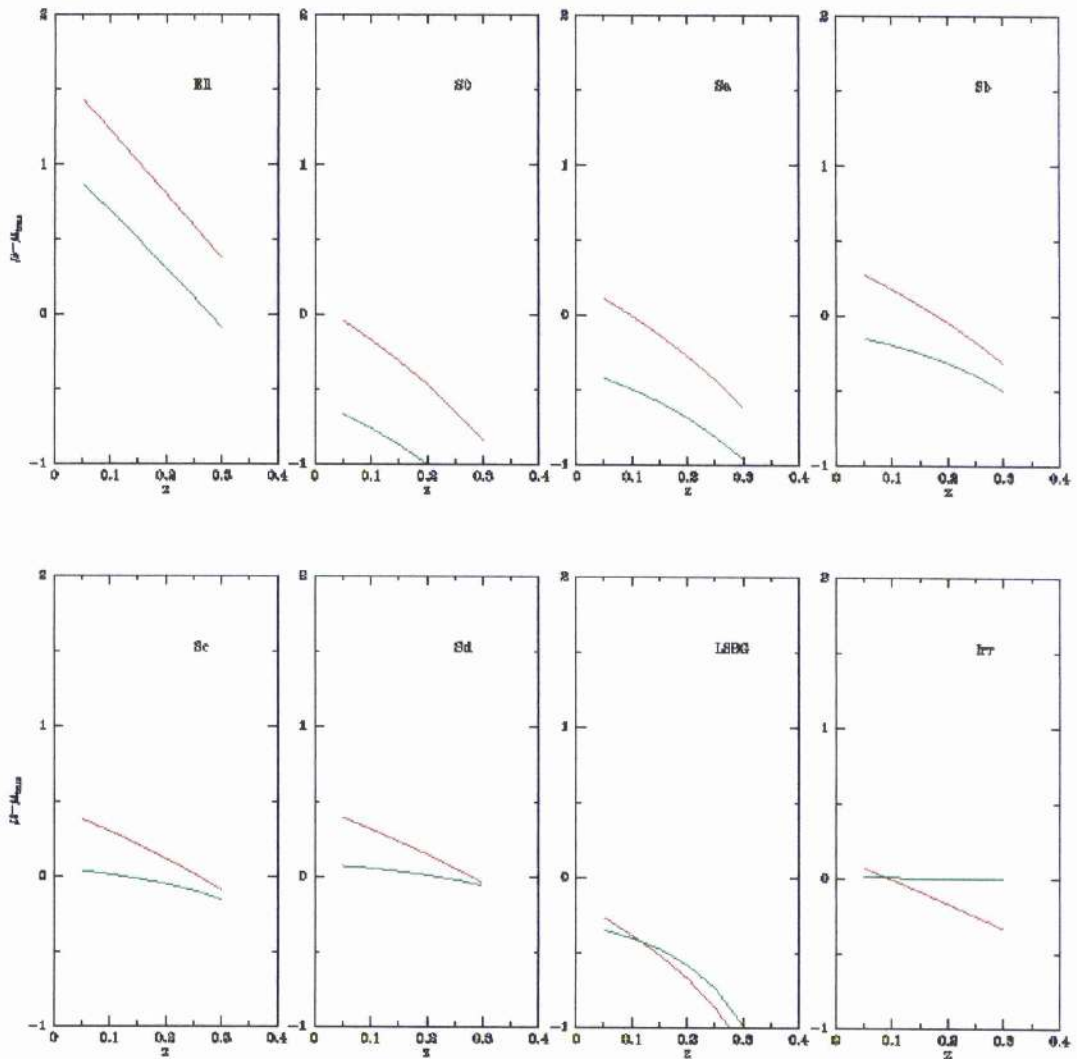


Figure A.5: This plot shows the bias in effective surface brightness as a function of redshift for each type of galaxy in the absence of seeing. The red line represents the Gaussian correction, the green represents exponential correction. The profiles are derived from the numbers in Table A.1. The isophotal limit is $26 \text{ mag arcsec}^{-2}$. The redshift varied from $z = 0.05$ to $z = 0.3$ in intervals of 0.05.

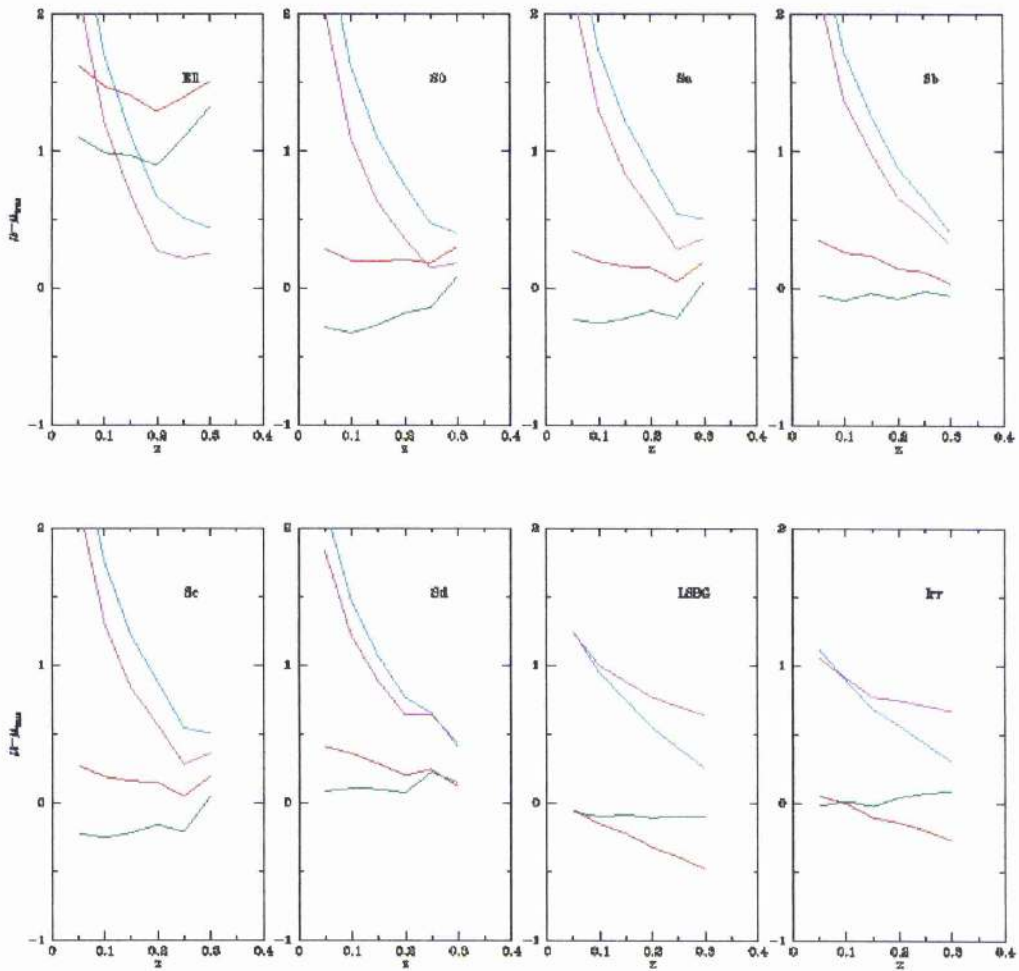


Figure A.6: This plot shows the bias in effective surface brightness as a function of redshift for each type of galaxy in the presence of seeing. The red line represents the Gaussian correction and the green represents exponential correction compared to the true effective surface brightness of the galaxy. The cyan and magenta lines represent the Gaussian and exponential corrections compared to the seeing corrected effective surface brightness of the galaxy. The profiles are derived from the numbers in Table A.1. The isophotal limit is $26 \text{ mag arcsec}^{-2}$ and the FWHM is $1.25''$. The redshift varied from $z = 0.05$ to $z = 0.3$ in intervals of 0.05 .

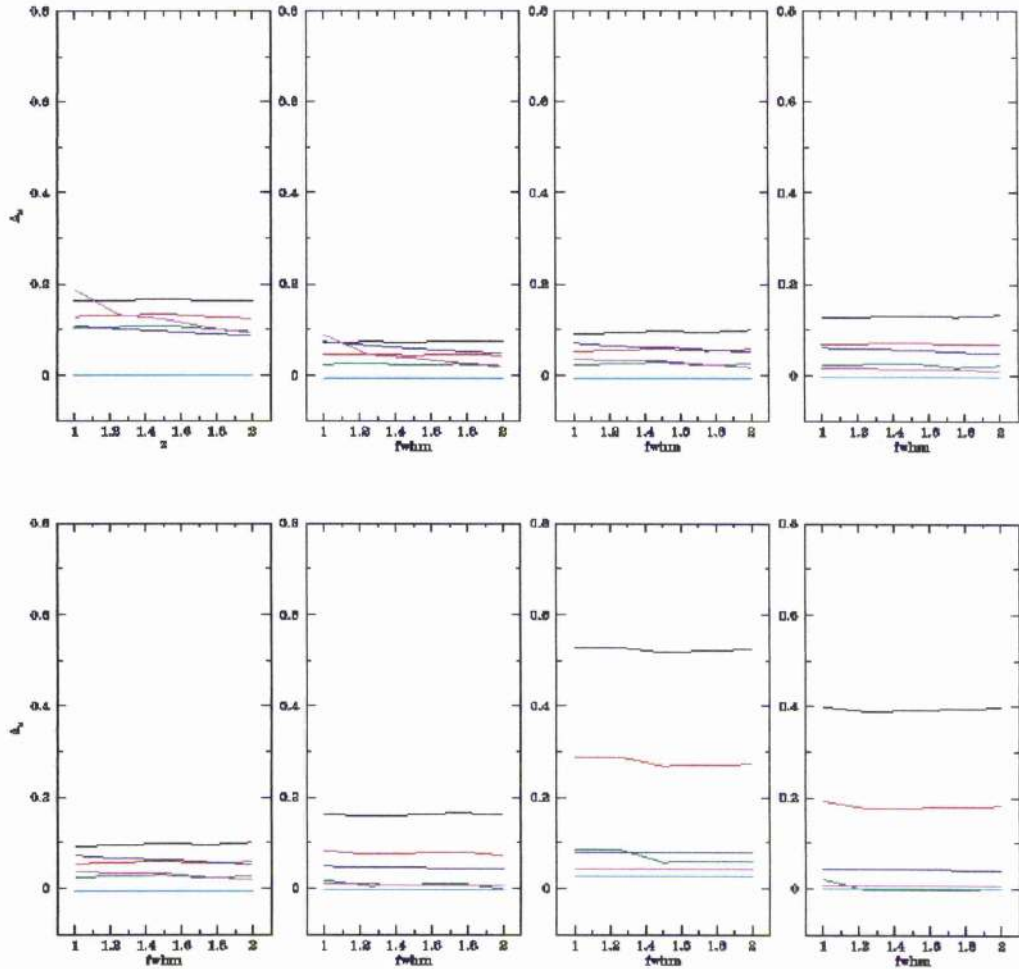


Figure A.7: This plot shows the bias in total magnitude as a function of seeing for each type of galaxy. The black line represents the isophotal magnitude, the red line represents the Gaussian corrected magnitude, the green represents the exponentially corrected magnitude, the blue represents the Kron magnitude and the magenta represents the Petrosian magnitude. The profiles are derived from the numbers in Table A.1. The isophotal limit is 26 mag arcsec⁻² and $z = 0.10$. The FWHM varied from 1.0'' to 2.0'' in intervals of 0.25''

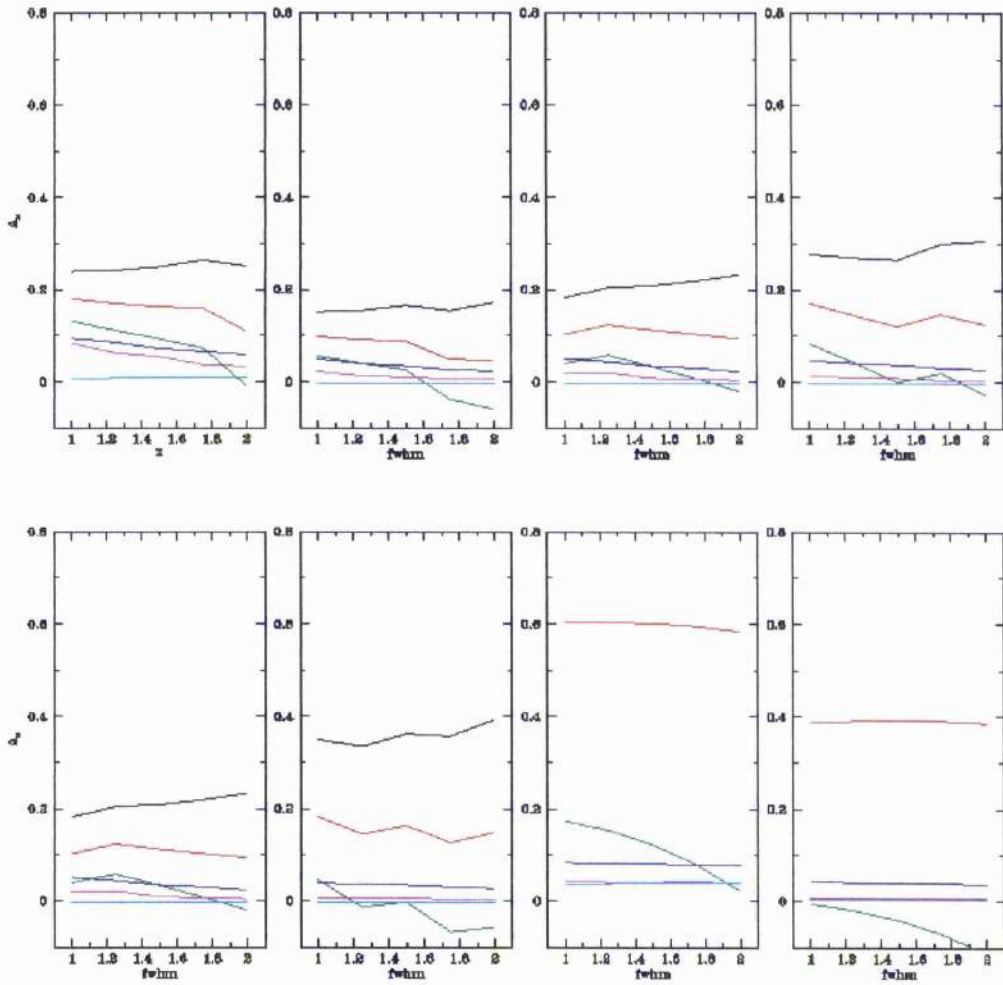


Figure A.8: This plot shows the bias in total magnitude as a function of seeing for each type of galaxy. The black line represents the isophotal magnitude, the red line represents the Gaussian corrected magnitude, the green represents the exponentially corrected magnitude, the blue represents the Kron magnitude and the magenta represents the Petrosian magnitude. The profiles are derived from the numbers in Table A.1. The isophotal limit is 26 mag arcsec⁻² and $z = 0.25$. The FWHM varied from 1.0'' to 2.0'' in intervals of 0.25''

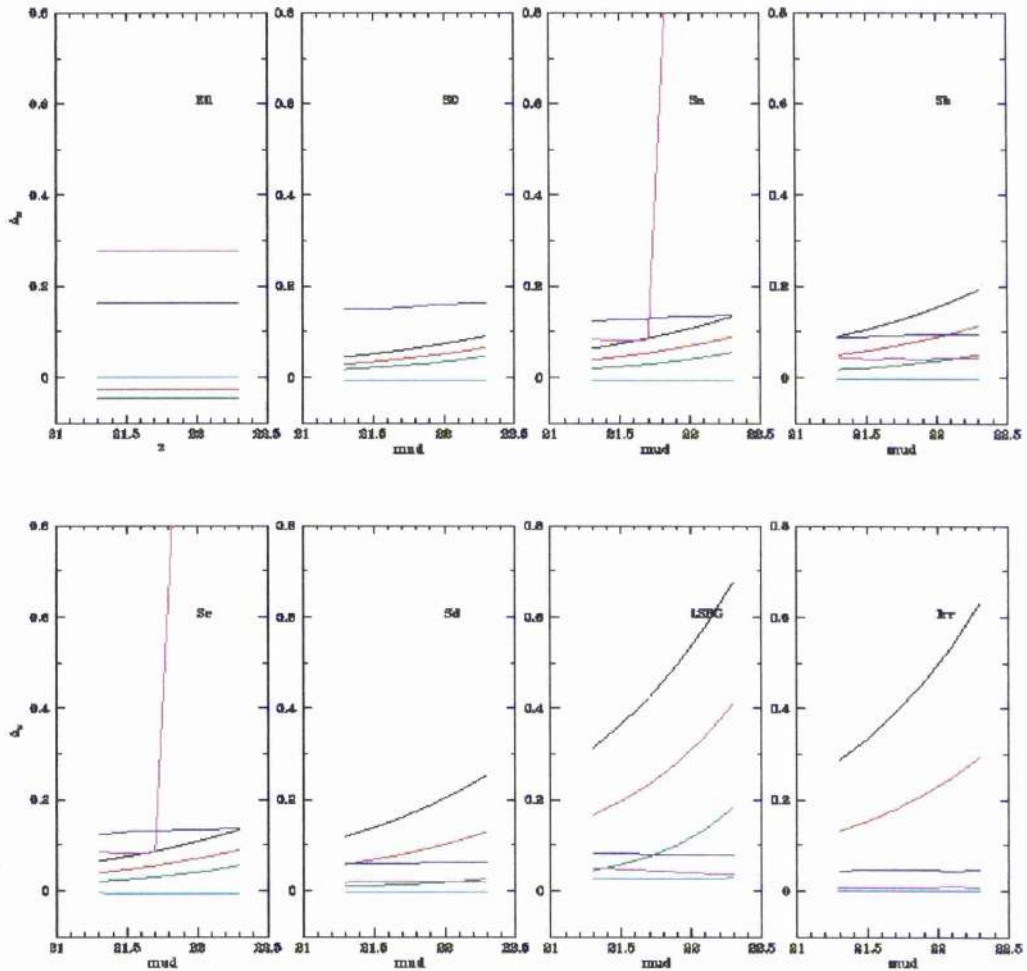


Figure A.9: This plot shows the bias in total magnitude as a function of disk central surface brightness for each type of galaxy in the absence of seeing. The black line represents the isophotal magnitude, the red line represents the Gaussian corrected magnitude, the green represents the exponentially corrected magnitude, the blue represents the Kron magnitude and the magenta represents the Petrosian magnitude. The profiles are derived from the numbers in Table A.1. The isophotal limit is $26 \text{ mag arcsec}^{-2}$ and $z = 0.1$. The disk central surface brightness varied from $21.30 \text{ mag arcsec}^{-2}$ to $22.30 \text{ mag arcsec}^{-2}$ in intervals of $0.2 \text{ mag arcsec}^{-2}$. The disk central surface brightness changed by a corresponding amount in the case of the LSBG ($22.60 - 23.60 \text{ mag arcsec}^{-2}$) and Irregular ($22.30 - 23.30 \text{ mag arcsec}^{-2}$) galaxies.

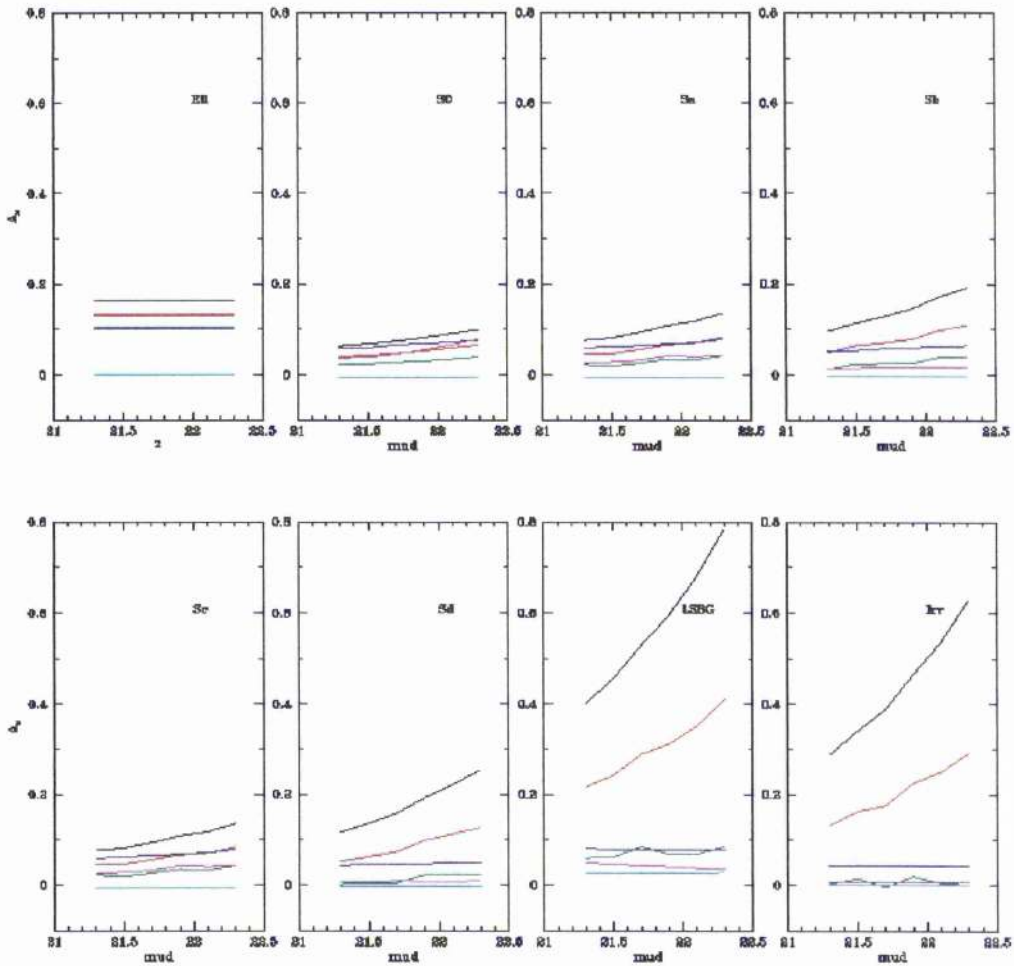


Figure A.10: This plot shows the bias in total magnitude as a function of disk central surface brightness for each type of galaxy in the presence of seeing. The black line represents the isophotal magnitude, the red line represents the Gaussian corrected magnitude, the green represents the exponentially corrected magnitude, the blue represents the Kron magnitude and the magenta represents the Petrosian magnitude. The profiles are derived from the numbers in Table A.1. The isophotal limit is $26 \text{ mag arcsec}^{-2}$, the FWHM is $1.25''$ and $z = 0.1$. The disk central surface brightness varied from $21.30 \text{ mag arcsec}^{-2}$ to $22.30 \text{ mag arcsec}^{-2}$ in intervals of $0.2 \text{ mag arcsec}^{-2}$. The disk central surface brightness changed by a corresponding amount in the case of the LSBG ($22.60 - 23.60 \text{ mag arcsec}^{-2}$) and Irregular ($22.30 - 23.30 \text{ mag arcsec}^{-2}$) galaxies.

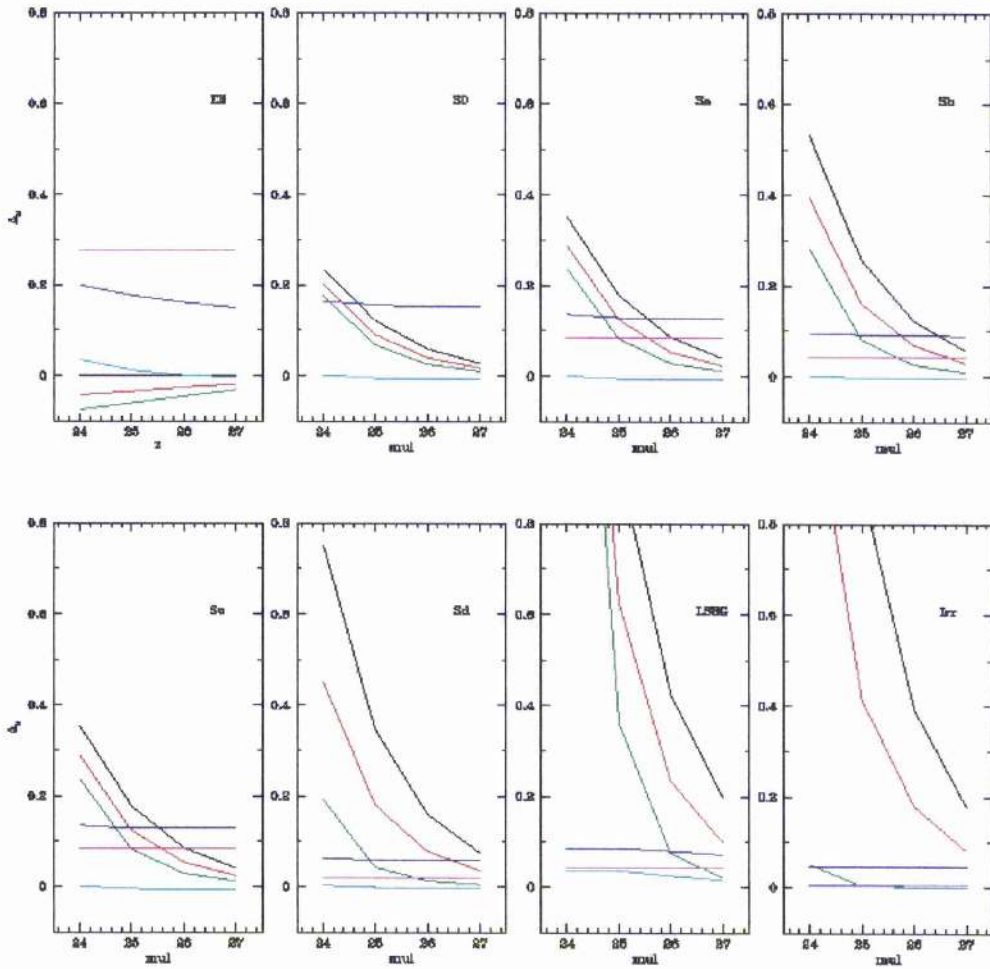


Figure A.11: This plot shows the bias in total magnitude as a function of isophotal limit for each type of galaxy in the absence of seeing. The black line represents the isophotal magnitude, the red line represents the Gaussian corrected magnitude, the green represents the exponentially corrected magnitude, the blue represents the Kron magnitude and the magenta represents the Petrosian magnitude. The profiles are derived from the numbers in Table A.1. $z = 0.1$. The isophotal limit varied from 24 mag arcsec⁻² to 27 mag arcsec⁻² in intervals of 1.0 mag arcsec⁻².

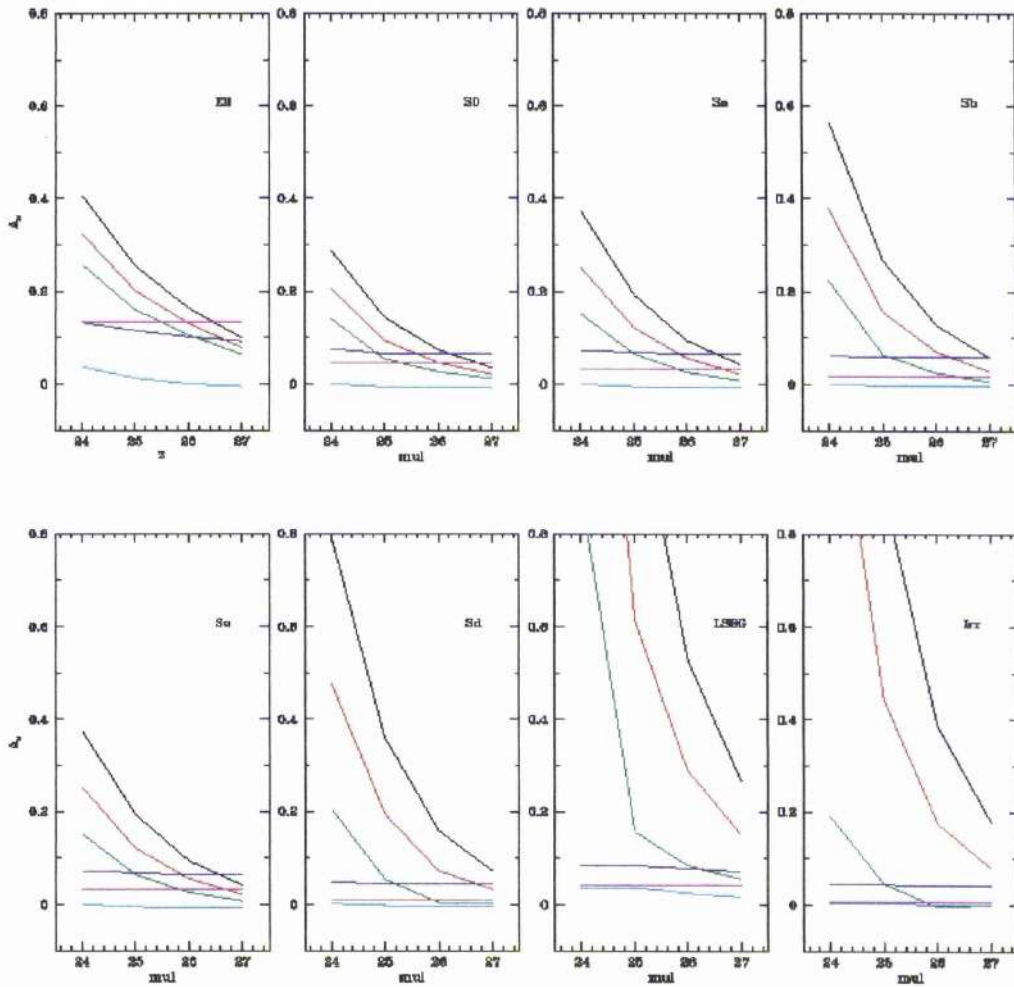


Figure A.12: This plot shows the bias in total magnitude as a function of isophotal limit for each type of galaxy in the presence of seeing. The black line represents the isophotal magnitude, the red line represents the Gaussian corrected magnitude, the green represents the exponentially corrected magnitude, the blue represents the Kron magnitude and the magenta represents the Petrosian magnitude. The profiles are derived from the numbers in Table A.1. The FWHM is $1.25''$ and $z = 0.1$. The isophotal limit varied from $24 \text{ mag arcsec}^{-2}$ to $27 \text{ mag arcsec}^{-2}$ in intervals of $1.0 \text{ mag arcsec}^{-2}$.

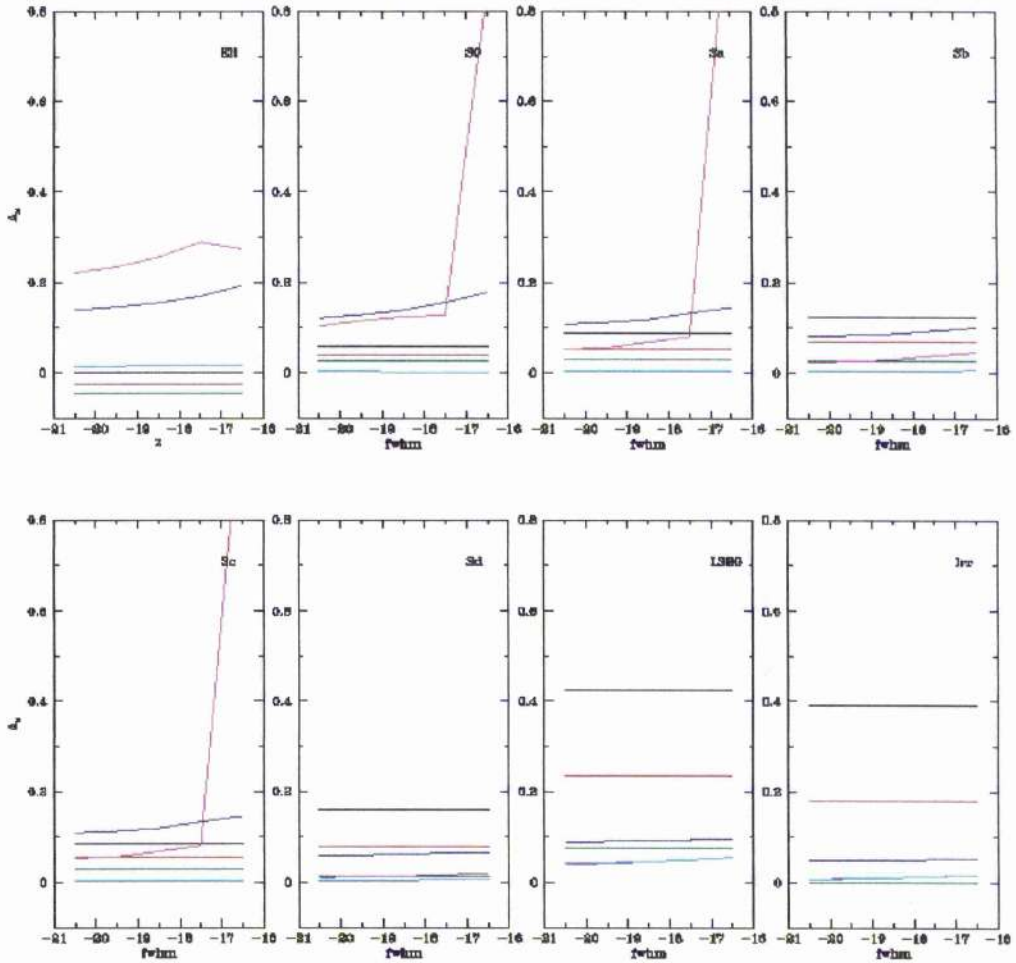


Figure A.13: This plot shows the bias in total magnitude as a function of absolute magnitude for each type of galaxy in the absence of seeing. The black line represents the isophotal magnitude, the red line represents the Gaussian corrected magnitude, the green represents the exponentially corrected magnitude, the blue represents the Kron magnitude and the magenta represents the Petrosian magnitude. The profiles are derived from the numbers in Table A.1. The isophotal limit is 26 mag arcsec⁻² and $z = 0.1$. The absolute magnitude varied from -20.5 mag to -16.5 mag in intervals of 1.0 mag.

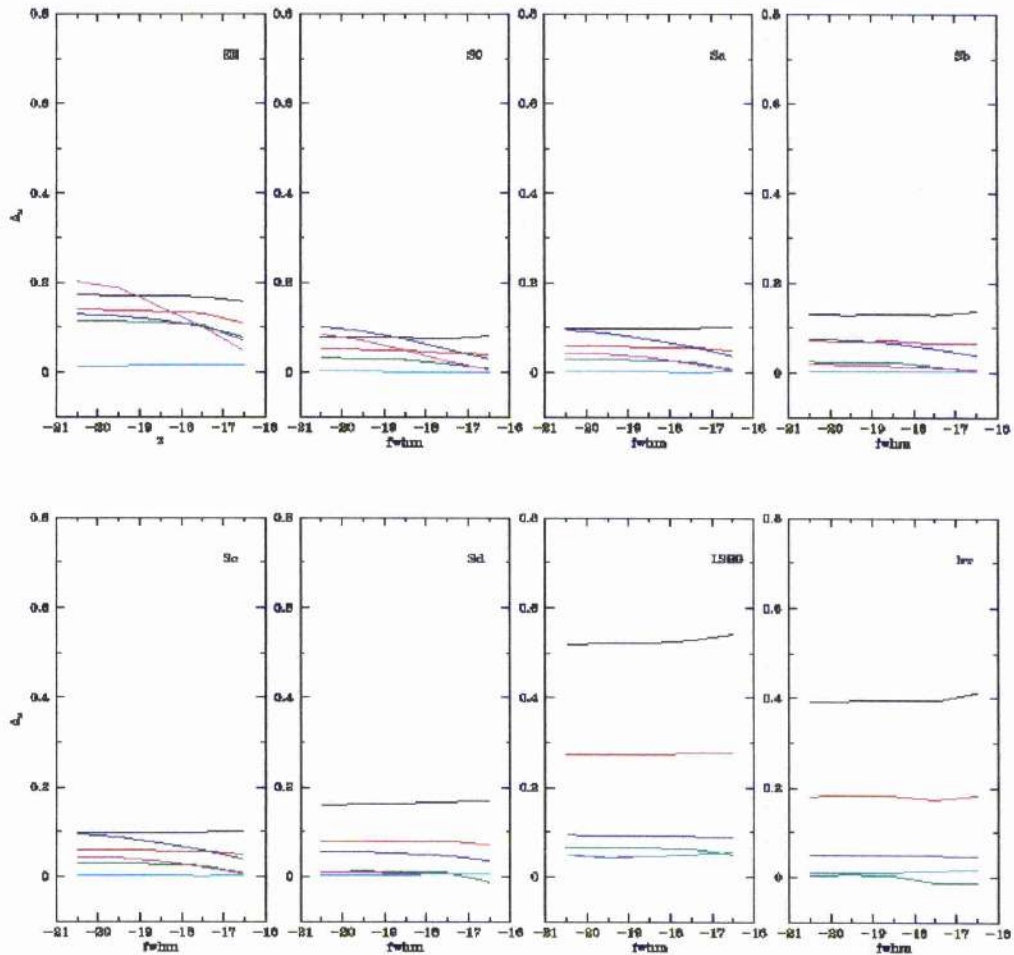


Figure A.14: This plot shows the bias in total magnitude as a function of absolute magnitude for each type of galaxy in the presence of seeing. The black line represents the isophotal magnitude, the red line represents the Gaussian corrected magnitude, the green represents the exponentially corrected magnitude, the blue represents the Kron magnitude and the magenta represents the Petrosian magnitude. The profiles are derived from the numbers in Table A.1. The isophotal limit is $26 \text{ mag arcsec}^{-2}$, the FWHM is $1.25''$ and $z = 0.1$. The absolute magnitude varied from -20.5 mag to -16.5 mag in intervals of 1.0 mag .

The Kron and Petrosian magnitudes are worst for galaxies with large B/T ratios. When there is no seeing the magnitudes get worse with redshift, although the redshift dependence is negligible for late-types. Kron magnitudes measure 91% of the flux for ellipticals, compared to only 81.5% measured by Petrosian magnitudes. However, Petrosian magnitudes will measure 99.3% of the flux for a purely exponential galaxy compared to 96% measured using Kron magnitudes. Thus Petrosian magnitudes have a stronger dependence on B/T .

When seeing is added in, Kron and Petrosian magnitudes actually do better at higher redshift. A pure Gaussian PSF will have 95% of its flux measured using Petrosian magnitudes and 99% using Kron magnitudes, so galaxies with large B/T ratios will benefit immediately. However, galaxies which are close to exponential should get worse. Fortunately, these galaxies are much larger than the seeing disk, and so seeing has only a negligible effect at these redshifts.

Fig. A.5 and Fig. A.6 show the difference in measured surface brightness for different magnitude systems in the absence and presence of seeing respectively. When there is no seeing, both Gaussian and exponential corrections produce surface brightnesses which become fainter with redshift. There is a strong profile dependency, with a 1 mag arcsec⁻² change in estimated surface brightness going from $z = 0.05$ to $z = 0.30$ for elliptical galaxies for both filters, but very little variation seen in late-types when the magnitude is corrected by an exponential profile. The surface brightness of elliptical galaxies is overestimated, for both corrections, but the surface brightness of spirals with large B/T is underestimated. As the spiral galaxy moves from early to late type, the error is reduced for the exponential profile and becomes overestimated for the Gaussian correction.

When seeing is taken into account, the situation becomes more complicated. The variation with redshift is not as strong, and indeed the effective surface brightness can increase with redshift. Galaxies at low redshift are larger, and less affected by seeing than galaxies at high redshift. Thus one would expect the $z = 0.05$ case to be similar in both Fig. A.5 and Fig. A.6, and any differences to increase with redshift. This is broadly the case. Table A.3 shows that the isophotal radii, before seeing, are very similar to the FWHM in the range $0.25 < z < 0.3$, leading to the complicated variation seen at the high redshift end of Fig. A.5.

Fig. A.7 shows the dependence of magnitude error on seeing. The FWHM varies between 1'' and 2'' for an isophote of 26 mag arcsec⁻² and $z = 0.1$. As can be seen, the seeing dependence is extremely small for all profiles and all magnitude types, apart from high B/T Petrosian magnitudes, and to a smaller extent Kron magnitudes. However, at $z = 0.25$ (see Fig. A.8) the seeing dependence increases significantly, as the galaxies appear smaller. In particular the exponential correction begins to overcompensate for late-type galaxies.

The disk central surface brightness, μ_d , dependence is shown in Fig. A.9 for no seeing and Fig. A.10 with seeing. Here the bulge is kept constant. The aperture magnitudes show no dependence on μ_d whereas the isophotal, Gaussian and exponential magnitudes all show a strong dependence.

The isophotal μ_{lim} dependence is shown in Fig. A.11 for no seeing and Fig. A.12 with seeing. The aperture profiles show almost no dependence on μ_{lim} whereas the isophotal, Gaussian and exponential magnitudes all show a very strong dependence. The Kron magnitude varies slightly for large B/T because the steep profiles of these galaxies hit noise limits for bright values of μ_{lim} .

The variation of Δm with M is shown in Fig. A.13 for no seeing and Fig. A.14 with seeing. There is no dependence on M for either the isophotal, the Gaussian corrected or the exponentially corrected magnitudes. However there is a M dependence for the Kron and Petrosian magnitudes especially for bulge dominated galaxies. In Fig. A.14 seeing effects dominate as both the Kron and Petrosian magnitudes *improve* at fainter absolute magnitudes when they are bulge dominated.

A.1.2 Problems of Inclination

However late types will be more effected by inclination. To model this, we have assumed that a disk galaxy is optically thin and has no internal extinction. We look at the problem of using the mean isophotal radius to calculate the effective surface brightness as in Cross et al. (2001).

A galaxy of area A_{iso} , was assumed to have an isophotal radius r_{iso} , given by:

$$A_{iso} = \pi r_{iso}^2 \quad (\text{A.17})$$

The isophotal magnitude and radius were used to calculate the total magnitude and the effective surface brightness μ_e as described in Cross et al. 2001.

However a disk galaxy, inclined at an angle, i with major axis a and minor axis b has an area

$$A_{iso} = \pi ab \quad (\text{A.18})$$

where

$$b = a \cos(i) \quad (\text{A.19})$$

The surface brightness has increased at each point by a factor $\frac{1}{\cos(i)}$, increasing the semi-major axis until $\mu(a) = \mu_{lim}$.

$$a = \alpha 0.4 \ln(10) [\mu_{lim} - \mu_0 - 2.5 \log_{10} \cos(i)] \quad (\text{A.20})$$

where α is the disk scale length. This increases the isophotal flux of the galaxy, as well as the isophotal radius.

$$r_{iso} = \sqrt{ab} \quad (\text{A.21})$$

$$\begin{aligned} m_{iso} &= m_{tot} - 2.5 \log_{10} f \\ f &= 1 - \left(1 + \frac{a}{\alpha}\right) e^{-\frac{a}{\alpha}} \end{aligned} \quad (\text{A.22})$$

An exponential profile is fitted to these parameters as in Cross et al. (2001). The central surface brightness and total magnitude are calculated for this galaxy assuming that the galaxy

is face on. The error in the central surface brightness is the difference between the true central surface brightness and the calculated central surface brightness. The error in the effective surface brightness is exactly the same, as the difference between central and effective surface brightness is a constant for an exponential profile. The total magnitude calculated above is the same as the true total magnitude.

$$\Delta \mu_0 = \mu_{0,meas} - \mu_{0,true} \quad (\text{A.23})$$

The probability of a galaxy of inclination θ lying between i and $i + di$ is:

$$P(i < \theta \leq i + di) = \frac{1}{2} \sin(i) di \quad (\text{A.24})$$

Therefore the mean difference in measured and face-on effective surface brightness is:

$$\Delta \bar{\mu}_e = \frac{1}{2} \int_0^{\pi/2} \Delta \mu_0 \sin(i) di = -0.477 \quad (\text{A.25})$$

Thus the calculated effective surface brightnesses of late-type galaxies may be 0.48 mag too bright. However more complicated effects such as seeing, the thickness of the disk and internal extinction will all tend to reduce the measured surface brightness of edge on disks to a greater degree than face-on disks, reducing the mean offset.

The overall effects of bulge-disk decomposition and inclination appear to be to make M^* brighter by 0.1 mag and μ_e^* fainter by 0.55 mag arcsec⁻², 0.5 mag arcsec⁻² for Sals due to the bulge and 0.1 mag arcsec⁻² for Sds due to the bulge and 0.5 mag arcsec⁻² due to inclination. It is difficult to be precise about this as the morphological mix of galaxies in the 2dFGRS is not known.

A.1.3 Summary and Discussion of Magnitude Systems.

Dalcanton (1998) showed that there isophotal magnitudes suffer from strong surface brightness and redshift dependence for both exponential and elliptical profiles. She found that the variation is almost constant until the redshift brings the central surface brightness close to the isophote and then ΔM rises "precipitously". Fig. A.3 & A.4 show this rise for the LSBG and Irregular galaxy. Dalcanton also showed that magnitudes could be better estimated in good seeing. At low redshifts there is little or no seeing effect with any magnitude system, as the isophotal radius is much larger than the FWHM, but at high redshifts (see Fig. A.8) the isophotal magnitudes get significantly worse with seeing. However, other systems such as the Gaussian correction and exponential correction increase the amount of flux detected with increased seeing. A Gaussian correction, of course, would be perfect when the seeing completely dominates the profile. In the case of a galaxy which is fitted well by an exponential profile, an exponential correction under poor seeing will overestimate the flux.

Dalcanton (1998) also looked at aperture magnitudes and found that Kron magnitudes give a $\Delta M > 0.3$ when $\mu_{lim} - \mu_0 < 3$. Neither Fig. A.9 & A.10 show this, and indeed show that

Kron magnitudes show little variation with μ_d . The conflict may be due to the slightly different definitions of Kron radius used. Here $r_K = 2.5r_1$, whereas Dalcanton used $r_K = 2.0r_1$. Driver (1998) argues for $r_K = 3.5r_1$ based on the smallest radius at which the photometric error had reduced to less than the zero-point. Bershadly et al. (1994) point out that increasing the radius can reduce the signal to noise ratio, as you pick up a lot more noise for little extra signal. Increasing the aperture also increases the chance of contamination by nearby neighbours and this leads to deblending problems.

Petrosian magnitudes can also be improved by increasing the magnification factor for the radius, but this suffers from the same problems as above. The main advantage is the surface brightness independence. Galaxies of with the same profile will have the same magnitude regardless of the isophote (see Fig. A.11 & A.12). The definition of the Petrosian radius, Eqn A.11 depends on the flux in a small annulus. In a real, pixelated system, the value of R_P can vary enormously, particularly at small radii, hence the abrupt changes in magnitude in Figs A.3 & A.4.

While surface brightnesses are determined from the fitted profiles for Gaussian and exponential profiles, there is no similar treatment available for Kron or Petrosian magnitudes. However half-light radii can be measured by growing apertures until half the flux of the Kron or Petrosian is found. If the error in the flux is small then the error in the half-light radius and effective surface brightness is small. The surface brightnesses obtained from the fitted profiles are poor, often out by 1 mag at low redshift and can lead to errors later when calculating the bivariate brightness distribution.

When all these effects are considered, Kron magnitudes are the most dependable. They have the least redshift and profile dependence. Petrosian magnitudes also have a low redshift dependence and no surface brightness dependence but unfortunately have a stronger dependence on B/T .

A.2 Detecting Galaxies and Separating them from Stars

If an object is going to be detected, it must have several connected pixels with a flux greater than the isophotal limit. For the MGC we set the isophotal limit at 26 mag arcsec⁻², and have a minimum of 10 pixels. This is done to limit the number of spurious noise and cosmic ray detections. If the limiting isophote is the level of 2σ variations in noise, then there is a 4.6% chance that any particular pixel is due to noise. Thus the chance that all 10 pixels are noise is 4×10^{-14} . With 0.333 arcsec wide pixels, the faintest detectable objects have $m = 25.89$.

Galaxies which have an even lower surface brightness, so that they have less than 10 connected pixels brighter than 26 mag arcsec⁻² will be missed. This will include 19th mag galaxies with a central surface brightness of 26.5 mag arcsec⁻², which is a problem if the survey is supposed to be complete to 20th mag. It will also miss a 25.5 mag arcsec⁻² galaxy with scale length smaller than 1 arcsec. Happily this galaxy would have a total magnitude of 23 and be well below the limit of most redshift surveys. Fig A.15 shows a plot of apparent total magnitude against central surface brightness for 3 profiles, an elliptical, an exponential and a spiral, with the criterion $r_{iso} = 0.564''$, the radius encircling an area of 10 pix². The Gaussian is the most important, because all objects of this size will be seeing dominated. The

lowest magnitude achievable is 25.08 mag.

Other detection problems include the dynamic range of the detector, the size of the detector and scale errors in the detection threshold. Detectors saturate at a certain flux level which will depend on the exposure time. As exposure times increase to go for deep objects to increase the completeness of the catalogue, high surface brightness objects such as stars and ellipticals will flood the CCDs or photographic plates. CCDs have a dynamic range of $\sim 10^4$, whereas photographic plates have a much lower dynamic range of $\sim 10^2$. The saturation level puts limits on the accurate measurement of high surface brightness objects. This can be remedied by taking multiple exposures to reduce saturation and adding them together to get to lower flux limits. This has another advantage as cosmic rays, satellite trails and noise can be more easily removed if 3 or more exposures are taken. These objects would be expected to appear on one image, so taking the mode or clipped mean of each pixel will remove these objects. However, the additional overhead in terms of CCD readout times puts limits on the number of exposures it is worth taking.

The maximum size of an object is limited by the boundaries of the detector for high surface brightness objects and the flatness of the isophote and the reliability of the background estimation for low surface brightness objects. The size of the detector is limited by technology. CCDs are smaller than photographic plates, but have increased in size dramatically over the past few years. The flatness of the isophote depends on how well the flat-fielding reduced pixel-to-pixel variations over the CCD. The software / hardware used to detect objects can also put constraints on the maximum size, e.g. the sky subtraction process in the APM (Maddox et al. 1990a) and the local background estimator used in SExtractor (Bertin & Arnouts 1996).

A minimum size can also be placed on galaxies, either due to the minimum number of connected pixels from signal-to-noise constraints, or due to star-galaxy separation. The star-galaxy separation is usually the stricter constraint, so it will override the signal-to-noise constraint. A star is essentially a point source, and a galaxy is an extended object. However, atmospheric turbulence (or just diffraction in the case of space based telescopes) produces a Point Spread Function which means that galaxies with isophotal radii smaller than the seeing may be mistaken for stars. In fact 5 un-resolved compact dwarf galaxies have been found in the Fornax cluster (Drinkwater et al. 1999) by taking the spectra of every object. However, unlike photometry which can be done for every object in the field of view, spectroscopy has to be targeted. The best multi-fibre spectrometers can do a few hundred redshifts in an hour (e.g. 2dFGRS Colless et al. 1999, SDSS, York et al. 2000), so large redshift surveys ($> 100,000$ z's) are very time consuming. Therefore it is not sensible to take redshifts of every object to increase the completeness of your catalogue as you will flood it with stars which outnumber galaxies by 3 to 1 at the magnitude limit of today's large surveys, even at high galactic latitudes.

This minimum size is seeing and magnitude dependent and can be reduced slightly by careful profiling of objects. To get around this problem, some galaxy catalogues (e.g. van der Kruit 1987, O'Neil & Bothun 2000, de Jong & Lacey 2000) have imposed a strict diameter limit (1-2 arcmin), much larger than the seeing. These galaxies are also much easier to profile, with accurate bulge and disk parameters. However, the samples are bright and small, and limited to a small region of the total parameter space of the BBD.

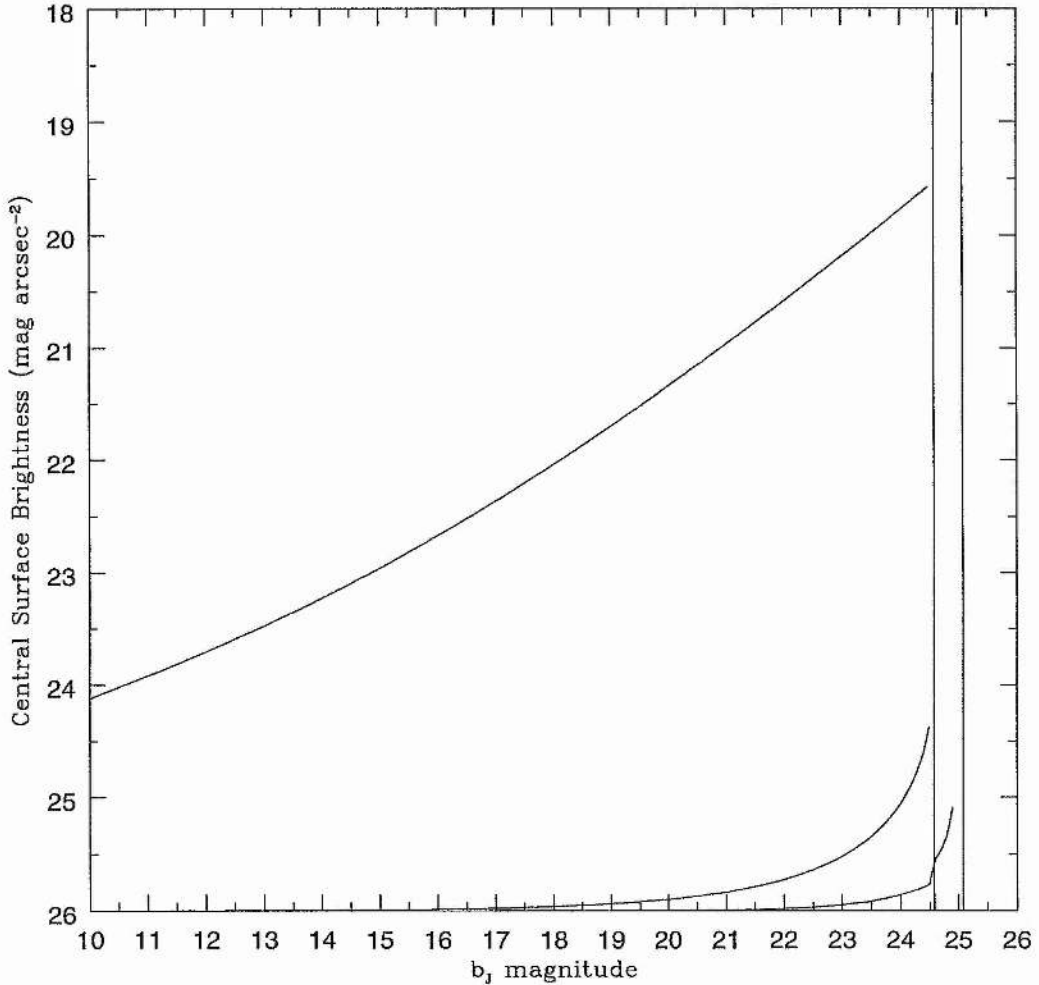


Figure A.15: This plot shows the lowest central surface brightness possible for different profile types as a function of apparent magnitude, when the isophote is $26 \text{ mag arcsec}^{-2}$ and the minimum size is 10 pixels, with a pixel size equal to $0.333''$, giving a minimum radius $r_{iso} = 0.564''$. The upper curve shows the variation for a de Vaucouleurs profile, the middle curve shows the variation for an exponential profile and the lower curve shows the variation for a Gaussian profile. The two vertical lines represent the apparent magnitude limits for each object. Both the de Vaucouleurs profile and exponential profile objects have a faintest apparent magnitude $m = 24.6 \text{ mag}$. The Gaussian profile objects are limited at $m = 25.08 \text{ mag}$. Since real objects of this size will be dominated by the seeing, this represents the faintest magnitude for all objects.

It is important to understand these detection limits when calculating the number counts or luminosity function. The detection limits can be reasonably well described by five numbers, the isophotal detection threshold μ_{lim} , the faint magnitude limit m_{faint} , the bright magnitude limit m_{bright} , the maximum diameter d_{max} , and the minimum diameter d_{min} . The faint magnitude limit is usually determined by the limit at which a redshift survey can maximise its science goals within a reasonable amount of time, rather than the limit to which objects can be detected (which tends to be several magnitudes fainter). The minimum diameter limit will be determined by the star-galaxy separation, the maximum diameter limit will be determined by flat-fielding/sky subtraction problems. The bright magnitude limit removes a few very large galaxies which will be either large or very high surface brightness. These tend to be partly outside the field of view (or at least the CCD) because of their large size. They are difficult objects for detection programs as they are likely to be merged with other objects or defects and are likely to be saturated at the centre. The contribution of large normal or high surface brightness to the overall number of galaxies is extremely small, and they can be easily picked out by eye, but the contribution of large low surface brightness galaxies is unknown.

A.2.1 Demonstrating Visibility

In § 2.4 we discussed visibility theory. In this section, we will demonstrate how the volume over which a galaxy can be seen varies with the different limits. Below are various plots demonstrating the problems associated with surface brightness, using the method developed above. All the plots below use exponential profiles and an Einstein-de-Sitter Universe. Fig. 2.13 shows how the visibility surface varies with surface brightness. The isophotal magnitudes as discussed above are shown as thin lines.

Fig. A.16 shows the complex Malmquist bias for $\mu_{lim} = 24, 24.5, 25.0, 25.5, 26.0, 26.5$ and 27.0 mag arcsec⁻² (top left to bottom right). The lines are contours of constant volume for that μ_{lim} . As the limiting isophote becomes brighter, the surface brightness dependency of the Malmquist bias increases. Luminosity functions constructed using a $1/V_{max}$ or an estimator which depend on the absolute magnitude of the galaxy but not the surface brightness, are implicitly assuming an infinite isophote as shown in the top left figure of Fig. A.16. However, even if total magnitudes are used, the visibility of galaxies does have a surface brightness component, due to the minimum isophotal size of an object. This can be very severe by 23 mag arcsec⁻², galaxies at all magnitudes are biased.

Davies (1990) showed that there was a noticeable decrease in visibility as the bulge-to-total ratio increases, implying that morphological mixes are biased towards the most visible later types. However LSBs have their visibilities improved by bulges. These two statements can be understood by considering the most important criteria, namely isophotal magnitude and isophotal diameter. For a given magnitude, an increased bulge-to-total ratio will decrease the scale length of the galaxy. If this galaxy is placed at increasing redshift then although it can be seen out further before its central surface brightness reaches the isophotal limit, a typical galaxy will reach the diameter limit more quickly. However, a LSBG, which is limited by the surface brightness limit rather than the diameter limit will be seen out further now that its central surface brightness has increased. Davies points out that two galaxies with extremely

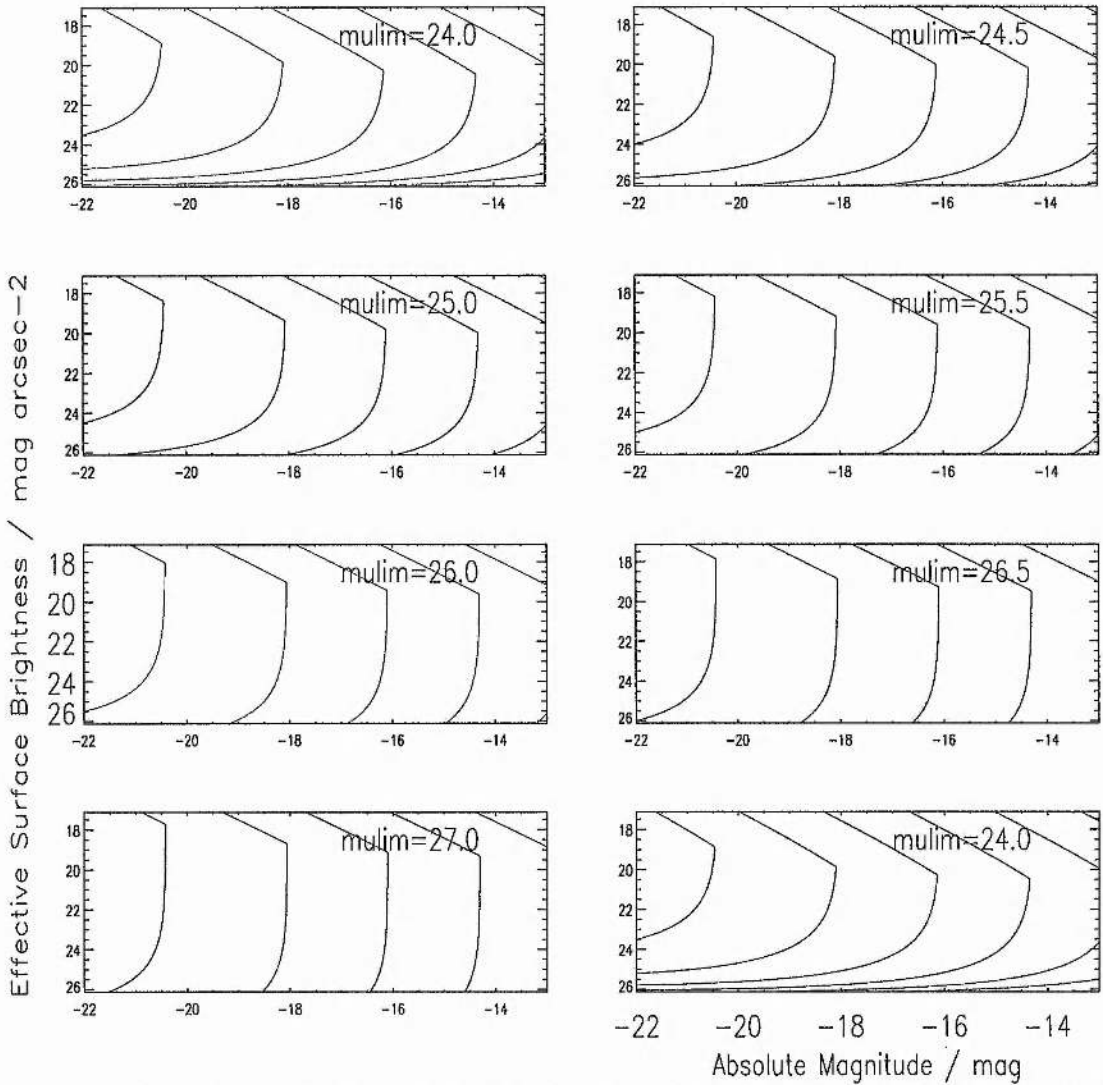


Figure A.16: This plot shows contours of equal volume for selection functions with different isophotal detection limits. The top, left plot shows the selection function for a limit of 24.0 mag arcsec⁻². The other plots show isophotal selection functions, for the limits 24.5, 25.0, 25.5, 26.0, 26.5 & 27.0 mag arcsec⁻². As one goes to brighter thresholds, the volume becomes a stronger function of surface brightness, and a narrow peak in surface brightness is seen.

LSB disks have been found with prominent bulges (Malin 1, Bothun et al. 1987 and GP1444a, Davies, Phillipps & Disney 1988). Davies shows that the surface brightness distribution has a narrow peak, but this is mainly due to a large value of d_{min} , as can be seen in Fig. A.17

In Davies (1990), the author looks at visibility for data with strict limits, $d_{min} = 10 - 15''$, so a narrow peak in surface brightness is expected. The advantages of having a large value of d_{min} are that the data will not be contaminated with stars and they will only be galaxies with well defined magnitudes and surface brightnesses and have minimal seeing effects. The disadvantages are clear: a very limited parameter space and horrendous surface brightness effects to take into account when estimating the luminosity function.

Fig A.18 demonstrates the visibility function produced from a combination of minimum isophotal diameter limits and total magnitude limits. For $d_{min} > 10''$, Fig A.18 is identical to Fig A.17 as the diameter limit dominates throughout the parameter space. At lower limits, the changeover between the two regimes is obvious.

Fig. A.19 and Fig. A.20 demonstrate the effects of a maximum diameter limit on observations. There appear to be no effects for maximum diameters above $50''$, and there are no strong effects at the $20''$ limit but there are strong effects for large low surface brightness galaxies below this limit. The limits due to the sizes of CCDs will generally be $\geq 100''$. Flat-fielding and sky-subtraction problems may occur on smaller scales, so these need to be monitored carefully. It seems unlikely that there will be serious problems on a scale of $< 20''$, so the maximum diameter is not a major issue.

In the previous sections the effects of visibility have discussed with regard to sampling the parameter space of galaxies. It is clear that the effect of some selection criteria is negligible up to a point and then it can dominate, as is clear from Fig A.17 for example. Some criteria such as the isophotal detection threshold are fairly clear cut and simple to understand. Either the galaxy has 10 connected pixels above the threshold or it does not - for all intents and purposes either its central surface brightness is higher or lower than this limit. However isophotal magnitude and diameter limits are sensitive functions of the apparent profile and the detection isophote. Even "corrected" magnitudes have at least a profile dependence, and with seeing included a redshift dependence. This means that the visibility function is a complex function of M and μ and will be different for each different type of galaxy. When seeing is added in it is incredible complicated to calculate how far out a galaxy can be seen.

A better method of calculating the luminosity function or a bivariate brightness distribution would be to limit the population of each type at a lower redshift than the furthest seen. To do this, first select your sample, with well understood selection boundaries and measure redshifts of all the galaxies over that range. Then take a sample selected from within these boundaries over a certain range in M and μ . For example, take the case of $\mu_{lim} = 26 \text{ mag arcsec}^{-2}$ and $d_{lim} = 3.0''$ and $m_{tot} = 20. \text{ mag}$, shown in Fig A.18. If one took a box over the range $-22 < M < -16.5$ and $21 < M < 24.5$, then any galaxy in this range could be seen out to at least $z = 0.05$. By restricting the galaxies to a small range in parameter space and redshift, a 100% complete sample that is free from selection biases is created. From the same data many of these volume limited cuts can be drawn, to probe different parts of parameter space, or to look at evolution, so very little data is wasted. Inevitable some data will be thrown away,

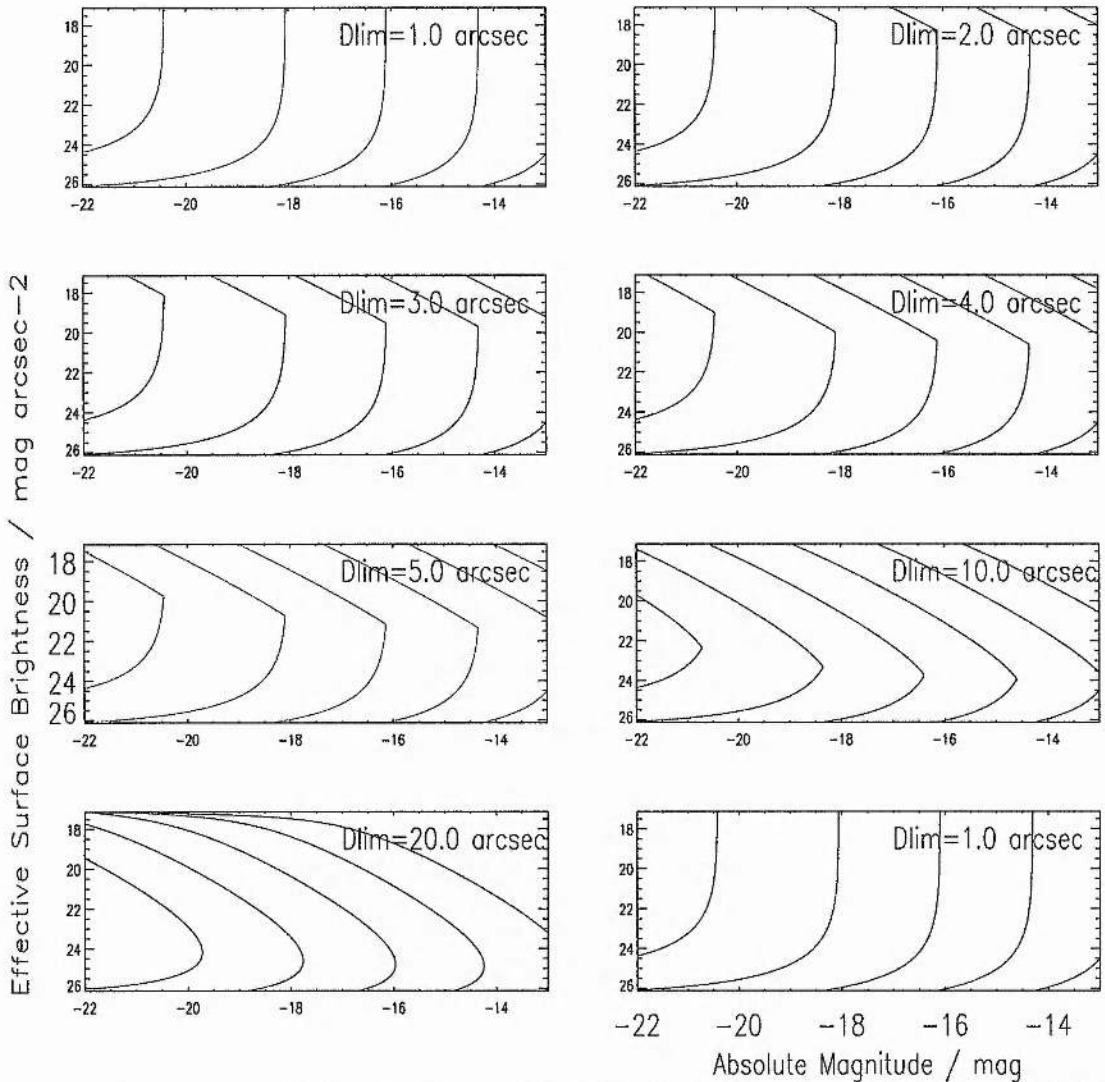


Figure A.17: This plot shows contours of equal volume for selection functions with different minimum diameter limits. The top, left plot shows the selection function for a diameter limit of 1.0". The other plots show isophotal selection functions, for the diameter limits 2.0, 3.0, 4.0, 5.0, 10.0 & 20.0". The threshold is 26 mag arcsec⁻². As one goes to larger minimum diameters, the volume becomes a stronger function of surface brightness, and a narrow peak in surface brightness is seen.

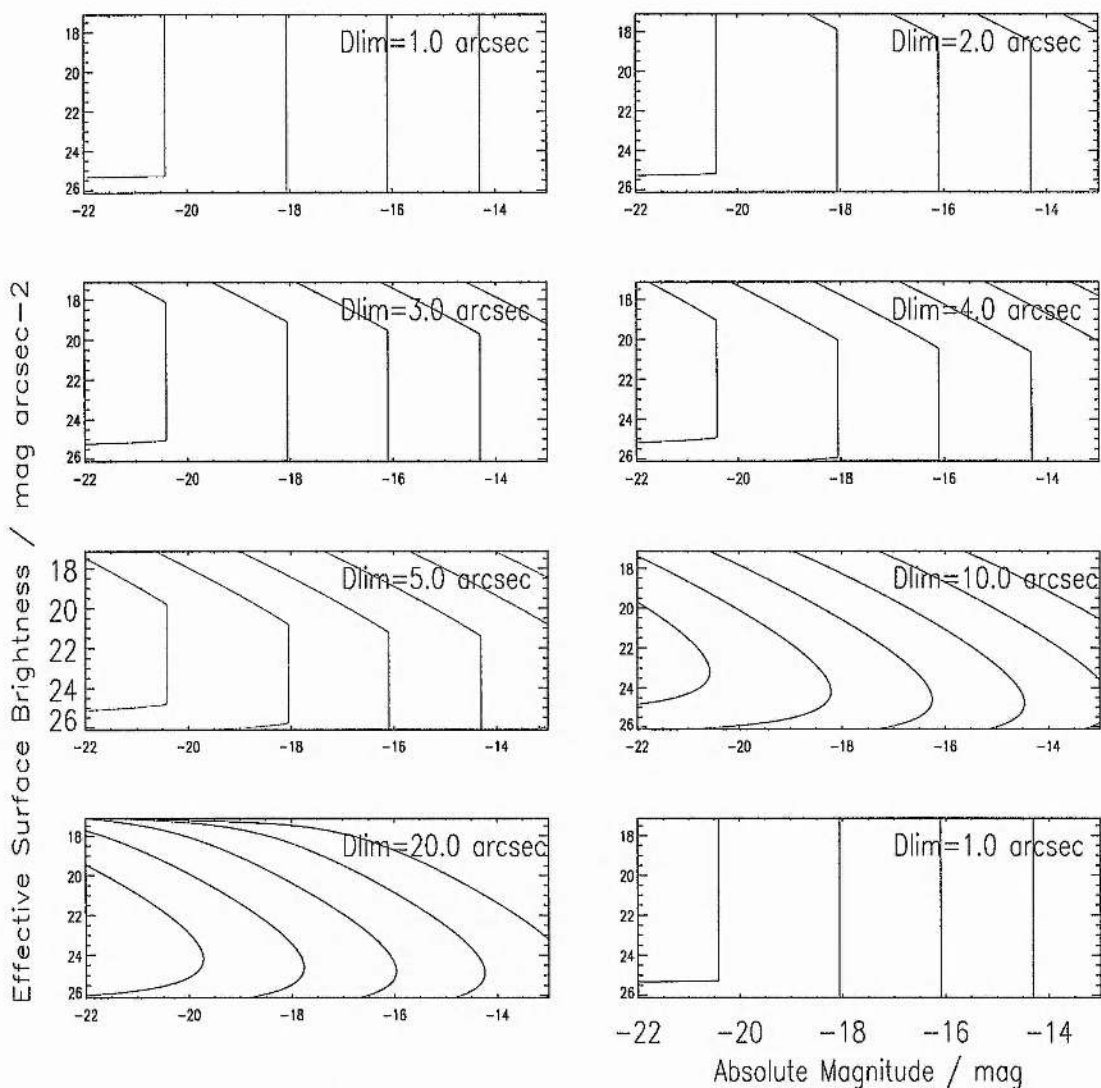


Figure A.18: This plot shows contours of equal volume for selection functions with different minimum diameter limits. The top, left plot shows the selection function for a diameter limit of 1.0". The other plots show total selection functions, for the diameter limits 2.0, 3.0, 4.0, 5.0, 10.0 & 20.0". The threshold is 26 mag arcsec⁻². As one goes to larger minimum diameters, the volume becomes a stronger function of surface brightness, and a narrow peak in surface brightness is seen.

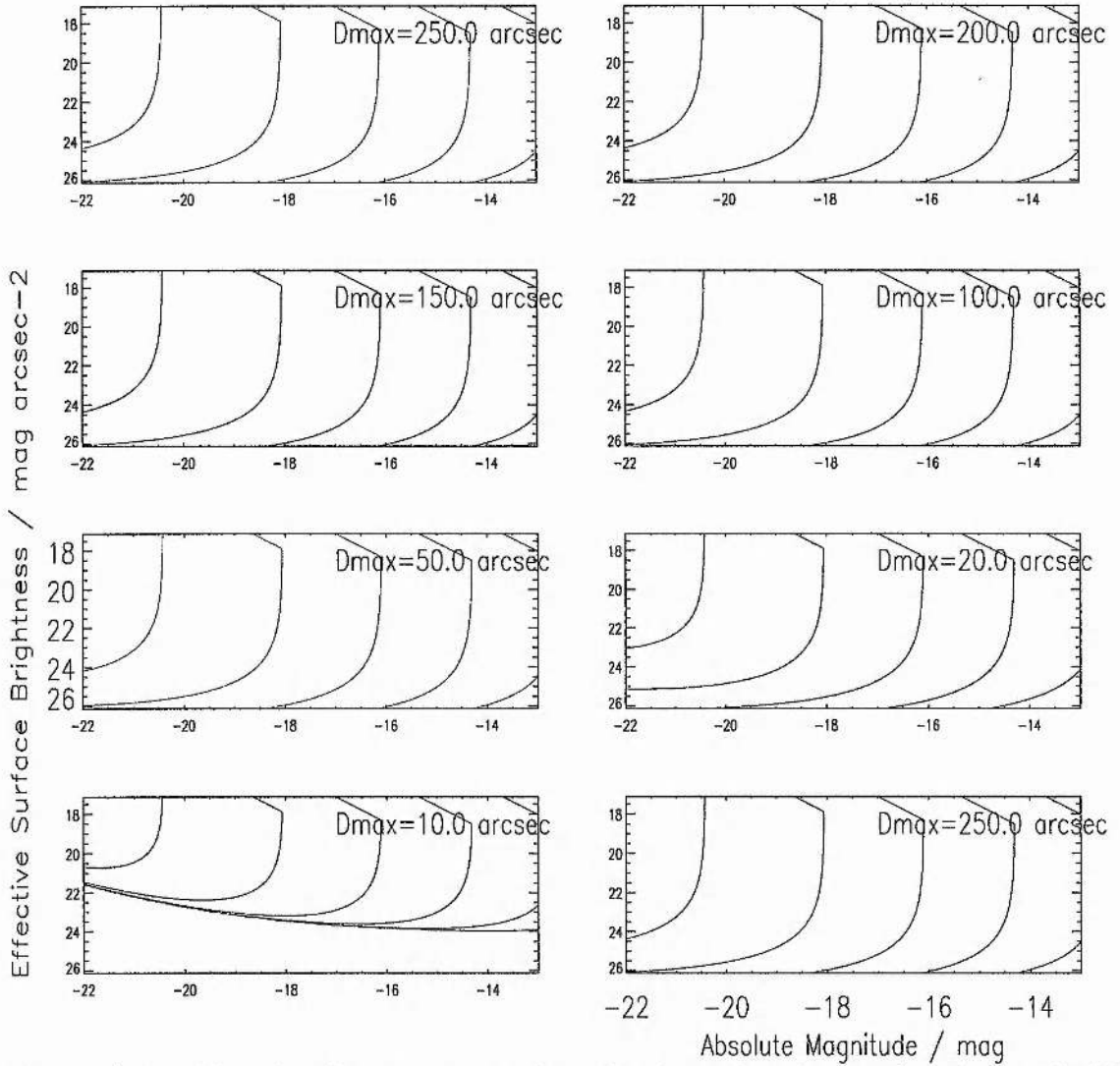


Figure A.19: This plot shows contours of equal volume for selection functions with different maximum diameter limits. The top, left plot shows the selection function for a diameter limit of 1.0". The other plots show total selection functions, for the diameter limits 2.0, 3.0, 4.0, 5.0, 10.0 & 20.0". The threshold is 26 mag arcsec⁻². As one goes to larger minimum diameters, the volume becomes a stronger function of surface brightness, and a narrow peak in surface brightness is seen.

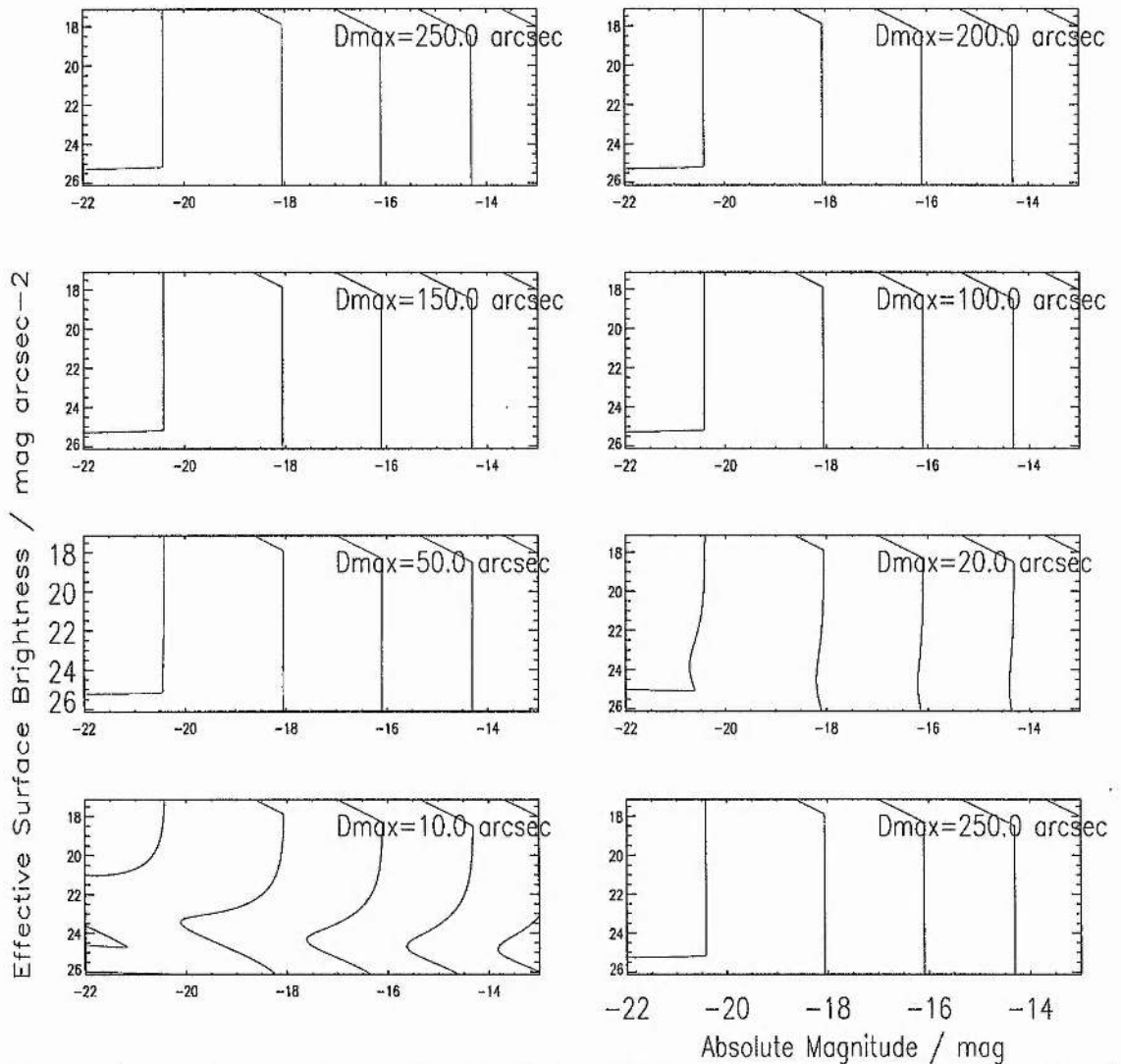


Figure A.20: This plot shows contours of equal volume for selection functions with different maximum diameter limits. The top, left plot shows the selection function for a diameter limit of 1.0". The other plots show total selection functions, for the diameter limits 2.0, 3.0, 4.0, 5.0, 10.0 & 20.0". The threshold is 26 mag arcsec⁻². As one goes to larger minimum diameters, the volume becomes a stronger function of surface brightness, and a narrow peak in surface brightness is seen.

but it will only be the data at the edge of the visibility surface, where photometric errors are greatest, even under the best magnitude systems. The information content of this data is poor, and the likely bias is too great for it to be worth using.